ANISOTROPY IN THE ELECTRICAL, MAGNETIC AND OPTICAL PROPERTIES OF $Pb_2Sr_2RCu_3O_8$

By

MAUREEN REEDYK, B.Sc., M.Sc.

A Thesis

Submitted to the Faculty of Graduate Studies

in Partial Fulfilment of the Requirements

for the Degree

Doctor of Philosophy

McMaster University

DOCTOR OF PHILOSOPHY(1992) McMASTER UNIVERSITY

(Physics) Hamilton, Ontario

TITLE: Anisotropy in the Electrical, Magnetic and Optical Properties of $Pb_2Sr_2RCu_3O_8$

AUTHOR: Maureen Reedyk, B.Sc. (Trent University)
M.Sc. (McMaster University)

SUPERVISOR: Professor T. Timusk

NUMBER OF PAGES: xii, 241

ELECTRICAL, MAGNETIC AND OPTICAL PROPERTIES OF $Pb_2Sr_2RCu_3O_8$

ABSTRACT

The layered structure of the cuprate superconductors leads to a significant anisotropy between *ab*-plane and *c*-axis properties which is significantly greater in $Bi_2Sr_2CaCu_2O_8$ (BSCCO) than in $YBa_2Cu_3O_{7-x}$ (YBCO); likely due to differences in intercalary structure since both systems contain double CuO_2 layers. $Pb_2Sr_2(Y/Ca)Cu_3O_8$ (PSYCCO) is another system containing double CuO_2 planes which are separated by a PbO-CuO_δ-PbO sequence, the PbO bi-layer analogous to the double BiO sheets in BSCCO and the CuO_δ layer comparable to an oxygen depleted chain layer such as in $YBa_2Cu_3O_6$. The structural similarities render this material a good candidate for further study.

Measurements of anisotropy in the dc-resistivity, magnetization and optical properties of PSYCCO are presented. The magnetization measurements are analyzed to extract both the in-plane and *c*-axis fundamental superconducting parameters of this material: T_c, the magnetic penetration depth, the coherence length, the upper and lower critical fields, and the upper critical field slope near T_c. The dc-resistivity is an order of magnitude larger than in both YBCO and BSCCO while the optically-derived plasma frequency is considerably smaller than in the other systems. Together with a large penetration depth this suggests that the carrier concentration is unusually small given the high transition temperature ($\approx$ 80 K), and represents a significant deviation from a proposed universal relationship between level of doping and T_c. The extent of the anisotropy in this system is found to be similar to that in YBCO. The low carrier density has facilitated observation of unusual behaviour in the optical properties such as a large finite frequency-centered peak which develops in the optical conductivity upon entry into the superconducting state.

The doping dependence of the *ab*-plane optical properties is investigated via the Ca-free $Pb_2Sr_2RCu_3O_8$ series, which exhibits a metal/insulator transition as a function of increasing ionic radius of the rare earth. A transfer of spectral weight from

the CuO charge transfer band to lower frequencies accompanies the progression to metallic character. As this electronic background develops phonons in the far infrared reflectance of the insulating members become weaker while concurrently there is an appearance of new phonon modes in the 400-600 cm^{-1} region of the spectrum. These phonons develop an antiresonant-like lineshape at higher doping levels. Examination of several high T_c superconductors with similar structure leads to the hypothesis that these features are due to the coupling of longitudinal c-axis phonons to the ab-plane mid infrared continuum. A surprising consequence, confirmed by experiment, is that due to momentum conservation the ab-properties are different when measured on the ab-plane face and along the a or b directions of a face containing the c-axis.

ACKNOWLEDGEMENTS

I am grateful to my supervisor, Dr. T. Timusk, for providing the opportunity to develop independent research skills by carrying out a very much self-directed project. His confidence, and continued support are a very much valued contribution, as are the many suggestions and helpful discussions. I am appreciative of the numerous opportunities to attend conferences, meet with visitors, and carry out collaborative research with groups outside of McMaster that he has provided. As well, I am grateful to the other members of my supervisory committee, Dr. J.E. Greedan, and Dr. C.V. Stager for their continued interest and participation in the project.

This research could not have been carried out without Simon Xue, together with whom I have experienced the many successes and occasional disappointments that this project has yielded. From Simon I have learned the true meaning of collaboration.

A very special thank you goes out to Barbara Zvan who for two summers with great skill and independence provided, among other things, much needed assistance with dc resistivity and mid infrared reflectance characterization measurements.

I am grateful to Dr. J.C. Irwin and the members of his group at Simon Fraser University, in particular Eric Altendorf, for their hospitality and assistance during the time that I spent there carrying out the Raman measurements.

I thank Dr. J.P. Carbotte for the opportunity to meet with other Canadians working in the field of superconductivity through two Canadian Institute for Advanced Research (CIAR) meetings.

I have benefited from discussions regarding various aspects of this work with Dr. A.J. Berlinsky, Dr. J.H. Brewer, Dr. J.P. Carbotte, D.A. Crandles, Dr. C.C. Homes, Dr. J.C. Irwin, Dr. F. Marsiglio, Dr. E.J. Nicol, Dr. J. Preston and Dr. D.B. Tanner.

I thank Thomas Krause for his comments regarding the section of this thesis concerning the magnetic field dependence of the resistivity.

As well, I am appreciative of contributions by Edmund Fok, Steven Lisgo, Milan Maric, and Alex Tran to the general research effort directed towards $Pb_2Sr_2RCu_3O_8$ at McMaster.

I thank Andy Duncan for expert technical and programming assistance throughout the course of this work, Bill Scott and Gord Hewitson for supplying liquid helium, and Venice, Gino, Clee, and Michael in the machine shop for assistance on numerous occasions. I am also appreciative of assistance from Marg, Wendy and Rose in the physics office.

I am grateful for having had the opportunity to work in a large group which has included over the course of these four years, Dimitry Basov, Doug Bonn, Ning Cao, Jinguo Chong, Dave Crandles, Andy Duncan, Chris Homes, Rob Hughes, Ho Fan Jang, Andrew McConnell, Hugo Navarro, Chris Rymaszewski, Thomas Strach, Xiucheng Wu and Lu Yong. In particular the contributions of Chris Homes, Dave Crandles, Rob Hughes, Ning Cao and Xiucheng Wu towards the development of the technique for reflectance measurement are appreciated. As well I have enjoyed knowing others in the general McMaster physics community including Jim Garrett (who can always be counted on for a helpful suggestion), Pash Ummat, Jake Vanderwaal, the members of the liquid state baseball team and the attendees of informal afternoon coffee breaks (from whom I learned everything I never wanted to know about hockey).

Finally I have been fortunate over the course of these four years to have had Dave Crandles as an office mate with whom I could always discuss difficulties and ideas, and my sister, Sharon, Elisabeth Nicol and John McFarlane as good friends.

For my parents, Kees and Christine Reedyk

Contents

Chapter 1

Introduction

The field of high temperature superconductivity began in the 1970's with the discovery of the binary A-15 compounds which exhibit transition temperatures as high as 23 K,[1] more than twice that of the highest T_c elemental superconductor, Nb ($T_c \approx 9$ K). A resurgence of interest occurred in 1986 with the discovery by Bednorz and Müller of a superconducting transition near 30 K in a Ba-doped sample of La_2CuO_4,[2] which was soon raised to 40 K by doping instead with Sr. The K_2NiF_4-like perovskite structure of this material is shown in figure 1.1.[3] The most notable features are the sheets of CuO_2 planes which are the common structural element of all of the subsequently discovered high T_c cuprate superconductors, and are believed to function as the primary conduction channel in these materials.

1.1 Electronic Structure of the Insulating Parent Compound

The undoped stoichiometric parent compound, La_2CuO_4 is insulating and non-superconducting. The Cu^{2+} sublattice of the CuO_2 plane has an electronic configuration of $[Ar]3d^9$. The 9 valence d electrons would thus be expected to fill an energy level scheme as shown in figure 1.2(a) leaving a half filled band which should

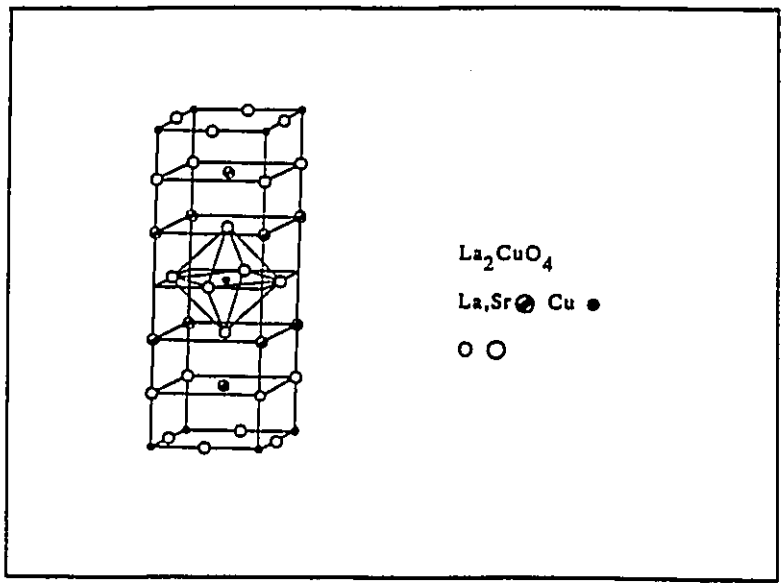

Figure 1.1: The structure of La_2CuO_4. Note the CuO_2 plane which is the common structural element of all the cuprate superconductors. (After [3]).

lead to metallic behaviour. To understand why this is not the case electron-electron correlations must be taken into account. The on-site Coulomb repulsion is greater than the nuclear attraction so that it is energetically favorable to have only one electron per site.[4, 5, 6, 7] The result is a splitting of the highest occupied 3d level into two; the lower and upper Hubbard bands, which, with an occupancy of one electron per site are full and empty respectively as shown in figure 1.2(b), thus leading to an insulating ground state.

The splitting between the upper and lower Hubbard bands has been found via photoemission experiments to be approximately 6 eV.[8] The first optical interband transition, as indicated by an onset of absorption, is observed near 2 eV as shown in figure 1.3, ($x = 0$), taken from Uchida *et. al.*.[9] This lead to a second important conclusion that the parent compound is a charge transfer (CT) rather than Mott-Hubbard (MH) insulator.

In a MH insulator the lowest unoccupied band is the upper Hubbard band and thus the first interband optical excitation will be from the lower to the upper

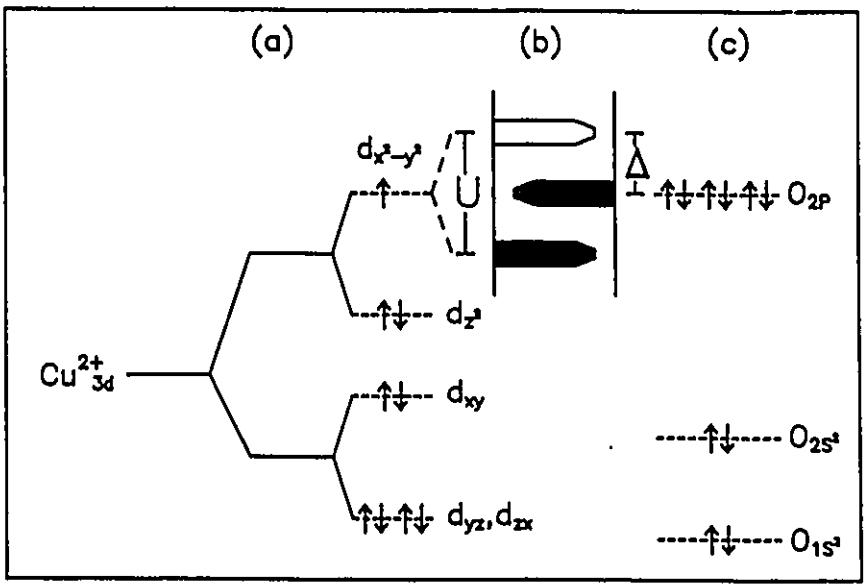

Figure 1.2: Energy level scheme for the Cu 3d levels in the absence (a) and in the presence (b) of electron-electron correlations. Note in (a) the half-filled $d_{x^2-y^2}$ level that splits into two bands with an occupancy of one electron per site in (b). These two bands, which are full and empty respectively, are referred to as the lower and upper Hubbard bands. (c) shows the O^{2-} levels. The fully occupied O^{2p} charge transfer band is situated between the lower and upper Cu^{3d} Hubbard bands. Note that the O^{2p} band has an occupancy of two electrons per site. (Adapted after [14]).

Hubbard band as illustrated schematically in figure 1.4(a). In a CT insulator [figure 1.4(b)] another fully occupied band of a predominantly different character is located between the upper and lower Hubbard bands and thus excitations from this level to the upper Hubbard band are possible.

The filled O 2p level of the CuO_2 plane is situated approximately 2 eV below the upper Cu 3d Hubbard level as shown in figure 1.2(c). The absorption edge near 2 eV shown in figure 1.3 is thus explained as due to a 'charge transfer' between these two bands.

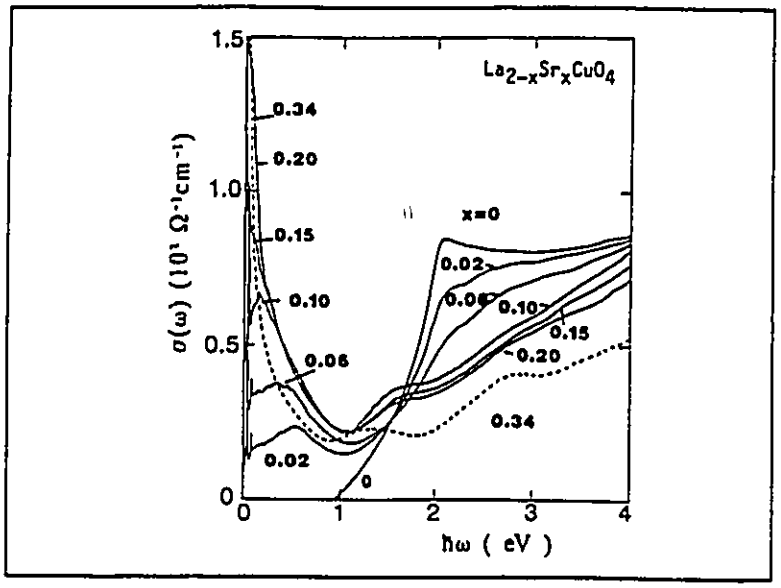

Figure 1.3: Optical conductivity of $La_{2-x}Sr_xCuO_4$ showing an absorption threshold near 2 eV for $x = 0$, which decreases in intensity as the level of doping increases; the spectral weight being transferred to lower frequencies in the form of a zero-frequency centered Drude absorption due to free carriers and a mid infrared band which appears to narrow and shift to lower frequency. (After [9]).

1.2 Hole doping

Stoichiometric insulating La_2CuO_4 becomes metallic and superconducting when some Sr (or Ba) is substituted for La. The substitution of divalent Sr for trivalent La causes holes to be doped into the CuO_2 planes. The simplest way to understand this is that the deficit of positive charge 'x' resulting from the substitution $La_{2-x}Sr_xCuO_4$ must be compensated for by the addition of x holes. The oxygen stoichiometry of the superconducting samples, $La_{2-x}Sr_xCuO_{4+y}$ is also typically greater than 4. In the same way charge neutrality dictates that the addition of negative charge, $2y$ (since oxygen has an oxidation state of 2^-), is compensated for by the presence of $2y$ holes.

The simple picture of a hole-doped charge transfer insulator does not however serve as an appropriate model for the doped material as shall now be discussed.

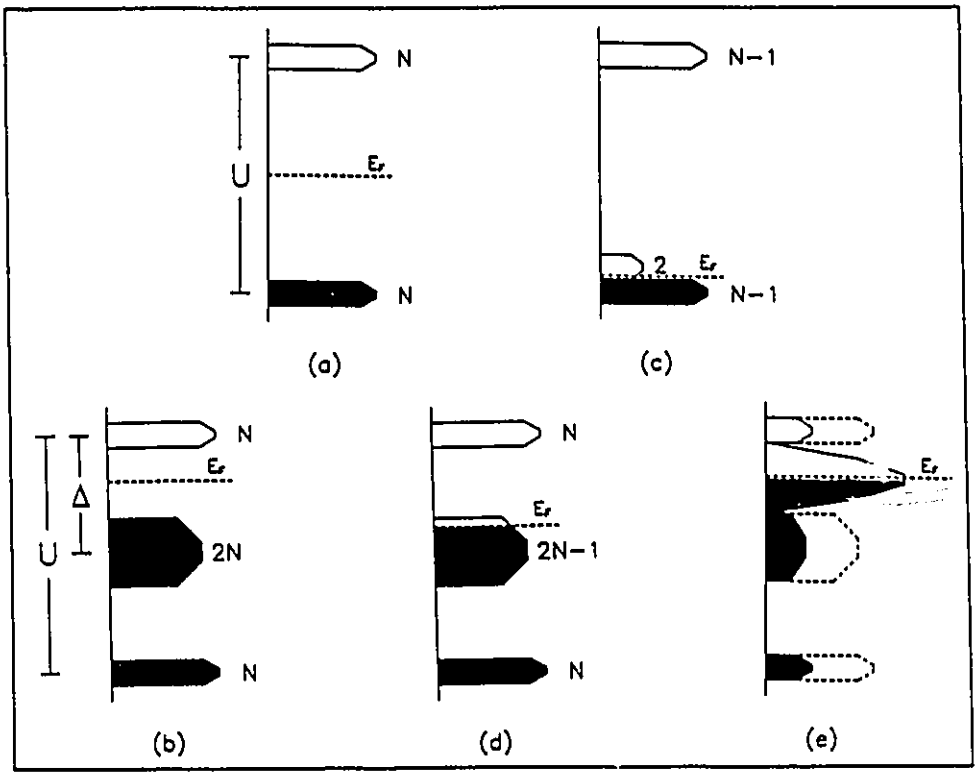

Figure 1.4: Schematic representation of a MH (a) and a CT (b) insulator. (c) and (d) respectively illustrate the situation upon doping with one hole, while (e) depicts a possible electronic band structure for a high-T_c cuprate. (Adapted after [9] and [10]).

1.3 Evolution of Band Structure with Doping

The effect of doping on the optical spectrum of $La_{2-x}Sr_xCuO_{4-\delta}$ can be seen in figure 1.3. These spectra show that as x, and hence the number of holes, increases, there is a transfer of spectral weight from high to low frequencies; the total integrated spectral weight remaining nearly constant. While this is expected for a doped MH-insulator it is in variance with the simple picture of a hole-doped charge transfer insulator. To see this consider doping the MH and CT insulators of figure 1.4 with one hole by removing an electron as shown in (c) and (d) respectively. For the MH insulator, (c), there is now one empty site which can be occupied by either a spin up or a spin

down electron such that there are two empty states for electron addition with energy corresponding to the lower band. The Fermi level separates these states from the filled lower Hubbard band. Because this is a correlated system, and since there are now only $N-1$ singly occupied states in the lower Hubbard band, there can be only a corresponding $N-1$ states in the upper band. Thus, although the total number of states remains $2N$, one state with energy corresponding to the upper band has been transferred to a lower energy scale. The situation is different for the CT-insulator shown in (d). Removal of one electron from the CT-band between the lower and upper Hubbard levels leaves one site which is occupied by a single *eg.* spin up electron. This implies that there is one available state for addition of a spin down electron. The Fermi level separates the filled portion of the CT-band from the empty state as shown in the figure. The spectral weight of the upper and lower Hubbard bands is unaffected and thus the added hole acts essentially as an uncorrelated free particle. This case is thus similar to the picture used to discuss doping in a semiconductor. It is believed that the observed transfer of spectral weight upon doping in the cuprate superconductors is caused by some hybridization of the Cu 3d states of the filled lower Hubbard band with the O 2p states such that holes in this hybridized band behave as correlated particles with restrictions on double occupancy.[9, 10]

1.3.1 The mid-infrared band

It is clear from figure 1.3 that at high doping levels a large zero-frequency centered peak due to the added free carriers replaces the CT-excitation observed near 2 eV at low doping levels. The intermediate doping levels show that in addition to Drude-like absorption at the origin, there is a finite-frequency centered peak which appears to narrow and shift down in frequency as the level of doping increases. This excitation was first noted in $La_{2-x}Sr_xCuO_{4-\delta}$ by Orenstein *et. al.*[11] and Herr *et. al.*[12], and has become known as the mid infrared absorption. The superposition of the mid-infrared band and the zero-frequency centered absorption gives rise to an overall non-

Drude behaviour for the optical conductivity which has become one of the defining characteristics of the cuprate superconductors.

In terms of the discussion of the previous section, the presence of this mid-infrared absorption suggests that the electronic band structure of the cuprates may be something like that depicted schematically in figure 1.4(e). That is, hybridized Cu 3d and O 2p states form a series of midgap states between what remains of the filled O 2p CT and the empty upper Hubbard Cu 3d band. The mid infrared absorption results from transitions from the filled levels of this hybridized band into the upper Hubbard states while the zero-frequency-centered absorption arises from transitions to the empty states above the Fermi level. Because the doping-induced hybridized band removes states from the lower Hubbard band, there will be a corresponding decrease in the number of states in the correlated upper level giving rise to the observed transfer of spectral weight from high to low frequencies with increased doping.

1.4 Anisotropy

The discussion presented in sections 1.1 to 1.3 is based on readings from references [9], [10], [13], and [14]. The interested reader should consult these for further details. Thus far only electronic transport parallel to the CuO_2 sheets, commonly referred to as the *ab*-plane, has been considered. The situation is quite different for perpendicular transport along the *c*-axis due to the highly anisotropic layered nature of the structure. In this direction the conductivity is more than an order of magnitude lower than in the *ab*-plane, and in some materials is several orders less. It is still a question of debate whether the intrinsic *c*-axis conductivity is quasi-metallic or semiconducting in nature.

1.5 Other Superconducting Cuprates

The layered nature of $La_{2-x}Sr_xCuO_{4-\delta}$ has the additional consequence that other structures can be built up by varying and adding to the layering sequence.

1.5.1 $YBa_2Cu_3O_{7-\delta}$ and $Bi_2Sr_2CaCu_2O_8$

The most familiar example is $YBa_2Cu_3O_{7-\delta}$, shown in figure 1.5(a).[15] By adding a second CuO_2 plane, separated from the first by a rare-earth layer thus forming a double perovskite-like sequence which will be referred to as the perovskite block, T_c is increased to 93 K. In this system the doping of the parent compound $YBa_2Cu_3O_6$ is realized by adding oxygen to a third Cu layer which separates perovskite-like blocks in adjoining unit cells. The oxygen enters this layer in the form of chains along the *b*-axis, and hence in the doped compound there is also an anisotropy within the *ab*-plane between the *a* and *b* axes.

A second example is $Bi_2Sr_2CaCu_2O_8$, another double-plane cuprate. The structure of $Bi_2Sr_2CaCu_2O_8$ which has a T_c near 85 K is shown in (b).[16] Here the two CuO_2 planes of the perovskite block are separated by Ca, while successive perovskite units are separated by double BiO rock-salt-like layers.

The primary difference between these two materials thus lies in that part of the structure which is intercalated between perovskite-like blocks; the CuO chains in $YBa_2Cu_3O_{7-\delta}$ and the double BiO sheets in $Bi_2Sr_2CaCu_2O_8$.

Since the *ab*-properties are mainly governed by transport within the CuO_2 planes of the perovskite unit they are similar for these two materials. The *c*-axis properties in contrast are primarily dictated by the intercalary structure separating perovskite-like blocks and have thus been found to be very different in these two materials. That is, the anisotropy between *ab*-plane and *c*-axis properties in $Bi_2Sr_2CaCu_2O_8$ is several orders of magnitude larger than in $YBa_2Cu_3O_{7-\delta}$ indicating a much lower interlayer transport.[17] It is likely that the CuO chain layer

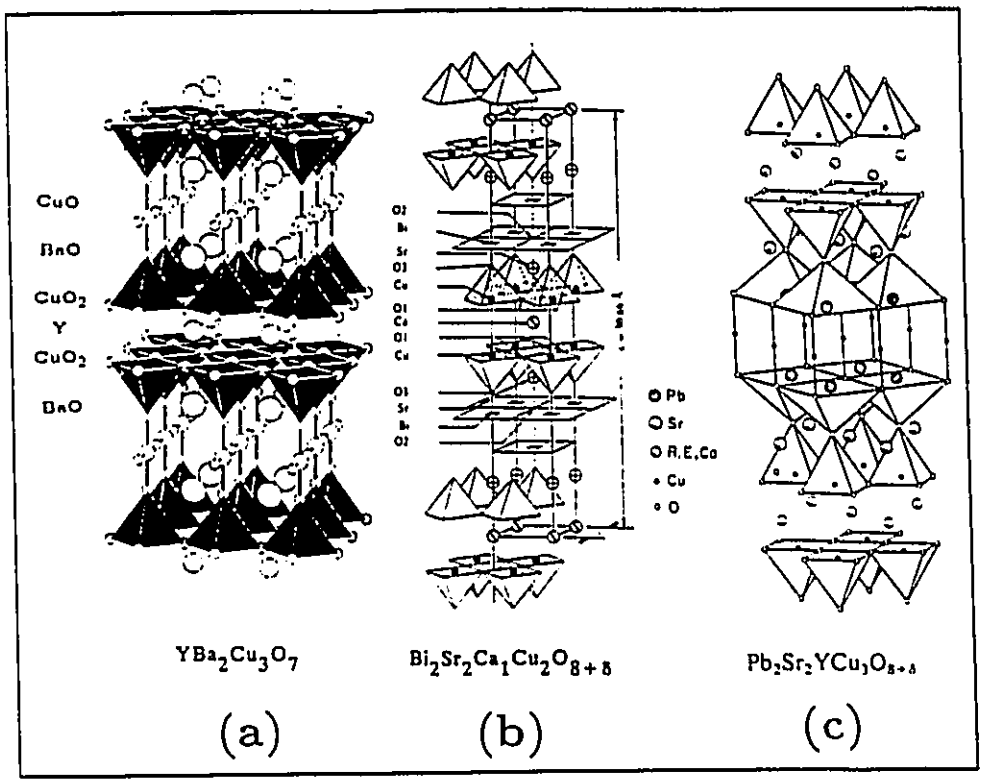

Figure 1.5: Structure of (a) $YBa_2Cu_3O_{7-\delta}$, (b) $Bi_2Sr_2CaCu_2O_8$, and (c) $Pb_2Sr_2RCu_3O_8$, reproduced from references [15], [16] and [19] respectively.

in $YBa_2Cu_3O_{7-\delta}$ provides some electronic coupling between successive CuO plane bilayers which is absent in $Bi_2Sr_2CaCu_2O_8$.

1.5.2 Importance of Single Crystal Samples

By noting both similarities and differences information regarding the presence of superconductivity in these materials may be inferred. The greater the number of different cuprate superconductors that are studied, the more complete will be the knowledge. A multitude of different such structures have been synthesized since the discovery of superconductivity in $La_{2-x}Ba_xCuO_4$. (See for example Harshman and Mills[18] and references therein). The caveat is that most have been synthesized only

as polycrystalline powder samples which are often multi-phase in nature, containing only a small fraction of the superconducting component. A further complication is that by definition such samples cannot be investigated in terms of anisotropy due to their unoriented nature, thus limiting their usefulness for experimental measurements considerably.

There are exceptions, where samples in the form of high quality single crystals (or oriented films) have been synthesized. These include the three materials already discussed, $La_{2-x}Sr_xCuO_{4-\delta}$, $YBa_2Cu_3O_{7-\delta}$, and $Bi_2Sr_2CaCu_2O_8$, as well as various closely related derivatives thereof. For example single crystals of $Bi_2Sr_2CaCu_2O_8$ can be made in one, two and three CuO_2-layer forms denoted by $Bi_2Sr_2Ca_{n-1}Cu_nO_{2n+4}$ where n = 1, 2 or 3. Also, by substituting Tl and Ba for Bi and Sr respectively, a second such series can be synthesized. Oriented crystals of the n = 3 member are however usually mixed phase in that they contain a significant intergrowth of n = 2. The one-layer $Bi_2Sr_2CaCu_2O_8$ compound is interesting because it has a T_c below 10 K, and hence can be used as a representative normal state analogue for the higher T_c materials. $YBa_2Cu_3O_{7-\delta}$ has a derivative containing double CuO chains, $YBa_2Cu_4O_8$, which can be synthesized in single crystal form under high oxygen pressure. $Nd_{2-x}Ce_xCuO_{4-y}$, like $La_{2-x}Sr_xCuO_{4-\delta}$ has a single CuO_2 layer. It is unique in that it is the only cuprate superconductor which is electron doped rather than hole doped. Also, the CuO_2 layer is more two-dimensional than in $La_{2-x}Sr_xCuO_{4-\delta}$.

1.5.3 $Pb_2Sr_2RCu_3O_8$

In 1988 Cava and co-workers at AT&T discovered another double CuO_2-layer cuprate superconductor the structure of which is shown in figure 1.5(c).[19] The significance, which is not yet appreciated by much of the high T_c community as evidenced by the comparatively small amount of work done on this material, is that $Pb_2Sr_2RCu_3O_8$ can be synthesized in single crystal form, providing a third structurally different double CuO_2-layer compound with which the properties of $YBa_2Cu_3O_{7-\delta}$

and $Bi_2Sr_2CaCu_2O_8$ can be compared.

The double CuO_2-layer perovskite block of the parent compound $Pb_2Sr_2RCu_3O_8$ is similar to that in $YBa_2Cu_3O_{7-\delta}$ where R, which separates the two CuO_2 layers, is also a lanthanide or Y. In $Bi_2Sr_2CaCu_2O_8$ this site is occupied by Ca. In $Pb_2Sr_2RCu_3O_8$ the perovskite blocks of successive unit cells are separated by an interlayer structure consisting of two rock-salt-like PbO layers analogous to the double BiO layers of $Bi_2Sr_2CaCu_2O_8$, sandwiched between which there is an additional oxygen-free Cu layer such as that in $YBa_2Cu_3O_6$, the parent compound for superconducting $YBa_2Cu_3O_{7-\delta}$.

Stoichiometric $Pb_2Sr_2RCu_3O_8$ becomes superconducting with a T_c near 80 K when approximately 30 % of the 3^+ rare earth ions are substituted by Ca^{2+}; the mechanism being similar to the substitution of Sr^{2+} for La^{3+} in $La_{2-x}Sr_xCuO_{4-\delta}$ as discussed above.

The oxygen-free Cu(1) layer in $Pb_2Sr_2RCu_3O_{8+y}$, so-called because Cu is in a 1^+ valence state rather than 2^+ as in the CuO_2 layers, has the interesting property that it can actually be close to fully occupied with oxygen to form a CuO_2 sheet (*ie.* $y \approx 2$).[19] This is however accompanied by oxidation of Pb^{2+} to a 4^+ valence state which in superconducting Ca-doped samples also drains holes from the CuO_2 planes of the perovskite block resulting in the loss of superconducting character.

In principle there are thus two methods by way of which to vary the level of doping and induce a metal-insulator transition in $Pb_2Sr_2(Y/Ca)Cu_3O_8$: (1) by altering the ratio of Y to Ca, and (2) by oxidation of the Cu(1) layer. In practice neither of these turns out to be practical for single crystal samples. The first because the crystal growth is stabilized for an Y:Ca ratio of 0.7:0.3 such that intermediate compositions are not obtained. The latter because incorporation of excess oxygen into the dense crystals takes place very slowly. It turns out however, that there is an unexpected third avenue open which is the incorporation of vacancies into the rare earth site. For a given growth environment, crystals seem to form for a narrow

range of effective ionic radius of the R site.[20, 21, 22] In Ca-doped, Y-containing samples this corresponds to mixed occupation in the ratio of 0.7 Y for every 0.3 Ca, and may explain why this composition is always obtained even though the starting or nominal composition is not in this ratio.[23] Since Ca^{2+} is larger than any of the rare earths the implication is that the structure is unstable for full or stoichiometric occupation with small rare earth ions such as Dy, Y and Ho. Ca-free single crystals with these rare earth ions can nevertheless be synthesized[20] and are surprisingly metallic and superconducting.[24] Furthermore, as increasingly larger rare earth ions are substituted the system undergoes a metal-insulator transition, exhibiting insulating and non-superconducting character for the largest rare earths such as La, Ce, Pr and Nd.[24]

This progression can be understood in terms of vacancies of the rare earth site.[20, 21, 22] The absence of the positively charged ion causes the oxygen atoms of the two adjacent CuO_2 layers to feel a stronger Coulomb repulsion and hence pushes the layers further apart acting in essence as a larger ion, and thus stabilizing the structure. The metallic and superconducting character can be understood from the viewpoint that the absence of a 3^+ rare earth ion implies to first order the addition of three holes, just as the substitution of Ca^{2+} implies one hole.

1.6 Overview

The common elements of the intercalary structure of $Pb_2Sr_2RCu_3O_8$ with both $YBa_2Cu_3O_{7-\delta}$ and $Bi_2Sr_2CaCu_2O_8$ as well as the novel doping mechanism which gives rise to a metal-insulator transition as a function of increasing ionic radius of the rare earth ion make it a good candidate for a complimentary study of the electronic structure and extent of anisotropy, and thus serves as the subject of this thesis. In chapters 2 through 4 the degree of anisotropy between *ab*-plane and *c*-axis properties of $Pb_2Sr_2(Y/Ca)Cu_3O_8$ is examined via magnetization, dc-resistivity and optical mea-

surements respectively from which it is concluded that although the carrier density is significantly lower than that in both $YBa_2Cu_3O_{7-\delta}$ and $Bi_2Sr_2CaCu_2O_8$, as indicated by a higher dc-resistivity, larger magnetic penetration depth and lower free-carrier plasma frequency, the extent of the anisotropy is similar to that in $YBa_2Cu_3O_{7-\delta}$ and therefore significantly smaller than in $Bi_2Sr_2CaCu_2O_8$.

The low concentration of *ab*-plane carriers is on its own significant given the relatively high value of T_c, 80 K. As a result a unique opportunity presents itself to observe unusual and interesting changes in the optical properties upon entry into the superconducting state. The reduced carrier density gives rise to an overall lower optical reflectance. The technique used to derive the optical conductivity from the experimentally measured reflectance, known as Kramers-Kronig analysis, becomes less accurate the closer the values approach unit reflectance due to unavoidable associated uncertainty. This, as will be discussed in chapter 4, leads to difficulties in the interpretation of superconducting state data in materials with a higher carrier density such as $YBa_2Cu_3O_{7-\delta}$ and $Bi_2Sr_2CaCu_2O_8$ where the reflectance at low frequencies is indistinguishable from unity within the noise level. Due to the lower level associated with the reflectance of $Pb_2Sr_2RCu_3O_8$ this problem is not encountered, and the superconducting state optical conductivity can be determined unambiguously, revealing unusual structure in the form of a peak centered near 100 cm^{-1}. This feature may be related to changes in the magnetic ordering of the system resulting from the onset of superconducting behaviour. The prominent nature of this feature in $Pb_2Sr_2RCu_3O_8$ may be associated with the presence of significant disorder in close physical proximity to the CuO_2 layers caused by the substitution on the R site. *c*-axis measurements reveal a similar feature.

The metal-insulator transition of the Ca-free single crystal series is discussed in chapter 5. The expected transfer of spectral weight from high to low frequencies as the carrier density increases is accompanied by an unusual evolution of sharp phonon structure in the optical conductivity which is argued, in chapter 6, to arise from a

doping-induced coupling of longitudinal *c*-axis phonons to the *ab*-plane mid-infrared continuum. The evidence is derived from a comparison of the *ab*-properties measured in the usual normal incidence, *ab*-face experimental configuration where these features are observed, and using polarized radiation on a face containing the *c*-axis where their ostentatiously surprising absence is dictated by momentum conservation. This finding suggests a resolution to a long-standing debate over the origin of these features, which are universally present in the cuprate superconductors.

The crystals of $Pb_2Sr_2(R/Ca)Cu_3O_8$ were synthesized and characterized via x-ray and elemental analyses by J.S. Xue, with some assistance from M. Maric. Precursors of $Sr_2(Y/Ca)Cu_3O_y$ with a starting ratio of R:Ca of 1:1 or 1:0 for the Ca-doped and Ca-free crystals respectively, were prepared by firing stoichiometric amounts of well-ground $SrCO_3$, $CaCO_3$, R_2O_3 and CuO powders at 950°C for 12 hours. The fired powder is then reground, combined with PbO and NaCl flux in the molar ratio of $Sr_2(R/Ca)Cu_3O_y$:PbO:NaCl = 1:4:30 and loaded into a covered platinum crucible. The mixture is heated rapidly in a vertical tube furnace under flowing N_2 gas to 200°C, and then allowed, over 4 hours, to reach a maximum temperature of 980-1050°C (depending on R and the ratio of R:Ca). The maximum temperature is maintained for 1 hour, followed by cooling at a rate of 5 to 10°C per hour to 760°C (30 to 60 hours). The crucible and its contents are then cooled over 4 hours to 200° after which the furnace is shut off. A NaCl layer, which can be removed mechanically, lines the top of the crucible. The melt below contains the crystals of $Pb_2Sr_2(R/Ca)Cu_3O_8$ embedded in a PbO-rich flux mixture. The crystals are easily extracted out of the flux which is generally of a powdery consistency, and are cleaned in methanol. For further details references [20] and [22-24] should be consulted.

The energy dispersive x-ray (EDX) analysis was carried out by Mr. J. Hudak. Some of the dc resistivity and infrared microscope-derived mid infrared reflectance measurements used to characterize the samples investigated herein were carried out with the assistance of Barbara Zvan.

Chapter 2

Anisotropy in Selected Magnetic Properties of $Pb_2Sr_2(Y/Ca)Cu_3O_8$

2.1 Background

2.1.1 Flux Shielding and the Meissner Effect

The fundamental defining characteristic of a superconductor is the transition to a state of perfect diamagnetism below T_c. To understand what is meant by this consider figure 2.1 and recall the Maxwell equation:

$$4\pi M + H = B, \tag{2.1}$$

where M is the magnetization, H is the applied field, and B is the magnetic flux. A diamagnetic material is one for which M is negative. A perfect diamagnet has $B = 0$ or $M = -\frac{1}{4\pi}H$. Figure 2.1(a) shows, at some temperature T_1, a non-magnetic substance in the absence of an external magnetic field, H. Assume that there is some temperature, T_c, such that this new state of matter characterized by $B = 0$ occurs. T_1 is greater than T_c. The sample is then cooled to a temperature, T_{II}, and an external field, H, is applied. One of two flux distributions results as illustrated in figures 2.1(b) and 2.1(c). Figure 2.1(b) is the expected result for a nonmagnetic

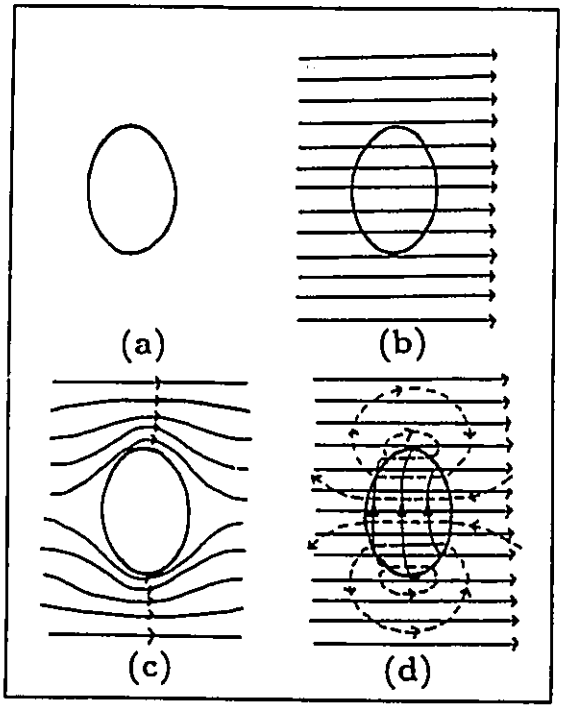

Figure 2.1: Temperature dependence of the flux distribution in a non-magnetic superconducting material. (a) shows the sample in the absence of an external field at a temperature $T_1 > T_c$. The field is subsequently applied at a lower temperature T_H. (b) shows the flux distribution when T_H is greater than T_c. (c) shows the flux distribution when $T < T_c$. If $T_H > T_c$ flux is expelled at T_c while if $T_H < T_c$ flux is excluded. (d) shows how the flux distribution of (c) arises from a combination of the external flux distribution and that of the shielding currents. (Adapted after [25]).

material in the presence of an applied field, that is, $M = 0$ so that $H = B$, and thus implies that $T_H > T_c$. Figure 2.1(c) shows the expected result for $T < T_c$. That is, a flux distribution where $B = 0$ inside the sample so that $M = -\frac{1}{4\pi}H$. Thus, when $T_H < T_c$ flux is *excluded* from entering the interior. If the temperature continues to decrease for the situation shown in figure 2.1(b), eventually when $T < T_c$ the flux distribution of figure 2.1(c) must result since the state of matter is defined by $B = 0$. Thus, when the field is applied above T_c flux will be *expelled* from the interior of the sample at T_c. This is known as the Meissner effect.

The difference between these two cases is subtle but important. Flux expulsion is the defining characteristic of a superconductor. Flux exclusion or shielding is a characteristic of both a superconductor and a perfect *normal* conductor. In the latter, when the field is applied above T_c the flux is, rather than being expelled from the interior of the sample at T_c, trapped within; such that if the field is then *removed* the flux inside remains, as shown in figure 2.2. Thus, in principle the magnetic properties can be used to distinguish between a superconductor and a perfect normal conductor. In practice however although a multitude of superconductors are known, no perfect normal conductor exists, the resistivity always being limited by impurity scattering at some level, and thus usually no rigorous distinction is made.

2.1.2 The Magnetic Penetration Depth

Next, the question of how this flux distribution comes about is addressed. This is illustrated in figure 2.1(d). Circulating currents develop in a thin layer at the surface of the sample which give rise to the flux distribution shown as dashed curves. Inside the sample the flux due to the applied field, and that due to these surface currents cancel to yield $B = 0$. Outside, the two combine to give the distribution of figure 2.1(c). The presence of surface currents implies that the flux can penetrate within this small layer at the surface of the sample. This is illustrated in figure 2.3. The distance the flux penetrates is characterized by a quantity, λ, given by:

$$\int_0^\infty B(x)dx = \lambda B(0) \tag{2.2}$$

where $B(0)$ is the flux density outside the sample and $B(x)$ that within the sample, a distance x from the surface. Thus, in figure 2.3 the area under the dashed curve is equal to the area under the solid curve. This characteristic length, λ, is called the magnetic penetration depth.

At T_c flux penetrates the entire sample, and thus λ must diverge. The temperature dependence of the magnetic penetration depth below T_c is shown schematically

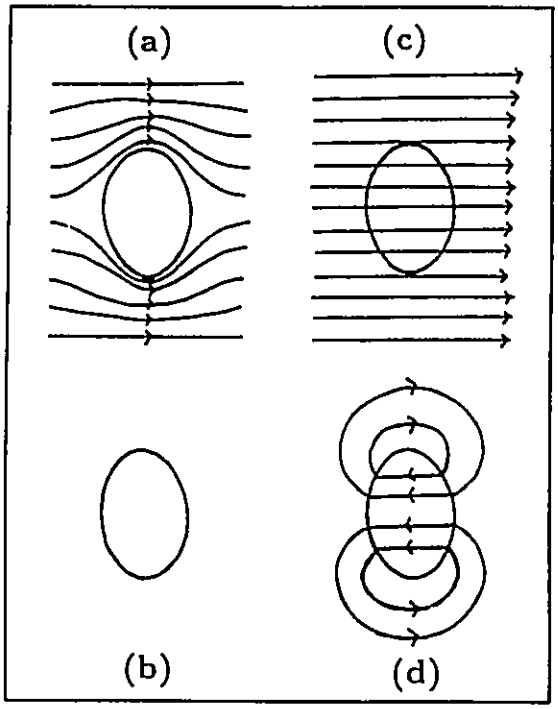

Figure 2.2: Flux distribution for $T < T_c$ in a perfect normal conductor. Here T_c refers to the onset of resistanceless behaviour. (a) shows the expected flux distribution if the field is applied when T is below T_c. Thus a perfect conductor also exhibits flux shielding. (b) shows the flux distribution when the field is then removed. (c) shows the flux distribution for $T < T_c$ when the field is applied above T_c. There is no flux expulsion as in a superconductor. (d) shows that if the field is then removed flux is trapped in the interior of the sample. For all (a)-(d) T is below T_c. (Adapted after [25]).

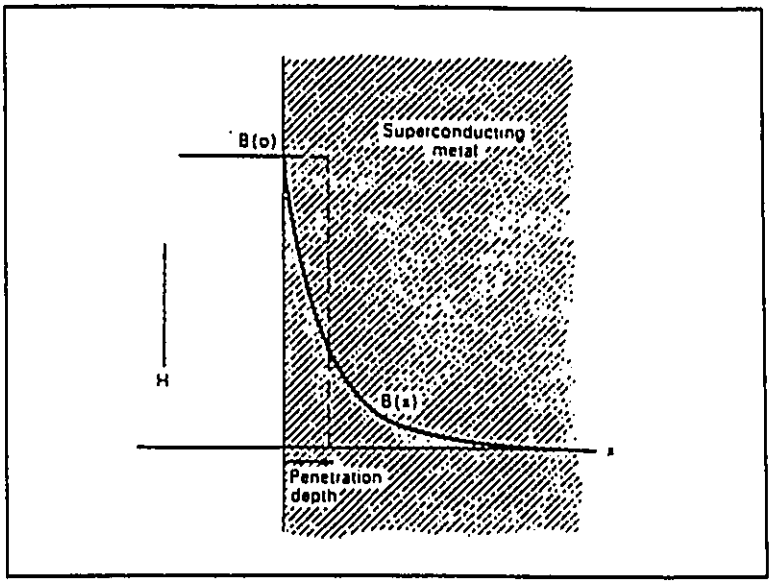

Figure 2.3: Flux penetration into a superconducting material. The solid curve shows the actual decay of the flux distribution in the sample, while the dashed curve shows how λ is defined. The areas under the two curves are equal. (After [25]).

in figure 2.4. An important intrinsic parameter characterizing a given superconducting material is the penetration depth at zero temperature, labelled λ_o in figure 2.4.

2.1.3 The Coherence Length

Within this surface layer where the supercurrents flow the material is in the normal state. The interior of the sample is in the superconducting state. At the boundary between the normal and superconducting regions the density of superconducting electrons, n_S, must rise from zero to some finite value as illustrated in figure 2.5. The length scale over which this occurs is characterized by a quantity known as the coherence length, ξ. Another important parameter characterizing a superconducting material is the value of the coherence length at zero temperature, ξ_o. Two situations arise depending on whether $\xi > \lambda$ (case 1) or $\xi < \lambda$ (case 2). Before discussing these

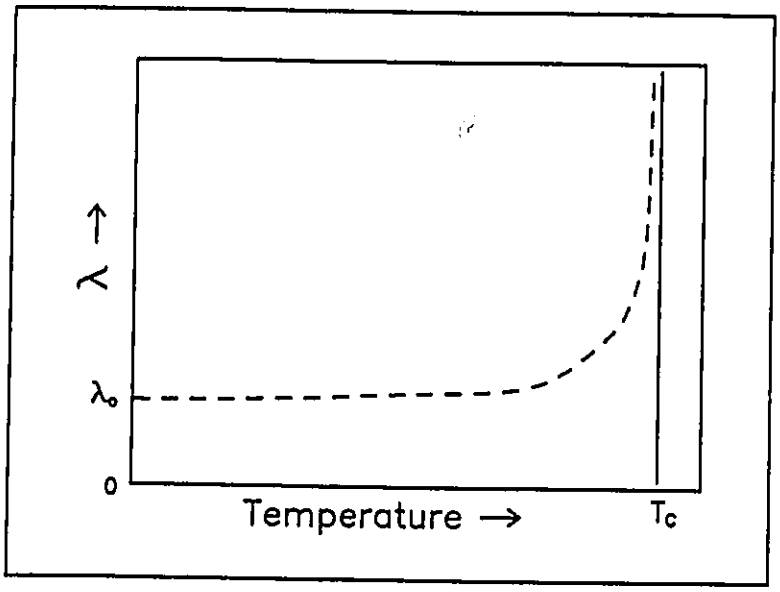

Figure 2.4: Schematic illustration of the temperature dependence of the magnetic penetration depth.

further the concept of a critical field will be introduced.

2.1.4 The Critical Field

Clearly one way of destroying the superconducting state is by raising the temperature above T_c. The temperature dependence of the magnetization of a superconductor is shown schematically in figure 2.6(a). The free energy of the superconducting state, g_S, begins to exceed that of the normal state, g_N, as the temperature is raised above T_c. An alternate method to destroy the superconducting state is to apply a magnetic field larger than a critical field, H_c. Above H_c, even if $T < T_c$, the free energy of the superconducting state exceeds that of the normal state. The field dependence of M is shown in figure 2.6(b). Up to H_c the sample is in the superconducting state, ($g_S < g_N$), and M varies linearly with H with slope $-\frac{1}{4\pi}$. At H_c the sample reverts to the normal state where $M = 0$. The temperature dependence of the critical field is shown schematically in figure 2.6(c). Near T_c only a small field is required to destroy the

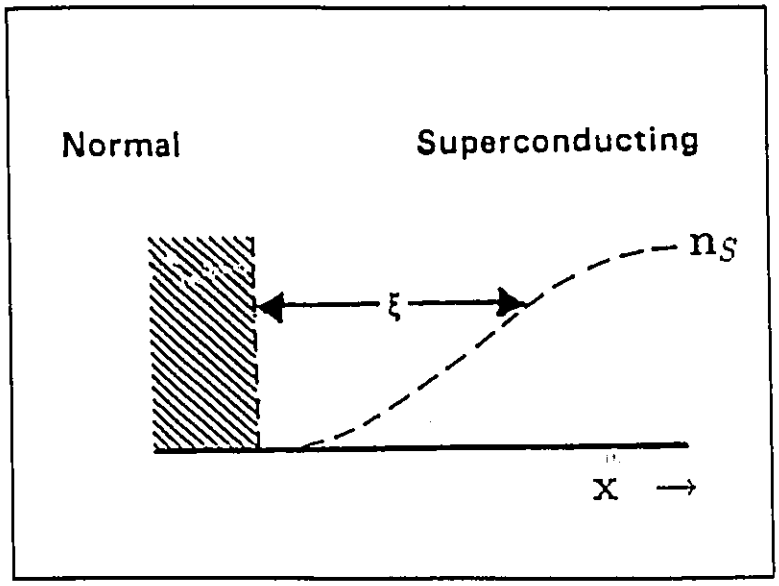

Figure 2.5: Spatial variation of the density of superconducting electrons at a boundary between normal and superconducting regions. In the normal state n_S is zero and then rises to some finite value in the superconducting state over a length scale characterized by the coherence length, ξ. (After [25]).

superconducting state while at low temperatures the superconducting state is stable with respect to higher applied fields. The zero temperature critical field $H_c(0)$ is a third parameter characterizing a superconducting material.

2.1.5 The Critical Current

The system reverts to the normal state at H_c because the surface currents which are set up to shield out the flux have exceeded a value known as the critical current, J_c. Another method of destroying the superconducting state, which will not be discussed further, but is mentioned here for completeness, is to apply a current in excess of J_c. The critical current is sample dependent and not an intrinsic property of a given superconducting material, although of considerable technological importance. For example, the greater the current that can be supported, the larger the magnetic field

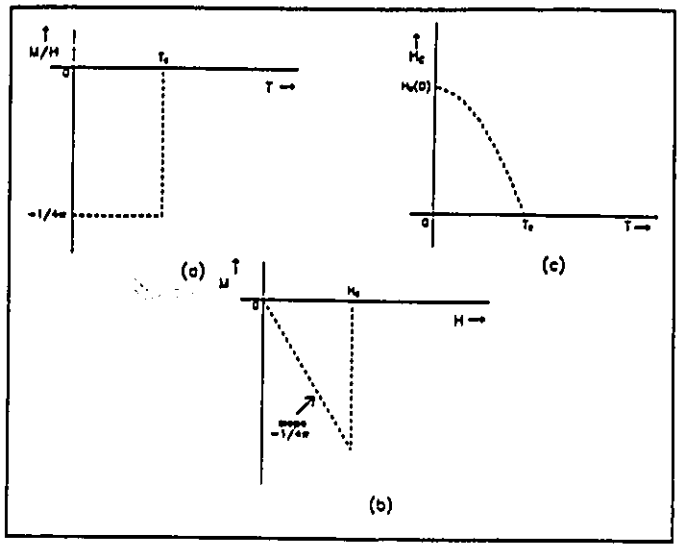

Figure 2.6: (a) Temperature dependence of the magnetization of a superconductor. (b) Field dependence of the magnetization. Note that there is a critical value, H_c, above which the sample reverts to the normal state. (c) Temperature dependence of the critical field.

that is created by a coil of superconducting wire. Hence magnets with high fields and no heat loss due to resistance can be constructed.

2.1.6 Type I and Type II Superconductors

There are two contributions which change the free energy of the superconducting state relative to that of the normal state. The free energy is lowered by a quantity g^{ξ} due to ordering of the superelectrons. This is however at a cost of g^{λ} as a result of acquiring a magnetization which cancels the flux density. Thus

$$g_S = g_N - g^{\xi} + g^{\lambda}. \tag{2.3}$$

The field dependence of the free energy can be summarized as follows:

$H < H_c(1-n)$	$g_S < g_N$	$g^\xi > g^\lambda$
$H_c(1-n) \leq H \leq H_c$	$g_S = g_N$	$g^\xi = g^\lambda$
$H > H_c$	$g_S > g_N$	$g^\xi < g^\lambda$

Here n is a quantity known as the demagnetization factor which is considered in Appendix A. For the remainder of the discussion it is assumed that $n = 0$ such that it is only for $H = H_c$ that $g_S = g_N$.

Above it was stated that at H_c the sample reverts to the normal state. The situation is not actually quite this simple. As mentioned, two cases exist depending on the relative magnitude of the penetration depth and the coherence length.

Consider a boundary between a normal and superconducting region when $\xi > \lambda$. The situation is illustrated in figure 2.7. The flux which has a value B_o in the normal region penetrates a distance characterized by λ into the superconducting region. The density of superconducting carriers rises from zero in the normal state to a value n_S in the superconducting state over a longer characteristic length, ξ. As shown in (b) the contribution to the free energy from the magnetization, g^λ, increases from zero in the normal state to some finite value over the same length scale as the magnetic penetration depth, λ. Similarly the contribution which lowers the free energy of the superconducting state relative to that of the normal state develops over the length scale of ξ. For a stable boundary at H_c, $g_S = g_N$ and thus at two points well within the normal and superconducting regions respectively $g^\lambda = g^\xi$. The total free energy is shown in figure 2.7(c). Due to the different length scales of λ and ξ there is a *positive surface energy*. Thus it costs energy to maintain a boundary between normal and superconducting states and hence the entire sample reverts to the normal state at H_c.

Now consider the second case where $\lambda > \xi$. This situation is illustrated in figures 2.8(a) through (c), and by extension of the above discussion leads to a *negative surface energy*. Thus a boundary between a normal and superconducting region at

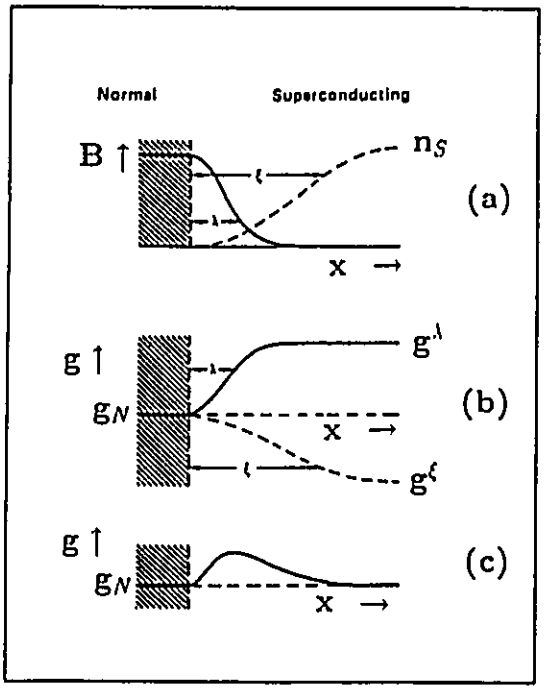

Figure 2.7: Case I ($\lambda < \xi$) (a) Spatial variation of the penetration depth and the coherence length across a normal-superconducting boundary. (b) spatial variation of the various contributions to the free energy. (c) Total free energy. Note that there is a positive surface energy. (Adapted after [25]).

H_c lowers the overall free energy of the system. The situation which arises is shown schematically in figure 2.9, and is known as the mixed state. Rather than the entire sample reverting to the normal state at H_c normal cores appear which are typically arranged in a triangular lattice. This situation persists above H_c, [which (for reasons that will soon become clear) is renamed H_{c1}], because the increase in the free energy due to the normal core is outweighed by the decrease due to the surface. Eventually at a field $H_{c2} > H_{c1}$ the two are equal and the entire sample reverts to the normal state. H_{c1} and H_{c2} are called the lower and upper critical fields respectively.

A material which behaves according to case 1 ($\xi > \lambda$) is referred to as a Type I superconductor while one which exhibits the characteristics of case II is a Type II superconductor. The field dependence of the magnetization for Type I and II superconductors is compared in figure 2.10.

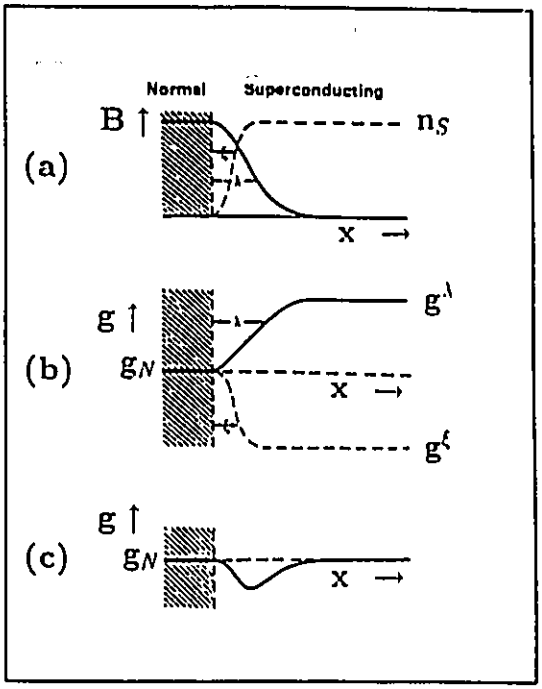

Figure 2.8: Case II ($\lambda > \xi$) (a) Spatial variation of the penetration depth and the coherence length across a normal-superconducting boundary. (b) spatial variation of the various contributions to the free energy. (c) Total free energy. Note that there is a negative surface energy. (Adapted after [25]).

The cuprates are Type II superconductors, and the zero temperature values of the upper and lower critical field constitute two other important parameters by which a given material is characterized.

2.2 Magnetization Measurements

In what follows a high quality single crystal of $Pb_2Sr_2(Y/Ca)Cu_3O_8$ is characterized in terms of the four fundamental parameters; λ, ξ H_{c1}, and H_{c2} via a study of its magnetic properties. In each case before turning to the results of the investigation the methods by way of which these quantities are extracted from experimental magnetization data will be discussed. Here the relevant results of Ginzburg-Landau theory, and the Bean critical state and Lawrence-Doniach models; the theoretical framework

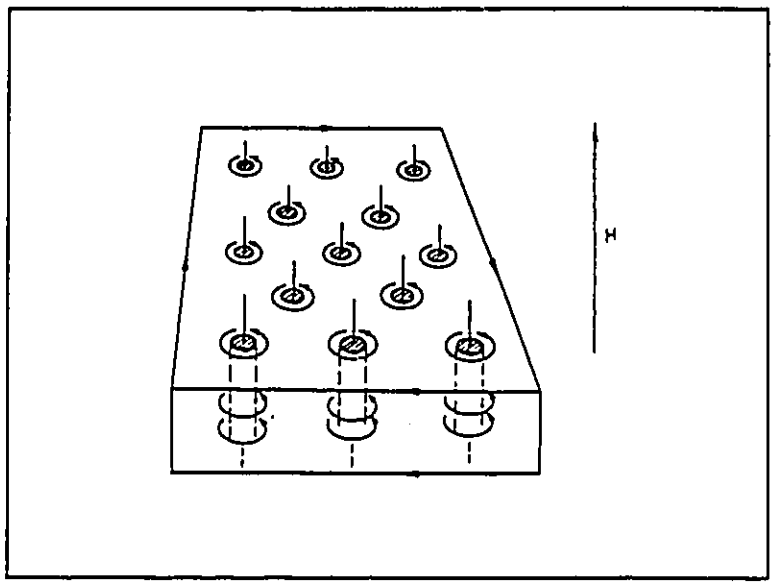

Figure 2.9: Schematic diagram of the mixed state in which cores of normal material are arranged in a triangular lattice. (After [25]).

upon which the analysis is based, will simply be stated. For further details the reader is referred to references [26] and [27].

2.2.1 Experimental Details

The crystal utilized for the magnetization measurements discussed in this chapter (approximate dimensions 0.7x0.6x0.2 mm^3) is shown in figure 2.11. Prior to measurement it was annealed for 40 hours in flowing nitrogen gas at 600° C, a procedure which has been found to improve the sharpness of the magnetic transition, and extend the range over which the magnetization is reversible (discussed later). Single-crystal x-ray analysis of this particular crystal using the Weissenberg technique showed it to be of good crystal quality[28] (all of the reflections in the Weissenberg photograph could be indexed to a primitive orthorhombic unit cell of a=5.383(1), b=5.423(1) and c=15.765(2) Å, implying no evidence for a secondary phase). Energy Dispersive X-ray (EDX) analysis of four randomly chosen locations on the surface of the crystal

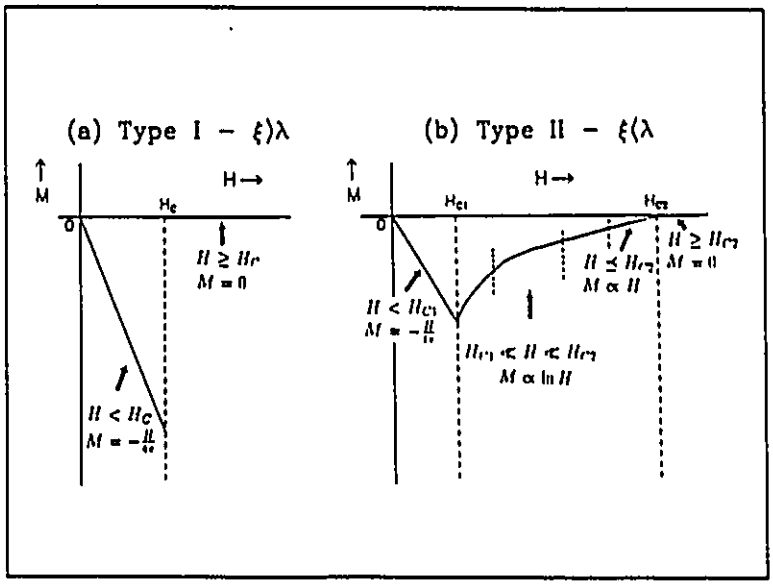

Figure 2.10: Field dependence of the magnetization for (a) a Type I superconductor, and (b) a Type II superconductor.

(marked on figure 2.11) showed that compositional differences in Pb, Sr, Ca and Y, as deduced from the ratio of the measured intensity of the Pb M-α, and Sr, Ca and Y K-α radiation to the Cu K-α were less than 2 percent in all cases except for Sr where a maximum of three percent difference was observed. The variation in the magnitude of the Cu K- α signal itself was no more than 3 percent. These results show that the crystal used was of good homogeneity in composition.

All magnetization measurements were carried out using a Quantum Design dc SQUID magnetometer. The crystal was mounted on a quartz rod using GE varnish. The quartz rod was then placed in a plastic drinking straw and the bottom sealed using a small plug of Kimwipe tissue. This unit was subsequently attached to the commercial measuring rod with a small wire.

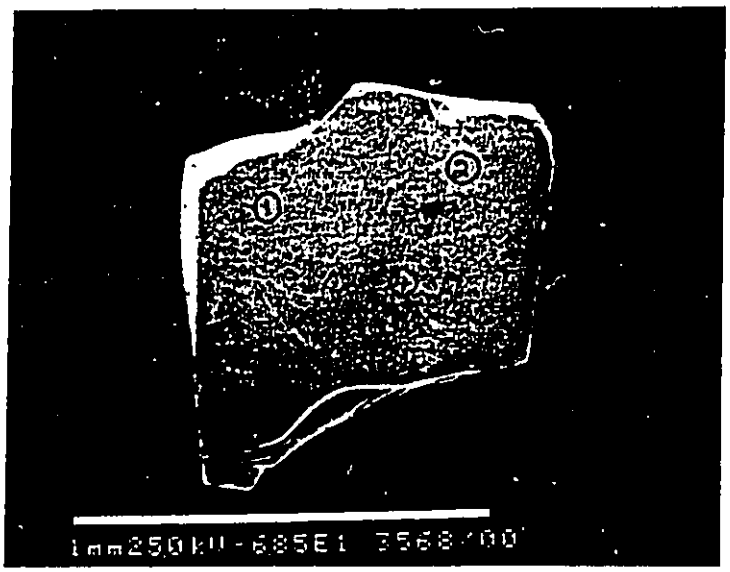

Figure 2.11: Photograph of the $Pb_2Sr_2(Y/Ca)Cu_3O_8$ crystal used in the magnetization measurements. The numbers refer to the randomly chosen locations for EDX analysis. Note that this photograph was taken after the magnetization measurements were completed, and that a piece chipped off the lower right hand corner when the crystal was removed from the sample mount so that the original geometry was more regular than that shown.

2.2.2 The Lower Critical Field

In principle H_{c1} and H_{c2} can be obtained directly from the M versus H curve as respectively the fields at which M deviates from linear behaviour at low fields and at which M goes to zero. In practice this is usually quite difficult.

Consider the situation for the determination of H_{c1}. In figure 2.10(b) H_{c1} is clearly indicated by a cusp in $M(H)$. In the cuprates at low temperatures the flux is heavily pinned and inhibited from entering the sample, giving rise to an almost imperceptible deviation from perfect diamagnetism at H_{c1} as shown schematically in figure 2.12. The approach often taken is to fit the low field data linearly and note where the fit deviates from the experimental curve. Estimates of H_{c1} using this technique have differed by as much as 50%.[29] The problem is that the deviation can

lie within the uncertainty of the data points for hundreds of Gauss.

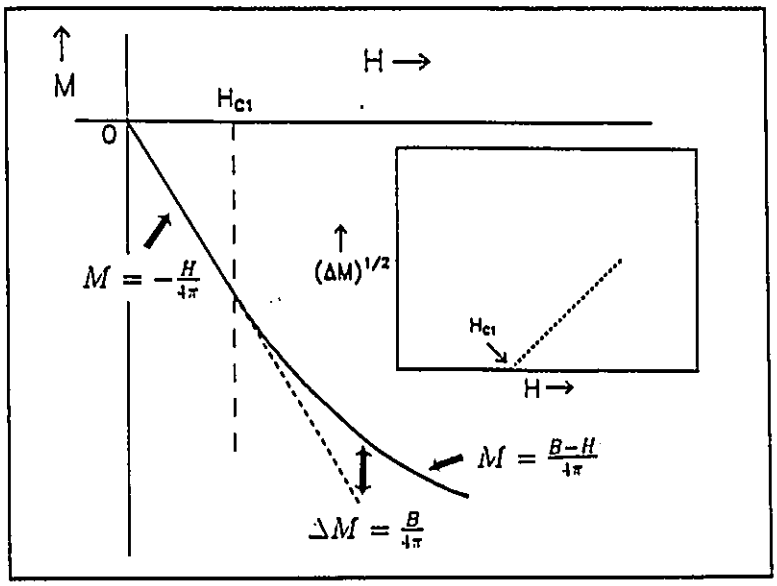

Figure 2.12: Schematic representation of flux penetration in a heavily pinned material. The short dashed line has slope $-\frac{1}{4\pi}H$. The inset shows the expected behaviour for the field dependence of $(\Delta M)^{1/2}$.

There is a way to delineate the change in behaviour more clearly. By definition for $H < H_{c1}$ the flux density, B, is zero so that $M = -\frac{1}{4\pi}H$. Above H_{c1} flux begins to penetrate the sample according to equation 2.1 so that:

$$M = \frac{1}{4\pi}(B - H). \tag{2.4}$$

Let ΔM represent the deviation from the linear behaviour as shown in figure 2.12. Then:

$$\Delta M = \frac{1}{4\pi}(B - H) - (-\frac{1}{4\pi}H) = \frac{B}{4\pi}. \tag{2.5}$$

The Bean critical state model predicts that just above H_{c1} the flux penetration is proportional to the square of the applied field.[27] Thus

$$\Delta M \propto H^2 \quad \text{or} \quad (\Delta M)^{1/2} \propto H. \tag{2.6}$$

Below H_{c1} $B = 0$ so $(\Delta M)^{1/2} = 0$. The expected field dependence of $(\Delta M)^{1/2}$ is shown in the inset to figure 2.12. H_{c1} is indicated by a change in the field dependence of $(\Delta M)^{1/2}$ from zero to a linear rise. This method was used by Naito *et. al.* to study the lower critical field of $La_{2-x}Sr_xCuO_{4-\delta}$.[30]

Due to the anisotropic nature of the structure of the cuprates the magnetic properties are different depending on whether the field is applied within or perpendicular to the CuO_2 planes. The effect of this anisotropy on the magnetic properties will be discussed in more detail later. For now it is sufficient to simply specify whether the measurement corresponds to an applied field perpendicular or parallel to the c-axis of the crystal.

For the determination of H_{c1} isothermal field dependent magnetization measurements were carried out for both crystal orientations ($H \parallel c$ and $H \perp c$) at various temperatures. ΔM was then determined by a linear fit to the very low field $M(H)$ data and subsequently subtracting this least squares result from the full data set.

Figure 2.13 shows the low field $M(H)$ data obtained at 5 K for the c-axis of the crystal oriented both perpendicular (a) and parallel (b) to the direction of the applied field together with a least squares fit to the very low field regime. The slopes are different in the two cases. This is due to demagnetization, which is discussed in Appendix A. The main consequence is that flux begins to penetrate the sample for fields smaller than H_{c1} because the internal field that the sample experiences is increased beyond the value of the applied field by an amount known as the demagnetizing field. This is purely a geometrical effect, and is less severe for $H \perp c$ than for $H \parallel c$ as a result of the plate-like geometry of the sample (the c-axis being the smallest dimension). Many crystals of different shapes and sizes, were measured and approximations made to the geometry in order to estimate the demagnetization factor for $H \parallel c$. In each case it was found that the volume fraction of superconducting material (also discussed in Appendix A) is within 10% or less of 100% from which it was concluded that there is essentially complete diamagnetic shielding in the crystals.

The most straightforward solution to the problem of accounting for the demagnetizing field is then to assume perfect shielding at low fields which together with the measured slope $\frac{dM}{dH}$ determines the demagnetization factor. (See also Appendix A).

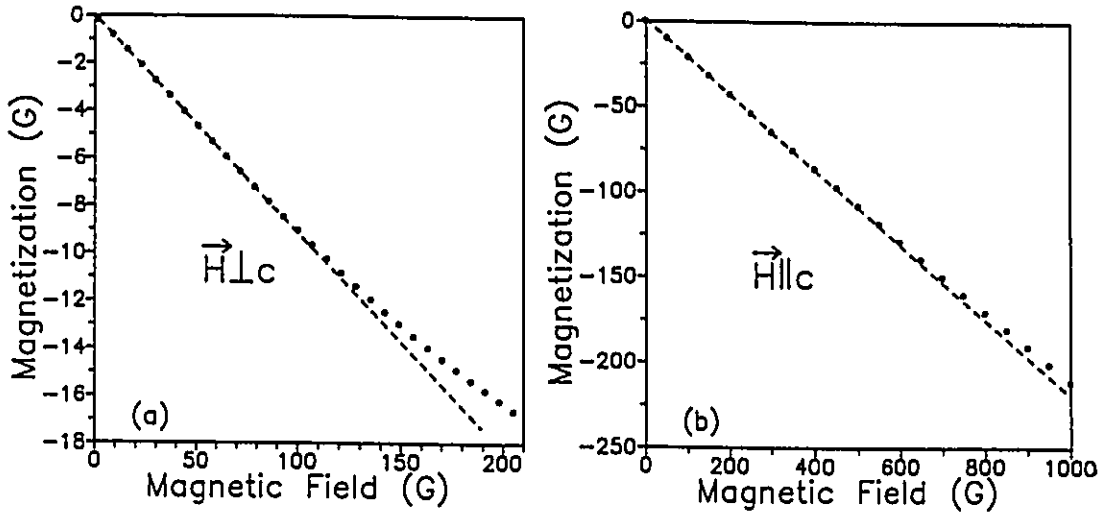

Figure 2.13: Low field magnetization, M, versus H for $Pb_2Sr_2(Y/Ca)Cu_3O_8$ at 5 K with the field applied (a) perpendicular and (b) parallel to the c-axis of the crystal. The dashed curves represent a least squares fit to the very low field data.

The demagnetization factors calculated in this manner are $n_{\|} = 0.64$ and $n_{\perp} = 0.14$ for $H \parallel c$ and $H \perp c$ respectively. (The approximation for the sample geometry using reference [31] yielded $n_{\|} = 0.62$ and $n_{\perp} = 0.19$). To obtain the effective field experienced by the sample the H-axis of figure 2.13 should thus be multiplied by $\frac{1}{1-n}$. Figure 2.14 shows $(\Delta M)^{\frac{1}{2}}$ versus the demagnetization corrected field, H_{eff}, for the two crystal orientations. Note that the expected behaviour is observed; $(\Delta M)^{\frac{1}{2}}$ is zero within experimental uncertainty (the noise is rectified so that the square root can be evaluated) up to a threshold value of H_{eff} at which point it begins to rise. There is some rounding of the non-zero portion of the curve near H_{c1} which may be attributed to the demagnetization field at the sharp corners of the crystal. It is therefore reasonable to extract H_{c1} by extrapolating the higher field linear regime of the $(\Delta M)^{\frac{1}{2}}$ versus H curve to the horizontal axis. Figure 2.15 shows

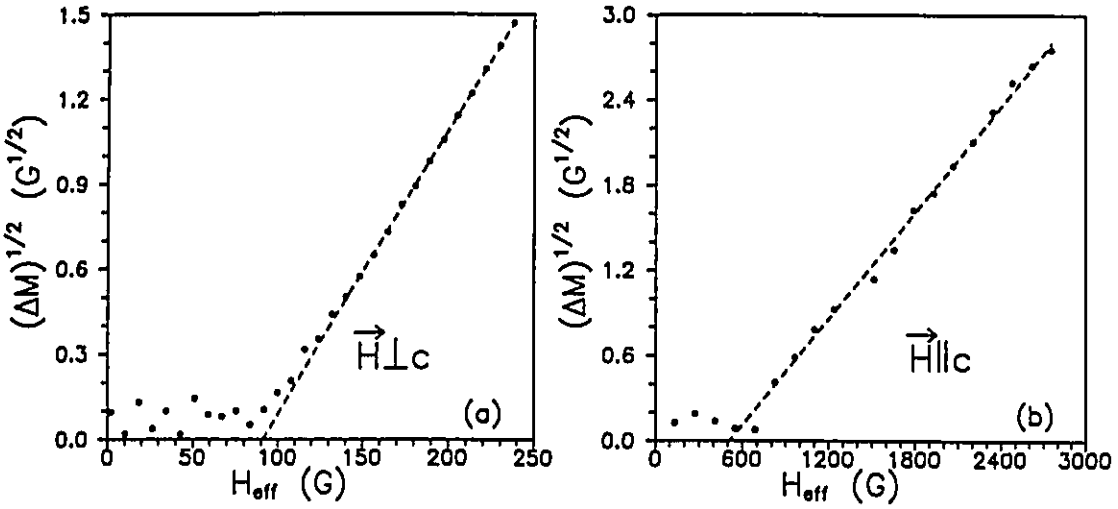

Figure 2.14: $\Delta M^{1/2}$ versus the demagnetization-corrected field, H_{eff} for $Pb_2Sr_2(Y/Ca)Cu_3O_8$ at 5 K with H (a) perpendicular and (b) parallel to the c-axis of the crystal. The dashed curves represent a least squares fit to the highest field data.

the temperature dependence of the lower critical field for $H \perp c$ ($H_{c1}^{\perp}$) and $H \parallel c$ ($H_{c1}^{\parallel}$) obtained via this procedure, the uncertainty reflecting different choices for the range of points used in the least squares fitting. The uncertainty is smaller and the threshold generally less smeared for $H \perp c$ where the demagnetizing effects are less severe and the slab geometry, assumed in the critical state model analysis, is more appropriate. The values for $H_{c1}(0)$ extrapolated from these results are 95 ± 10 G and 505 ± 20 G for H perpendicular and parallel to the c-axis of the crystal respectively.

2.2.3 The Upper Critical Field

In the 3-dimensional Ginzburg-Landau (GL) theory the magnetization is found to approach zero linearly with $(H - H_{c2})$ near H_{c2}.[26] Thus, for constant temperature, M vanishes linearly with H as shown in figure 2.10(b). Alternatively, the temperature dependence of H_{c2} near T_c (the only experimentally accessible region due to the large magnitude of the upper critical field of the cuprates at low temperatures) can be

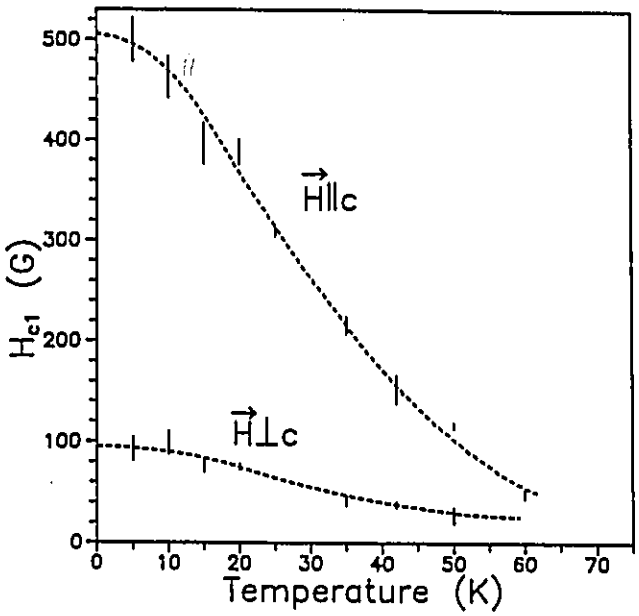

Figure 2.15: Temperature dependence of the lower critical field for the c-axis of the crystal oriented perpendicular ($H_{c1}^{\perp}$) and parallel ($H_{c1}^{\parallel}$) to the field direction. The dashed curves serve as a guide to the eye. These results yield estimates for the zero-temperature critical field of 95 ± 10 G and 505 ± 20 G for $H_{c1}^{\perp}(0)$ and $H_{c1}^{\parallel}(0)$ respectively and an anisotropy ratio of $H_{c1}^{\parallel}(0)/H_{c1}^{\perp}(0) \approx 5$.

extracted from measurements of the temperature dependence of the magnetization. In the GL theory H_{c2} is given by:[26]

$$H_{c2} = \frac{\Phi}{2\pi\xi^2}, \tag{2.7}$$

where $\Phi = \frac{hc}{2e} = 2.07\text{x}10^{-7}$ G-cm^2 is the flux quantum. Near T_c:[26]

$$\xi^2 \propto \frac{1}{(1 - T/T_c)}, \tag{2.8}$$

so that

$$H_{c2} \propto (1 - T/T_c). \tag{2.9}$$

Thus, since near H_{c2} the magnetization goes to zero linearly with $(H_{c2} - H)$, for constant H, M will vanish linearly with T.

Once again measurements were carried out with the *c*-axis oriented both perpendicular and parallel to the field direction. For each orientation the magnetization was measured as a function of temperature in the vicinity of T_c (~76 K) for magnetic fields of 0.1, 0.4, 0.7 and 1.0 to 5.5 T in steps of 0.5 T. Generally the field was turned on after a zero field cool to 55 K and the resulting magnetization measured upon warming although some field cooled sequences were performed in order to determine the regime of reversible magnetization as discussed below.

Several of the resulting curves, with a background diamagnetic moment that is temperature independent and linear in field subtracted, are shown in figures 2.16(a) and (b) for the *c*-axis of the crystal oriented perpendicular and parallel to the magnetic field respectively. In figure 2.16(a), for clarity, since the magnetization is close to an order of magnitude smaller and hence has a much lower signal to noise ratio than that for $H \parallel c$ only curves for three magnetic field strengths are shown. Although the temperature range shown constitutes in all cases the region in which the magnetization was found to be reversible, (a requirement of the GL theory) the inset to figure 2.16(b) shows both field cooled and zero-field cooled results for $H \parallel c$ for magnetic field strengths of 1.0 and 5.0 T in order to illustrate the extent of the reversible magnetization. The region of reversibility is smaller for H perpendicular to *c* than for H parallel to *c*.

The basic premise of the technique is to determine the temperature at which there is an onset of a linear temperature dependence to the magnetization below T_c. Note however that in particular for $H \parallel c$ there is considerable rounding of the transition. This is due to diamagnetic fluctuations and will be discussed below. T_c(H) is defined to be the point of intersection of the extrapolation of the T-linear reversible magnetization below T_c to the normal state background. This is illustrated for three representative field strengths for $H \perp c$ and $H \parallel c$ in figures 2.17(a) and (b) respectively. Note that for clarity, in (a) the 1.0 and 3.5 T curves have been shifted down by 0.01 and 0.005 emu/g respectively, while in (b) those for 1.0 and 3.0 T have

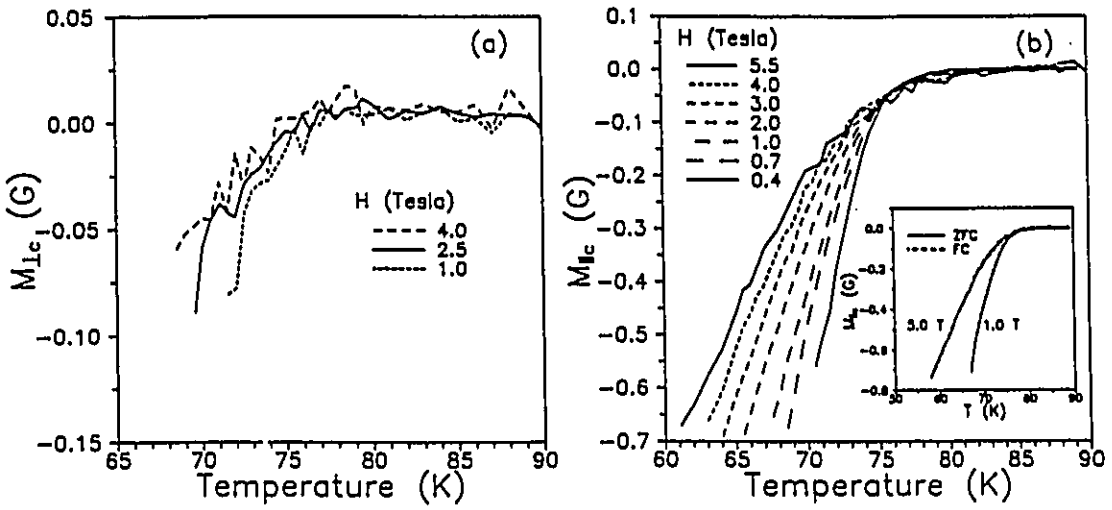

Figure 2.16: Temperature dependence of the magnetization of $Pb_2Sr_2(Y/Ca)Cu_3O_8$ at various magnetic field strengths for the c-axis of the crystal oriented (a) perpendicular ($M_{\perp c}$) and (b) parallel ($M_{\parallel c}$) to the field direction. [Inset to (b)] Field (FC) and zero-field cooled (ZFC) curves to illustrate the extent of the reversibility of $M_{\parallel c}$.

been similarly adjusted by 0.05 and 0.025 emu/g respectively.

The temperature dependence of H_{c2} for both orientations as derived via this procedure is plotted in figure 2.18. The upper critical field slopes for $H \parallel c$ and $H \perp c$ obtained by a linear least squares fit to the data, and shown with the dashed curves, are -1.8 ± 0.1 and -11 ± 4 T/K respectively. The small offset between the extrapolated $T_c(0)$ for $H \perp c$ and $H \parallel c$ may be due to a rapid initial low field suppression of T_c for $H \parallel c$ as has also been found for $YBa_2Cu_3O_{7-\delta}$.[32, 33, 34]

The zero temperature value of the upper critical field can be estimated using the Werthamer-Helfand-Hohenberg (WHH) formula which is given by:[26]

$$H_{c2}(0) = 0.7(\frac{dH_{c2}}{dT})\,|_{T_c}\,T_c, \tag{2.10}$$

where T_c is T_c(H=0), and is taken to be 76.5 K based on the extrapolated value for $H \perp c$. The values obtained for $H \parallel c$ and $H \perp c$ are 96 and 590 T respectively, and interpolate between values obtained for $YBa_2Cu_3O_{7-\delta}$ crystals with T_c's of 62 and 92 K.[32, 33] The derived critical field slope does however change somewhat depending on

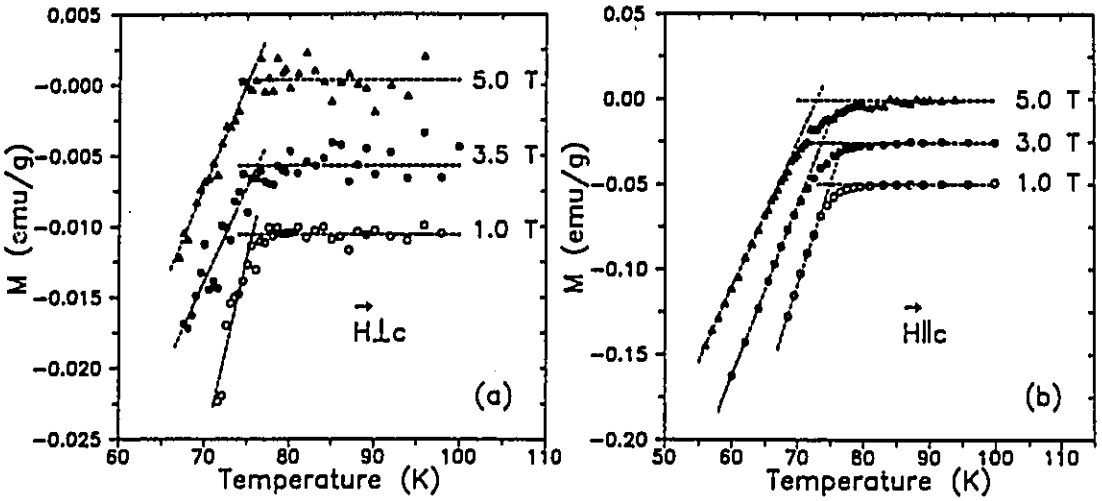

Figure 2.17: Temperature dependence of the magnetization in the vicinity of T_c for (a) $H \perp c$ and (b) $H \parallel c$ for representative field strengths. The dashed curves are linear least squares fits to the data above and below T_c. Lines of zero slope were used above T_c. The intersection is interpreted to be T_c for a given field strength. Note that for clarity the results for 1.0 and 3.5 T in (a) have been shifted down by 0.01 and 0.005 emu/g respectively while in (b) those for 1.0 and 3.0 T have been similarly adjusted by 0.05 and 0.025 respectively.

the range of points used in the fitting, and thus there is some uncertainty associated with these values, especially for $H \perp c$ where it can be almost as large as a factor of two. For $H \parallel c$ the error is smaller, approximately ± 10 T, and comes mostly from uncertainty in the value of $T_c(0)$.

2.2.4 The Coherence Length

At this point it is instructive to examine the effect of anisotropy in more detail. Using equation 2.7 the zero temperature coherence length can be obtained from the zero temperature upper critical field. But, as can be seen from the above analysis the upper critical field takes on a different value depending on the orientation of the field with respect to the crystallographic axes. This of course is due to the anisotropic

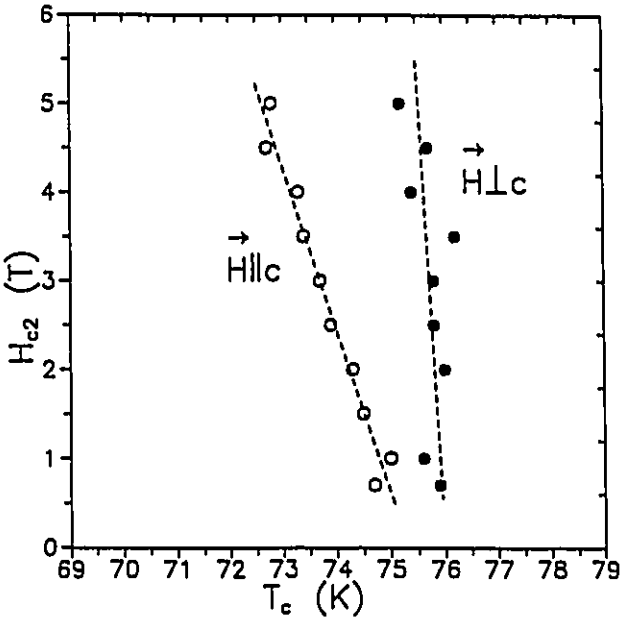

Figure 2.18: The upper critical field as derived from the linear extrapolation technique for both $H \perp c$ and $H \parallel c$. The critical field slopes obtained are -11 ± 4 and -1.8 ± 0.1 T/K respectively. The considerable scatter in the $H \perp c$ data is due to the fact that $M^{\perp c}$ is an order of magnitude smaller than $M^{\parallel c}$ (see figure 2.16).

nature of the cuprates. Equation 2.7 should therefore be written in tensor format:

$$H_{c2}^{k} = \frac{\Phi}{2\pi\xi_i\xi_j}, \tag{2.11}$$

where H_{c2}^{k} is the upper critical field when the field is applied along the k-axis, and ξ_i and ξ_j are the components of the coherence length along the i and j axes respectively. Consider figure 2.19 which shows the induced currents due to the application of a magnetic field (a) perpendicular and (b) parallel to the CuO_2 planes. In $Pb_2Sr_2(Y/Ca)Cu_3O_8$ which contains no chains the anisotropy between the a- and b-directions is negligible and hence for simplicity it is assumed that the physical properties are isotropic within the planes. Thus in figure 2.19(a) where the currents flow within the planes:

$$H_{c2}^{c} = \frac{\Phi}{2\pi\xi_{ab}^{2}}, \tag{2.12}$$

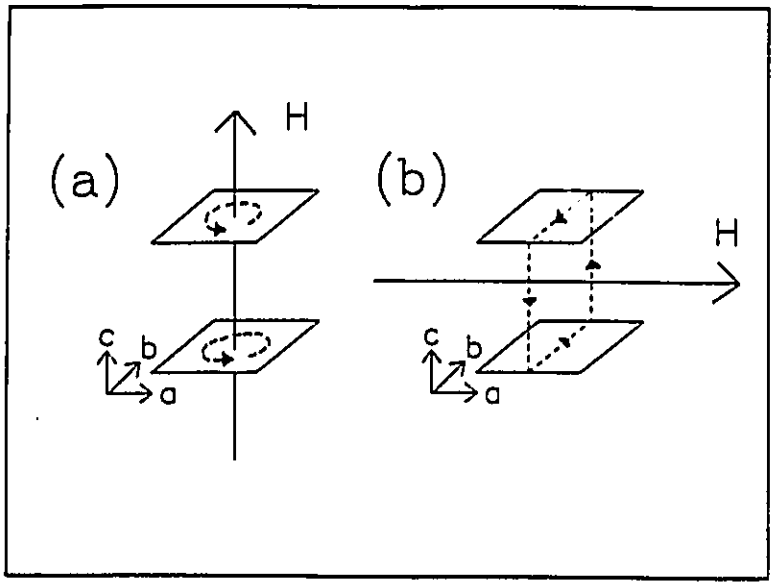

Figure 2.19: Induced currents in a double plane cuprate due to the application of a magnetic field (a) perpendicular and (b) parallel to the CuO_2 layers. Note that for simplicity only the two dimensional planes are shown.

where $\xi_a \approx \xi_b \equiv \xi_{ab}$ is the coherence length within the planes. When the field is applied parallel to the planes, as in (b), the currents flow both within and perpendicular to the CuO_2 layers and thus:

$$H_{c2}^{ab} = \frac{\Phi}{2\pi\xi_{ab}\xi_c}, \tag{2.13}$$

where ξ_c is the coherence length along the c-axis. For $H_{c2}^{\parallel}(0) = 96 \pm 10$ T a value of $\xi_{ab}(0) = 18.5 \pm 1.0$ Å is obtained. Using this value for $\xi_{ab}(0)$ and $H_{c2}^{\perp}(0) = 590 \pm 200$ T gives $\xi_c(0) = 3.0 \pm 1.1$ Å.

2.2.5 Superconducting Fluctuation Diamagnetism

The two-dimensional aspect of the structure of the cuprates enables the observation of superconducting fluctuation effects which gives rise to a second method by way of which estimates for the zero-temperature ab-plane coherence length and the upper critical field slope near T_c can be obtained. In figure 2.20 the magnetization in the

vicinity of T_c is plotted for a field of 1.5 Tesla (T) oriented both perpendicular and parallel to the c-axis of the crystal of $Pb_2Sr_2(Y/Ca)Cu_3O_8$.

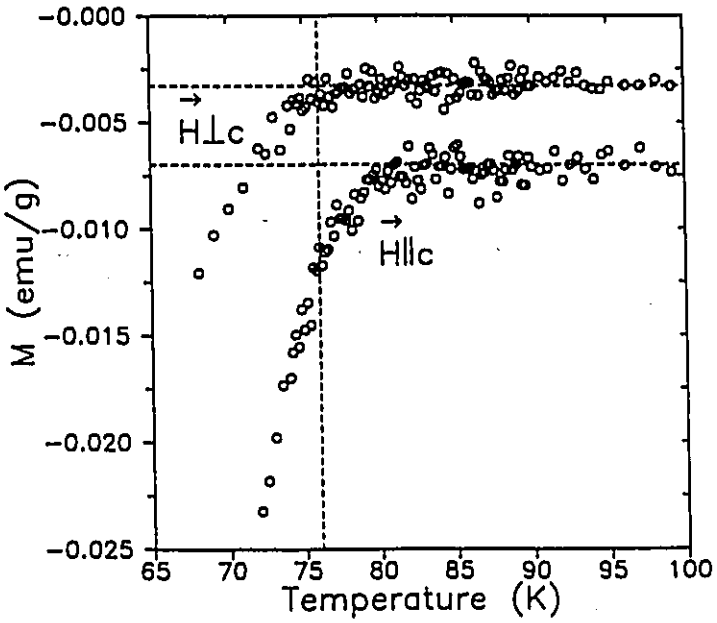

Figure 2.20: Temperature dependence of the magnetization of $Pb_2Sr_2(Y/Ca)Cu_3O_8$ in the vicinity of T_c for H=1.5 T for the c-axis of the crystal oriented both perpendicular and parallel to the field direction. The dashed curves are guides to the eye. The vertical line is at T=76 K, while the horizontal lines approximate the normal state magnetization for both field orientations. Note that for $H \perp c$ the data follows a temperature independent behaviour such as is shown by the horizontal dashed curve up to $\approx$ 76 K, whereupon there is an onset of T-linear diamagnetism, while for $H \parallel c$ there is already a clear deviation above 80 K.

A notable difference between the curves of figure 2.20 is the rounding of the transition for $H \parallel c$. For $H \perp c$ the magnetization is essentially temperature independent above $\approx$ 76 K at which point there is a relatively linear onset of diamagnetism due to the start of superconducting behaviour. The onset of superconducting diamagnetism begins above 80 K for $H \parallel c$. Its presence above T_c is due to superconducting fluctuations; that it is so readily observed for this field orientation is a consequence of the two dimensional character of the system.

The temperature dependence of the fluctuation contribution to the magnetization with the field, H, along the c axis of the crystal is given in the static 2D low-field Lawrence-Doniach model by:[35]

$$M_{fl}(T) = -\frac{g_{eff}\pi k_B \xi_{ab}^2(0) HT}{3\Phi^2 s}\frac{T_c}{T - T_c}. \tag{2.14}$$

Here g_{eff} is the number of two dimensional fluctuating (in this case CuO_2) layers, while s is the distance between such sets of layers, $\xi_{ab}(0)$ is the zero temperature ab-plane coherence length, and Φ is the flux quantum. For $Pb_2Sr_2(Y/Ca)Cu_3O_8$ $g_{eff} = 2$ and $s = 15.765$ Å.

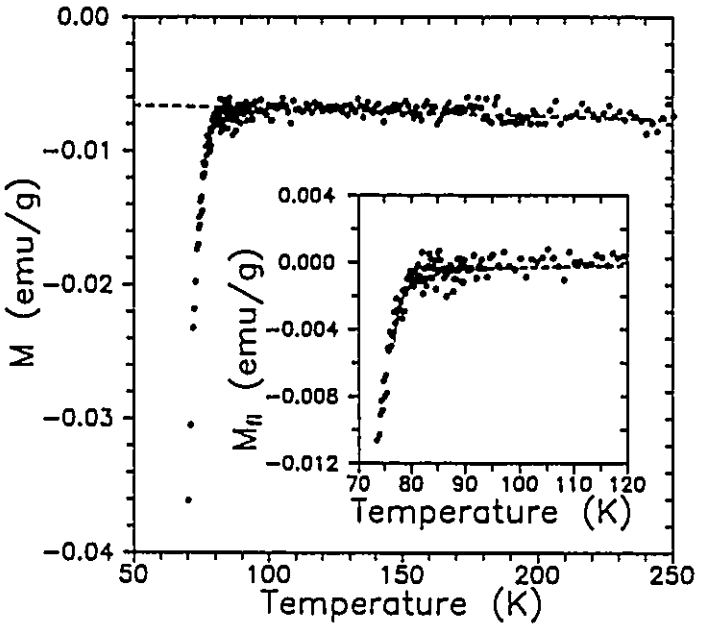

Figure 2.21: Temperature dependence of the magnetization of $Pb_2Sr_2(Y/Ca)Cu_3O_8$ for $H \parallel c$ (H=1.5 T) over an extended temperature range. The dashed curve is a linear least squares fit to the data above 150 K, and is interpreted as the normal state background. The inset shows an expanded view of the magnetization near T_c with this normal state background subtracted, which above T_c is regarded as the superconducting fluctuation diamagnetism (SFD). The dashed curve shows a fit to the 2D SFD theory with T_c=75.5 K and $\xi_{ab}(0)$ = 11.0 Å.

Figure 2.21 shows the temperature dependence of the magnetization up to

250 K for $H \parallel c$. Since fluctuation effects are generally limited to temperatures below $\approx 2T_c$, M_{fl} is determined by subtracting a linear fit to the data above 150 K (shown as the dashed curve in figure 2.21) from the full data set. This represents the normal state background. The fluctuation magnetization so obtained is plotted as a function of temperature in the vicinity of T_c in the inset to figure 2.21 and as $\log(-M_{fl}/T)$ versus $\log \frac{T-T_c}{T_c}$ in figure 2.22, where T_c is taken (with hindsight) to be 75.5 K. Note that from equation 2.14 a linear behaviour with slope -1 is expected. In the Lawrence-Doniach theory, there should be a transition to three dimensional (3D) fluctuations very near T_c, which is signified by a change to slope $-1/2$.[36] The dashed and solid curves in figure 2.22 represent lines of slope -1 and $-1/2$ respectively. Although there is considerable scatter in the data, this is essentially what is observed in figure 2.22. From the crossover in behaviour the critical region wherein the fluctuations are 3D in character is estimated to be approximately 2 K in size.

A least squares fit of the temperature dependence of M_{fl} above T_c to equation 2.14, excluding data in the 3D critical region, was then undertaken, minimizing χ^2 with respect to both T_c and $\xi_{ab}(0)$. The best fit was found to be for $T_c = 75.5 \pm 0.5$ K, $\xi_{ab}(0) = 11.0 \pm 0.5$Å, and is plotted in the inset to figure 2.21.

Note that in equation 2.14 T_c is actually $T_c(H)$. This implies that if this procedure is carried out for various magnetic field strengths, $H \parallel c$, the field dependence of T_c can be determined; or in other words, the temperature dependence of the upper critical field, $H_{c2}^{\parallel}$.

The fluctuation analysis can be applied to the series of curves shown in figure 2.16(b) for $H \parallel c$ in order to extract the temperature dependence of $H_{c2}^{\parallel}$. Because the measured temperature range is not so extensive $\xi_{ab}(0)$ is fixed at 11.0 Å, as found above and χ^2 is minimized only with respect to T_c. A typical fit is shown in the inset to figure 2.23 for $H = 3.0$ T where T_c was found to be 74.6 K. The upper critical field at a temperature of 74.6 K is thus so determined to be 3.0 T. The temperature dependence of $H_{c2}^{\parallel}$ obtained in this manner is shown in figure 2.23 as the open circles.

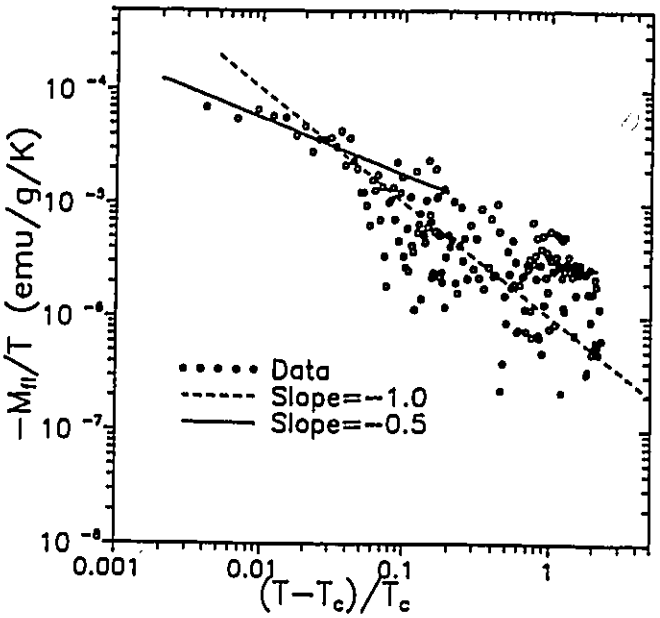

Figure 2.22: Log-Log plot of $\frac{-M_{\parallel}}{T}$ versus $\frac{T-T_c}{T_c}$. The dashed and solid curves are lines of slope -1 and -0.5 respectively. A change in slope is observed $\approx$ 2 K above T_c which may be indicative of a crossover from 3D fluctuations near T_c to 2D behaviour at higher temperatures.

The dashed curve represents a linear least squares fit to the data and gives a value of -1.7 ± 0.3 T/K for the upper critical field slope near T_c, $(\frac{dH_{c2}^{\parallel}}{dT})\,|_{T_c}$.

2.2.6 Comparison of Results

Note that this value for the upper critical field slope (-1.7 T/K) is in good agreement with that of section 2.2.3 (-1.8 T/K). It is noteworthy that the *ab*-plane critical field slope determined via analysis of the magnetization *above* T_c (the fluctuation-derived result) and that determined from the magnetization *below* T_c (the more direct linear extrapolation technique) are in agreement, although the scatter in the $H_{c2}(T_c)$ data from the fluctuation analysis (figure 2.23) is larger than it is for the linear extrapolation technique (figure 2.18) as is also indicated by the estimated uncertainties in the results of the two methods (-1.7 ± 0.3 and -1.8 ± 0.1 respectively).

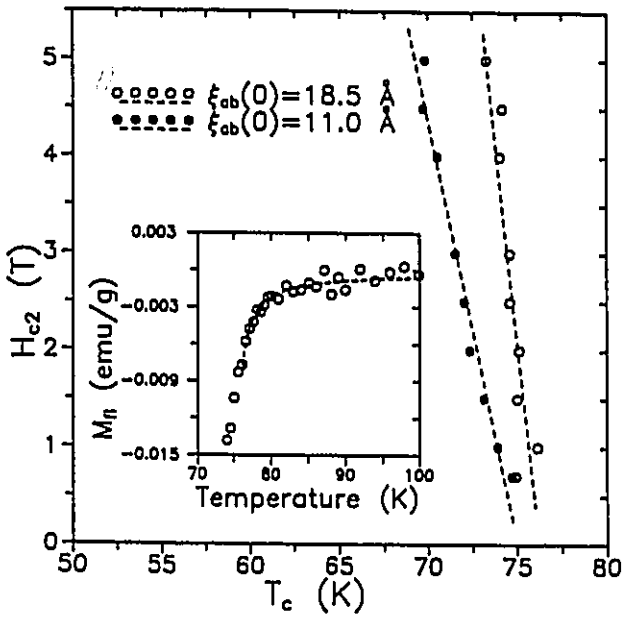

Figure 2.23: The in-plane ($H \parallel c$) upper critical field as derived from the fluctuation analysis for $\xi_{ab}(0)$=11.0 Å (open circles) and 18.5 Å (filled circles). The critical field slopes obtained are -1.7 ± 0.3 and -0.9 ± 0.3 T/K respectively. The inset shows a typical fit for $\xi_{ab}(0)$=11.0 Å. (In this case H=3.0 T, and the fitted value of T_c is 74.6 K).

The value for $\xi_{ab}(0)$ derived from the WHH relation is however considerably larger than that obtained from the fluctuation analysis which is somewhat unexpected since the critical field slopes are in good agreement. To determine whether it is possible to distinguish between an *ab*-plane coherence length of 11.0 Å and one of 18.5 Å, the fluctuation analysis was repeated with $\xi_{ab}(0)$ = 18.5 Å. The result is shown as the solid circles in figure 2.23. Again, the dashed curve is a linear least squares fit, the slope of which is -0.9 T/K. This is noticeably smaller than that obtained using $\xi_{ab}(0)$ = 11.0 Å, and clearly not in agreement with the slope derived using the linear extrapolation method. Since the critical slope obtained from the fluctuation analysis for $\xi_{ab}(0)$ = 11.0 Å agrees with that obtained via analysis of the T-linear magnetization below T_c, and because it is possible to distinguish between an *ab*-plane coherence length of 11.0 and 18.5 Å in the fluctuation analysis, it appears that the

WHH extrapolation may overestimate the coherence length somewhat. An alternate explanation would be that in the fluctuation analysis g_{eff} should not be taken as 2.[29] If this were the case $\xi_{ab}(0)$ from the fluctuation analysis would increase by a factor of $\sqrt{2}$ to 15.5 Å, which is in closer agreement with the WHH estimate.

Given the uncertainties involved in removing the normal state background, the fact that the crystal is small and hence the signal near T_c is weak, and that both results for the *ab*-plane coherence length are within the range of values typically quoted for other cuprate superconductors as derived from both magnetization measurements[32, 33, 35, 37, 38, 39] and fluctuation conductivity studies,[40] one should perhaps not place too much emphasis on the difference in the values of $\xi_{ab}(0)$ as determined directly from the fluctuation analysis (11.0 Å) and from the critical field slope via the WHH formula (18.5 Å). In general, however, it does appear that the *ab*-plane coherence length obtained via a superconducting fluctuation analysis, either diamagnetism,[35, 37, 38] or conductivity,[40] is smaller (typically 11-13 Å) than that obtained directly from the critical field slope[32, 33, 39] (typically 16-20 Å) which might indicate that there is a systematic difference in the results derived from the two methods. Hao *et. al.* have found that the linear extrapolation technique may overestimate the critical field slope somewhat, which would lead to still larger values for the coherence length.[39]

2.2.7 The Magnetic Penetration Depth

While H_{c1} is determined from low field magnetization measurements, the temperature dependence of the penetration depth in the vicinity of T_c can be obtained from measurements at intermediate fields. It is well established that for fields between the lower and upper critical fields, $H_{c1} \ll H \ll H_{c2}$, the reversible magnetization of an isotropic type II superconductor varies as $\ln H$ according to:[26]

$$M = \frac{H_{c1}}{8\pi \ln(\frac{\lambda}{\xi})} \ln(\frac{H}{H_{c2}\beta}), \tag{2.15}$$

where λ and ξ are, as above, the magnetic penetration depth and coherence length respectively and β is a constant which depends on a cutoff, chosen to overcome an unphysical logarithmic singularity in evaluating an integral approximation to a sum over the reciprocal vortex lattice (and therefore also on the form of the lattice). With H_{c1} given by the approximate London formula:

$$H_{c1} = \frac{\Phi}{4\pi\lambda^2}[\ln(\frac{\lambda}{\xi}) + 0.5], \tag{2.16}$$

where the additive factor of 0.5 is neglected in the high $\kappa = \frac{\lambda}{\xi}$ limit, (justified for the cuprates since the penetration depth is approximately two orders of magnitude larger than the coherence length) equation 2.15 becomes

$$M = \frac{\Phi}{32\pi^2\lambda^2}\ln(\frac{H}{H_{c2}\beta}). \tag{2.17}$$

Again this analysis can be extended to include electronic anisotropy by replacing the isotropic penetration depth, λ, by a tensor. Neglecting distinctions between the a- and b-directions the magnetization for the c-axis of the crystal oriented parallel or perpendicular to the field direction is then given by:

$$M_{\|c} = \frac{\Phi}{32\pi^2\lambda_{ab}^2}\ln(\frac{H}{H_{c2}^{\|}\beta}) \quad \text{and} \quad M_{\perp c} = \frac{\Phi}{32\pi^2\lambda_{ab}\lambda_c}\ln(\frac{H}{H_{c2}^{\perp}\beta}) \tag{2.18}$$

respectively, where λ_{ab} is the ab-plane penetration depth and λ_c the penetration depth along the c-direction. A plot of $M_{\|c}$ as a function of $\ln H$ will therefore have slope $\frac{dM_{\|c}}{d\ln H} = \frac{\Phi}{32\pi^2\lambda_{ab}^2}$. It is clear that the temperature dependence of the ab-plane penetration depth may then be extracted by evaluating this quantity at several different temperatures. Similarly, once $\lambda_{ab}(T)$ is known, the experimental slope values, $\frac{dM_{\perp c}}{d\ln H} = \frac{\Phi}{32\pi^2\lambda_{ab}\lambda_c}$, can be used to determine the temperature dependence of the c-axis penetration depth. In general λ^{-2} is expected to vary linearly with temperature in the vicinity of T_c so that a plot of $\frac{dM}{d\ln H}$ as a function of temperature should be linear near T_c. Furthermore from equation 2.18 the ratio of $\frac{dM_{\|c}}{d\ln H}$ to $\frac{dM_{\perp c}}{d\ln H}$ yields $\frac{\lambda_c}{\lambda_{ab}}$ which, since λ^2 is proportional to the effective mass, m, is equal to the effective mass anisotropy parameter $\gamma = (m_c/m_{ab})^{1/2}$ used to characterize the extent of the anisotropy in the

system. Thus, since $\frac{dM}{d\ln H}$ is linear in temperature near T_c, γ can be obtained from the ratio of the slopes corresponding to the two field orientations:

$$\gamma = \frac{\frac{d}{dT}\left(\frac{dM_{\parallel c}}{d\ln H}\right)}{\frac{d}{dT}\left(\frac{dM_{\perp c}}{d\ln H}\right)}. \tag{2.19}$$

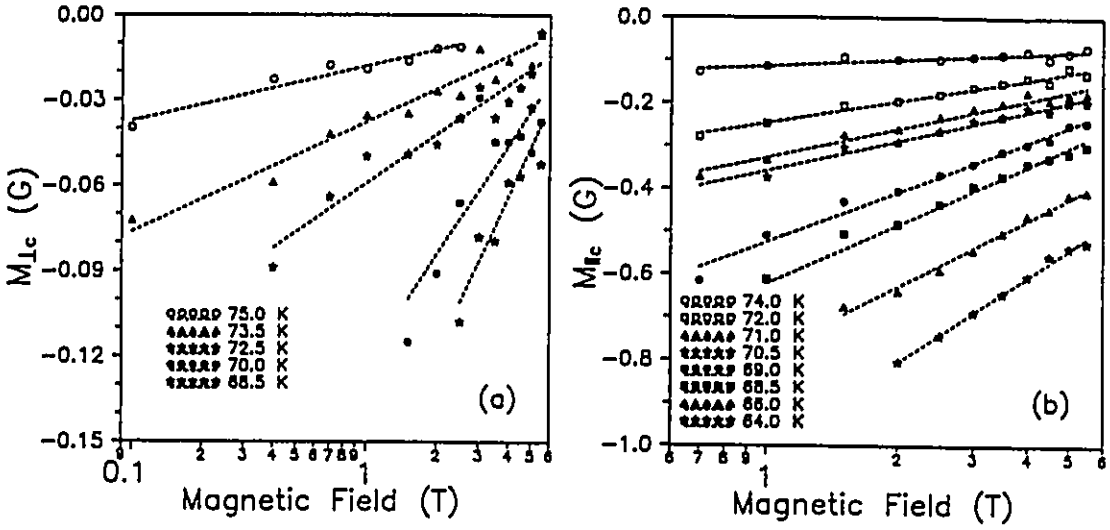

Figure 2.24: Magnetic field dependence of the magnetization of $Pb_2Sr_2(Y/Ca)Cu_3O_8$ at various temperatures for (a) $H \perp c$ and (b) $H \parallel c$. The dashed curves represent least squares fits to the data.

The magnetization data of figure 2.16 were replotted as a function of $\ln H$ for temperatures in the reversible regime in 0.5 K steps. Some representative results are shown in figures 2.24(a) and (b) for H perpendicular and parallel to c respectively. The expected linear behaviour is seen clearly for H parallel to c. Due to the much smaller signal to noise ratio in the H perpendicular to c data, the linearity is less obvious. Proceeding nevertheless with the analysis figure 2.25 shows the temperature dependence of the least-squares determined slopes of the $M(\ln H)$ curves. Note that for both orientations the linear behaviour expected near T_c is present which provides an *a posteriori* justification for the use of the H perpendicular to c data.

The effective mass anisotropy parameter, γ, can be determined from the ratio

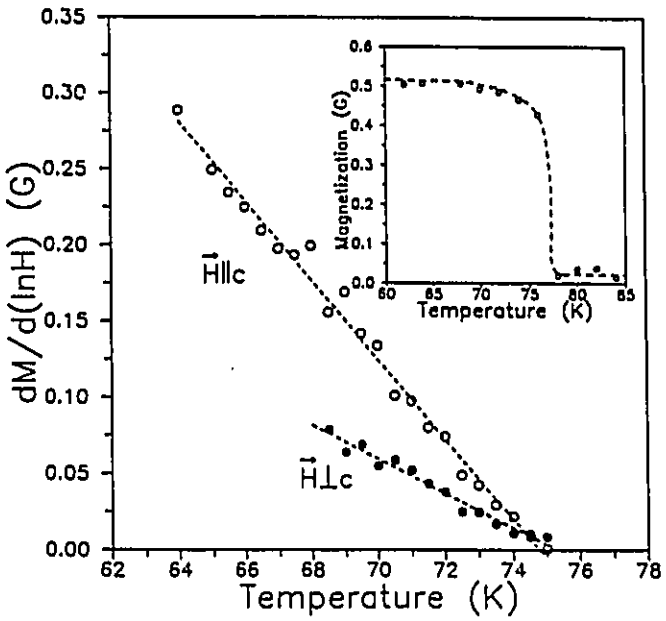

Figure 2.25: Temperature dependence of $dM/d(\ln H)$ for the two crystal orientations of interest. Note the expected linear behaviour. The dashed curves represent least squares fits to the data. The ratio of the slopes gives the anisotropy parameter $\gamma = (m_c/m_{ab})^{1/2} \approx 2.5$. The horizontal intercept gives T_c. Note that the value obtained ($\sim$ 75 K) corresponds to the 90% saturation value of the low field ($-1 < H < 0$ G) FC magnetic transition shown for $H \parallel c$ in the inset.

of the least squares slopes of the two curves in figure 2.25 according to equation 2.19. The result is $\gamma = 2.5$ or $m_c/m_{ab} = \gamma^2 \approx 6$.

Figure 2.26(a) shows the temperature dependence of λ_{ab} and λ_c calculated as discussed above. Of primary interest is the zero temperature penetration depth. From the restricted temperature range investigated it is difficult to extract $\lambda(0)$, although an estimate is possible by comparing the experimental results with the expected behaviour for various models. The usual procedure is to plot $[\lambda(0)/\lambda(T)]^2$ as a function of reduced temperature T/T_c. The fitting parameters are then $\lambda(0)$ and T_c. Note however that T_c can be discerned directly from figure 2.25 since at T_c $dM/d\ln H$ is zero. Comparable values are found for the two orientations, 74.7 K for H parallel to c and 75.3 K for H perpendicular to c. These values correspond closely to

the 90% criterion for determining T_c from the low field magnetic transition measured with a small negative field ($-1 < H < 0$ G) and shown in the inset to the figure.

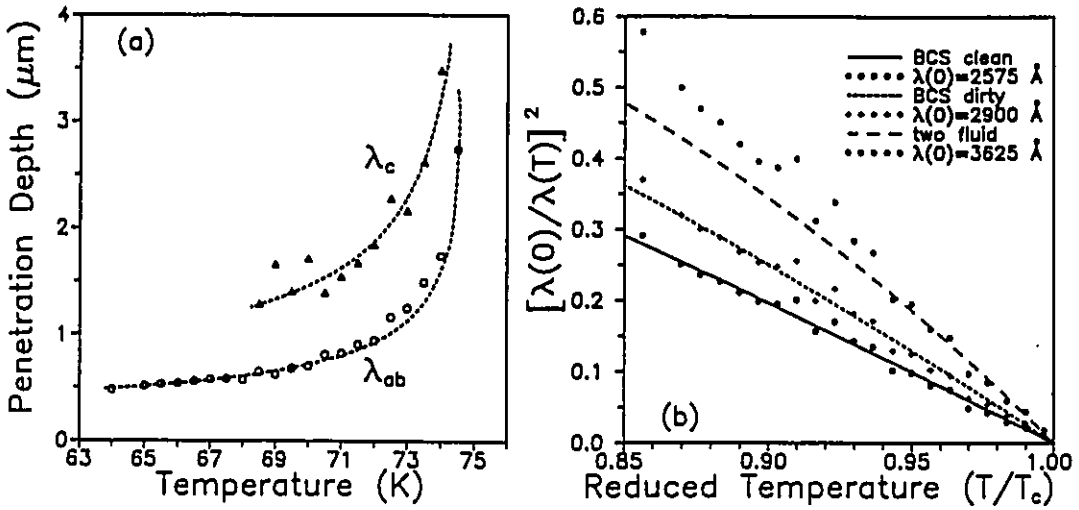

Figure 2.26: Temperature dependence of the penetration depth of $Pb_2Sr_2(Y/Ca)Cu_3O_8$. (a) Absolute determination of λ_{ab} and λ_c in the vicinity of T_c. The dashed curves are a guide to the eye. (b) Fit of $[\lambda(0)/\lambda_{ab}(T)]^2$ versus T/T_c data (points) to theory (curves). While it is clear that the data are less-well described by the two-fluid curve (for which the fit has been optimized near T_c, yielding a clear deviation at lower temperatures), it is difficult to distinguish between the clean and dirty-limit BCS results since reasonable agreement can be obtained within the range of temperatures investigated in both cases. The BCS clean-limit fit yields a lower limit for $\lambda_{ab}(0)$ of 2575 Å.

In figure 2.26(b) the best fit of the ab-plane data (fitting parameter $\lambda_{ab}(0)$ with T_c=74.7 K) to the prediction for $[\lambda(0)/\lambda(T)]^2$ for the two fluid model and in the BCS dirty and clean (or London) limits[41] is shown. In this restricted temperature range the data appear to be described better by BCS than by two-fluid behaviour (*ie* if, as has been done in figure 2.26(b), $\lambda(0)$ is chosen such that the data points follow the two-fluid behavior near T_c then the data points at lower temperature fall significantly above the theoretical curve whereas in the BCS cases a value can be

chosen for $\lambda(0)$ such that the data points follow the theoretical behavior reasonably well throughout the range of temperatures investigated). The scatter in the data is such that it is difficult to distinguish between dirty and clean-limit BCS behaviour. Thus one can conclude simply that from the fit to BCS clean-limit behaviour a lower limit for $\lambda_{ab}(0)$ of 2575 Å is obtained. Recent muon spin rotation (μSR) measurements yield a preliminary estimate for $\lambda_{ab}(0)$ based on clean limit BCS of 2700 Å,[42] in good agreement with this magnetization derived result. The c-axis penetration depth data are more scattered and limited in extent and thus rather than predict $\lambda_c(0)$ by fitting to theory it is convenient to make use of the experimentally determined effective mass anisotropy. With $\lambda_{ab}(0)$ given by the BCS clean limit result (2575 Å) and $\lambda_c(0)/\lambda_{ab}(0) = (m_c/m_{ab})^{1/2} = 2.5$ 6425 Å is obtained for $\lambda_c(0)$.

2.2.8 Relation to H_{c1}

It is now generally agreed that $\lambda_{ab}(0)$ for $YBa_2Cu_3O_{7-\delta}$ is of the order 1500 Å (values typically range from 1300 Å to 1700 Å).[43, 44] Measurements for $Tl_2Ba_2CaCu_2O_8$ films yield a value of 2000 Å for $\lambda_{ab}(0)$ [45] while for single crystal $Bi_2Sr_2CaCu_2O_8$ $\lambda_{ab}(0)$ has been found to be 3000 Å.[46] According to equation 2.16 for $\lambda_{ab}(0)$ to be 3000 Å one would expect H_{c1} to be approximately four times smaller in $Bi_2Sr_2CaCu_2O_8$ than in $YBa_2Cu_3O_{7-\delta}$ since the coherence lengths in $Bi_2Sr_2CaCu_2O_8$ are presumably of the same order of magnitude as in $YBa_2Cu_3O_{7-\delta}$. This reduction in H_{c1} should then also manifest itself to a somewhat smaller extent in $Pb_2Sr_2(Y/Ca)Cu_3O_8$.

The values obtained for H_{c1} of $Pb_2Sr_2(Y/Ca)Cu_3O_8$ at low temperatures are not noticeably smaller than in $YBa_2Cu_3O_{7-\delta}$ (for single crystal $YBa_2Cu_3O_{7-\delta}$ Krusin-Elbaum *et al.*[47] estimate $H_{c1}(0) = 180 \pm 20$ G for $H \perp c$ and 530 ± 50 G for $H \parallel c$ while Scheidt *et al.*[44] find respectively 113 ± 30 G and 340 ± 50 G for oriented powder samples). The problem then is of reconciling the ab-plane penetration depth determined for $Pb_2Sr_2(Y/Ca)Cu_3O_8$ (which is close to twice that

of $YBa_2Cu_3O_{7-\delta}$) with a value for $H_{c1}(0)$ that is comparable to that of $YBa_2Cu_3O_{7-\delta}$. One possibility is that there is an inherent problem with the method used to extract $\lambda_{ab}(T)$. This however, seems unlikely since Mitra *et al.*[46] have obtained, using this method, reasonable values of $\lambda_{ab}(0)$ for polycrystalline (Y/Gd)$Ba_2Cu_3O_7$, and grain-aligned $YBa_2Cu_3O_{7-\delta}$, while Schilling *et al.*,[48] maintaining that no exact knowledge of the value of the anisotropy parameter is required provided $\gamma \geq 5$, extracted an equally credible value of $\lambda_{ab} = 1390$Å for polycrystalline $YBa_2Cu_3O_{7-\delta}$. In addition, the magnetization data presented by Welp *et al.*[32] for single crystal $YBa_2Cu_3O_{7-\delta}$ has been analyzed according to the procedure in question and with the limited data set available (Welp *et al.* show the temperature dependence of $M_{\|c}$ for four magnetic field strengths which dictates that each $M(\ln H)$ curve be constructed from only three or four points depending on the temperature) good agreement is found with the expected trends of the method together with a convincing estimate of 1100 Å for $\lambda_{ab}(0)$ based on a fit to clean limit BCS behaviour.

It is well known that the penetration depth can be enhanced over the London value, λ_L, as a result of disorder when the mean free path, l, is not large in comparison to the coherence length, ξ. As has been determined above the ab-plane coherence length is already very small (approximately 10-20 Å), implying that the mean free path would have to be of the order of a few lattice spacings if a disorder correction were to be important. $YBa_2Cu_3O_{7-\delta}$, for instance has been found to be within the clean limit where $l \gg \xi$.[49] The situation may well be different in $Pb_2Sr_2(Y/Ca)Cu_3O_8$.

A portion of this discrepancy may also lie with errors associated with the determination of the lower critical field. A major contributor of error to the experimentally determined value of the lower critical field is the geometry of the sample. This is important for two reasons. Firstly, sample geometry dictates the demagnetization factor that must be used in order to extract the actual value of the lower critical field from the measured field at which the first onset of flux penetration is observed. In general the demagnetization factor is not a constant for a given sample geometry

and field orientation as has been assumed in the analysis. Since the demagnetization correction for the $H \parallel c$ orientation of the sample is large, a small error in the determination of n can lead to considerable changes in the derived magnitude of $H_{c1}^{\parallel}$. Secondly, the sample morphology determines the relative importance of processes such as surface pinning which can inhibit the entry of flux at the value of H_{c1} predicted by the Bean model wherein only internal flux pinning is considered. The crystals of $Pb_2Sr_2(Y/Ca)Cu_3O_8$ are in general more cubic-like in their growth habit than crystals of the other materials. The more oblate-like shape of the $Pb_2Sr_2(Y/Ca)Cu_3O_8$ crystals, indicated as well by the magnitude of the experimentally derived demagnetization factors, may imply a comparatively greater contribution by surface pinning. The relative importance of the surface pinning should increase as the temperature is lowered, providing a possible explanation for the unusual temperature dependence of the in-plane lower critical field, $H_{c1}^{\parallel}$ shown in figure 2.15.

The fact that the magnitude of the zero temperature in-plane lower critical field appears to be too large is most likely caused by a combination of the effects discussed: surface pinning, uncertainty in the value of the demagnetization correction, and the questionable appropriateness of the slab geometry (utilized in the analysis of H_{c1}) for this sample orientation. In contrast, for the penetration depth no explicit sample geometry is assumed in the analysis, and because the data are obtained at intermediate field strengths demagnetization corrections are negligible.

2.3 Summary of Results

The magnetization-derived results for the various fundamental superconducting parameters of $Pb_2Sr_2(Y/Ca)Cu_3O_8$ are summarized in table 2.1. Also included is an estimate of the extent of the anisotropy between ab-plane and c-axis properties. In general the extent of the anisotropy observed is closer to that of $YBa_2Cu_3O_{7-\delta}$ than to that of the highly anisotropic $Bi_2Sr_2CaCu_2O_8$.

Table 2.1: Magnetization derived fundamental superconducting parameters of $Pb_2Sr_2(Y/Ca)Cu_3O_8$. For $\lambda(0)$ and $\xi(0)$ the two columns labelled '*ab*' and '*c*' represent actual *ab*-plane and *c*-axis components. For properties of the upper and lower critical field these two columns imply the value when the applied field is within the planes and along the *c*-axis respectively. 'Ratio' refers to the ratio of the larger to smaller quantity. The 'Method's are summarized as follows: (a) best estimate based on low field magnetization curves and the extrapolated values from the penetration depth and upper critical field studies, (b) ln H behaviour of M at intermediate fields, (c) deviation from perfect diamagnetism, (d) diamagnetic fluctuation analysis, (e) analysis of the T-linear magnetization below T_c, (f) WHH extrapolation, and (g) GL relationship between H_{c2} and ξ.

Property		*ab*	*c*	Ratio	Method
T_c(H=0)	(K)	76±1			a
$\lambda(T=0)$	(Å)	2575	6425	2.5	b
$H_{c1}(T=0)$	(G)	95±10	505±20	5.3	c
$-dH_{c2}/dT_c$	(T/K)		1.7±0.3		d
(T≈ T_c)		11±4	1.8±0.1	6.1	e
$H_{c2}(T=0)$	(T)	590±200	96±10	6.1	f
$\xi(T=0)$	(Å)	11.0±0.5			d
		18.5±1.0	3.0±1.1	6.2	g

Chapter 3

Anisotropy in the dc Resistivity of $Pb_2Sr_2(Y/Ca)Cu_3O_8$

3.1 Background

3.1.1 Resistivity: Definition and Temperature Dependence

The second defining characteristic of a superconductor is the onset of zero resistance below T_c. Consider a sample of uniform cross-sectional area, A, as shown in figure 3.1. The resistance, R, between two points, C and D, is determined by measuring the potential drop, V, upon application of a constant uniform current, I, according to Ohm's law:

$$R = \frac{V}{I}. \tag{3.1}$$

The potential drop is given by the line integral of the electric field vector between these two points:

$$V = \int_C^D E \cdot dl = EL', \tag{3.2}$$

where L' is the distance between C and D. This dependence of the experimental result on sample dimensions is eliminated by considering instead the resistivity which

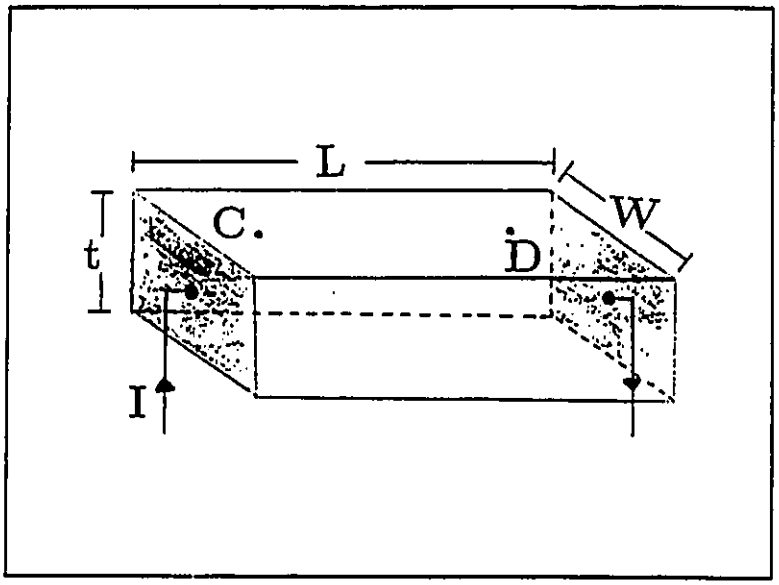

Figure 3.1: Sample of dimensions $L \times W \times t$ with uniform cross-sectional area $A = Wt$ (shaded) used to introduce the concept of resistivity. The configuration for experimental determination of the resistivity described in the text is also shown.

is an intrinsic property. Writing the current in terms of the current density, J as:

$$I = JA, \tag{3.3}$$

together with equations 3.1 and 3.2 yields:

$$E = R\frac{A}{L}J. \tag{3.4}$$

Since E and J are independent of sample dimensions, the quantity $R\frac{A}{L}$, which is defined as the electrical resistivity, ρ, is also geometry invariant.

Electrical resistivity in ordinary metals arises as a result of the scattering of electrons by thermal lattice vibrations (phonons) and defects. As the temperature is lowered in a normal metal, the available thermal energy also decreases, and hence the rate of scattering due to phonons. This gives rise to a decreasing resistivity. The rate of decrease is found to be linear. That is,

$$\rho \propto T, \tag{3.5}$$

with an intercept on the temperature axis at some fraction of the Debye temperature. At very low temperatures there is expected to be a transition to a T^5 dependence due to the decreasing number of phonons available to contribute to the scattering process, and the increasing predominance of forward scattering events (for a discussion see eg. reference [50]). Figure 3.2, shows schematically the expected temperature dependence of the resistivity. In real materials, however the scattering is usually limited by lattice defects before the onset of T^5 behaviour. In this case the fixed impurity sites give rise to a constant scattering rate and hence a temperature independent residual resistivity as shown by the long dashed curve in figure 3.2. The superconducting state is characterized by a sudden drop to zero resistance at a temperature labelled T_c; also illustrated in figure 3.2 (short dashed curve).

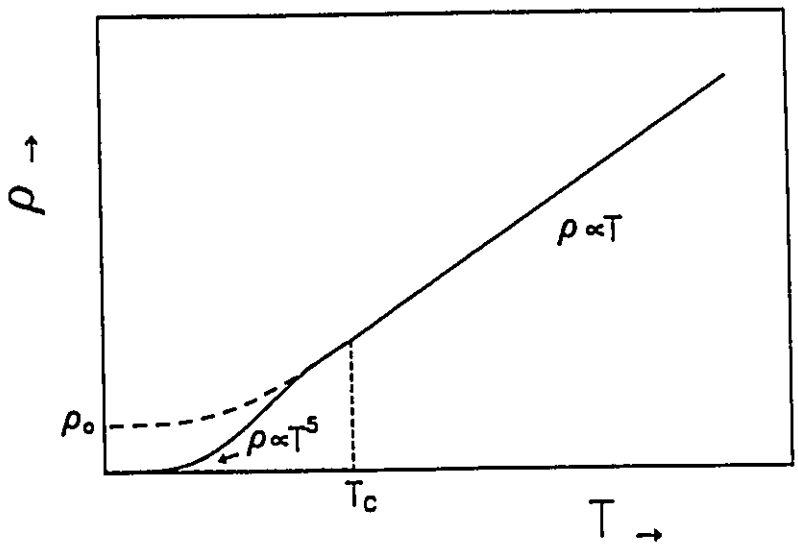

Figure 3.2: Temperature dependence of the electrical resistivity. The solid curve shows the theoretical expectation with a T^5 dependence at low temperatures, while the long dashed curve shows the usual experimentally observed impurity-limited behaviour. The short dashed curve shows a transition to the superconducting state ($\rho = 0$) at a temperature T_c.

3.1.2 Anisotropic van der Pauw Technique

As noted in the previous chapter, the anisotropic nature of the structure of the cuprates manifests itself in the physical properties, and consequently the resistivity must also be expressed as a tensor. Once again, however, it is assumed that $Pb_2Sr_2(Y/Ca)Cu_3O_8$ is essentially isotropic within the *ab*-plane and hence only two components; ρ_{ab} and ρ_c, need be considered. These are the resistivities within the *ab*-plane and along the *c*-axis respectively.

There exist many methods by way of which the dc-resistivity can be measured, but the most common approach is a four-probe technique. The basic premise is that a current is passed through two contacts while the resulting voltage drop is measured across another two. Since there is no current flowing through the voltage contacts (except the small amount drawn by the voltmeter itself) this configuration eliminates contact resistance from the measurement. The most useful of the four-probe techniques for samples of somewhat irregular geometry is the van der Pauw method.[51] The theory underlying the technique has been described previously,[52] thus only the main results will be stated here.

The technique requires a singly connected (*ie.* it should contain no isolated holes) sample of homogeneous thickness, d, and otherwise arbitrary shape with four point contacts A, B, C, and D located along its boundary (figure 3.3). The resistivity ρ, is found to satisfy the identity:

$$e^{-\frac{\pi d}{\rho}R_{AB,CD}} + e^{-\frac{\pi d}{\rho}R_{BC,DA}} = 1, \tag{3.6}$$

where $R_{AB,CD}$ is the potential difference between contacts D and C per unit current through contacts A and B and similarly $R_{BC,DA}$ is the potential difference between the contacts A and D per unit current through contacts B and C. The resistivity can be written explicitly in the form:

$$\rho = \frac{\pi d}{\ln 2}\frac{R_{AB,CD} + R_{BC,DA}}{2} f\left(\frac{R_{AB,CD}}{R_{BC,DA}}\right), \tag{3.7}$$

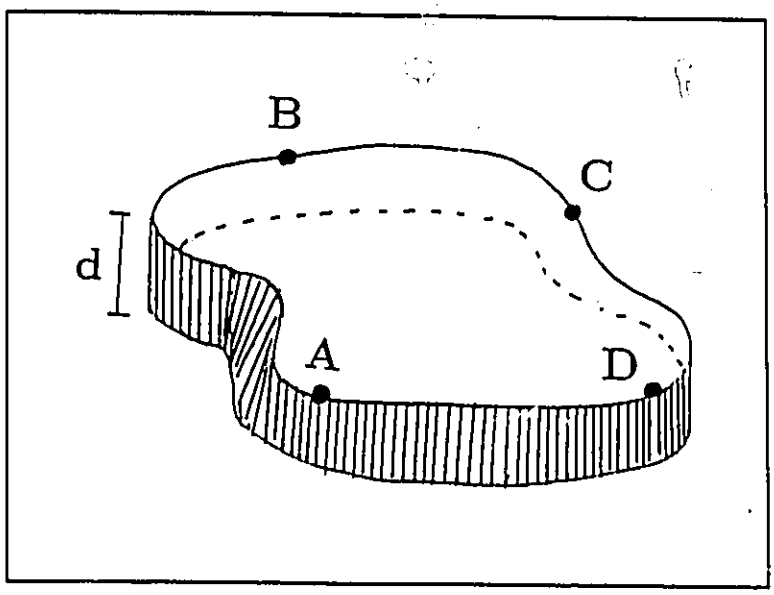

Figure 3.3: Sample geometry satisfying the van der Pauw method of determining resistivity.

where f is a function of the ratio $k = \frac{R_{AB,CD}}{R_{BC,DA}}$, and satisfies the relation:

$$e^{-\frac{2\ln 2}{f(1+\frac{1}{k})}} + e^{-\frac{2\ln 2}{f(1+k)}} = 1. \tag{3.8}$$

Thus, by measuring $R_{AB,CD}$, $R_{BC,DA}$ and the thickness of the sample, d, the resistivity can be calculated.

This analysis can be easily extended to include anisotropic samples.[53] An anisotropic material generally has three resistivity components, ρ_a, ρ_b and ρ_c corresponding to the three orthogonal directions, the a-, b-, and c-axes of the resistivity tensor of the crystal. It can be shown that in general the resistivity measured on an ij face, ρ_{ij}, is the geometrical mean of the components ρ_i and ρ_j; that is $\rho_{ij} = \sqrt{\rho_i \rho_j}$.[53] Now suppose that the sample has been prepared such that the two plane parallel surfaces of figure 3.3 are perpendicular to the c-axis. In this case:

$$\rho_{ab} = \sqrt{\rho_a \rho_b}, \tag{3.9}$$

where ρ_{ab} is the resistivity determined using equation 3.7. Similarly by preparing

ac-plane and bc-plane samples the quantities:

$$\rho_{ac} = \sqrt{\rho_a \rho_c} \tag{3.10}$$

and

$$\rho_{bc} = \sqrt{\rho_b \rho_c} \tag{3.11}$$

can be determined. Equations 3.9, 3.10, and 3.11 can then be used to solve explicitly for the three components of the resistivity tensor ρ_a, ρ_b, and ρ_c.

The situation is somewhat simpler for $Pb_2Sr_2(Y/Ca)Cu_3O_8$ because the properties are essentially isotropic within the ab-plane, that is,

$$\rho_a \approx \rho_b \equiv \rho_{ab}. \tag{3.12}$$

Thus in order to determine the two components of the resistivity tensor of $Pb_2Sr_2(Y/Ca)Cu_3O_8$, ρ_{ab} and ρ_c, one need only measure the sample configuration corresponding to equation 3.9 and one of either equation 3.10 or 3.11.

3.2 Anisotropy in the dc-Resistivity of $Pb_2Sr_2(Y/Ca)Cu_3O_8$

3.2.1 Experimental Details

Small silver paint contacts were painted onto six corners of the crystal such that there are four contacts on the ab-face, and four on the *eg.* $a'c$-face. The primed notation is used to indicate that the morphological edges of the sample run in the [110] (a') and [1$\bar{1}$0] (b') directions, not along the [100] (or a) and [010] (or b). Since $\rho_a \approx \rho_b \equiv \rho_{ab}$ then $\rho_{a'} = \rho_{b'} = \rho_{ab} \approx \rho_a \approx \rho_b$. The configuration is shown schematically in figure 3.4. In order to obtain low contact resistance (typically $< 1\Omega$) a heat treatment consisting of an anneal in flowing N_2 gas at 600°C for approximately 6-12 hours was necessary. 25 μm gold wires were then attached to the contacts using silver paint.

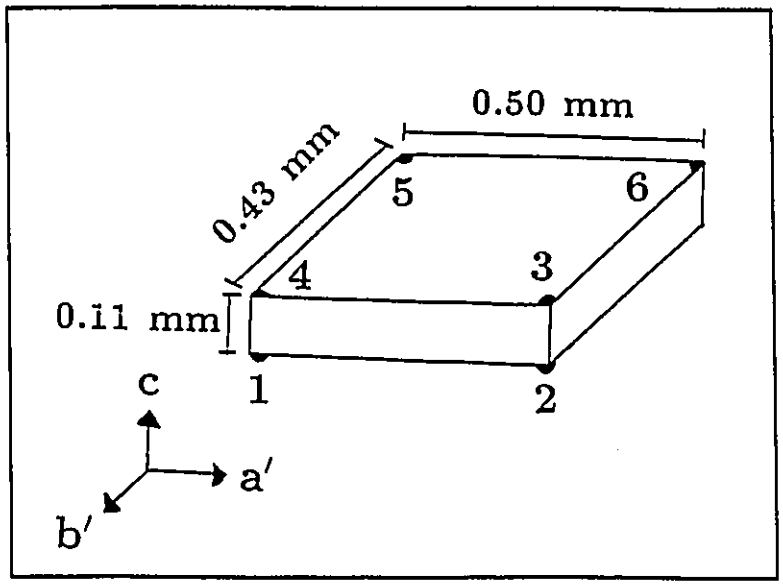

Figure 3.4: Dimensions and contact arrangement of the crystal used to determine the anisotropy in the dc resistivity of $Pb_2Sr_2(Y/Ca)Cu_3O_8$. The contacts are labelled from 1-6. Contacts 1-4 are used to measure the $a'c$-face while 3-6 are used to measure the ab-face. The a' and b' directions were assigned arbitrarily.

The experimental arrangement for measuring the resistivity has also been described previously,[52] so only a brief summary is presented here. The measurements were made as a function of temperature from liquid helium temperature (≈ 4 K) to room temperature (≈ 300 K) using a probe which fits directly into a helium storage dewar thereby eliminating the need to perform a helium transfer. The probe tip houses four electrodes. The sample can be electrically connected to these electrodes with the 25 μ gold wires using silver paint. Often an intermediate stage is engaged such that these fine gold wires are first attached to larger contact pads on an insulating substrate. The latter are then soldered or connected with silver paint to the probe electrodes with thicker wire. This enables detailed work to be carried out under a microscope prior to attaching the sample to the probe. The sample (or the substrate upon which the sample is mounted) sits directly above the temperature sensor which is a silicon diode. The storage dewar has a temperature gradient ranging

from 4.2 K near the bottom at the level of the liquid helium to room temperature at the top of the dewar. The temperature of the sample is thus varied simply by changing the height of the probe tip above the level of the liquid helium in the storage dewar. Due to the small size of the crystals, the temperature gradient across a given sample is expected to be only a small fraction of a degree. The data collection is fully automated as described previously.[52]

3.2.2 Results

Figure 3.5(a) shows the temperature dependence of the resistances $R_{12,34}$ and $R_{23,41}$ corresponding to the measurement of the $a'c$-face of a crystal of $Pb_2Sr_2(Y/Ca)Cu_3O_8$, the dimensions of which are shown in figure 3.4, using the van der Pauw method as described above. That the c-axis resistivity is significantly larger than that in

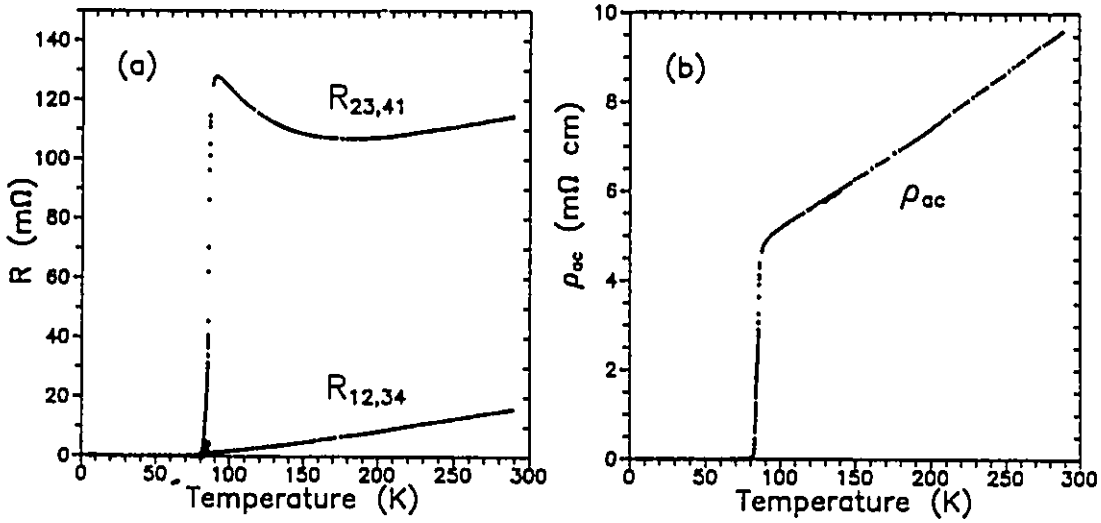

Figure 3.5: (a) Temperature dependence of the resistances $R_{12,34}$ and $R_{23,41}$ corresponding to the measurement of the $a'c$-face of the crystal illustrated in figure 4 using the van der Pauw method as described above. (b) The derived result for ρ_{ac}.

the ab-plane can already be deduced from the raw data. Even though the c-axis dimension (0.11 mm) is smaller than the a'-axis dimension (0.50 mm) $R_{23,41}$ where the current flows along the c-axis is more than an order of magnitude larger than $R_{12,34}$

where the current flows along the a'-direction. The resistivity $\rho_{a'c}$, extracted using equation 3.7 is shown in (b). Similarly figures 3.6(a) and (b) show respectively the measured resistances $R_{34,56}$ and $R_{45,36}$ and the calculated resistivity ρ_{ab}. Although the

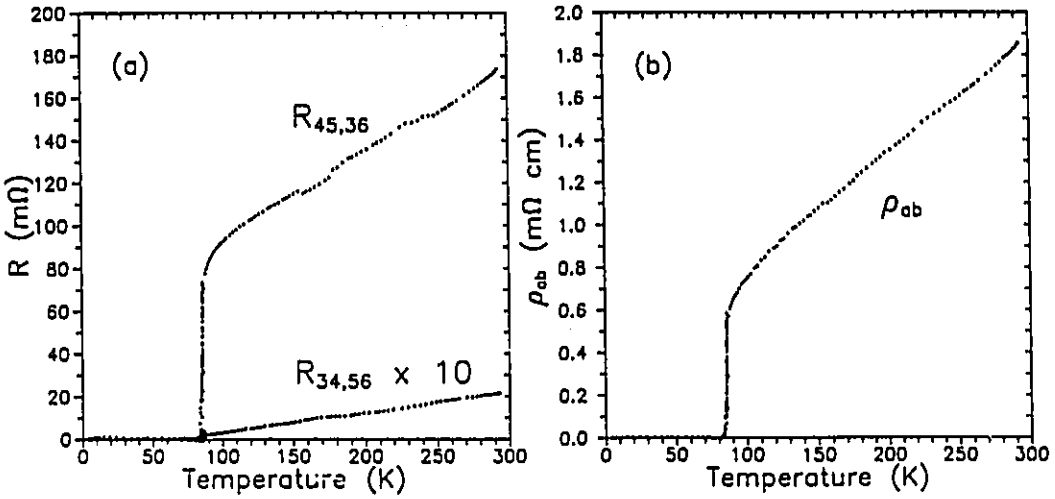

Figure 3.6: (a) Temperature dependence of the resistances $R_{34,56}$ and $R_{45,36}$ corresponding to the measurement of the ab-face of the crystal illustrated in figure 4 using the van der Pauw method as described above. (b) The derived result for ρ_{ab}.

b' dimension is smaller than the a' dimension the resistance $R_{45,36}$ seems comparatively large. It could be that due to the finite size of the contacts with respect to the small crystal the effective length along the b'-axis is significantly shorter, or that a small component of ρ_c is contained in $R_{45,36}$. The derived resistivity, ρ_{ab} is however in reasonable agreement (within a factor of two) with ab-plane measurements that have been carried out on 4 other crystals from the same batch as shown in figure 3.7(a). The variation is believed to be due mainly to experimental uncertainty in the absolute value caused by the finite size contacts on the small samples and inaccuracy in the thickness measurement rather than a sample to sample dependence since other properties (crystallographic, magnetic, and optical) of crystals from this same batch have been found to be reproducible. Further evidence that this is so comes from normalizing each curve to the value of the resistivity at 200 K as shown in figure

3.7(b). All five curves lie virtually on top of one another with similar slope and intercept, indicating an intrinsic temperature dependence. From figure 3.7(a) it is concluded that the room temperature *ab*-plane resistivity is $1.25 \pm 0.5 m\Omega cm$.

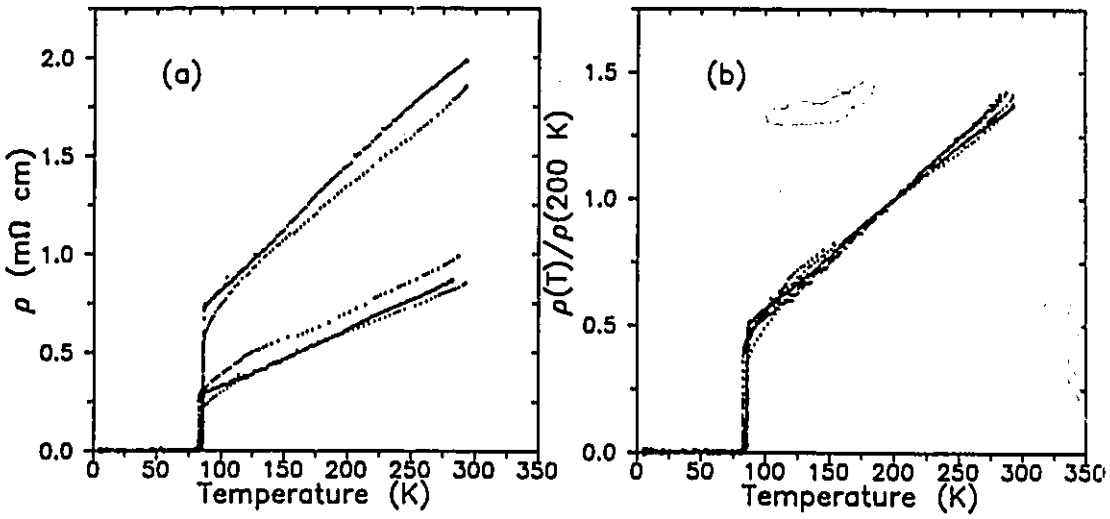

Figure 3.7: (a) Comparison of the experimentally derived *ab*-plane resistivity for 5 crystals from the same batch. Variations are believed to be due mainly to experimental error in the absolute value rather than intrinsic sample to sample dependences as can be seen from (b) where all curves have been normalized to their value at 200 K and are observed to obey the same temperature dependence.

The crystals from this particular batch were found to exhibit the best properties of all of the batches of crystals of $Pb_2Sr_2(Y/Ca)Cu_3O_8$ that were synthesized; that is, the resistivity is lowest, the optical reflectance highest, and the magnetic and resistive transitions are the sharpest. For this reason a crystal from this same batch was chosen for the magnetization study discussed in chapter 2, as well as for the optical reflectance study to be discussed in chapter 4.

Figure 3.8 shows the *ab*-plane and *c*-axis resistivity of the crystal discussed above, (a), (extracted from the results of figures 3.5 and 3.6(b) via equation 3.10 with $\rho_{a'} \approx \rho_{ab}$), compared to that obtained, via the same technique, for a crystal from another batch (b). The crystal in (a) shows a positive temperature coefficient for ρ_c

except very near T_c while the crystal in (b) which has an ab-plane resistivity, ρ_{ab}, similar to that of crystal (a) shows a negative coefficient for ρ_c. The magnetically measured transition for crystals from the batch of crystal (b) is not as sharp as it is for those of the batch of crystal (a). It is also the case in $YBa_2Cu_3O_{7-\delta}$ that as the sample quality improved metallic-like behaviour along the c-axis began to prevail.[54, 55]

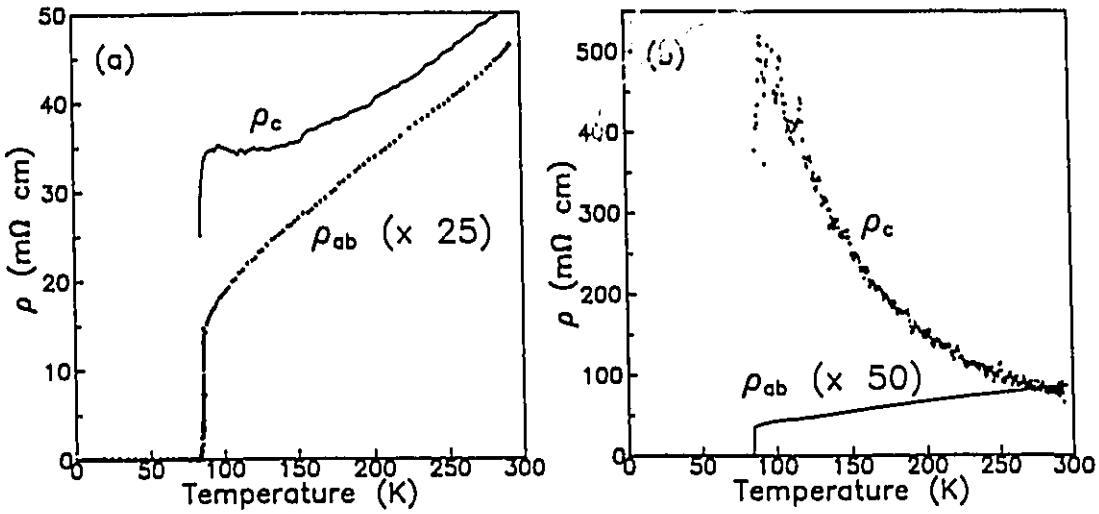

Figure 3.8: Anisotropic temperature dependence of the resistivity for a good (a) and poorer (b) quality $Pb_2Sr_2(Y/Ca)Cu_3O_8$ crystal.

The extent of the anisotropy is described by the anisotropy ratio $\frac{\rho_c}{\rho_{ab}}$, which for crystal (a) is about 30 at room temperature and increases to approximately 50 near T_c. This is within the range of values typically reported for $YBa_2Cu_3O_{7-\delta}$,[54, 55] and shows that the extent of the anisotropy in this system is closer to that of $YBa_2Cu_3O_{7-\delta}$ than to that of the highly anisotropic $Bi_2Sr_2CaCu_2O_8$ where the c-axis resistivity is several orders of magnitude larger than that in the ab-plane.[17]

The absolute magnitude of the ab-plane resistivity is however close to an order of magnitude larger than in the other two systems. Based on optical reflectivity measurements which reveal a significantly lower effective optical carrier density (chapter 4) and on the intermediate field magnetization measurements discussed in chapter

2 from which a considerably larger low temperature penetration depth was extracted it can be concluded that the higher absolute resistivity reflects an intrinsically lower carrier concentration in this system.

3.3 Magnetic Field Dependence of the Resistivity

Another way to estimate the extent of the anisotropy between *ab*-plane and *c*-axis properties is to examine the effect of a magnetic field on the superconducting transition. From the discussion in chapter 2 of the temperature dependence of the upper critical field one would expect that as the field increases T_c decreases and hence there should be a shift of the resistive transition to lower temperature as illustrated diagramatically in figure 3.9(a). This is the behaviour observed in most conventional type II superconductors. Furthermore, since the upper critical field slope is steeper for a field applied perpendicular to the *c*-axis than for one applied parallel, the shift should be correspondingly larger for $H \parallel c$.

3.3.1 Flux Motion

The experimental situation in the cuprates deviates somewhat from this. What is observed is that instead of shifting, the resistive transition *broadens* upon application of a magnetic field. This is shown in figure 3.9(b). In order to try to understand this the consequences of applying an electrical current to a superconducting sample in the presence of a magnetic field must be examined.

Recall that for $H > H_{c1}$ there is the development of a flux line lattice in the mixed state as illustrated in figure 2.9 of chapter 2. If a transport current is now applied perpendicular to the direction of the magnetic field the flux vortices come under the influence of the Lorentz force:

$$\mathbf{F} = \mathbf{v} \times \mathbf{B}, \tag{3.13}$$

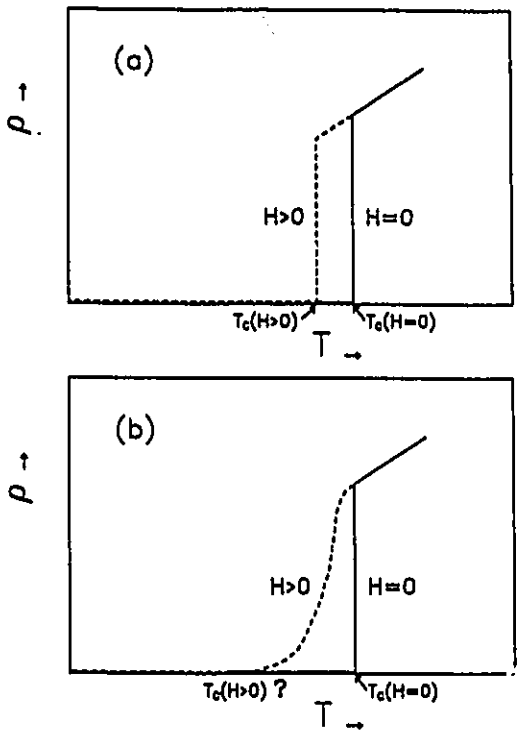

Figure 3.9: Magnetic field dependence of the resistive transition. (a) Expected behaviour for a conventional type II superconductor. (b) Broadening observed in the cuprates.

where v is the current velocity. That is, the magnetic field which penetrates the vortices acts on the passing current with the Lorentz force. The current also acts on the vortex cores and the latter start moving. The force on the vortices, and hence the direction of motion of the cores, will thus be perpendicular to both the direction of current flow and the applied field as illustrated in figure 3.10. This motion of the vortex cores leads to dissipative losses in the superconductor. For example, as the cores move through the crystal the normal electrons within will be scattered by thermal lattice vibrations and point impurities leading to finite resistance as discussed above. This implies that the critical current is exceedingly small since the application of even a very small current will result in losses.

The situation can be remedied by the addition of so-called pinning sites

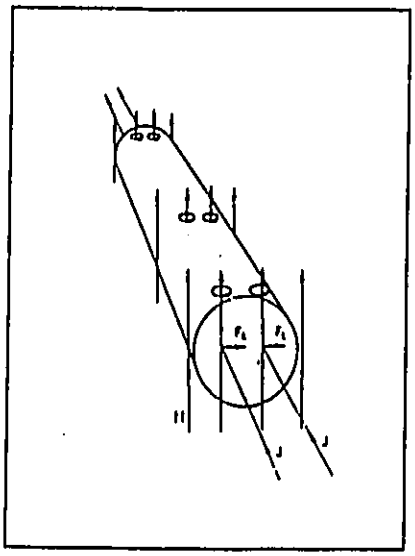

Figure 3.10: Effect of a transport current on the vortex lattice of a type II superconductor. (After [25]).

which are simply inhomogeneities in the sample such as impurities, defects, stresses, admixtures of phases *etc.*. The vortex lines are attracted to these inhomogeneities and are pinned by them. Upon application of a transport current the vortices will begin moving only if the Lorentz force becomes strong enough to overcome the pinning potential. Thus moderate current flow will not be accompanied by vortex motion and hence a finite critical current exists. From this it is seen why the critical current is sample dependent and not an intrinsic property of a given material.

Returning to the cuprate superconductors: for these materials the high transition temperatures, comparatively small density of pinning sites, and the low pinning potential barrier due to the small size of the coherence length causes various processes of flux motion to become important which lead to the broadening of the resistive transition. Consider figure 3.11(a) which shows the spatial variation of a pinning potential in the absence of a transport current. As illustrated in (b) the application of a current reduces the barrier height by an amount U_L due to the Lorentz force. De-pinning occurs at J_c when the barrier height goes to zero as shown in (c). In figure 3.11(b)

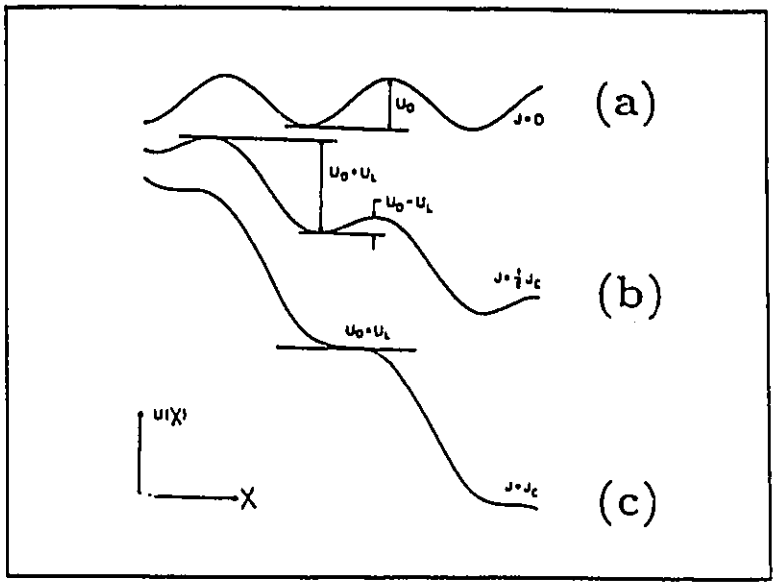

Figure 3.11: Effect of a transport current, J, on a spatially random pinning potential for (a) $J = 0$, (b) $J < J_c$, and (c) $J = J_c$. (After [56]).

however, the vortices can overcome the pinning potential via thermal activation. The resistivity is then expected to vary according to:

$$\rho = \rho_o \exp \frac{-U_o}{T}, \tag{3.14}$$

where U_o is an activation energy, and ρ_o is a constant prefactor. Thus,

$$\ln \rho = \ln \rho_o - \frac{U_o}{T}, \tag{3.15}$$

and,

$$\frac{d \ln \rho}{d \ln T^{-1}} = -U_o, \tag{3.16}$$

so that a plot of $\ln \rho$ versus T^{-1} will be linear with slope $-U_o$. When $U_o > T$ a hopping model is invoked. This is referred to as flux creep. If the barriers become comparable to thermal energies ($U_o < T$) then diffusive motion referred to as thermally activated flux flow becomes possible.

That the broadening of the resistive transition of the cuprates shows thermally activated behaviour at low resistivity has been shown.[56] Whether or not such

processes as flux creep and flow are responsible is less clear. One point that brings under scrutiny such an interpretation is the finding that the width of the transition depends only on the orientation of the field relative to the *c*-axis of the crystal, and not on the current direction.[57] That is, the broadening is the same regardless of whether the current is along, or perpendicular to, the field direction where the Lorentz force exerted on the fluxoid lines by the current should be zero, and maximum, respectively. This implies that the Lorentz force is not involved (or plays a significantly reduced role) in the broadening mechanism which would seem to eliminate models based on flux flow. Superconducting fluctuations have been proposed as an alternative[58] although flux flow models have not been entirely ruled out.

The apparent independence of the width of the resistive transition on the Lorentz force implies that the extent of the broadening should be interpreted as a direct effect of the magnetic field on the pinning volume, V, which in turn is related to the superconducting coherence lengths that are, as determined in chapter 2 for $Pb_2Sr_2(Y/Ca)Cu_3O_8$. extremely small and anisotropic in the double CuO_2 layer cuprate superconductors.

The activation energy, U_o is expected to vary as:[26]

$$U_o \propto H_c^2 V, \tag{3.17}$$

where H_c is the thermodynamic critical field, and has the same linear dependence on T near T_c as the upper critical field discussed in chapter 2 (equation 2.9). The pinning volume may be expressed as:

$$V \propto \xi^n a_o^{3-n}. \tag{3.18}$$

Here ξ is the coherence length, and a_o a parameter related to the flux lattice spacing. At low fields, $n = 3$ and the relevant volume is the superconducting coherence volume, $\xi_{ab}^2 \xi_c = \xi^3$. As the field increases, the flux line spacing decreases and eventually the relevant volume becomes ξa_o^2, (*ie.* n=1) because in the plane perpendicular to the direction of the flux lines the energy per vortex is spread out essentially evenly through

the flux lattice and U_o becomes limited in these two dimensions by a_o. Since it appears that the anisotropy between the ab-plane and the c-axis plays a role in the behaviour of the resistive transition subject to a magnetic field it is of interest to examine this process for $Pb_2Sr_2(Y/Ca)Cu_3O_8$ and thereby further our knowledge regarding the extent of the anisotropy in this system.

3.3.2 Transition Broadening in $Pb_2Sr_2(Y/Ca)Cu_3O_8$

Experimental Details

The data collection system utilized for the zero field anisotropy measurements discussed in section 3.2.1 was also used to carry out the magnetic field-dependent resistivity measurements of $Pb_2Sr_2(Y/Ca)Cu_3O_8$. The magnetic field was supplied by the Quantum Design superconducting magnet. Temperatures from 5 K to approximately 100 K were achieved using the temperature control of the Quantum Design system. The sample was mounted on a Quantum Design sample rod, modified to allow a number of electrical wires. The sample was mounted alternately with the ab-plane face either perpendicular or parallel to the field direction with an estimated uncertainty of $\pm 10°$. The sample contacts were located on the ab-face so that the in-plane resistivity was measured. As described in section 3.2.1, the sample contacts were electrically connected to contact pads on an insulating substrate with small gold wires. The probe wires were then connected to these contact pads. All wires and the sample were securely fastened by potting them in GE varnish. Additional leads were used to mount a platinum resistance thermometer in the vicinity of the sample to monitor its temperature. Agreement between this thermometer and that of the Quantum Design system was found to be very good. The $H \parallel c$ orientation was measured first in various fields ranging from zero to 5.5 T. The sample orientation was then changed and the $H \perp c$ configuration measured. In each case the curves were measured in successively higher fields; that is, the low field curves were measured first.

Results

The magnetic field dependence of the resistive transition of $Pb_2Sr_2(Y/Ca)Cu_3O_8$ is shown for the two orientations $H \parallel c$ and $H \perp c$ for an in-plane transport current in figures 3.12(a) and (b) respectively. Note that as expected the broadening is greater when the field is along the c-axis. There are a few features that deserve mention.

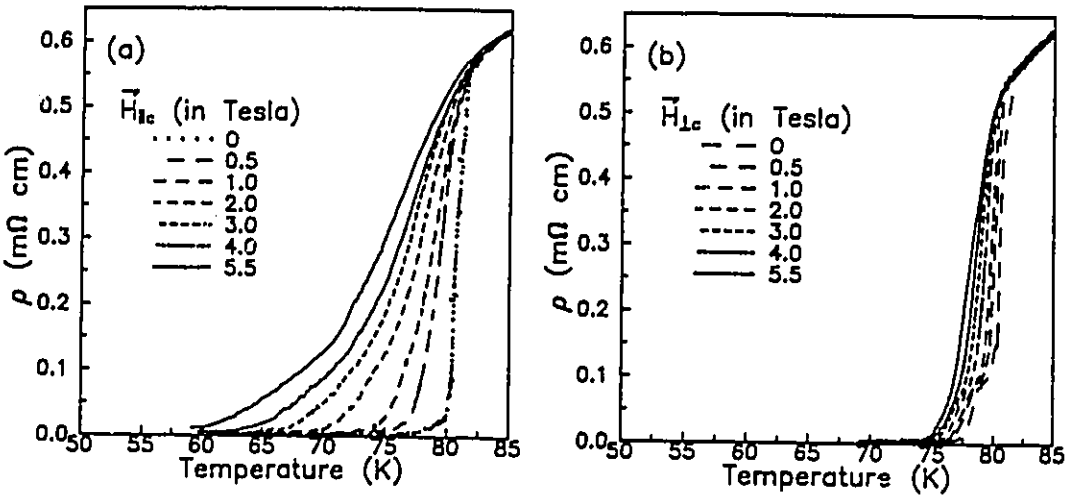

Figure 3.12: In-plane magnetic-field-dependent resistivity of $Pb_2Sr_2(Y/Ca)Cu_3O_8$ near T_c for the field oriented parallel (a) and perpendicular (b) to the c-axis of the crystal.

Although the zero-field transition is relatively sharp at 80 K, there is a small foot which extends to approximately 75 K. This foot is always present in zero field dc resistivity measurements of $Pb_2Sr_2(Y/Ca)Cu_3O_8$. The foot seems larger in absolute magnitude in (b) than it does in (a). Since these are both zero field measurements this is not expected. A possible explanation is that in (b) there was a small residual field present after the application of the 5.5 T field used for the final $H \parallel c$ orientation measurement, which caused a slight broadening of the foot. The analogue of this foot also appears to be present in magnetization data as shown in figure 3.13, where a small peak occurs in the low field magnetization just below T_c. A curious point is that it seems to be asymmetric with respect to the applied field direction. Recent

muon spin rotation experiments have also observed a small upward deflection of the mean field inside the grains between 70 and 80 K, as well as a slight increase in the muon relaxation rate in the same range.[42] The combined evidence points to an intrinsic physical origin for this feature, thus warranting further study.

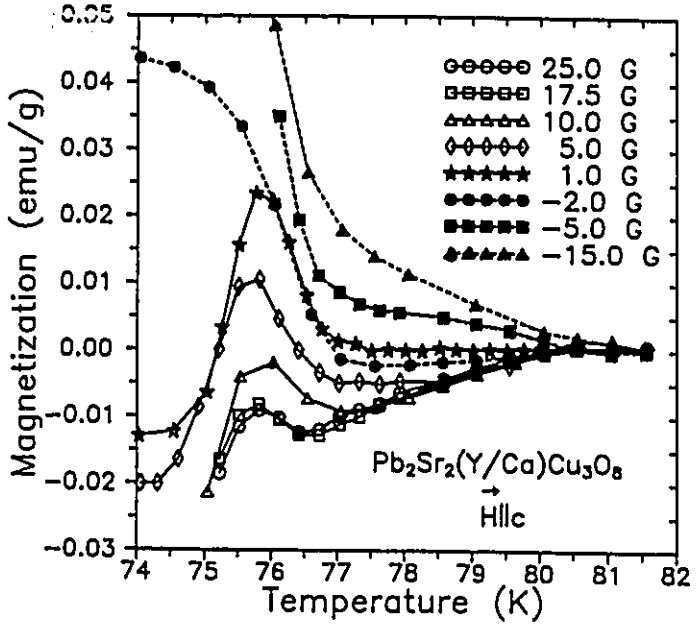

Figure 3.13: Low field peak in the magnetization of $Pb_2Sr_2(Y/Ca)Cu_3O_8$ just below T_c. This feature may be the magnetic analogue to the foot observed in the resistivity in this same temperature range.

Annealing the sample in a nitrogen atmosphere at 600°C greatly improves the magnetically measured transition width. Even though all crystals used in the measurements presented herein have undergone an annealing procedure it is possible that by extending the duration of the anneal further improvement in the transition width might be realized.

As discussed above the transition is expected to show thermally activated behaviour. Figures 3.14(a) and (b) show $\log \rho$ as a function of T^{-1} for the field oriented parallel and perpendicular to the c-axis of the crystal of $Pb_2Sr_2(Y/Ca)Cu_3O_8$ respectively. As can be seen the expected linear dependence for a thermally activated process sets in when the resistivity drops below a few percent of the normal

state value. Palstra *et. al.* have shown however, that although the behaviour is to a very good approximation linear over four orders of magnitude in ρ, the slope actually varies continuously never reaching a constant value.[56] This is because the temperature dependence of the superconducting parameters which dictate the value of the activation energy, U_o, must be taken into account explicitly.

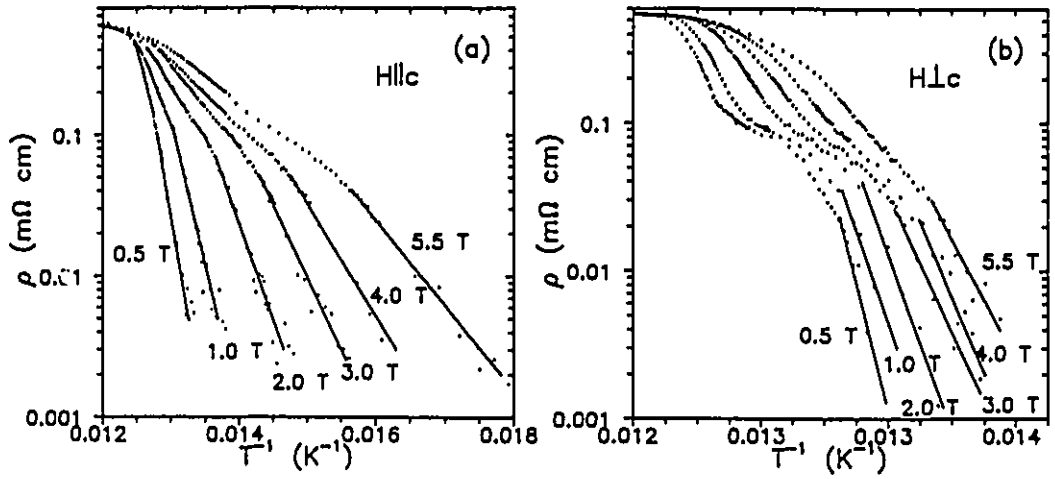

Figure 3.14: Magnetic field dependence of $\log \rho$ on T^{-1} for (a) $H \parallel c$ and (b) $H \perp c$. The solid curves are lines of best fit to the region of the transition exhibiting thermally activated behaviour.

As discussed above, the activation energy depends on the critical field and the coherence length according to:

$$U_o(t) \propto H_c^2(t)\xi^n(t), \tag{3.19}$$

where $t = T/T_c$, and n is 0, 1, 2 or 3 depending on the relevant length scale for the pinning energy of the flux lines. That is, the choice $n = 1$, 2 or 3 corresponds to the assumption that the correlated volume depends on ξ along one, two, or all three directions. With the temperature dependences of the coherence length and the critical field near T_c given by equations 2.8 and 2.9 of chapter 2 respectively (it is assumed that the temperature dependence of the *thermodynamic* critical field, H_c is

the same as that of the upper critical field, H_{c2} near T_c) the temperature dependence of the activation energy is given by:

$$U_o(t) \propto (1-t)^2 \frac{1}{(1-t)^{n/2}} = (1-t)^{\frac{4-n}{2}} \tag{3.20}$$

so that one may write

$$U_o(t) = U_o(0)(1-t)^{\frac{4-n}{2}} \tag{3.21}$$

where $U_o(0)$ is the zero temperature value of the activation energy. Substituting into equation 3.15 one finds:

$$\ln \rho = \ln \rho_o - \frac{U_o(0)}{T}(1 - T/T_c)^{\frac{4-n}{2}} \tag{3.22}$$

Thus,

$$\frac{d \ln \rho}{dT^{-1}} = -U_o(0)(1-t)^{\frac{4-n}{2}}(1 + \frac{4-n}{2}\frac{t}{1-t}) \tag{3.23}$$

and with equation 3.21:

$$\frac{d \ln \rho}{dT^{-1}} = -U_o(t)(1 + \frac{4-n}{2}\frac{t}{1-t}) \tag{3.24}$$

so that the slopes of the Arrhenius plot near T_c are enhanced from the real activation energy $U_o(t)$ by a factor of $(1 + \frac{4-n}{2}\frac{t}{1-t})$.

The results for the other double CuO_2 layer compounds $YBa_2Cu_3O_{7-\delta}$ and $Bi_2Sr_2CaCu_2O_8$ suggest that $n = 1$ is consistent with the data for the range of field strengths used.[56, 59] Thus, as an example in order to extract some actual values for the zero temperature activation energy the analysis has been carried out using this value for n. The choice of larger values for n leads to an overall reduction in the activation energy.

Figure 3.15 shows the field dependence of $U_o(0)$ for both field orientations extracted from the measured slopes of figures 3.14(a) and (b) assuming $n = 1$. T is the midpoint of the range of temperatures used to obtain the slope, and is sufficiently close to T_c (= 80 K) that the approximations made above are valid. Strictly speaking the field dependence of T_c should also be considered. $U_o(t)$ for a given field strength

was determined from the measured slope using equation 3.24 and then $U_o(0)$ was extracted from $U_o(t)$ with equation 3.21. The dashed curve shows the result of a fit to:

$$U_o(0) = H^{-\alpha}. \tag{3.25}$$

For the field oriented perpendicular and parallel to the c-axis of the crystal $\alpha = 0.38$ and 0.97 are found respectively.

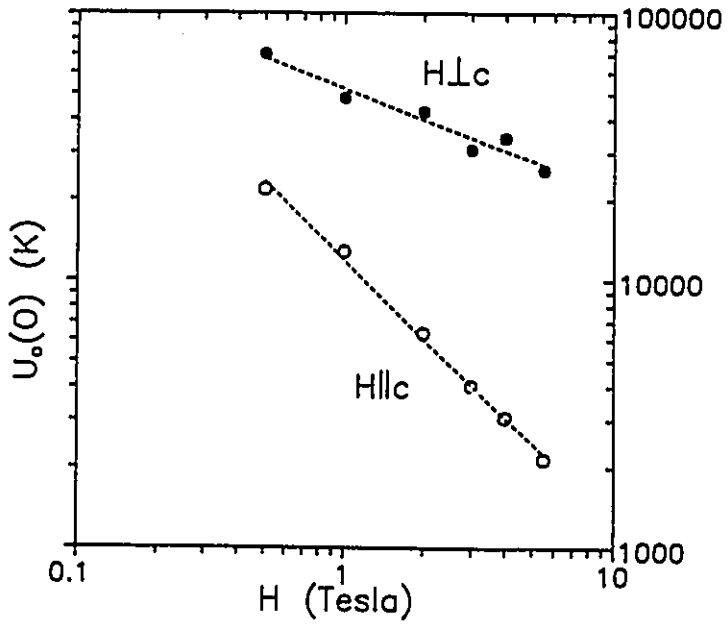

Figure 3.15: Thermal activation energies for $H \perp c$ and $H \parallel c$ for single crystal $Pb_2Sr_2(Y/Ca)Cu_3O_8$.

The goal in this study was to further investigate the anisotropy between ab-plane and c-axis properties in $Pb_2Sr_2(Y/Ca)Cu_3O_8$. The results here confirm the previous conclusions based on the magnetization and zero field dc-resistivity measurements which indicate that the anisotropy in $Pb_2Sr_2(Y/Ca)Cu_3O_8$ is moderate. To see this consider figure 3.16 taken from Palstra *et. al.*[56] which summarizes the temperature dependence of the resistive broadening under a field of 5 T parallel to the c-axis of the crystal for various double CuO_2 layer high temperature superconductors. Also included for comparison is the result from this work for $Pb_2Sr_2(Y/Ca)Cu_3O_8$

at 5.5 T for $H \parallel c$. Note that the extent of the broadening, and hence presumably the extent of the anisotropy for $Pb_2Sr_2(Y/Ca)Cu_3O_8$ is intermediate to that of fully oxidized and oxygen reduced $YBa_2Cu_3O_{7-\delta}$ and significantly smaller than that of the highly anisotropic Bi and Tl '2212' materials.

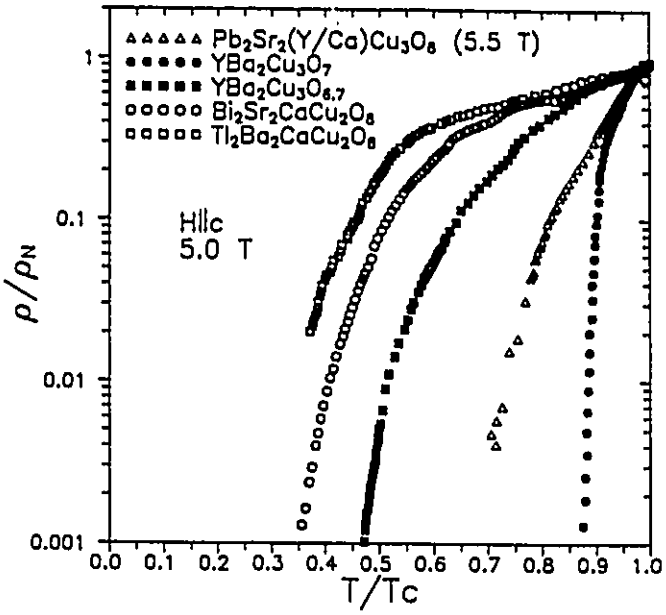

Figure 3.16: Comparison of magnetic field induced broadening under a field of 5 T parallel to the c-axis of the crystal for various double CuO_2 layer high temperature superconductors, taken from Palstra *et. al.*. The result from this work for $Pb_2Sr_2(Y/Ca)Cu_3O_8$ at 5.5 T for $H \parallel c$ is also included. Note that it lies between the curves for fully oxidized and oxygen deficient $YBa_2Cu_3O_{7-\delta}$ and is significantly smaller than for the Bi and Tl 2212 materials indicating relatively moderate electronic anisotropy.

One alternative explanation for the material to material differences is that they are due to variations in the extent of the pinning due to the defect structure. Several pieces of experimental evidence rule against this interpretation. One is that as seen in figure 3.16 the broadening increases dramatically between the fully oxidized and the 60 K phase of $YBa_2Cu_3O_{7-\delta}$ even though both compounds are orthorhombic with a similar defect structure due to the twin boundaries. Secondly a comparison

between $Y_2Ba_4Cu_8O_{16}$ and $YBa_2Cu_3O_{7-\delta}$ by Budhani *et. al.*[60] shows much greater broadening of the transition for $Y_2Ba_4Cu_8O_{16}$ whose tetragonal structure is stabilized against the formation of twin boundaries due to the double chain layer, although they do point out that there is still evidence for an abundance of planar defects.

The general consensus is that the differences in pinning energies arise directly from differences in the electronic anisotropy. A large anisotropy in the electronic properties results in a reduction of the tilt modulus of the flux lines which implies that the correlation length along the flux lines is reduced. A short correlation length along the vortices results in small activation energies due to the small flux bundle.[56]

Thus the relative extent of the anisotropy can also be determined by comparing directly the activation energies obtained for various materials since an enhancement of the two-dimensionality of the system (larger anisotropy) appears to be responsible for poorer pinning (lower activation energies). The activation energies in $Pb_2Sr_2(Y/Ca)Cu_3O_8$ are roughly 3 to 5 times lower than in $YBa_2Cu_3O_{7-\delta}$[56], and close to an order of magnitude higher than in the Bi[56] and Tl[57] 2212 materials. In their study of $Y_2Ba_4Cu_8O_{16}$ ('248'), Budhani *et. al.*[60] find that the activation energies are 5 to 6 times smaller than in twinned $YBa_2Cu_3O_{7-\delta}$, ('123'). Since both systems have a similar susceptibility to defects (twin boundaries in 123 and planar defects in 248) they conclude that the difference in electronic anisotropy is structural, in that $Y_2Ba_4Cu_8O_{16}$ has a larger separation between the CuO_2 planes of 10.2 Å (as opposed to 8.3 Å in $YBa_2Cu_3O_{7-\delta}$). They point out that in $Bi_2Sr_2CaCu_2O_8$ the distance is larger yet, 12 Å, and hence conclude that the spacing between the superconducting planes plays an important role in enhancing the two dimensional nature of the system. The present results for $Pb_2Sr_2(Y/Ca)Cu_3O_8$, which has an interplanar separation of 12 Å as in $Bi_2Sr_2CaCu_2O_8$ but is significantly less anisotropic as indicated both by less broadening of the transition under a magnetic field, and higher activation energies, and those of Palstra *et. al.*[56] for oxygen reduced $YBa_2Cu_3O_{7-\delta}$, where the anisotropy increases significantly while the separation between the planes

remains essentially constant, show that this is not the only factor. That is, the actual interplanar structure must also play an important role.

Chapter 4

Anisotropy in the Normal and Superconducting State Optical Conductivity of $Pb_2Sr_2(Y/Ca)Cu_3O_8$

In this chapter anisotropy in the optical properties of single crystals of $Pb_2Sr_2(Y/Ca)Cu_3O_8$, of the same quality as those used for the magnetization and resistivity measurements of the two previous chapters, will be discussed.

4.1 Background

The present state of knowledge regarding the superconducting state *ab*-plane optical properties of the cuprates arises mainly from reflectance studies of $YBa_2Cu_3O_{7-\delta}$,[49, 61, 62, 63] although $Bi_2Sr_2CaCu_2O_8$ [64] and $Tl_2Ba_2CaCu_2O_8$ [45] have been shown to exhibit similar trends. Below T_c low energy spectral weight appears to be transferred to a delta function at zero frequency representing the superconducting condensate; thereby revealing a detailed background conductivity (the mid infrared absorption).

A point of debate is whether the remaining conductivity corresponding to Drude-like carriers exhibits a gap at low frequencies wherein the conductivity is identically zero as expected for a conventional superconductor. To address this one must question how reliably the low frequency behaviour of the conductivity in the superconducting state can be determined from reflectance measurements. The answer unfortunately is not well. This is mainly a consequence of the fact that these materials are in the clean limit where the free carrier scattering rate, Γ, is smaller than the superconducting energy gap, 2Δ. In this case essentially all of the Drude conductivity is gapped below T_c and thus there is expected to be a virtually complete condensation of the free carriers into the zero-frequency delta function (which leads to the infinite dc-conductivity of a superconductor). This causes the reflectance to become very high at low frequencies, essentially indistinguishable from unity within the limits of uncertainty of the experiment. A superconducting energy gap in the conventional sense is denoted by a deviation from unit reflectance or alternatively from the onset of absorption in the optical conductivity. Since the optical conductivity is derived from the reflectance via Kramers-Kronig analysis, (discussed in Appendix B), and because this process demands knowledge of the reflectance over all frequencies, low and high frequency extrapolations to the measured data range must be supplied. Presumably the reflectance can be measured to high enough frequency such that any physically reasonable choice for the high frequency extrapolation will not affect the conductivity below 1000 cm^{-1}. (This is of course not true if one is interested in examining the conductivity beyond the far infrared region of the spectrum). The increasing susceptibility of the Kramers-Kronig integral to both noise and small changes in slope as the reflectance approaches unity implies that the low frequency extrapolation poses a more serious difficulty. Thus, usually the reflectance is set to unity at low frequencies, a perhaps not so unreasonable choice given the circumstances. However, small deviations from unity, essentially within the experimental uncertainty can give rise to large variation in the Kramers-Kronig derived optical conductivity as has been

discussed by Orenstein *et. al.*[62] and recently by Miller and Richards.[65] An experimental technique that is more sensitive than reflectance spectroscopy is bolometric absorption. Such studies of $YBa_2Cu_3O_{7-\delta}$ indicate that there is non-zero absorption to the lowest experimentally accessible frequencies, giving rise to finite conductivity at low frequencies.[65, 66]

$Pb_2Sr_2(Y/Ca)Cu_3O_8$ provides an opportunity to study the superconducting state optical properties of another cuprate superconductor with double CuO_2 planes. Due to the intrinsically lower carrier density in this material, as has been concluded from the studies presented in the previous two chapters, the level of the reflectance in the superconducting state remains distinguishable from unity to the lowest accessible frequency ($\approx$ 50 cm.$^{-1}$). It shall be argued that this is not due to poor superconducting properties, and that rather, to the contrary, the onset of superconducting behaviour can be observed clearly by dramatic changes in the optical conductivity at T_c. This is further supported by measurements polarized along the c-axis where the condensation of the superconducting carriers can also be observed. This work represents the first study of the temperature dependence of the optical properties of $Pb_2Sr_2(Y/Ca)Cu_3O_8$.

4.2 Experimental Details

Temperature dependent far and mid infrared *ab*-plane measurements (50-5500 cm^{-1}) were carried out using a rapid scan Michelson interferometer with focused optics on a mechanically polished *ab*-face of a single crystal of $Pb_2Sr_2(Y/Ca)Cu_3O_8$ mounted in a continuous flow cryostat using a technique which has been optimized for the measurement of small, irregularly shaped samples.[67] The basic premise of the method is that the sample and reference mirror (a polished stainless steel disc of dimensions similar to those of the sample) are glued to the tips of solid, polished-brass, cone-shaped mounts. The focused incident beam is larger than either the sample or the

discussed by Orenstein *et. al.*[62] and recently by Miller and Richards.[65] An experimental technique that is more sensitive than reflectance spectroscopy is bolometric absorption. Such studies of $YBa_2Cu_3O_{7-\delta}$ indicate that there is non-zero absorption to the lowest experimentally accessible frequencies, giving rise to finite conductivity at low frequencies.[65, 66]

$Pb_2Sr_2(Y/Ca)Cu_3O_8$ provides an opportunity to study the superconducting state optical properties of another cuprate superconductor with double CuO_2 planes. Due to the intrinsically lower carrier density in this material, as has been concluded from the studies presented in the previous two chapters, the level of the reflectance in the superconducting state remains distinguishable from unity to the lowest accessible frequency ($\approx$ 50 cm^{-1}). It shall be argued that this is not due to poor superconducting properties, and that rather, to the contrary, the onset of superconducting behaviour can be observed clearly by dramatic changes in the optical conductivity at T_c. This is further supported by measurements polarized along the *c*-axis where the condensation of the superconducting carriers can also be observed. This work represents the first study of the temperature dependence of the optical properties of $Pb_2Sr_2(Y/Ca)Cu_3O_8$.

4.2 Experimental Details

Temperature dependent far and mid infrared *ab*-plane measurements (50-5500 cm^{-1}) were carried out using a rapid scan Michelson interferometer with focused optics on a mechanically polished *ab*-face of a single crystal of $Pb_2Sr_2(Y/Ca)Cu_3O_8$ mounted in a continuous flow cryostat using a technique which has been optimized for the measurement of small, irregularly shaped samples.[67] The basic premise of the method is that the sample and reference mirror (a polished stainless steel disc of dimensions similar to those of the sample) are glued to the tips of solid, polished-brass, cone-shaped mounts. The focused incident beam is larger than either the sample or the

reference so that the entire exposed surface is illuminated. The optical arrangement is such that the light which impinges upon the sample or reference (measured alternately by rotating the cryostat cold-finger through 90 degrees) is reflected back into an $f/2.5$ toroidal collecting mirror, while that which misses falls upon the polished cone, and is subsequently scattered out of the beam path (confirmed by background tests using a bare cone). From the collecting mirror, the beam is then focussed onto the detector [1.2 K and 4.2 K Si bolometers for the ranges 40-250 cm^{-1} and 150-700 cm^{-1} respectively, and a liquid nitrogen cooled HgCdTe detector in the mid infrared (500-5500 cm^{-1}) - see also table 4.1]. In order to obtain the absolute value of the reflectance, the difference in dimensions of the sample and reference and geometrical scattering losses due to surface irregularities of the sample are accounted for by *in situ* evaporation of a metallic film (Au for these frequency ranges) onto the surface of the sample. The coated sample is then remeasured versus the pristine stainless steel reference and the absolute value of R given by the ratio of spectra before and after plating, corrected for the absolute reflectance of the metallic film:

$$R_{absolute} = \frac{\left[\frac{R_{sample}}{R_{reference}}\right]}{\left[\frac{R_{coatedsample}}{R_{reference}}\right]} \times R_{metallicfilm} = \frac{R_{sample}}{R_{coatedsample}} \times R_{metallicfilm}. \qquad (4.1)$$

The stainless steel disc thus acts simply as an intermediate reference to cancel time dependent changes in the power spectrum due to *eg.* drift in the electronics, detector sensitivity, source intensity *etc.*, while ultimately the sample acts as its own reference.

To extend the range in order to facilitate Kramers-Kronig analysis of the data, a grating spectrometer was utilized for room temperature measurements to 40000 cm^{-1}. For these measurements the conventional arrangement where the incident beam is smaller than both the sample and the reference was used. Geometrical scattering losses were still accounted for by evaporation of a metallic film (Au and Al for ω less than and greater than 10000 cm^{-1} respectively). Various sources, detectors and filters were used as summarized for the entire range, 40-40000 cm^{-1}, in table 4.1.

Table 4.1: Summary of experimental details corresponding to the various frequency regions investigated. CG: Corning Glass, PolyE: Polyethylene, PolyP: Polypropylene, bol: bolometer, DP: Diamond Powder, Cermet: Ceramic Metal Element, pd: photodiode, PM: photomultiplier, Film cap: Grey plastic cap from Kodak film canisters, D_2: Deuterium. (Note: 4G= 1μ)

Spectrometer:					
Grating or Beamsplitter	Source	Window	Detector	Filter	Range (cm^{-1})
Michelson:					
• 50G Mylar	Hg-Arc or Cermet	PolyP	1.2 K Si bol.	Film cap, 5μ DP in Black PolyE	40-250
• 12G Mylar	Cermet	"	4.2 K Si bol.	5μ DP in Black PolyE	150-700
• 6G Mylar	Tungsten	KBr, KRS-5	HgCdTe	Ge	500-5500
Grating:					
• 400l/mm	Tungsten	Quartz	PbS	Ge	3800-6300
• "	"	"	"	Si	5500-10000
• 1200l/mm	"	"	Si pd	CG #245 (red)	9200-16700
• "	"	"	PM	CG #3486 (yellow)	11000-23000
• "	"	"	"	CG #4303 (blue)	15000-30000
• "	D_2	"	"	CG Purple 7	20000-35000
• "	"	"	"	CG #9863	25000-44000

For c-axis measurements, eleven crystals were polished to expose in each case an optical quality face containing the c-axis. Polarized mid infrared measurements were then carried out on each crystal using a Bomem/Spectra-Tech Infrared microscope with a Cambridge Physical Sciences (CPS) IGP-225 polarizer in order to (a) confirm the orientation of the polished surface, and (b) choose several crystals from which to construct a mosaic. Five crystals which exhibited the highest reflectance when the polarizer was oriented such that the electric field vector, E, was along the a, b-direction were selected. The five crystals were aligned side by side with the c-axis along a common direction. Epoxy was applied between adjoining crystals at points of contact such that the amount exposed was negligible. Due to the cone geometry of the measurement cracks between crystals are also inconsequential. It is thus felt that the mosaic nature of this sample had no detrimental effect on the measurement, and introduced no additional uncertainties.

The c-axis measurements were carried out between 40 and 5000 cm^{-1} only due to the lack of an appropriate polarizer beyond the mid infrared (MIR) region of the spectrum. Kircher *et. al.* have determined ellipsometrically the E$\|c$ reflectance to 47000 cm^{-1}[68] and thus their data was used to extend the measurements of this work in the Kramers-Kronig analysis. In the far-infrared (FIR) a copper strip polarizer with 0.38-μm spacing, effective up to 700 cm^{-1}[69], was employed, while the MIR measurements made use of the CPS IGP-225 polarizer, effective to 5000 cm^{-1}. The spectrometer beam itself is highly polarized, and thus care had to be taken to mount the axis of interest (in this case the c-axis) along the direction of beam polarization in order to maximize the signal to noise of the measurement. The precise angle at which the polarizer was placed was determined by measuring the ratio of the chopped signal of the sample to that of the reference as a function of polarizer angle. This yields a sinusoidal curve, the minimum of which gives the polarizer angle corresponding to the less highly-reflecting c-axis of the sample. An example is shown in the lower curve of figure 4.1 (open circles) from which it is seen that in this case the polarizer

should be placed at an angle of 55 degrees. The upper curve of figure 4.1 (solid circles) shows the angular dependence of the chopped signal from the stainless steel reference alone which has no intrinsic anisotropy. The variation observed thus reflects the polarization of the spectrometer beam. It is seen that the beam maximum also occurs near 55 degrees as is desired in order to optimize signal to noise.

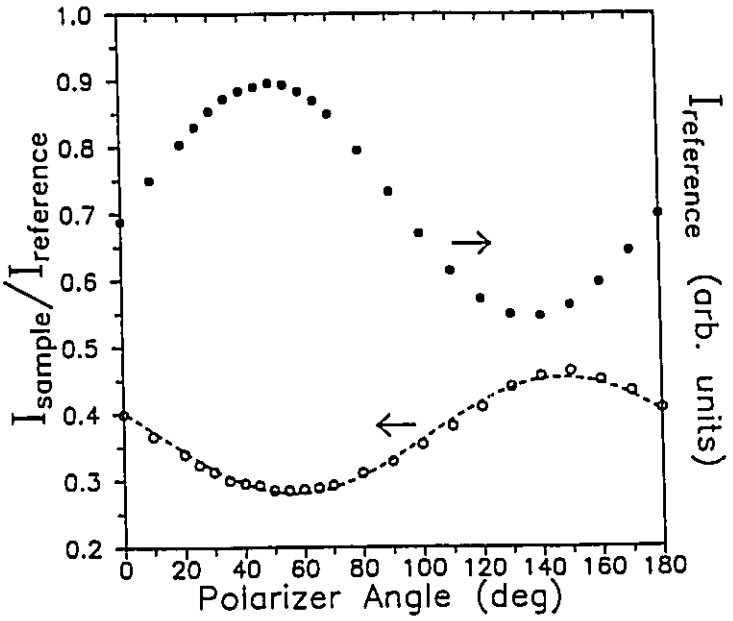

Figure 4.1: Dependence of the ratio of chopped signal from the sample to that of the stainless steel reference (lower curve, open circles) and, the stainless steel chopped signal alone (upper curve, solid circles) on polarizer angle. The latter gives the polarization dependence of the intensity of the infrared beam. Note that the minimum in the ratio (E$\|$ *c*-axis of sample) has been aligned with the maximum in the beam intensity to optimize signal to noise.

4.3 High-Frequency *ab*-plane Optical Properties

The room temperature *ab*-plane reflectance is shown over the entire measured frequency range in figure 4.2, and is in reasonable agreement with an ellipsometrically derived result by Kircher *et. al.*[68]. The Kramers-Kronig derived optical conductiv-

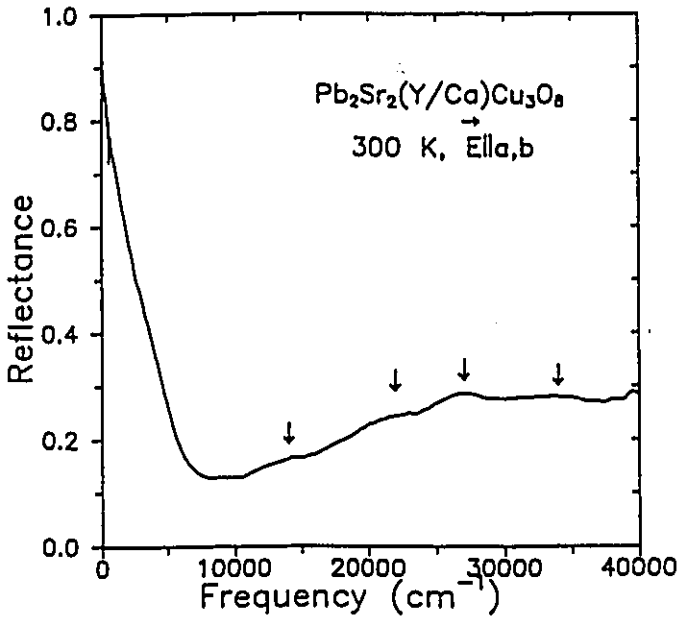

Figure 4.2: *ab*-plane room temperature reflectance of $Pb_2Sr_2(Y/Ca)Cu_3O_8$ over a wide frequency range. Arrows indicate features due to interband transitions as discussed in the text.

ity is shown in figure 4.3. For the Kramers-Kronig integral, beyond 40000 cm^{-1} the reflectance of $YBa_2Cu_3O_{7-\delta}$ measured by Romberg *et. al.* up to 50 eV[70] was used followed by an ω^{-4} power law. At low frequencies, a Drude extrapolation consistent with the measured dc-resistivity, shown in figure 3.7(a) of chapter 3, was used. Based on tests with various high frequency extrapolations beyond 50 eV, the absolute magnitude of the conductivity shown up to 37500 cm^{-1} in figure 4.3 is reliable to within 10 percent. The gap-like suppression of the conductivity between 16600 and 19200 cm^{-1} (2.0-2.4 eV) was most sensitive to the extrapolation chosen. In order to obtain a non-negative conductivity in this region the power α of the $\omega^{-\alpha}$ extension applied beyond the experimental data (50 eV) had to be greater than or equal to 4. With α larger than 4 (where 4 is the expected dependence for free electrons) the conductivity is non-zero in this region. Further evidence for the reliability of the absolute magnitude of the conductivity in figure 4.3 is derived from the fact that it is in reasonable agreement with the level of the ellipsometric result of Kircher *et. al.*[68] which is

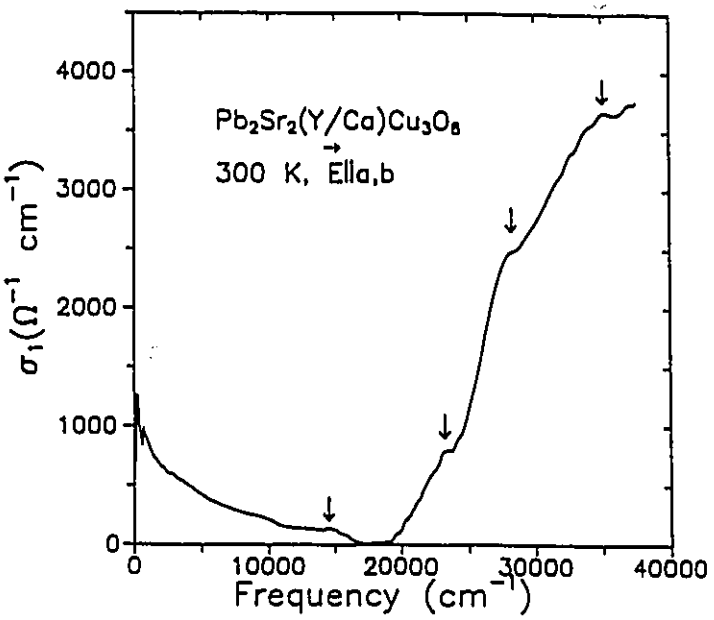

Figure 4.3: Real part of the room temperature *ab*-plane optical conductivity of $Pb_2Sr_2(Y/Ca)Cu_3O_8$ over a wide frequency range. Arrows indicate features due to interband transitions as discussed in the text.

independent of Kramers-Kronig analysis. For example, the ellipsometrically-derived conductivity at 3.5 eV (28000 cm^{-1}) is roughly 2350 Ω^{-1} cm^{-1}, while the present result gives 2500 Ω^{-1} cm^{-1}.

The arrows in figure 4.3 indicate four features which arise due to the four corresponding structures marked in the reflectance of figure 4.2. The lowest structure, centered near 14500 cm^{-1} (1.8 eV) is the remainder of the charge transfer band due to transitions between the O^{2p} and Cu^{3d} levels (discussed in more detail in the following chapter). The second peak near 23000 cm^{-1} (2.8 eV) has been assigned by Kircher *et. al.* to another interband transition within the CuO_2 planes based on the fact that this peak can be observed in $YBa_2Cu_3O_{7-\delta}$ as well, at all oxygen doping levels[71], and that the Raman modes of $Pb_2Sr_2(Y/Ca)Cu_3O_8$ which involve a strong motion in the Cu(2)-O(3) plane according to lattice dynamical calculations of the phonon eigenvectors by Kress *et. al.*[72], show resonances near 1.8 and 2.6 eV.[73] Again based on the resonant Raman work of Heyen *et. al.*, which shows that modes primarily

associated with motion in the rocksalt-like part of the structure containing the PbO layers have a resonance in the ultraviolet, Kircher *et. al.* associate the higher frequency peaks near 28000 and 35000 cm^{-1} (3.5 and 4.3 eV) with transitions from O(2) p_x and O(2) p_y-like bands to those with Pb p_z character. Support for these assignments is also derived from band structure calculations by Mattheiss and Hamann which show a similar energy separation between bands of the proposed character.[74]

4.4 Low Frequency *ab*-plane Properties

In this section, the temperature dependence of the low frequency *ab*-plane properties is examined. In particular, the goal is to investigate changes in the electronic background upon entry into the superconducting state. The dependence of the optical properties on level of doping will be studied in chapter 5.

Figure 4.4 shows the far infrared reflectance measured at room temperature (300 K), just above T_c at 85 K, and at 10 K, the lowest attainable temperature. Three antiresonant-like structures are observed at 430, 525 and 585 cm^{-1} which are due to a doping induced coupling of phonons to the mid infrared continuum, the detailed discussion of which is the emphasis of chapter 6. Small peaks, for example, the most obvious ones located at 190, 300 and 360 cm^{-1} are due to ordinary infrared active phonons which have not been fully screened by the electronic background. (The ordinary phonon structure of $Pb_2Sr_2RCu_3O_8$ will be discussed in detail in the following chapter). A significant difference between the 85 K and 10 K spectra occurs at low frequencies where the reflectance of the 10 K spectrum appears to decrease with decreasing frequency below 150 cm^{-1}. A similar broad low frequency peak was also observed in measurements on a $Pb_2Sr_2(Er/Ca)Cu_3O_8$ single crystal using the same experimental arrangement and a mosaic of $Pb_2Sr_2(Y/Ca)Cu_3O_8$ single crystals using light-pipe optics in an immersion cryostat, as shown in figure 4.5, thus attesting to the reproducibility of the result.

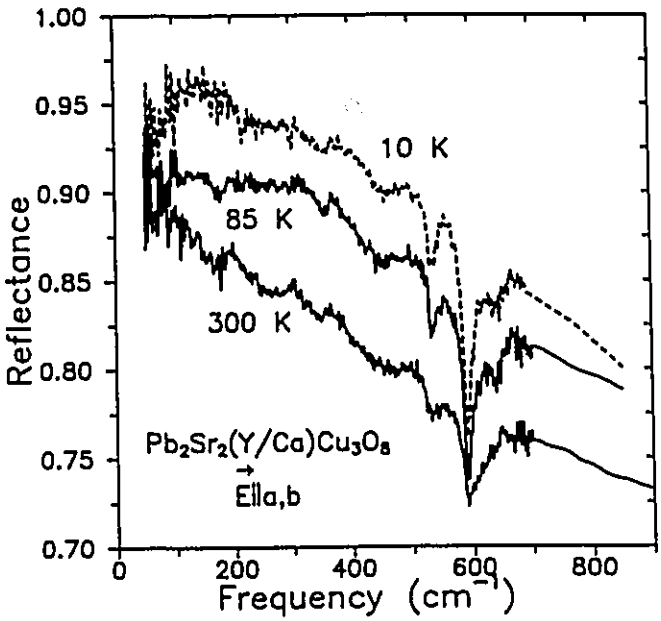

Figure 4.4: Far infrared reflectance of *ab*-plane oriented $Pb_2Sr_2(Y/Ca)Cu_3O_8$ at room temperature (300 K), just above T_c at 85 K, and at 10 K in the superconducting state.

A Kramers-Kronig analysis of the reflectance was carried out to obtain the optical conductivity which is shown in the normal and superconducting states at 85 and 10 K respectively in figure 4.6. For the high frequency extrapolation the temperature dependent data up to 5500 cm^{-1} was joined smoothly with the measured high frequency room temperature result shown in figure 4.2. At low frequencies in the normal state a Drude extrapolation consistent with the measured dc-resistivity was used. The choice for the superconducting state is, as discussed above, more difficult; in this case due to the decidedly non-Drude behaviour of the low frequency reflectance. It was found, however, that any reasonable extrapolation, from continuing linearly the decreasing reflectance, to a constant, to free carrier-like behaviour which joins smoothly at the lowest measured frequency and approaches one at zero frequency gives qualitatively similar behaviour for the conductivity above 60 cm^{-1}, *ie.* at 10 K a large peak centered near 100 cm^{-1}. In fact, even joining smoothly with a Drude-like function at 150 cm^{-1} and thereby neglecting the decreasing low frequency reflectance completely does not change this result qualitatively. As can be seen from figure 4.5 the

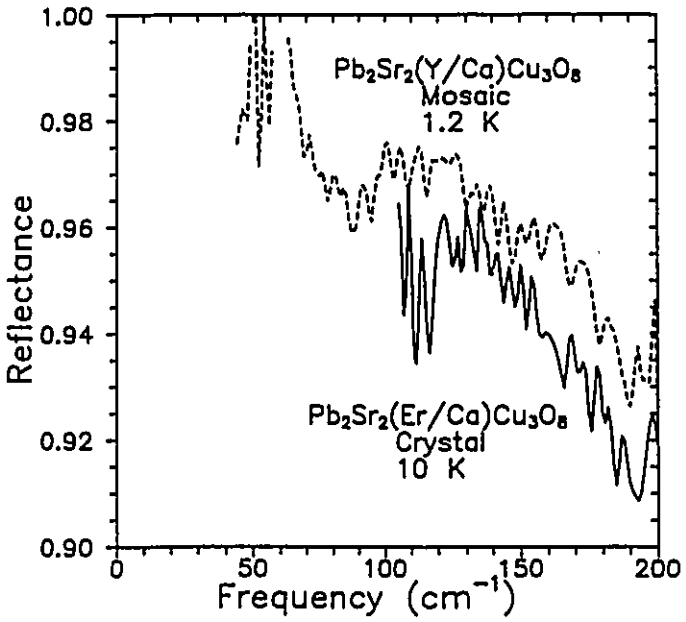

Figure 4.5: Low-frequency *ab*-plane reflectance of a $Pb_2Sr_2(Er/Ca)Cu_3O_8$ single crystal at 10 K, (solid curve) and a $Pb_2Sr_2(Y/Ca)Cu_3O_8$ mosaic at 1.2 K (dashed). Note the presence of a broad peak in the 100-150 cm^{-1} region in both cases.

data for the mosaic of crystals indicates that the reflectance rises towards unity with decreasing frequency below the peak and thus a Drude-like extrapolation consistent with this observed behaviour was chosen in the final analysis.

Note that although the antiresonances are prominent in the reflectance, they appear in the optical conductivity as relatively small features on the slowly decreasing background above 400 cm^{-1}, while the more subtle evolution of the low frequency reflectance structure with temperature gives rise to considerably more dramatic changes.

Comparison of the 300 and 85 K normal state optical conductivity shown in figure 4.7 reveals what appears to be a broad band centered near 200 cm^{-1} and extending to approximately 400 cm^{-1} which grows in intensity as the temperature is lowered. The progression of this feature with temperature can be more clearly seen in figure 4.8 which shows the (smoothed for clarity) conductivity below 400 cm^{-1} at several temperatures in the normal state. The dc-conductivities at 300 and 85 K, calculated from the measured resistivity shown in figure 3.7(a) of chapter 3, are

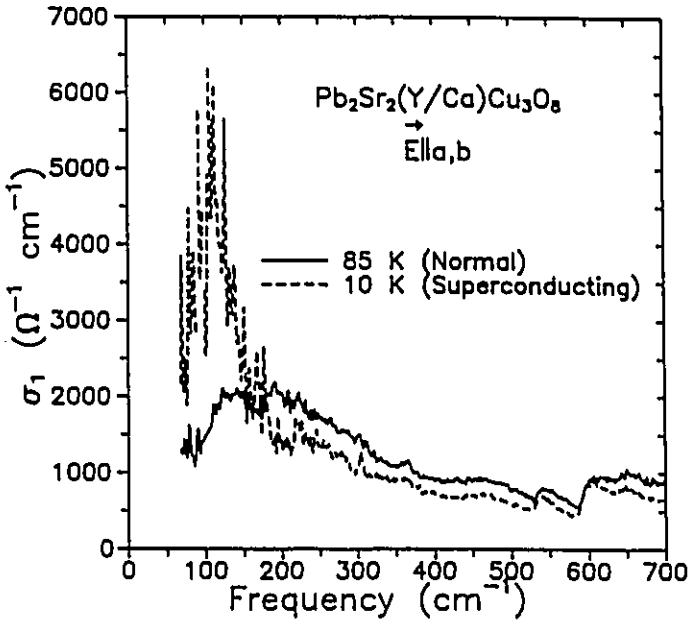

Figure 4.6: Kramers-Kronig derived *ab*-plane real optical conductivity of $Pb_2Sr_2(Y/Ca)Cu_3O_8$ at 85 K in the normal state and at 10 K in the superconducting state.

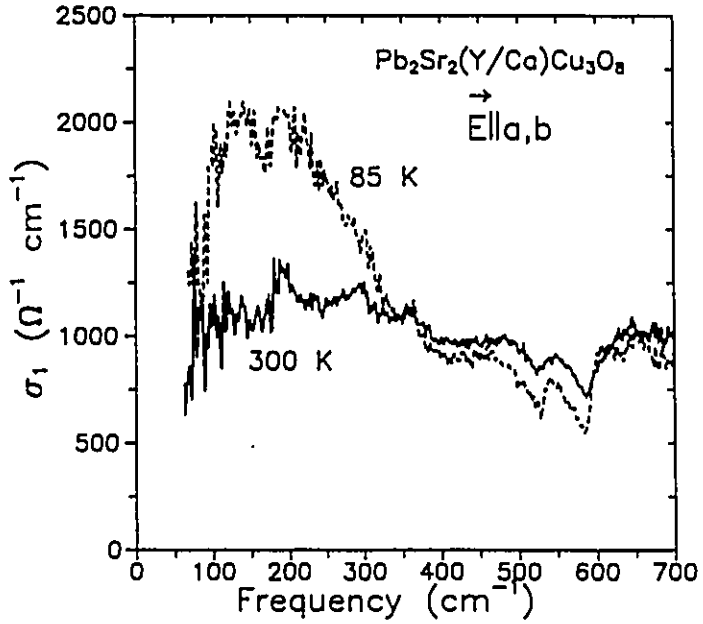

Figure 4.7: Comparison of the 300 and 85 K normal state *ab*-plane optical conductivity of $Pb_2Sr_2(Y/Ca)Cu_3O_8$.

marked along the vertical axis. Note that they are noticeably lower than the value of the frequency dependent conductivity maximum, indicating that the mid infrared continuum is making a considerable contribution. That is, it shall be shown that as for the other cuprates, this band can be deconvolved into two optical channels, a strongly temperature dependent, but in this case quite weak, Drude component due to the free carriers, in addition to a mid infrared bound carrier contribution.

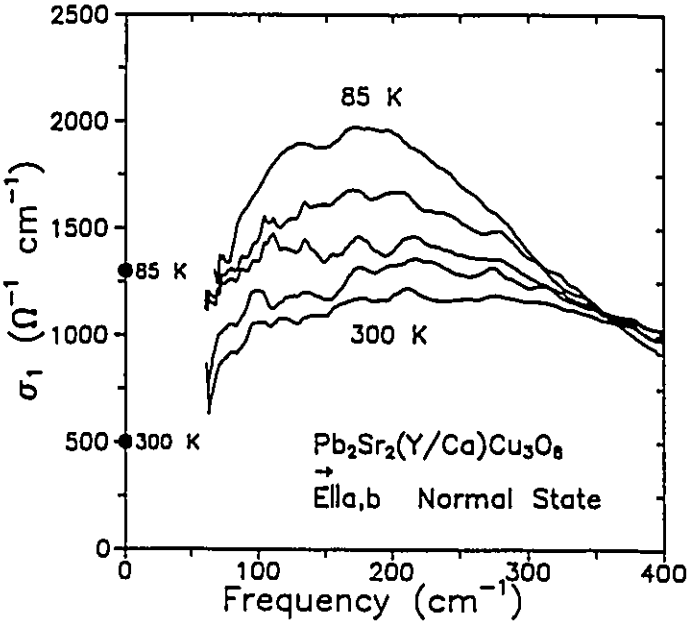

Figure 4.8: Temperature dependence of the low-frequency *ab*-plane normal state conductivity. The temperatures between 85 and 300 K are 150, 200 and 250 K. The dc-conductivities at 85 and 300 K are marked along the vertical axis. A considerable contribution from the mid infrared absorption band is inferred.

Figure 4.9 shows the evolution of the optical conductivity as the temperature is lowered below T_c (again, smoothed for clarity). The gradual development of this strong broad peak centered near 100 cm^{-1} is observed.

A finite frequency peak in the superconducting state optical conductivity is unusual. In $YBa_2Cu_3O_{7-\delta}$ the generally accepted interpretation of the optical properties derived from reflectance and transmission studies is that the conductivity in the normal state Drude peak disappears below T_c into a delta function at the

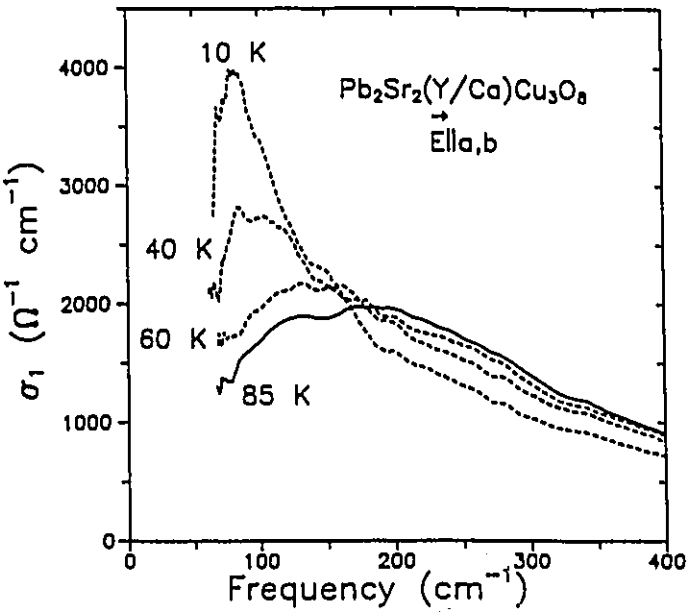

Figure 4.9: Evolution of the low-frequency ab-plane conductivity with temperature below T_c.

origin; the evidence being derived from model fits (discussed in Appendix B) which bear out a rapidly collapsing scattering rate for the Drude carriers below T_c,[75] and the observation of an ω^{-2} dependence to the real part of the dielectric function, ϵ_1, below T_c.[45, 49] This last point can be understood by considering the form of ϵ_1; given for a classical oscillator with center frequency ω_o, scattering rate, Γ and plasma frequency ω_p by:

$$\epsilon_1 = \frac{\omega_p^2(\omega_o^2 - \omega^2)}{(\omega_o^2 - \omega^2)^2 + \omega^2\Gamma^2}. \tag{4.2}$$

For Drude carriers $\omega_o = 0$. If the scattering rate collapses below T_c (*ie.* the system is in the clean limit) then Γ is also zero. Equation 4.2 then reduces to:

$$\epsilon_1 = \frac{-\omega_p^2}{\omega^2}, \tag{4.3}$$

so that a plot of ϵ_1 as a function of ω^{-2} is linear with slope $-\omega_p^2$. In general the plasma frequency derived by this method is in reasonable agreement with the oscillator-fit value for the normal state just above T_c, lending support to this view.

An increasing body of knowledge is however surfacing, primarily from bolometric absorption measurements which are more sensitive to the level of the low frequency absorption, which indicates that the situation is not this simple. The bolometric absorption measurements of both Pham *et. al.*[66] and Miller *et. al.*[65] as well as careful temperature dependent reflectance measurements of Renk *et. al.*[61] point towards a non-zero *rising* conductivity at low frequencies, which seems to increase in magnitude as the quality of the sample improves.[65] As an example, in figure 4.10 the low temperature conductivity of $Pb_2Sr_2(Y/Ca)Cu_3O_8$ is compared with the bolometric absorption-derived result for $YBa_2Cu_3O_{7-\delta}$ of Miller *et. al.*[65]. It is seen that the absolute magnitude of the absorption is similar in the two materials. Renk

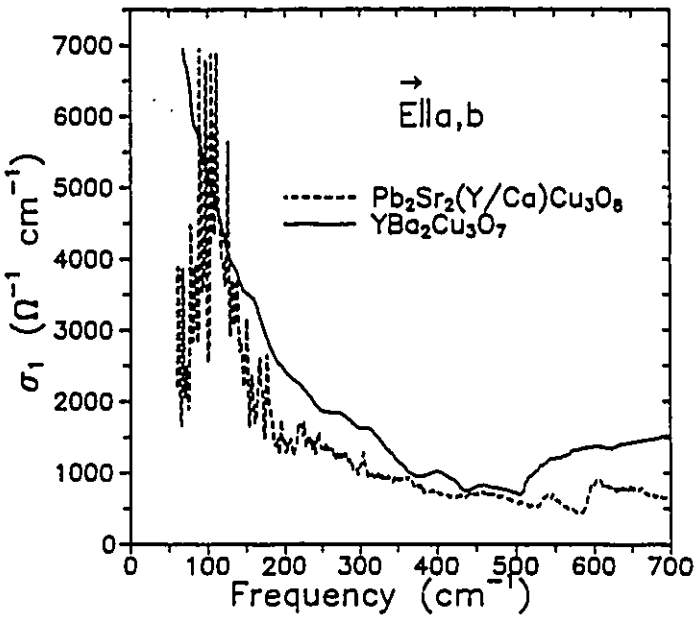

Figure 4.10: Comparison of the low-temperature *ab*-plane optical conductivity of $YBa_2Cu_3O_{7-\delta}$ derived from a bolometric absorption technique by Miller *et. al.* with that of $Pb_2Sr_2(Y/Ca)Cu_3O_8$. In both cases a strong low frequency absorption feature is observed which appears to be centered at zero (or very low) frequency in $YBa_2Cu_3O_{7-\delta}$ and near 100 cm^{-1} in $Pb_2Sr_2(Y/Ca)Cu_3O_8$. The origin of this absorption in these two materials may be related.

et. al. fit their low temperature (10 K) result for a $YBa_2Cu_3O_{7-\delta}$ film with a zero

frequency centered oscillator of width $\Gamma = 11$ cm^{-1} and a plasma frequency of 7800 cm^{-1}. Although, as a result of sample to sample variation in the strength of this feature Renk *et. al.* suggest that it is of non-intrinsic nature, arising from intergrain or impurity-induced absorption by normal carriers.

The peak in the optical conductivity of $Pb_2Sr_2(Y/Ca)Cu_3O_8$ may be related to this rising low frequency conductivity in $YBa_2Cu_3O_{7-\delta}$. The fact that it develops suddenly upon entry into the superconducting state suggests that it is associated with the *superconducting* carriers. As discussed above one way of determining the amount of spectral weight transferred to low frequencies upon entry into the superconducting state is to examine the ω^{-2} dependence of ϵ_1. For a finite frequency peak at ω_o this behaviour is obeyed to a good approximation for frequencies above $\omega_o + \Gamma$. When this procedure is carried out for $Pb_2Sr_2(Y/Ca)Cu_3O_8$ for frequencies between 200 and 700 cm^{-1} at 10 K a value of 4250 cm^{-1} is obtained for ω_p. Note that the 10 K conductivity is comprised of a component due to the superconducting carriers as well as a mid infrared contribution. Since the mid infrared band is very wide (Γ is large) and it is centered near the region of interest so that $(\omega_o^2 - \omega^2)$ in equation 4.2 is in comparison small, its contribution will be minimal. It can however be taken into account using the following approach.

With the derived estimate for ω_p of 4250 cm^{-1} and the known dc-resistivity just above T_c in the normal state (0.75 mΩ cm) the Drude contribution to the 85 K dielectric function can be evaluated and subtracted leaving the mid infrared component. Assuming that this component is temperature independent between 10 and 85 K, it is then subtracted from the 10 K dielectric function and ω_p is re-evaluated; this time yielding a value of 4500 cm^{-1}. The Drude contribution to the 85 K optical properties is then re-evaluated and the mid infrared component re-determined as illustrated for the optical conductivity in figure 4.11. This new estimate for the mid infrared contribution is once again subtracted from the 10 K dielectric function and ω_p is again evaluated to be 4500 cm^{-1} as shown in figure 4.12, indicating that a self-

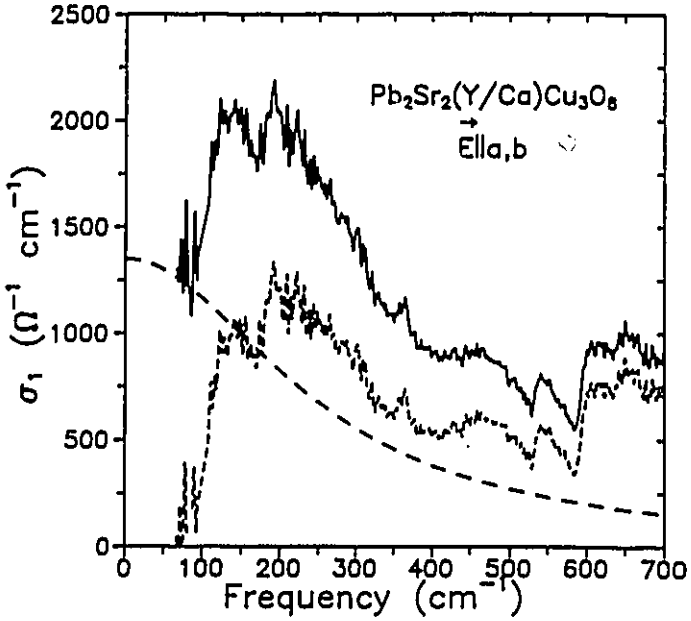

Figure 4.11: 85 K normal state *ab*-plane optical conductivity of $Pb_2Sr_2(Y/Ca)Cu_3O_8$ (solid curve). The smooth curve (long dashes) is an estimate of the Drude contribution as described in the text. The short-dashed curve shows the difference and represents the mid infrared contribution.

consistent value has been reached. The relative insensitivity of ϵ_1 to the mid infrared component is manifest in the small difference between the original estimate (4250 cm^{-1}) and the final result (4500 cm^{-1}). This value of 4500 cm^{-1} for ω_p corresponds to the combined oscillator strength of the peak centered at 100 cm^{-1} [$\omega_p(peak)$] and the zero frequency delta function condensate [$\omega_p(\delta)$] according to:

$$\omega_p^2(total) = \omega_p^2(peak) + \omega_p^2(\delta). \tag{4.4}$$

Figure 4.13 shows the 10 K conductivity with the mid infrared component of figure 4.11 subtracted. The remaining conductivity above 200 cm^{-1} may be due to temperature dependence of the mid infrared band or to the high frequency tail of the Lorentzian-like absorption peak. Integrating the area under this broad low frequency peak up to 200 cm^{-1} according to the sum-rule:

$$\int_o^{\omega c} \sigma_1(\omega) d\omega = \frac{\omega_p^2}{8} \tag{4.5}$$

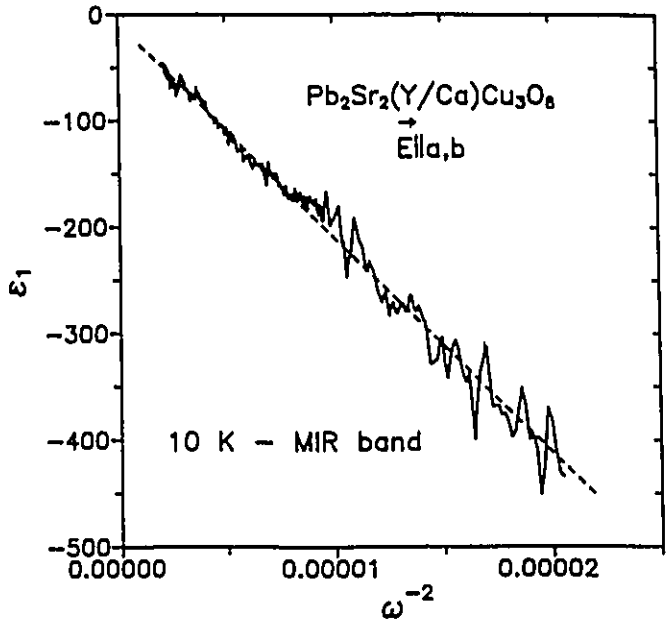

Figure 4.12: ω^{-2} dependence of ϵ_1 for frequencies above 200 cm^{-1} for ab-plane oriented $Pb_2Sr_2(Y/Ca)Cu_3O_8$ at 10 K with the mid infrared contribution subtracted.

where ω_C is the cutoff frequency (in this case 200 cm^{-1}), using, arbitrarily, a linear extrapolation to zero conductivity at zero frequency as shown by the short-dashed curve in figure 4.13, a value of 3900 cm^{-1} is obtained for $\omega_p(peak)$. A sharper gap-like cut-off (long-dashed curve in figure 4.13) yields a value of 2150 cm^{-1}. Using equation 4.4 values of 2250 and 4000 cm^{-1} are thus found for $\omega_p(\delta)$ respectively. The fraction, f of the total free carrier spectral weight in the peak is determined from:

$$f = \frac{\omega_p^2(peak)}{\omega_p^2(total)}. \tag{4.6}$$

For the two cases considered $f = 0.75$ and 0.23 respectively. That is up to three-quarters of the total itinerant carrier spectral weight above T_c may be transferred below T_c into this finite frequency peak.

Interpretation of this behaviour is difficult along conventional lines. One possible explanation for the appearance of the finite frequency peak is that in concert with the onset of superconductivity there is, for example, a change in the magnetic ordering resulting in the formation of a low frequency gap. If the superconducting

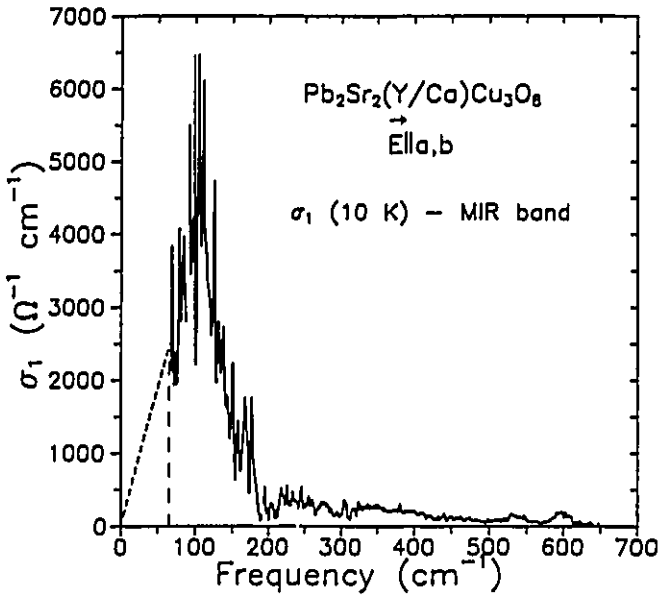

Figure 4.13: 10 K conductivity of *ab*-plane oriented $Pb_2Sr_2(Y/Ca)Cu_3O_8$ with the mid infrared contribution subtracted. The long- and short-dashed lines show the extrapolations to zero frequency used in the sum-rule analysis discussed in the text.

gap is anisotropic, a possibility that is being presently explored in the literature,[76] then portions of the Fermi surface can be gapped by the magnetic excitation and other parts by the superconducting condensate. Superconductivity-induced magnetic structure changes have been observed in $La_{2-x}Sr_xCuO_{4-\delta}$ by Mason *et. al.*[77] using neutron scattering methods. As discussed in the previous chapter both resistivity and magnetization measurements indicate unusual behaviour in $Pb_2Sr_2(Y/Ca)Cu_3O_8$ within a few degrees of T_c. Since infrared spectroscopy probes the spectrum of charge excitations one might not expect the technique to be sensitive to spin excitations. However, Barker *et. al.*[78] and Bonn *et. al.*[79] have shown that in chromium and URu_2Si_2 respectively the development of a spin-wave state can be clearly seen in the reflectivity-derived optical properties. In these materials a peak in the conductivity sets in abruptly at the Néel temperature in agreement with theoretical considerations which predict a temperature dependent gap that removes a fraction of the Fermi surface leading to an absorption threshold in the infrared spectrum. Preliminary muon

spin rotation (μSR) results for $Pb_2Sr_2(Y/Ca)Cu_3O_8$ find no evidence for *static* moments down to 2.5 K in zero field experiments.[42] This does not rule out a fluctuating moment associated with a spin density wave.

In principle for the present situation one would expect to see a second absorption threshold corresponding to the superconducting gap. The absence of such a threshold could indicate that as in $YBa_2Cu_3O_{7-\delta}$ and $Bi_2Sr_2CaCu_2O_8$ in the *ab*-plane this system too is in the clean limit such that essentially none of the normal state conductivity remains to be gapped. This is likely true although upon examination of figure 4.13 one can discern a small second absorption edge near 200 cm^{-1}. As pointed out however, the remaining conductivity above 200 cm^{-1} can be equally well attributed to temperature dependence of the mid infrared band below T_c or to the high frequency tail of the 100 cm^{-1} centered absorption.

Some discrepancy exists with the magnetization derived result for the zero temperature penetration depth which suggests that ω_p associated with the superconducting *condensate*, ie. $\omega_p(\delta)$, is 6000 cm^{-1}, while the infrared measurements yield only 2250-4000 cm^{-1} (depending on the low frequency extension for the integrated spectral weight – see figure 4.13). It should be kept in mind that this value of 6000 cm^{-1} is based on a model-dependent extrapolation to zero temperature of data in a narrow region near T_c although, the preliminary μSR results for $Pb_2Sr_2(Y/Ca)Cu_3O_8$ yield an experimental low temperature value that is the same within experimental error as the estimate from the magnetization measurements.[42] For the cuprates such missing conductivity estimates of the plasma frequency are often found to be somewhat lower than the values derived from magnetization and μSR experiments.

One point that may be of relevance to the seemingly unusual aspects of the optical conductivity of $Pb_2Sr_2(Y/Ca)Cu_3O_8$ is the likely presence of significant disorder in this system. An important difference between $Pb_2Sr_2(Y/Ca)Cu_3O_8$ and other structurally similar cuprates is the location of the charge reservoir. In $YBa_2Cu_3O_{7-\delta}$ holes are doped into the CuO_2 planes by oxidation of the CuO_δ chains. These two

layers are separated by a BaO buffer. Similarly in $Bi_2Sr_2CaCu_2O_8$ a SrO layer separates the CuO_2 planes from the BiO layers which are believed to be the source of the doping. In $Pb_2Sr_2(Y/Ca)Cu_3O_8$ the doping results from chemical substitution in the Y layer *within* the double CuO_2 plane complex. Due to the close proximity of the doping sites to the CuO_2 planes the physical properties may be susceptible not only to changes in the level of doping but also to variation in the surrounding environment. The unusual behaviour of the optical conductivity may thus reflect a higher sensitivity to the disorder invoked by the chemical substitution.

Note that the situation is similar for $La_{2-x}Sr_xCuO_{4-\delta}$. Here as well the doping is by chemical means, and takes place in the LaO layers which are directly adjacent to the CuO_2 plane.

Another closely related point is that $YBa_2Cu_3O_{7-\delta}$ with $\delta = 0$ is a stoichiometric compound, as is nominally $Bi_2Sr_2CaCu_2O_8$, while $Pb_2Sr_2(Y/Ca)Cu_3O_8$ is not. Thomas has recently discussed problems associated with interpreting results derived from non-stoichiometric materials, the main issue being the homogeneity of the sample relative to the length scale characterizing the experiment.[80] For the optical conductivity Thomas suggests that macroscopic effective homogeneity arises when the spatial variation of the impurity or substitution is smaller than the inelastic scattering length, Γ_{in}, such that the *average* distribution over a length scale of the order Γ_{in} is constant. For the cuprates this is typically of the order 10-100 unit cells. Thus for $Pb_2Sr_2(Y/Ca)Cu_3O_8$ one would require the Y:Ca ratio (approximately 7:3) to be constant over this distance. Reproducibility and a normal to superconducting transition which takes place over a narrow temperature range are suggested characteristics which indicate good homogeneity. Both criteria are satisfied by the $Pb_2Sr_2(Y/Ca)Cu_3O_8$ crystals studied here.

As alluded to above, a view that is beginning to emerge is that the superconducting energy gap in the cuprates may be anisotropic in nature. Nodes (zeroes) of the gap function on the Fermi surface would allow finite conductivity within the

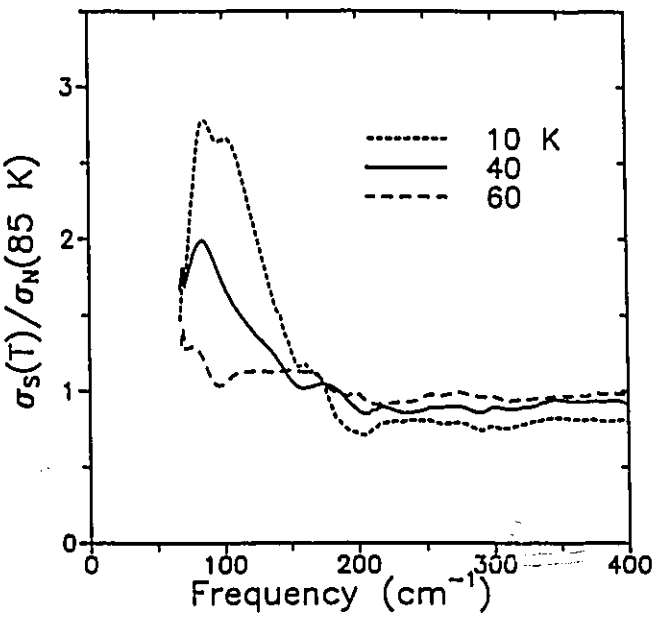

Figure 4.14: Ratio of superconducting to normal state (85 K) *ab*-plane conductivity of $Pb_2Sr_2(Y/Ca)Cu_3O_8$ at 10, 40 and 60 K.

gap. The quantity that is often used to compare with theory is the ratio of the superconducting to normal state conductivity, shown for $Pb_2Sr_2(Y/Ca)Cu_3O_8$ at three temperatures in figure 4.14. Theoretical modeling of an anisotropic superconductor in the clean limit indicates that under strong scattering conditions a peak can arise for this ratio centered at a frequency below 2Δ,[81, 82, 83] (where Δ is the superconducting energy gap), in qualitative agreement with what is observed in figure 4.14. One caveat that should be pointed out is that in theoretical treatments, the normal state conductivity, σ_N, corresponds to the same temperature as the superconducting state. That is, the scattering rate, Γ is the same for both σ_N and σ_S. In conventional type I superconductors, this can be measured experimentally by causing the sample to revert to the normal state via application of a magnetic field. For the cuprates σ_N is measured at a temperature above T_c, while σ_S is measured at the lowest experimentally accessible temperature in order to compare with T= 0 predictions. Due to the rapid suppression of the quasiparticle scattering rate below T_c, $\Gamma_N(T > T_c)$ is much larger than $\Gamma_S(T \approx 0)$. It is not known what $\Gamma_N(T \approx 0)$ is, and thus some

caution must be exercised when making such comparisons.

4.5 Low Frequency *c*-axis Optical Properties

In this section a discussion of the optical properties of $Pb_2Sr_2(Y/Ca)Cu_3O_8$ along the *c*-axis is presented which in principle should be simpler to interpret since the complication of the mid infrared absorption is absent although a new one is added by the unscreened *c*-axis phonons. Their contribution to the optical conductivity can however be quite reliably removed since they are sharp, distinct, and have a lineshape that is easily modeled.

The *c*-axis conductivity of $YBa_2Cu_3O_{7-\delta}$ has been evaluated by several groups with similar results;[S4, S5, S6, S7] the most recent being a careful and detailed study by Homes *et. al.*[S7]. The work of Homes *et. al.* indicates that the low frequency normal state background conductivity, obtained by subtracting the contribution of the prominent *c*-axis phonons, can be modeled by a free carrier Drude response with a large scattering rate of the order of several thousand wavenumbers. An estimate of the mean free path, l, reveals however that the transport along the *c*-axis cannot be conventional free-carrier absorption because a number smaller than the lattice spacing is obtained. The zero-frequency centered peak also rules out localization as the source of the *c*-axis scattering since in that case a finite frequency-centered peak is expected. In the superconducting state the conductivity is depressed with respect to the normal state conductivity for frequencies below approximately 700 cm^{-1}, remaining finite to the low frequency experimental limit of the data. The missing conductivity goes into the delta function at the origin. Here as well there is approximately a factor of two discrepancy with the estimates for the condensate spectral weight from magnetization and μSR experiments; the infrared measurement being lower. Homes *et. al.* find that the temperature and frequency dependence of the superconducting state *c*-axis conductivity is in better agreement with a model for an anisotropic gap than for a

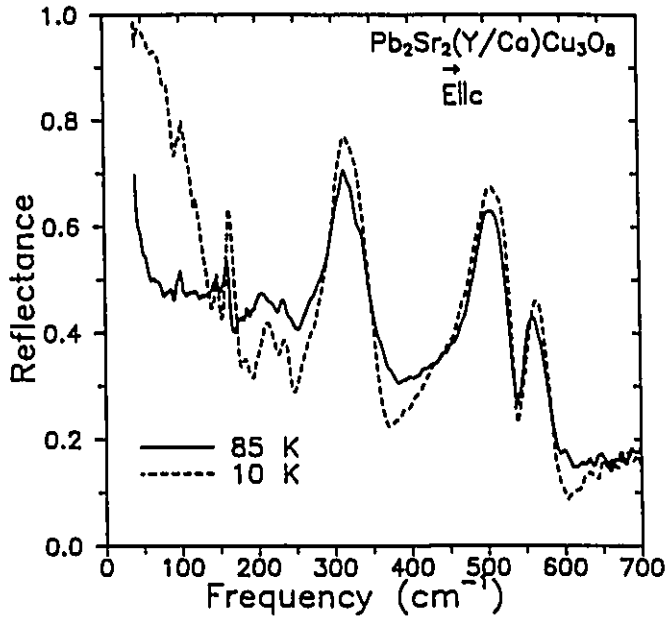

Figure 4.15: Normal (85 K) and superconducting state (10 K) reflectance of a mosaic of five $Pb_2Sr_2(Y/Ca)Cu_3O_8$ crystals for $E \| c$.

conventional isotropic BCS gap.

With the exception of $YBa_2Cu_3O_{7-\delta}$ to date very little work has been done on the low frequency c-axis optical properties of the cuprate superconductors. Recently Tamasaku *et. al.* have examined the temperature dependence of the c-axis conductivity in $La_{2-x}Sr_xCuO_{4-\delta}$.[88] The present measurements of $Pb_2Sr_2(Y/Ca)Cu_3O_8$ thus correspond to only the third cuprate superconductor to be investigated in the superconducting state along the c-axis.

Figure 4.15 shows the reflectance at 85 K in the normal state compared to that at 10 K in the superconducting state for $Pb_2Sr_2(Y/Ca)Cu_3O_8$ along the c-axis. The most significant changes occur at low frequencies where in the superconducting state the reflectance rises dramatically towards unity similar to what has been observed in $YBa_2Cu_3O_{7-\delta}$. At higher frequencies the level of the superconducting state reflectance is lower than that of the normal state. The Kramers-Kronig derived optical conductivity is shown in figure 4.16. The phonons clearly make a large contribution. Since it is the background conductivity that is of primary interest, the phonons were

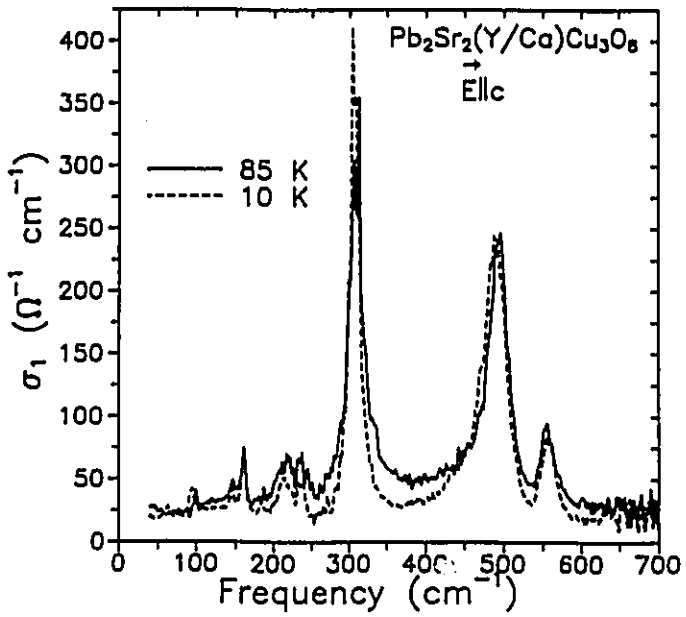

Figure 4.16: Kramers-Kronig derived optical conductivity of $Pb_2Sr_2(Y/Ca)Cu_3O_8$ in the normal (85 K) and superconducting (10 K) states for $\mathbf{E}\|c$.

fitted individually over a small frequency range with a linear background and a Fano-lineshape of the form:

$$\sigma_1(\omega) = A + B\omega + C\frac{(q+\epsilon)^2}{(1+\epsilon^2)}, \tag{4.7}$$

where $q = \frac{(\omega-\omega_o)}{\Gamma}$ and allows for an asymmetric lineshape. All phonons were symmetric (that is, in the fit q is large and hence there is little interaction with the electronic background) except for the 485 cm^{-1} mode which is noticeably asymmetric. The fitted contribution of the phonons to the conductivity of figure 4.16 is shown in figure 4.17, while the remaining background conductivity is plotted in figure 4.18.

The normal state background is relatively featureless, showing perhaps a broad maximum near 450 cm^{-1}, which could be indicative of a hopping-type transport. The superconducting state conductivity on the other hand shows three distinct features; a prominent decrease from the normal state value beginning near 700 cm^{-1} and reminiscent of the behaviour of $YBa_2Cu_3O_{7-\delta}$, a gap-like region between 250 and 300 cm^{-1}, and once again, a low frequency absorption. It is difficult to discern

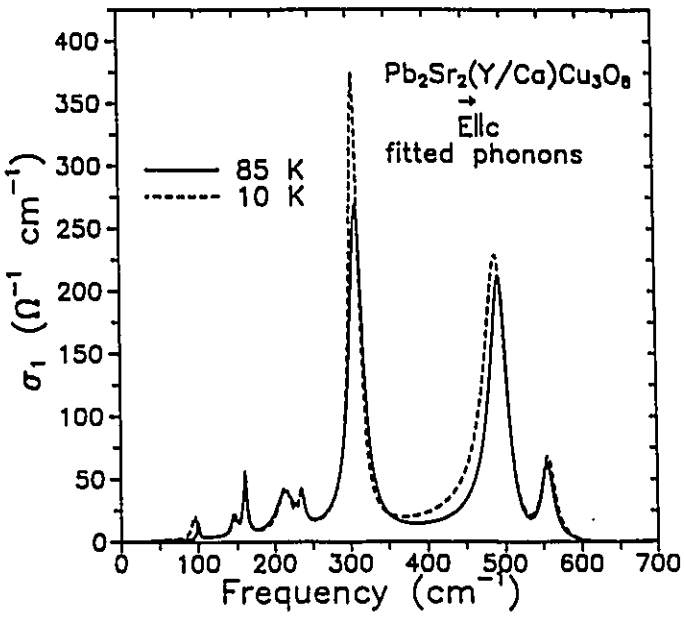

Figure 4.17: Fitted contribution of the phonons to the E$\|$ c conductivity of $Pb_2Sr_2(Y/Ca)Cu_3O_8$ at 10 and 85 K. The only mode with a noticeable assymetric lineshape is that at 485 cm^{-1}.

whether this latter feature is zero- or finite-frequency centered although there does appear to be a maximum near 125 cm^{-1}. The similar energy scale of this feature with the peak observed in the *ab*-plane conductivity suggests that they may be of the same origin.

Further evidence comes from a sum-rule analysis. Choosing extrapolations to zero-frequency as shown in figure 4.18, the effective plasma frequency corresponding to the integrated spectral weight according to equation 4.5 between zero and 700 cm^{-1} in the normal state is 880 cm^{-1}. For the superconducting state 605 cm^{-1} is obtained. The missing spectral weight corresponding to 275 cm^{-1} resides in the delta function condensate. The integrated spectral weight under the superconducting state low frequency absorption feature corresponds to a plasma frequency of 385 cm^{-1}. Note that the ratio of the plasma frequency corresponding to the zero-frequency condensate along the *c*-axis to that in the *ab*-plane, (0.07-0.12) is close to the corresponding ratio for the low frequency absorption, (0.10-0.18), indicating that the division of spectral

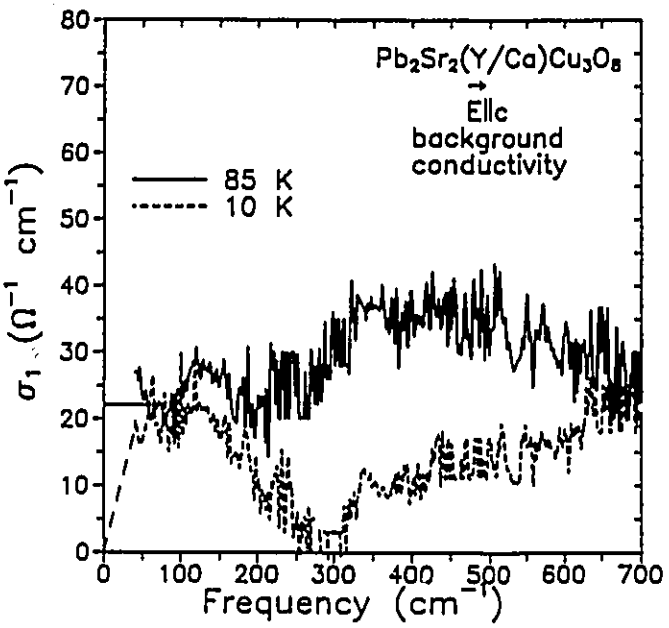

Figure 4.18: Background conductivity of $Pb_2Sr_2(Y/Ca)Cu_3O_8$ along the c-axis after removing the prominent c-polarized phonons at 85 K in the normal state and at 10 K in the superconducting state. The low frequency extrapolations used in the sum-rule analysis discussed in the text are also shown.

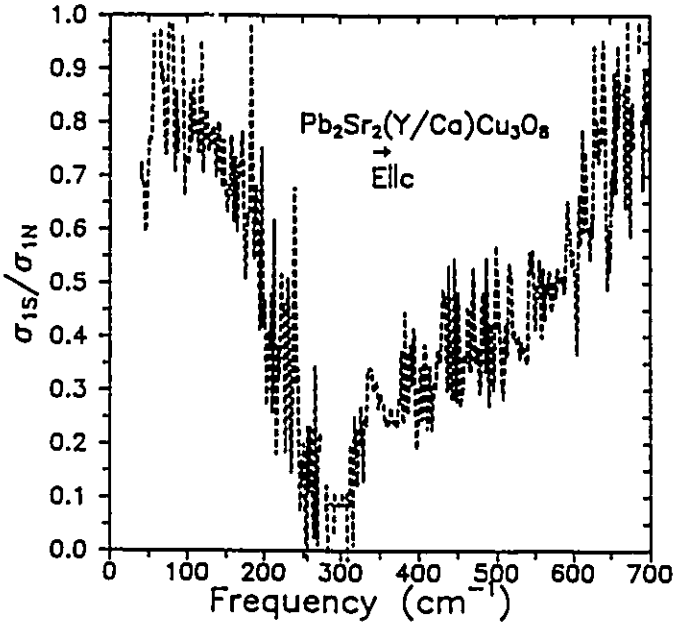

Figure 4.19: Ratio of the superconducting (10 K) to normal state (85 K) background conductivity of $Pb_2Sr_2(Y/Ca)Cu_3O_8$ for $E \| c$.

weight between these two processes is similar along the c-axis to that in the ab-plane. The extent of the anisotropy [approximately 8-10 for $\frac{\omega_p^{ab}}{\omega_p^c} = (\frac{m_c}{m_{ab}})^{\frac{1}{2}}$] is moderate as expected from the results of the previous chapters.

The ratio of the superconducting state to normal state conductivity is shown in figure 4.19. Comparison to zero temperature model calculations for various gap symmetries[81, 82] shows no quantitative agreement with figure 4.19, although qualitatively once again, due to the presence of finite conductivity at low frequencies an anisotropic order parameter may be indicated.

4.6 Conclusions

In summary, the temperature dependence of the normal and superconducting state optical conductivity has been presented for $Pb_2Sr_2(Y/Ca)Cu_3O_8$ both in the ab-plane and along the c-axis. Due to the intrinsically lower reflectance of this material the evolution of the optical conductivity with temperature is qualitatively unaffected by the choice of low frequency extrapolation in the Kramers-Kronig procedure. Both orientations reveal unconventional behaviour in the superconducting state. Along with the observation of a condensation of superconducting carriers there is a redistribution of a portion of the normal state Drude spectral weight into a peak centered near 100 cm^{-1}; the origin of which is yet unknown. Although it is not proposed that this behaviour is universal to the cuprates there is evidence in the literature that in $YBa_2Cu_3O_{7-\delta}$ too there is, for the ab-plane at least, some low frequency spectral weight which does not reside in the delta function condensate. This suggests that there is still room for some re-examination of the present interpretation of the superconducting state optical conductivity of the cuprate superconductors in general.

In the following two chapters the emphasis switches from the superconducting state to some of the more unusual aspects of the normal state optical properties of $Pb_2Sr_2RCu_3O_8$. In particular the evolution of the phonon structure with doping will

be examined. The discussion will lead to an explanation for a detail of the normal state optical properties of the cuprates that has been unresolved since the start of high-T_c work in 1986.

Chapter 5

The Superconductor–Insulator Transition in Ca–Free $Pb_2Sr_2RCu_3O_8$

5.1 Insulating, Lightly Doped and Poorly Metallic Materials

As discussed in chapter 1 the insulating parent compound $Pb_2Sr_2RCu_3O_8$ where 'R' is a rare earth can be made superconducting with $T_c \approx$ 80 K by partial substitution of divalent calcium for the trivalent rare earth. The properties of $Pb_2Sr_2R_{1-x}Ca_xCu_3O_8$ with R $\equiv$ Y and $x \approx 0.3$ have been the focus of the last three chapters. In this chapter we will examine the series of rare earth substituted Ca-free compounds $Pb_2Sr_2RCu_3O_8$ with R $\equiv$ La, Ce, Pr, Nd, Sm, Eu, Gd, Tb, Dy, Ho, and Y. In the apparent absence of a doping mechanism each of these compounds is expected to be electronically insulating. Surprisingly however the system is found to undergo a metal (superconductor)–insulator transition as a function of increasing ionic radius of the rare earth.

5.1.1 Resistivity

The *ab*-plane dc-resistivity of the series of single crystal samples was measured using the van der Pauw four probe technique as discussed in Chapter 3. The samples were polished to uniform thickness in order to ensure an accurate absolute value for the purposes of comparison. Figure 5.1 shows the temperature dependence of ρ for selected members of the series. An insulator-superconductor (I–S) transition takes place between R≡Sm and R≡Eu. Note that for R≡Eu the *ab*-plane resistivity shows a

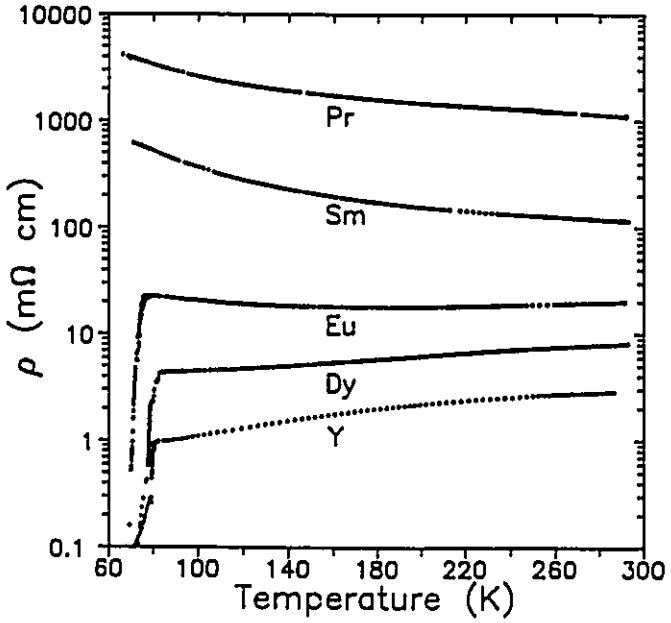

Figure 5.1: *ab*-plane dc-resistivity for selected members of the Ca-free $Pb_2Sr_2RCu_3O_8$ series. Note the superconductor-insulator transition which takes place as a function of increasing ionic radius of the rare earth ion.

negative temperature coefficient at temperatures below approximately 200 K, turning up noticeably before undergoing the transition to the superconducting state. This may indicate that the I–S transition is three dimensional in nature. In a two dimensional transition the resistivity extrapolates to a temperature independent constant as T→ 0 at the I–S transition, with a sheet resistance of the order $h/4e^2 \approx 6.5\text{k}\Omega$ where h is Plancks constant and e is the electron charge.[89] In $Bi_2Sr_2CaCu_2O_8$, which is

highly anisotropic and significantly more two dimensional than $Pb_2Sr_2(Y/Ca)Cu_3O_8$, a S–I transition can be induced by partial substitution of a trivalent rare earth such as Y for divalent Ca. Mandrus *et. al.* find that a sheet resistance of 8 kΩ separates superconducting and insulating ground states in a series of such Y-doped single crystals.[90] In another study, Seidler *et. al.* find a value near 14 kΩ at the magnetic field-induced S–I transition in an oxygen-reduced single crystal of $YBa_2Cu_3O_{7-\delta}$ with a T_c of only 2 K.[91] Extrapolation to zero temperature is difficult for the curves of figure 5.1 although it is clear that the sheet resistance will be more than an order of magnitude larger than $h/4e^2$. (The sheet resistance is obtained by dividing the measured resistivity by the distance between conducting two-dimensional layers, *ie.* the *c*-axis lattice constant if one assumes that the two CuO_2 planes are coupled). Further evidence for the three dimensional nature can be derived from the measurements of the *c*-axis resistivity shown for R≡ Eu, Dy in figure 5.2. In both cases measurements on three different crystals were carried out to obtain an estimate of the uncertainty in the absolute value. Clearly as for the Ca-doped compound discussed in chapter 3 the anisotropy at these doping levels is still moderate (approximately one to two orders of magnitude at room temperature) although the extent of the anisotropy appears to increase somewhat as the level of doping decreases. That is, the *c*-axis resistivity increases at a comparatively larger rate as the samples become less metallic in the *ab*-plane. This is similar to the trend observed in $YBa_2Cu_3O_{7-\delta}$ as δ decreases and T_c is lowered.[91, 92]

5.1.2 Mid Infrared Reflectance

That a metal-insulator transition takes place as a function of increasing ionic radius of the rare earth can also be deduced from measurements of the room temperature mid infrared (MIR) reflectance, shown for all members of the series with the exception of R≡ La in figure 5.3. The measurements were carried out using a Bomen/Spectra-Tech infrared microscope with a liquid nitrogen cooled Hg-Cd-Te detector. Clearly the

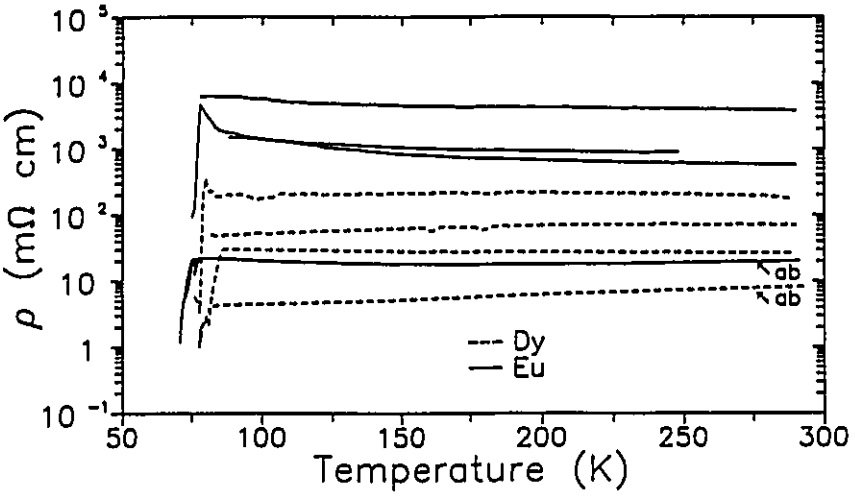

Figure 5.2: Anisotropy in the dc-resistivity of $Pb_2Sr_2RCu_3O_8$ with R≡ Eu, Dy. Three measurements of the *c*-axis resistivity are shown for each (unlabelled curves) in order to gain some feeling for the extent of the uncertainty in the absolute value. Note that the anisotropy which is moderate at these doping levels increases somewhat as the level of doping decreases (*ie.* the *c*-axis resistivity increases at a comparatively higher rate than the *ab*-plane resistivity).

samples with R≡ Y, Ho, Dy exhibit a metallic-like MIR reflectance which decreases linearly with increasing frequency similar to that of Ca-doped $Pb_2Sr_2(Y/Ca)Cu_3O_8$ in the *ab*-plane while R≡ Ce, Pr, Nd exhibit the essentially flat and featureless spectrum characteristic of an insulator. The reflectance of R≡ Sm, Eu, Gd, Tb appears intermediate in nature, evolving from exhibiting a very small rise at low frequencies (Sm) to increasingly larger plasma-like edges indicating a growing metallicity.

5.1.3 Classification

Based on the observations of the previous two sections regarding the electronic character of these materials the series can be divided into three groups; (1) insulators, (2) lightly doped materials and (3) poor metals. The classification is summarized in figure 5.4 which also indicates where the I–S transition takes place. The only excep-

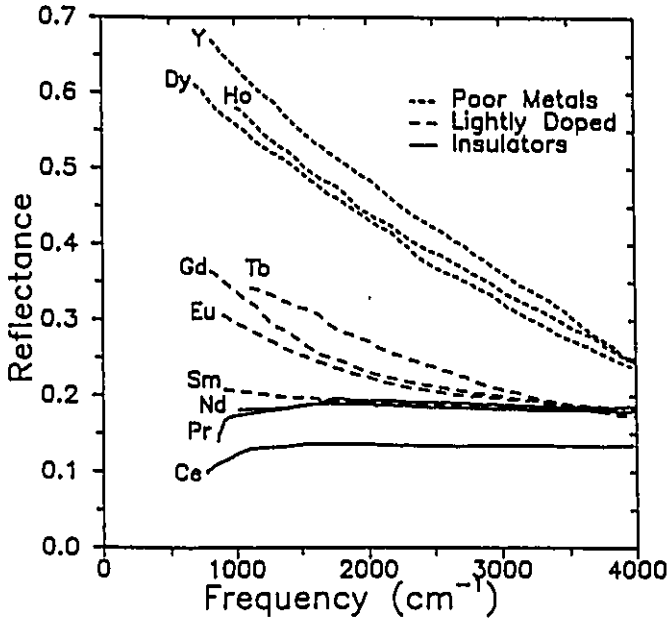

Figure 5.3: Mid infrared *ab*-plane reflectance of the Ca-free $Pb_2Sr_2RCu_3O_8$ series.

tion to the trends summarized in figure 5.4 is Tb, which although it was found to exhibit a doping level comparable to the other lightly doped materials according to the MIR reflectance measurements (figure 5.3) did not undergo a superconducting transition; exhibiting instead a temperature induced metal-insulator (M–I) transition in the resistivity (figure 5.5). This point will be revisited when the doping mechanism is addressed in section 5.1.5.

5.1.4 MIR Transmission Measurements of R≡ La, Ce

The omission of a reflectance spectrum for R≡ La in figure 5.3 was intentional. When both La and Ce were examined, interference fringes were observed in the reflectance. In the curve shown for Ce in figure 5.3 the fringes were removed. The presence of fringes suggested that these materials were transparent to the MIR radiation. Subsequent room temperature transmission measurements carried out using the Bomem interferometer confirmed this conclusion as shown in figures 5.6(a) and (b) for La and Ce respectively. The transmission spectra are referenced to a hole. Absorption due

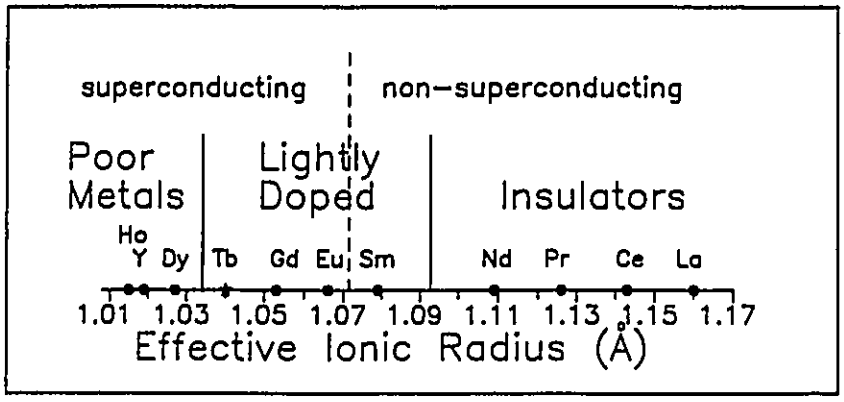

Figure 5.4: Summary of trends in the electronic structure of the Ca-free $Pb_2Sr_2RCu_3O_8$ series. The series is divided into three groups; (1) insulators, (2) lightly doped materials, and (3) poor metals. The S–I transition takes place within the lightly doped group between Sm and Eu. The only exception is Tb, marked with a star instead of a solid circle, which does not undergo a superconducting transition in spite of the fact that the room temperature MIR reflectance indicates a carrier density comparable to the other lightly doped and superconducting members.

to phonons at low frequencies can be clearly seen. These results suggest that even within the insulating group of materials there is a progression from very insulating (and transparent) to less insulating character.

An interesting possibility for further work presents itself in that these materials would be ideal for photoinduced absorption experiments where changes in the optical properties arising from photo- as opposed to chemically–doped carriers are investigated. In a photoinduced absorption experiment the changes in transmission are monitored as carriers are created via photoexcitation using a laser. Photoinduced absorption studies performed on non-superconducting derivatives of the cuprates have shown that the MIR band can be photoinduced.[93, 94, 95] As of yet the measurements have been carried out on semiconducting thin film samples or with a powder of undoped material *eg.* $YBa_2Cu_3O_{6+\delta}$ embedded in a transparent matrix such as KBr

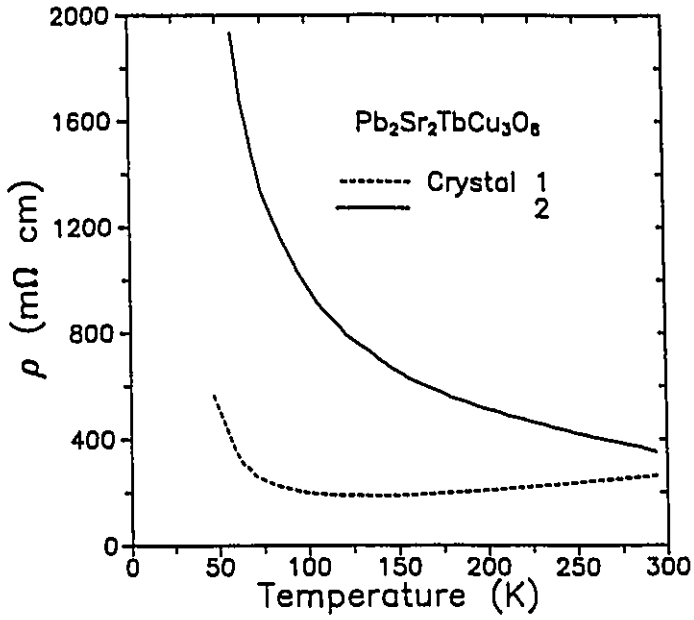

Figure 5.5: *ab*-plane dc-resistivity of a R≡ Tb crystal showing the absence of a superconducting transition and a temperature induced metal-insulator transition (Crystal 1). A second crystal showed only semiconducting behaviour indicating considerable crystal to crystal variation as well.

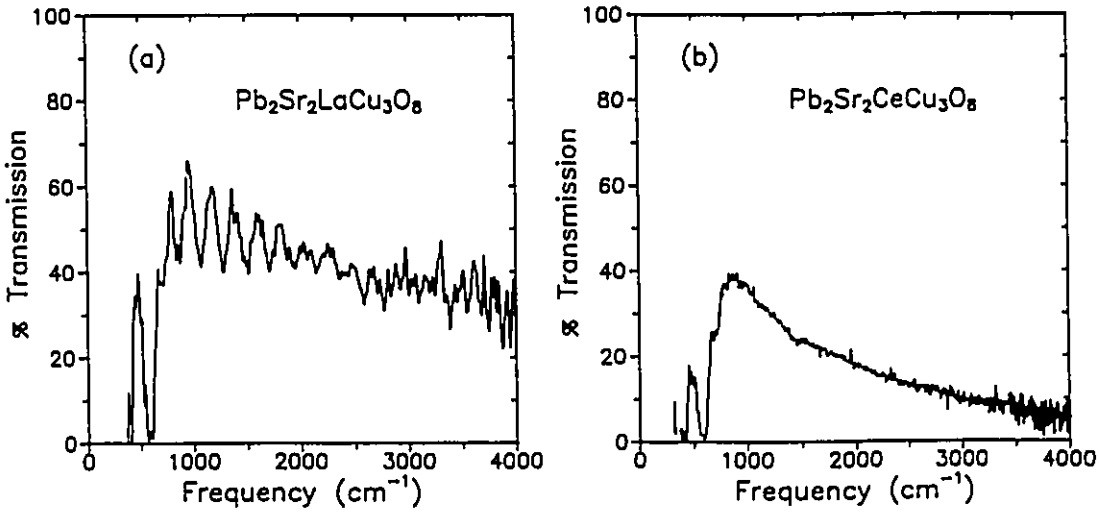

Figure 5.6: Bulk MIR transmission measurements of (a) La and (b) Ce single crystals referenced to a hole. Note the phonon absorption at low frequencies.

because crystals of $YBa_2Cu_3O_{6+\delta}$ have not been prepared with low enough doping levels to allow bulk transmission. This results in the complications of either interpreting data for an unoriented sample with possible unwanted effects from the transparent medium or being limited by the dielectric properties of the thin film substrate.

5.1.5 Cation Vacancy Mechanism

The nature of the hole doping in this series is curious. It is unrelated to oxygenation of the Cu(1) layer since the crystals are synthesized and annealed in a nitrogen atmosphere to avoid excess oxygen which, as discussed in the introduction, in contrast to $YBa_2Cu_3O_{7-\delta}$ is detrimental to the superconducting properties of this system.

Based on crystallographic and elemental analyses a cation vacancy mechanism has been proposed[20] to explain the M–I transition in the Ca-free $Pb_2Sr_2RCu_3O_8$ series elucidated via the resistivity and MIR reflectance measurements discussed above. While the evidence will be summarized here, the reader is referred to references [20], [21], and [22] for further details.

Refinement of single crystal x-ray diffraction data indicated an electron deficiency of the order of 9% at the rare earth site for the lightly doped and metallic crystals R≡ Eu, Tb, Dy, while the site was determined to be fully occupied for those with R≡ La, Nd, Pr (insulators).[21] This electron deficiency is the source of the hole doping in the lightly doped and metallic members of the series. There are two possible explanations; partial substitution of the site by a divalent ion such as Sr, or alternatively, by vacancies. Energy Dispersive X-ray Analysis showed no detectable Na content which might have provided another possible divalent substitutional ion due to its presence in the flux.[20] The crystallographic analysis cannot distinguish between these two models in that a 23% strontium excess will account for the observed electron deficiency equally well as 9% vacancies, although since strontium is significantly larger than both calcium and the rare earth ions the former would seem the least likely of the two models.

Elemental analysis via electron probe microanalysis and inductively coupled plasma/mass spectroscopy seems to confirm the cation vacancy hypothesis by showing within experimental error a fully occupied rare earth site for the insulating members of the series, no evidence for a strontium excess, and a deficiency of the order of the expected 9% at the rare earth site in those crystals exhibiting lightly doped or metallic character.[20]

Further evidence that the doping in this series is promoted by cation vacancies at the rare earth site arises from work on polycrystalline samples.[20] In polycrystalline form it is possible to prepare stoichiometric (that is, containing a fully occupied rare earth site) samples of $Pb_2Sr_2RCu_3O_8$ with smaller rare earth ions, *eg.* R ≡ Y. As expected an insulating and non-superconducting compound is obtained (figure 5.7 inset). When rare-earth vacancies are intentionally incorporated into the samples, superconducting behaviour begins to appear (main figure). These observations thus further corroborate the proposed cation vacancy doping mechanism for the Ca-free single crystal $Pb_2Sr_2RCu_3O_8$ series.

Now the situation for the Tb crystals is briefly re-addressed. The crystallographic electron density at the rare earth site was found to be lower for R≡Tb (4.5%) than for R≡ Eu, Dy (9.4% and 8.9% respectively);[21] both of which exhibit a superconducting transition. Since Tb has a stable 4^+ valence state considerable care was used during synthesis to promote the 3^+ valence.[28] It is thought that despite the precautions taken the suppression of superconducting behaviour may arise from the presence of a small amount of Tb^{4+} which will absorb holes doped into the system via the cation vacancies.

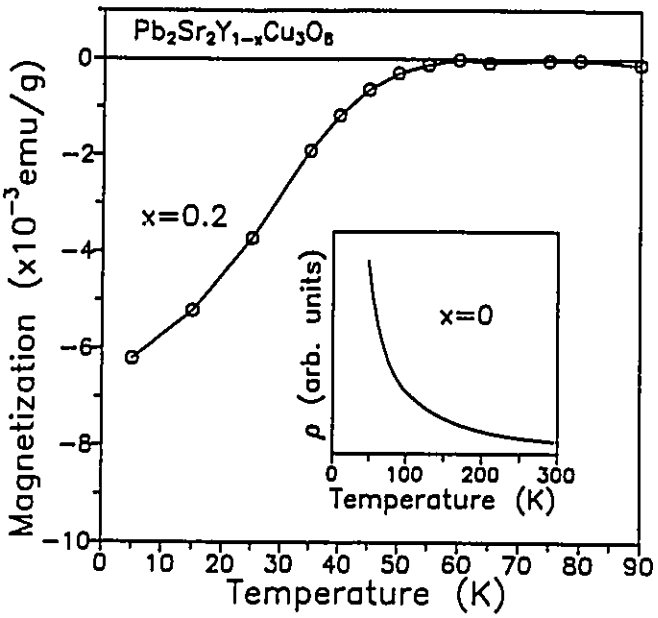

Figure 5.7: dc resistivity of a stoichiometric powder sample of $Pb_2Sr_2YCu_3O_8$ showing insulating and non superconducting character (inset). The main figure shows that intentional incorporation of vacancies at the rare earth site leads to superconducting behaviour.

5.2 Infrared Optical Properties of the M–I Transition

In this section the evolution of the optical properties as the Ca-free $Pb_2Sr_2RCu_3O_8$ series progresses through the metal-insulator transition will be examined. As described in chapter 4, reflectance data is collected and then analyzed via Kramers-Kronig analysis and model fits to the dielectric function.

5.2.1 Experimental

The reflectance measurements were carried out on both mechanically polished (R≡ Y, Ho, Dy, Gd, Eu, Sm, Nd, Pr) and natural (R≡ Tb, Ce, La) surfaces, in both the *ab*-plane (R≡ Y, Ho, Dy, Tb, Gd, Eu, Sm, Nd, Pr, Ce, La) using an unpolarized source

and along the *c*-axis (R≡ Dy, Gd, Eu, Sm, Nd) with polarized radiation. A mosaic of crystals was not required to investigate the *c*-axis reflectance, since these Ca-free $Pb_2Sr_2RCu_3O_8$ samples were large enough (the *c*-axis dimension ranged from 0.2–0.5 mm while the in-plane dimension was typically 0.5–1.0 mm) to allow measurement of an individual crystal.

The details of the experimental procedure are essentially identical to those outlined in chapter 4. The far infrared (FIR) reflectance measurements were carried out using a home-built rapid scan Michelson-type interferometer with focused optics. The crystals were mounted in a continuous flow cryostat, the temperature of which could be varied from 10 K to room temperature. For most members of the series only temperatures above liquid nitrogen (77 K) were investigated with the exception of R≡ Y, Ho, Eu, Sm in the *ab*-plane and R≡ Dy along the *c*-axis which were also examined at liquid helium temperatures. In the mid infrared the reflectance was measured at room temperature using the above arrangement and/or the Spectra-Tech infrared microscope while room temperature near infrared–visible measurements were carried out with the appropriate detector–filter combinations as outlined in chapter 4 using the SPEX grating spectrometer. As before, the absolute value of the reflectance was determined by accounting for geometrical scattering losses via *in situ* evaporation of a metallic film (Au or Al) onto the surface of the sample. The coated sample was remeasured and the absolute value of R given by the ratio of spectra before and after plating, corrected for the absolute reflectance of the metallic film.

5.2.2 High Frequency *ab*-plane Electronic Structure

The high frequency near IR–visible measurements were again only carried out for *ab*-plane oriented samples due to the inavailability of an appropriate polarizer beyond 5000 cm^{-1}. To establish the general trends in the evolution of the high frequency *ab*-plane electronic structure it was considered sufficient to examine only one or two representative members from each of the three groups of materials.

The reflectivity from 100-30000 cm^{-1} is shown on a log – log plot for several such representative members of the series in figure 5.8.

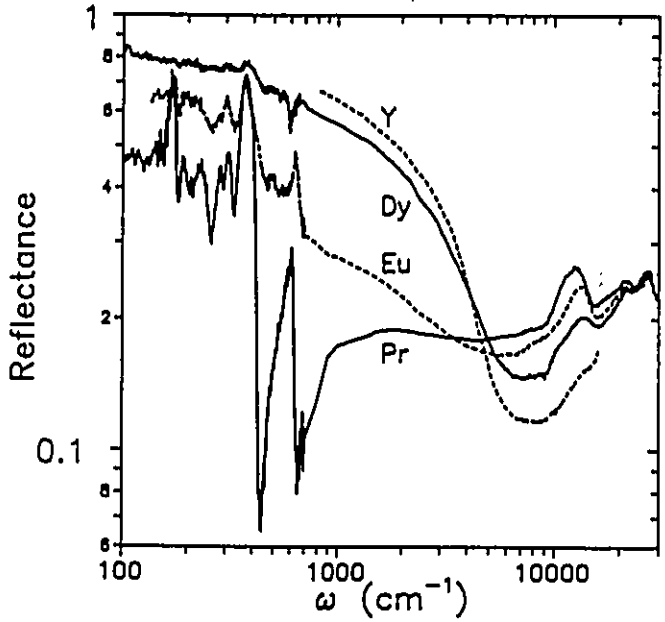

Figure 5.8: *ab*-plane reflectivity of representative members of the $Pb_2Sr_2RCu_3O_8$ series over a wide frequency range. Note the log – log scale.

The reflectance of the insulator (Pr) shows structure due to phonons at low frequency, is essentially flat and featureless in the mid infrared region and then develops a series of peaks beyond the infrared region of the spectrum resulting from interband transitions. The peak near 14000 cm^{-1} is due to the onset of charge transfer excitations while those near 22000 and 27000 cm^{-1} arise from another interband transition within the CuO_2 planes and from $O(2)p_z$–$Pb_{x,y}$ transitions respectively as discussed in the previous chapter. Light doping (Eu) brings about growth in the low frequency reflectance; the phonons, all still evident, are now superimposed on a background absorption, the mid infrared reflectance develops a small plasma-like edge, and the Cu-O charge transfer peak decreases in magnitude. These changes become more pronounced for the more metallic samples (Dy and Y); the phonons become less prominent, the plasma edge shifts to somewhat higher frequency and the 14000 cm^{-1} peak continues to decrease in intensity. Recall as well that this peak was

comparatively weak in the Ca-doped sample examined in chapter 4.

Interpretation of the progression from insulator to metal can be more readily facilitated by examining the optical conductivity (figure 5.9) obtained via Kramers-Kronig transformation of the reflectivity data of figure 5.8. In order to evaluate the

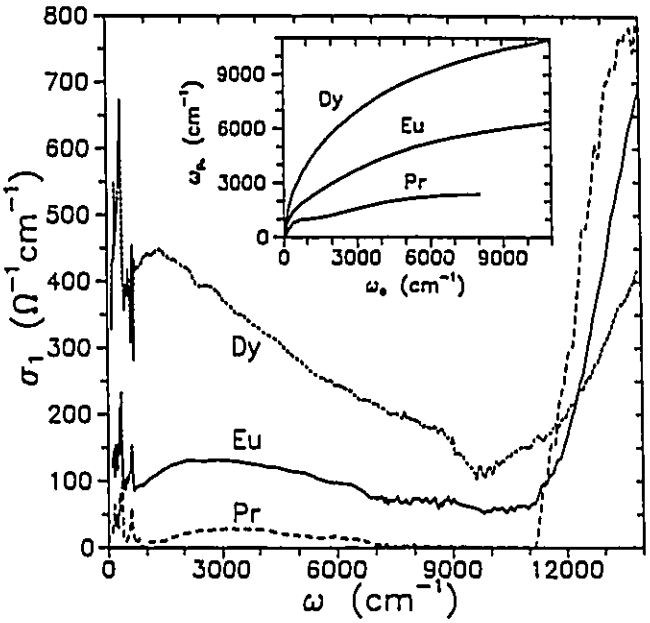

Figure 5.9: Real part of the *ab*-plane optical conductivity of representative members of the $Pb_2Sr_2RCu_3O_8$ series over a wide frequency range. The inset shows the integrated spectral weight as a function of cutoff frequency, ω_C.

Kramers-Kronig integral a Drude extrapolation was used at low frequencies with a scattering rate and plasma frequency consistent with the measured dc-resistivity for metallic samples while a constant was used for insulators. At high frequencies the *ab*-plane data of Kircher *et. al.*[68] for a single crystal of $Pb_2Sr_2(Y/Ca)Cu_3O_8$ was used from the end of the data of figure 5.8 (30000 cm^{-1}) to the end of theirs (47000cm^{-1}) followed by that of Romberg *et. al.*[70] for $YBa_2Cu_3O_{7-\delta}$ up to 50 eV. Above this an ω^{-4} power law was used.

Figure 5.9 shows clearly a transfer of spectral weight from high frequencies to the mid and far infrared with increased doping. Note that the maximum of the mid infrared band shifts to lower frequencies as its strength increases. This effect has also

been seen in $YBa_2Cu_3O_{7-\delta}$ and $La_{2-x}Sr_xCuO_{4-\delta}$ (references [62] and [9] respectively).

The inset of figure 5.9 shows the plasma frequency, ω_{p_c}, obtained by integrating the conductivity up to a cutoff frequency, ω_c, according to the partial sum-rule:

$$\int^{\omega_c} \sigma d\omega = \frac{\omega_{p_c}^2}{8}. \tag{5.1}$$

The effective number of electrons contributing to the optical conductivity below the cutoff frequency is given by:

$$N_{eff}(\omega_c) = \frac{m V_{cell} \omega_{p_c}^2}{4\pi e^2}, \tag{5.2}$$

where m and e are the electronic mass and charge respectively, and V_{cell} is the volume of one unit cell. Thus, N_{eff} for a cutoff frequency of 10000 cm^{-1} is found to be 0.22, 0.07, and 0.01 for Dy, Eu, and Pr respectively, of which the Drude contribution is estimated to be 0.003, 0.001 and $\approx$0 respectively (see section 6.1.1 of chapter 6). As expected N_{eff} decreases as the level of doping is reduced. What is noteworthy is the small magnitude of N_{eff} given the high value of T_c ($\approx$ 75 K). For a crystal of $YBa_2Cu_3O_{7-\delta}$ with a comparable T_c of 80 K, Orenstein *et. al.* find an N_{eff} of 0.86, of which the Drude component is 0.22.[62] Thus, not only is the free carrier concentration much lower in the $Pb_2Sr_2RCu_3O_8$ system, but that of the bound carriers in the mid infrared band as well.

Note that in figure 5.8 there is also an overall shift of the Cu-O charge transfer peak to higher frequency with decreasing size of the Lanthanide. This can be seen more clearly in figure 5.10 which shows the imaginary part of the dielectric function, ϵ_2, (related to the optical conductivity via $\sigma_1 = \frac{\omega}{4\pi}\epsilon_2$) in the vicinity of the charge transfer peak for the representative rare-earth substituted members of the series. The shift is a direct consequence of the sensitivity of the charge transfer gap, Δ_{CT}, to the in-plane Cu-O distance, d, which as indicated by a systematic decrease of the a and b lattice parameters,[20] decreases with decreasing ionic radius of the rare earth.

The peak in ϵ_2 (or alternatively the midpoint of the absorption edge) can be associated with the value of the charge transfer gap Δ_{CT}. The variation of Δ_{CT}

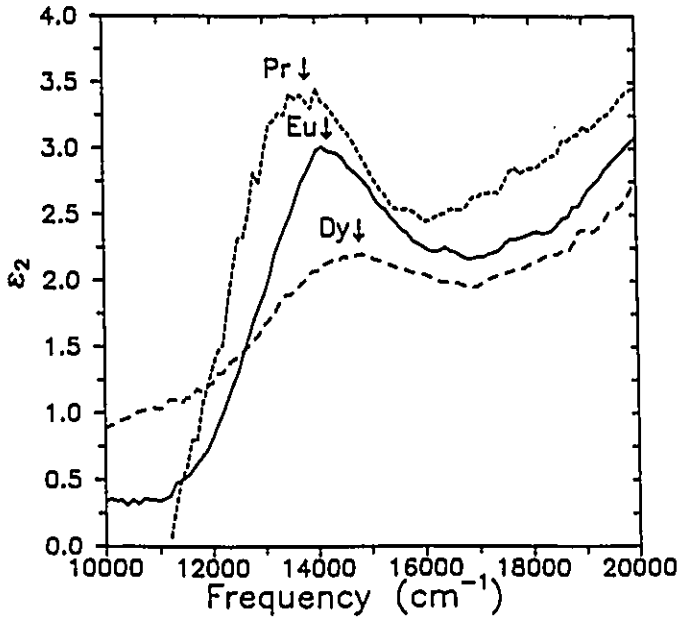

Figure 5.10: Imaginary part of the *ab*-plane dielectric function, ϵ_2, for representative members of the rare-earth substituted $Pb_2Sr_2RCu_3O_8$ series. Note that the maximum of the charge transfer peak shifts to higher frequency, as indicated by the arrows, as the ionic radius of the rare-earth decreases.

for $Pb_2Sr_2RCu_3O_8$ with R≡ (Pr, Nd, Sm, Eu, Dy) (based on the midpoint of the absorption edge) with the inverse of the effective tetragonal in-plane Cu-O distance, $d = \sqrt{ab}$ where a and b are the lattice parameters determined by x-ray diffraction[20] is shown in figure 5.11. The solid points are those of Cooper *et. al.*[13] for various related materials based upon which they proposed a simple general scaling behaviour for the cuprates of the form:

$$\Delta_{CT} = \Delta_o + a_o/d \tag{5.3}$$

which is shown as the dashed line with Δ_o and a_o given by -7×10^4 cm^{-1} and 1.6×10^5Å-cm^{-1} respectively. Note that the data for the $Pb_2Sr_2RCu_3O_8$ series seems to deviate somewhat from this relationship. This is in agreement with the claim by Arima *et. al.*[96] that it is not the in-plane Cu-O distance d that primarily sets the scale for Δ_{CT} but rather the oxygen coordination of, or more generally, the total negative valence of anions, Q, surrounding copper. In figure 5.12 Δ_{CT} for the rare-

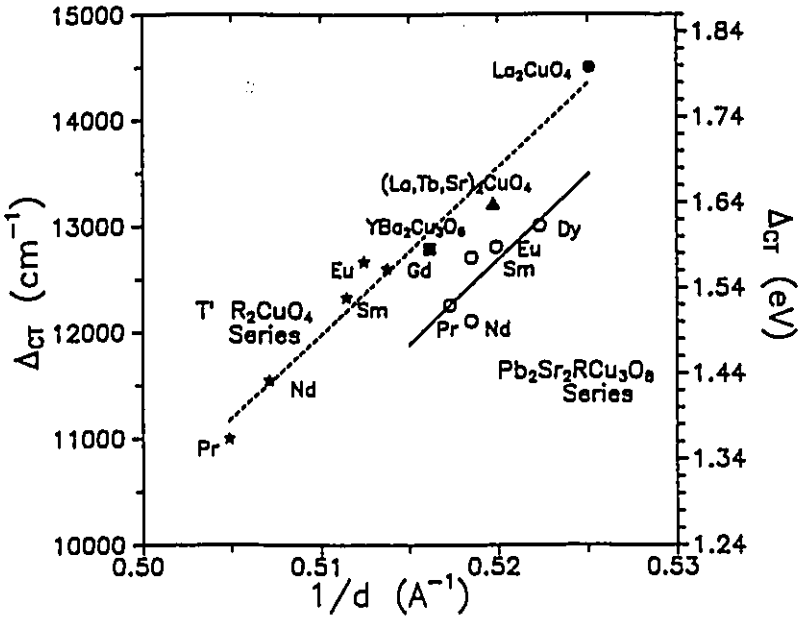

Figure 5.11: Δ_{CT} versus d^{-1} where Δ_{CT} is defined as the midpoint of the absorption edge in ϵ_2. The solid points are those of Cooper *et. al.* upon which a general scaling behaviour shown by the dashed line was proposed. The open circles show the data for the $Pb_2Sr_2RCu_3O_8$ series. Note the deviation from the proposed scaling behaviour.

earth substituted series (this time defined as the peak in ϵ_2) is plotted directly as a function of d (open circles). The solid circles are the data of Arima *et. al.*. The two dashed horizontal lines separate the points corresponding to compounds with an anion valence of 8, 10 and 12 (lower, middle, upper respectively). Note that it is the points for the infinite-layer compound (Ca,Sr)CuO_2 (which has a comparatively low value of Δ_{CT} relative to d^{-1}) and the CuO_2Cl_2 compound (which has a relatively large value of Δ_{CT} and the smallest value of all the compounds shown for d^{-1}) that are the strongest indication that a general scaling law fails. Since the in-plane Cu of $Pb_2Sr_2RCu_3O_8$ is 5-coordinated with oxygen it has $Q = 10$. The data points of the present study are thus in good agreement with the delineation proposed by Arima *et. al.*, and although they seem to disagree with a general scaling behaviour of Δ_{CT} with d^{-1} for *all* of the cuprates, the data support a view that *within* a given series of isostructural materials (*eg.* the T′ rare-earth substituted insulators as studied by

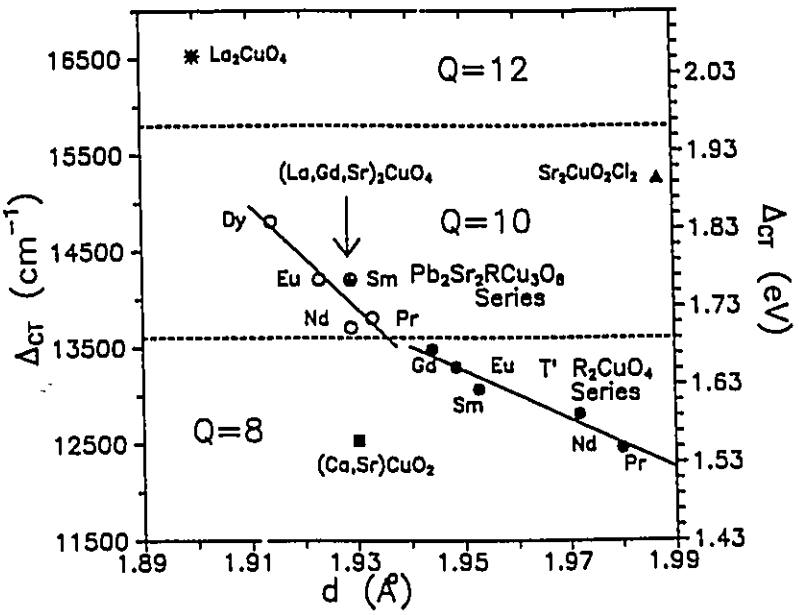

Figure 5.12: Δ_{CT} versus d where Δ_{CT} is defined as the peak in ϵ_2. The solid points are those of Arima *et. al.*. The horizontal dashed lines delineate the range of energies for Q = 8, 10, and 12 (see text). Note that the data for the $Pb_2Sr_2RCu_3O_8$ series (open circles) falls within the $Q = 10$ range as expected.

both Cooper *et. al.*[13] and Arima *et. al.*[96], and now the rare-earth substituted $Pb_2Sr_2RCu_3O_8$ series) there is indeed an inverse scaling of the charge transfer gap with the in-plane Cu-O distance.

The sensitivity of the charge transfer gap in the cuprates to both the in-plane Cu-O distance, d, and to the electronic coordination of Cu, reflects the importance of Madelung-type interactions associated with the Cu-O planes and suggests that such energies dominate bandwidth effects which, as a result of the increasing hybridization of the Cu3(d) and O2(p) bands as the lattice contracts, are expected to decrease Δ_{CT} in proportion to the increasing band width.[13]

5.3 *ab*-plane Optical Properties in the Far Infrared

We now turn to the low frequency region of the spectrum. Figure 5.13 shows the far infrared reflectivity at room temperature (300 K) and near liquid nitrogen temperature (80 K) for the three representative members of the $Pb_2Sr_2RCu_3O_8$ series. For

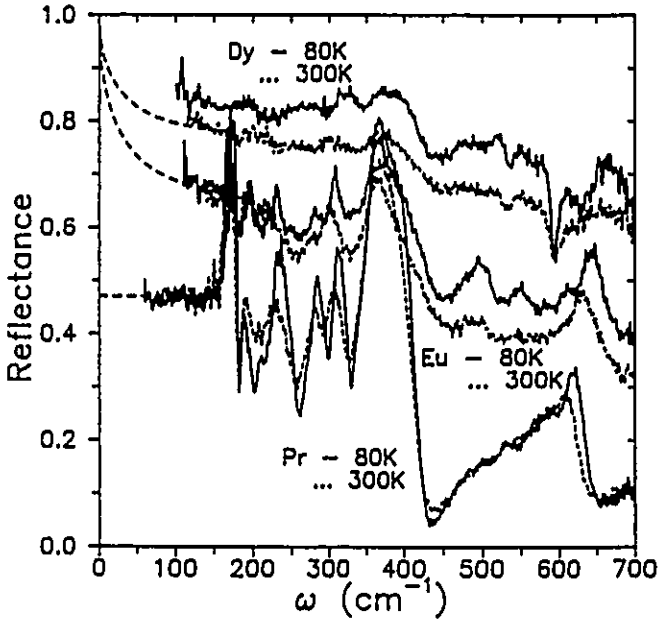

Figure 5.13: Far infrared *ab*-plane reflectivity of representative members of the $Pb_2Sr_2RCu_3O_8$ series at 300 and 80 K. The dashed curves at low frequency show the extrapolations used in the Kramers-Kronig analysis.

the insulating sample (Pr) the only changes occurring with decreasing temperature are a sharpening and a shift in position of the phonon features. Upon doping an overall upward shift in the magnitude of the reflectance with decreasing temperature becomes evident. With light doping (Eu) this change is restricted primarily to the high frequency end of the far infrared while further doping (Dy) leads to a higher reflectance at lower frequencies as well. This suggests that the initial shift may be a manifestation of the temperature dependence of the mid infrared band while the

changes at higher doping levels result from that of both the mid infrared continuum and the free carriers. In fact, as pointed out in the previous section the Drude contribution in these Ca-free materials is very weak and hence much of the temperature dependence observed is that of the mid infrared absorption band, the position of which, shifts to lower frequency with increased doping.

The most notable aspect of figure 5.13 is the evolution that occurs in the phonon structure between 400 and 600 cm^{-1}. In this region the spectrum of Pr is comprised simply of the essentially smoothly rising reflectance edge of the highest frequency phonon, superimposed upon which one might discern some very weak structure. Upon light doping (Eu), while the 'ordinary' phonons are less prominent, two clearly perceptible peaks develop in the region of interest. The progression continues in the spectrum for Dy where these phonons now appear as two sharp minima at 525 and 585 cm^{-1}. In addition there is a third broad minimum near 430 cm^{-1} (seen more clearly in the 80 K spectrum). These features were also observed in the Ca-doped sample examined in the previous chapter (see figure 4.4). Note as well a pronounced temperature dependence of the phonon structure between 400 and 600 cm^{-1}; the peaks in the Eu spectrum become more intense, and the antiresonance at 580 cm^{-1} in the Dy spectrum much deeper.

The curious nature of this phonon structure in comparison to that of the ordinary phonons (here 'ordinary' refers to symmetry allowed *ab*-plane infrared active modes) is more clearly put into perspective by examining the optical conductivity which is shown in figure 5.14 at room temperature for the same three materials.

The low frequency conductivity of Pr is typical of that of an insulator. It is comprised simply of a series of phonon peaks, with negligible background absorption. The conductivity of the lightly doped sample (Eu) is similar except that now these ordinary phonons are superimposed on an electronic background which is attributed mainly to the mid infrared absorption band. In addition two peaks appear between 400 and 600 cm^{-1} which are barely resolved in the conductivity spectrum of the

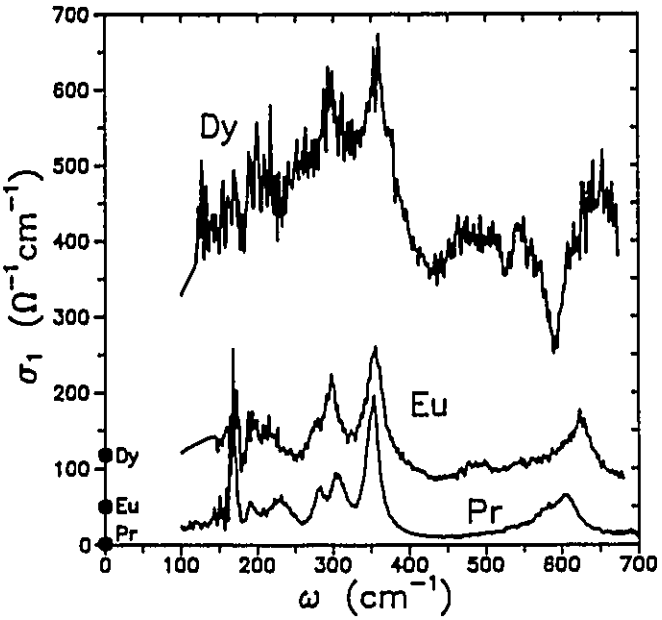

Figure 5.14: Room temperature *ab*-plane far infrared Kramers-Kronig derived optical conductivity for representative members of the $Pb_2Sr_2RCu_3O_8$ series. The dc-conductivity values are shown as the solid circles at $\omega = 0$. Note the offset of the experimental limit of the optical conductivity and the dc value.

insulator. In the spectrum for Dy the minima corresponding to these peaks develop sharply giving rise to antiresonant-like lineshapes.

The physical origin of these features will be discussed in chapter 6. What follows now is a comprehensive survey of the reflectance and conductivity of the entire series; presented in sections 5.3.1, 5.3.2, and 5.3.3 for the insulating (R ≡ La, Ce, Pr, Nd), lightly doped (Sm, Eu, Gd, Tb) and metallic (Dy, Ho, Y) members respectively.

5.3.1 Insulators (R ≡ La, Ce, Pr, Nd)

The reflectivity at 300 K and 80 K of the four insulating members of the series is shown in figure 5.15. The corresponding Kramers-Kronig derived conductivity spectra are presented in figure 5.16. The reflectance was fitted to a model dielectric function consisting of a high frequency dielectric constant, ϵ_∞, and a series of Lorentzian

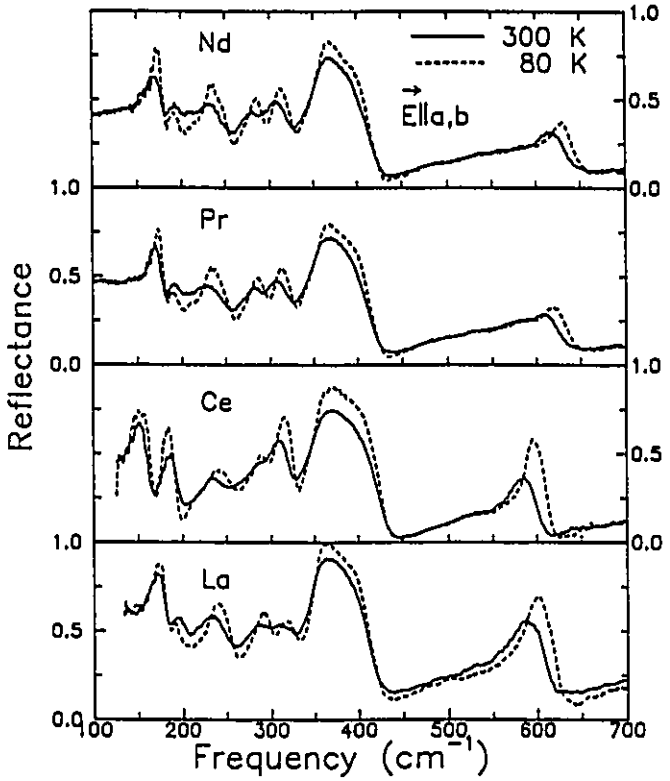

Figure 5.15: Far infrared ab-plane reflectance at 80 and 300 K for the insulating members of the $Pb_2Sr_2RCu_3O_8$ series.

oscillators to represent the phonons of the form:

$$\epsilon = \epsilon_\infty + \sum_j \frac{S_j \omega_{TO_j}^2}{\omega_{TO_j}^2 - \omega^2 - i\omega\Gamma_j}, \tag{5.4}$$

where ω_{TO_j}, S_j, and Γ_j are respectively the center position (transverse optical phonon frequency), oscillator strength and scattering rate for phonon j. A general discussion of the model dielectric function is presented in Appendix B. Note that above $S_j\omega_{TO_j}^2 = \omega_{p_j}^2$. The parameters derived from the fit are listed in tables C.1 through C.4 of appendix C. Also listed are values for the longitudinal optical phonon frequencies, ω_{LO}, which can be obtained from the fit parameters via:[97]

$$\omega_{LO_j} = [1 + \frac{S_j}{\epsilon_\infty}]^{1/2}\omega_{TO_j}. \tag{5.5}$$

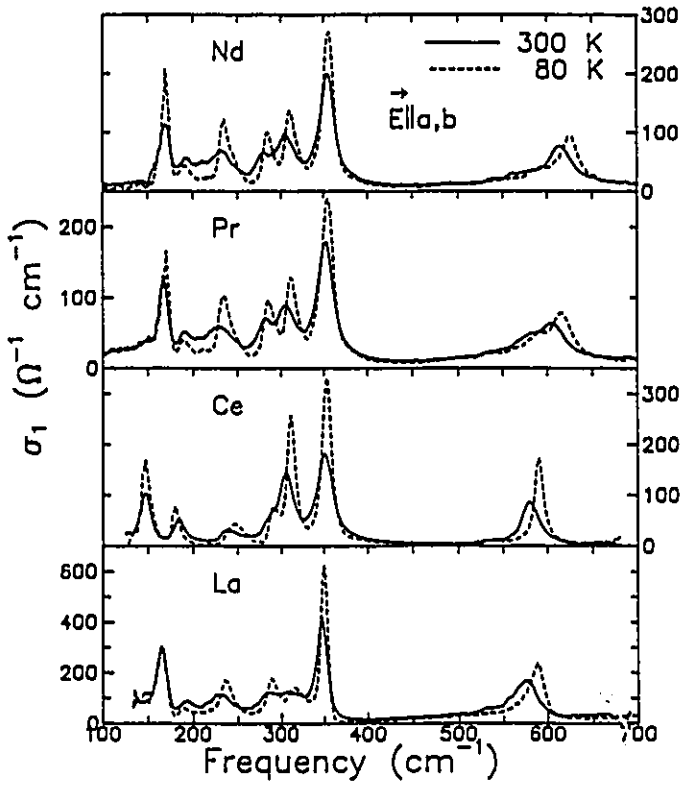

Figure 5.16: Low frequency Kramers-Kronig derived ab-plane optical conductivity at 80 and 300 K for the insulating members of the $Pb_2Sr_2RCu_3O_8$ series.

Alternatively the phonon parameters can be determined directly from the Kramers-Kronig derived optical properties. ω_{TO} and ω_{LO} are estimated from the peak positions of the real part of the optical conductivity, σ_1 (or from peaks in ϵ_2), and the dielectric loss function, $\Im(\frac{-1}{\epsilon}) = \frac{\epsilon_2}{\epsilon_1^2+\epsilon_2^2}$ (or from zeros in ϵ_1) respectively. The oscillator strength is determined from σ_1 by multiplying the full width at half maximum, Γ, by the peak height, σ_1^{max}, and dividing by $\frac{\omega_{TO}^2}{4\pi}$. That is, σ_1 is a maximum when $\omega = \omega_{TO}$. Evaluating the imaginary part of equation 5.4,

$$\sigma_1 = \frac{\omega}{4\pi}\epsilon_2 = \frac{\omega^2\Gamma S\omega_{TO}^2}{4\pi[(\omega_{TO}^2-\omega^2)^2+\omega^2\Gamma^2]}, \tag{5.6}$$

so that when $\omega = \omega_{TO}$:

$$S = \frac{4\pi\sigma_1^{max}\Gamma}{\omega_{TO}^2}, \tag{5.7}$$

where the subscript j has been omitted for convenience, and σ_1^{max}, Γ and ω_{TO} are all in cm^{-1}.

The parameters obtained in this manner are also summarized in tables C.1 through C.4 of appendix C. Upon comparison it is seen that there are differences in the parameters derived via the two methods, especially in the oscillator strengths although in most cases the value obtained from the fit is contained within the experimental uncertainty associated with the more direct analysis. This discrepancy is mainly the result of deviations from the Lorentzian lineshape used in the fit. There are also differences in the oscillator strength derived from fitting the reflectance and alternatively, the conductivity. This is because for the reflectance the fit may be optimized by *eg.* increasing the linewidth to account for the deviations from the model lineshape while for the conductivity optimization occurs by adjusting the oscillator strength. In the next two sections, due to the increasing complexity of the dielectric function resulting from the addition of terms due to the anomalous phonon structure and the development of an electronic background composed of both Drude and mid infrared carriers, the Kramers-Kronig technique will be used exclusively to extract the phonon parameters of the lightly doped and metallic samples.

5.3.2 Lightly Doped Members (R≡ Sm, Eu, Gd, Tb)

The reflectivity at 300 K and 80 K of the four lightly doped members of the series is shown in figure 5.17. The corresponding Kramers-Kronig derived conductivity spectra are presented in figure 5.18. The LO and TO phonon frequencies as extracted using the Kramers-Kronig technique described in the previous section, are summarized in tables C.5 through C.10 of appendix C. The background conductivity was too large to render accurate estimates of the phonon peak height and width at half maximum and thus only values for the relative oscillator strength:

$$\frac{S}{\epsilon_\infty} = \frac{\omega_{LO}^2}{\omega_{TO}^2} - 1, \tag{5.8}$$

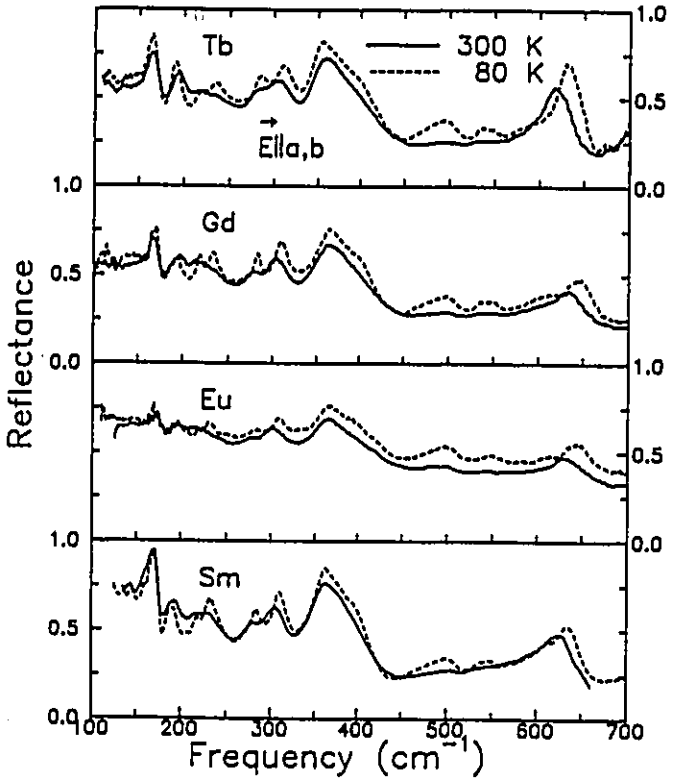

Figure 5.17: Far infrared *ab*-plane reflectance at 80 and 300 K for the lightly doped members of the $Pb_2Sr_2RCu_3O_8$ series.

are tabulated.

Included as well are parameters for the two most distinct doping induced phonon modes obtained using the same procedure. Strictly speaking this method of analysis is not applicable to these coupled phonons which arise as a result of a Fano interaction between a discrete mode and a broad electronic continuum. The distinction between these modes and the ordinary phonons will be discussed in more detail in chapter 6. We thus apply the method as a means of parameterizing the data with the understanding that the values of S/ϵ_∞ are not to be interpreted as the oscillator strength of the mode in the usual sense, but rather as an indication of the strength of the coupling.

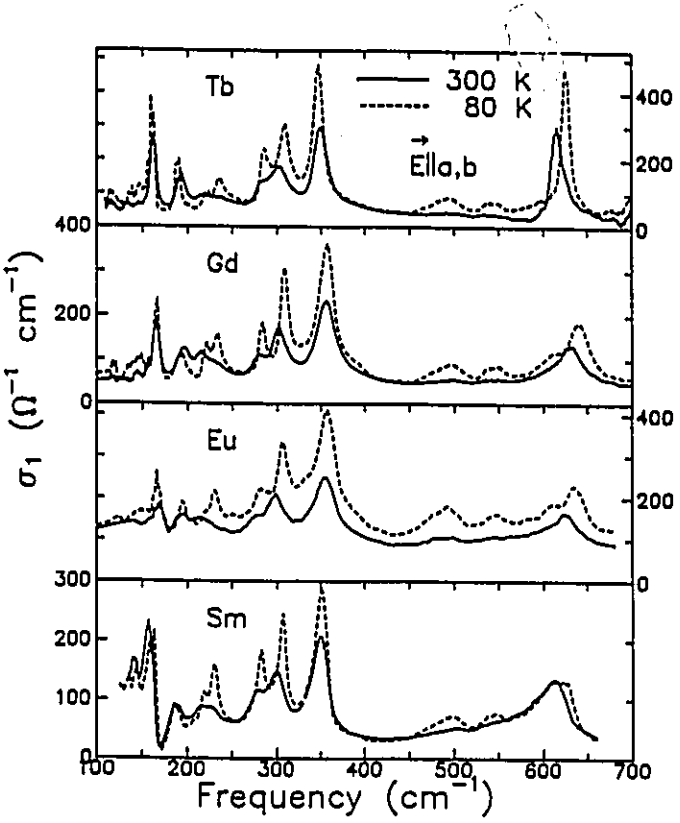

Figure 5.18: Low frequency Kramers Kronig derived *ab*-plane optical conductivity at 80 and 300 K for the lightly doped members of the $Pb_2Sr_2RCu_3O_8$ series

5.3.3 Poor Metals (R≡ Dy, Y, Ho)

The reflectivity at 300 K and at 80 K of the three more metallic members of the series is shown in figure 5.19. The corresponding Kramers-Kronig derived conductivity spectra are presented in figure 5.20. The phonons are now much smaller features in the reflectivity. This does not imply that they are becoming screened by the growing electronic background. As can be seen in the optical conductivity the phonon peaks near 650, 350 and 300 cm^{-1} have essentially the same spectral weight (that is, they take up the same area under the conductivity curve – see figure 5.14) as they did in the insulating and lightly doped samples.

The lower frequency phonons are for the most part unresolved. This once

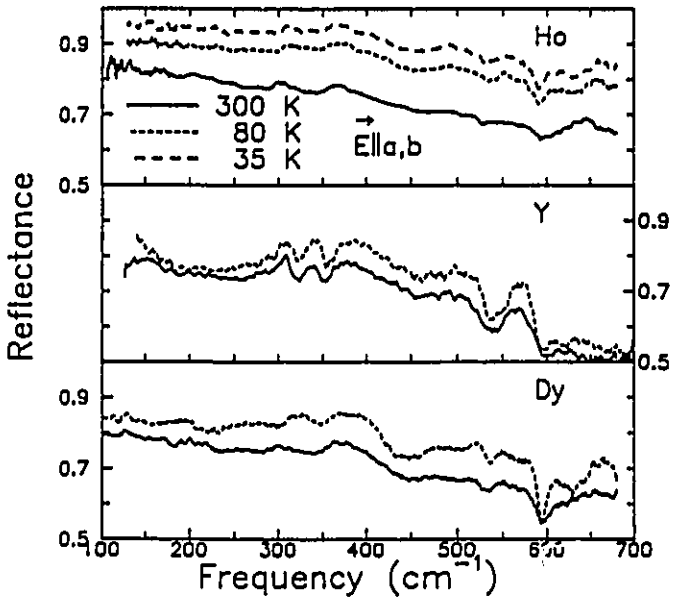

Figure 5.19: Far infrared *ab*-plane reflectance at 80 and 300 K for the more metallic members of the $Pb_2Sr_2RCu_3O_8$ series. The 35 K superconducting state result is shown for Ho as well.

again does not imply screening. The reflectance is much more susceptible to noise at lower frequencies which results in a loss in the ability to resolve the small features due to the phonons. Thus, in tables C.11–C.13 of appendix C which summarize the phonon parameters for the more metallic samples, it was only possible to determine the LO and TO frequencies and hence the relative oscillator strengths for the highest frequency modes. Also, since the 'coupled' modes now appear as minima in both the reflectance and the conductivity it is not clear how to estimate their effective oscillator strength using the method invoked in the previous section.

Note that for R≡Ho the 35 K result shows a condensation of the superconducting carriers and evidence for the development of the low frequency conductivity peak discussed in the previous chapter.

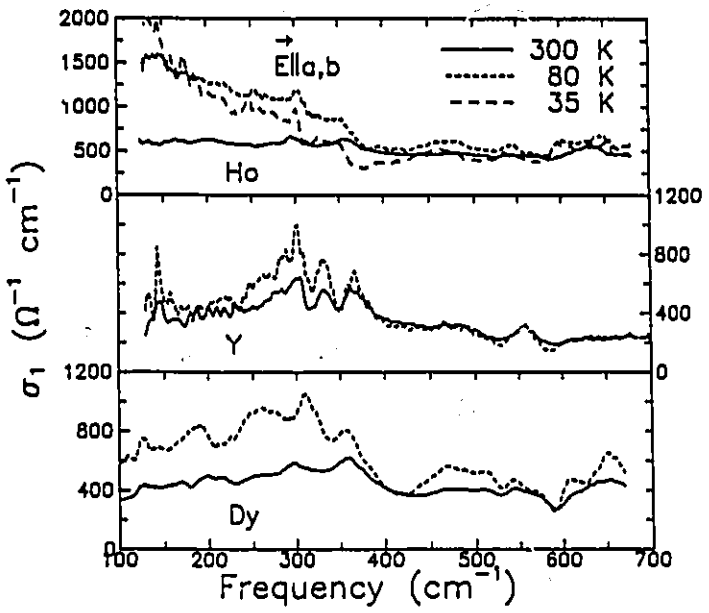

Figure 5.20: Low frequency Kramers Kronig derived *ab*-plane optical conductivity at 80 and 300 K for the more metallic members of the $Pb_2Sr_2RCu_3O_8$ series. The 35 K superconducting state result is shown for Ho as well.

5.4 Dependence of Phonon Parameters on Temperature, Doping, and Rare Earth Substitution

In the previous sections reflectance spectra for the various members of the Ca-free $Pb_2Sr_2RCu_3O_8$ series were presented and fitting and Kramers-Kronig techniques were subsequently used to extract phonon parameters. In this section the dependence of these parameters on temperature, level of doping, and rare earth substitution is examined.

5.4.1 Dependence on the Rare Earth Ionic Radius

Figures 5.21(a) and (b) show the dependence of the TO frequencies of the symmetry-allowed phonon modes (determined via KK analysis) on the six-coordinated, 3^+ ionic radius of the rare earth at 300 and 80 K respectively. In a simple model where neutral atoms are vibrating in a periodic harmonic potential the phonon frequency depends on the lattice constant, a, as $\omega_{TO} \propto a^{-3/2}$. Since the scatter in the data of figures 5.21(a) and (b) is too large to determine a power law dependence, the trend is simply parameterized in each case with a linear fit. The slopes of the best fit lines

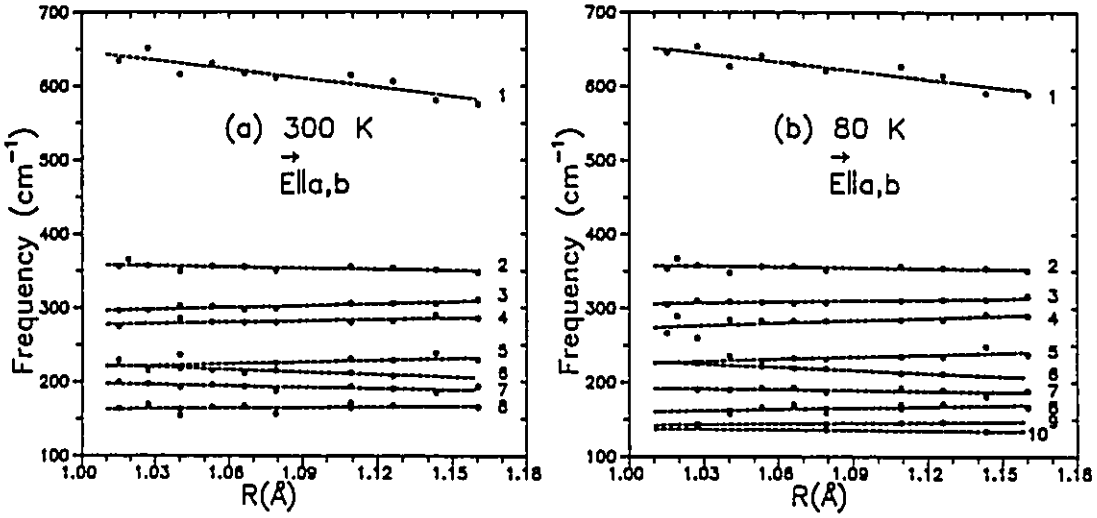

Figure 5.21: Dependence of the Kramers-Kronig derived *ab*-plane TO frequencies of the allowed phonon modes on the ionic radius of the rare earth at (a) 300 and (b) 80 K.

are summarized in table 5.1. The shifts are generally relatively small, of the order $\pm 50 - 80$ cm^{-1}/Å or roughly 10 cm^{-1} from one end of the series to the other with some phonons showing an increase and others a decrease. The exception is the highest frequency phonon (mode 1^{ab}) which shows a large shift of approximately 50-75 cm^{-1} in progressing from La to Ho. This has also been observed for the highest frequency mode of the rare-earth substituted $La_{2-x}Sr_xCuO_{4-\delta}$ series studied by Tajima *et. al.*

who argue that it is related to the shift of the charge transfer gap energy to higher frequency with decreasing ionic radius.[98]

Table 5.1: Least squares fitted slopes corresponding to the dependence of the ab-plane phonon frequencies on rare-earth ionic radius at 300 and 80 K in $cm^{-1}/Å$.

Mode	80 K	300 K
1^{ab}	-385	-409
2^{ab}	-35	-54
3^{ab}	49	85
4^{ab}	30	60
5^{ab}	98	79
6^{ab}	-138	-115
7^{ab}	-36	-59
8^{ab}	62	28
9^{ab}	32	
10^{ab}	-23	

Modes 5^{ab} and 6^{ab} also exhibit larger than average shifts as the ionic radius of the rare earth varies. This suggests that these modes may also correspond to motion that is sensitive to the in-plane Cu-O distance. Note that the shifts are in opposite directions such that at small ionic radius, the two modes are indistinguishable.

The 350 cm^{-1} mode (phonon 2^{ab}) shows one of the smallest shifts. This mode is observed at essentially this same frequency in all of the cuprates, and is assigned to an in-plane bond-bending motion of O(3) and Cu(2). (See *eg.* reference [98]).

Another mode whose position is relatively independent of the size of the rare earth is that at 190 cm^{-1} (phonon 7^{ab}). This is the so-called external mode which represents translational motion of the A-site atom of the ABO_3 perovskite structural unit against the BO_2 layer. (In this case A≡Sr and B≡Cu). The position of this

mode is higher in frequency than in $La_{2-x}Sr_xCuO_{4-\delta}$[98] and $YBa_2Cu_3O_{7-\delta}$[99, 100] because Sr is much lighter than Ba and La.

The mode near 170 cm^{-1} (phonon 8^{ab}) is assigned to motion of the rare earth by comparison to $RBa_2Cu_3O_7$ where the corresponding mode is located near this frequency. In $RBa_2Cu_3O_7$ the assignment is made based on the large shift observed when much lighter Y is substituted for a lanthanide.[100] Unfortunately as discussed above due to the more metallic nature of the Y substituted $Pb_2Sr_2RCu_3O_8$ sample the low frequency modes cannot be unambiguously resolved. This, however is not the case along the c-axis as shall be seen in section 5.5.

5.4.2 Dependence on Temperature

In general as the temperature is lowered the lattice becomes stiffer (increased k, where k is the spring constant) and hence the phonons are expected to increase in frequency (harden) since $\omega = \sqrt{k/m}$. It is clear upon examination of tables C.1–C.13 that this is true for all of the allowed TO modes except number 7^{ab} which has been assigned to the external mode which softens in every case and possibly number 8^{ab} which shows a small softening (≈ 1 cm^{-1}) in a few cases. The Tb spectra show softening of some of the other modes. The reason for this is unclear although as discussed previously Tb in general appears to exhibit somewhat anomalous behaviour.

A detailed temperature dependence has been carried out for Sm and Eu. The reflectance and the corresponding Kramers-Kronig derived conductivity was shown at 300 and 80 K in figures 5.17 and 5.18 respectively. The discussion will concentrate on the Sm sample since the electronic background is smallest, and hence the phonons are best resolved. In all cases, however the same trends were observed for the Eu sample. Originally the idea was to compare these two samples because they lie on opposite sides of the superconductor/non-superconductor transition, however it turns out that the effect of the superconductivity on the optical spectra is too weak to observe in these Ca-free samples, except for the most metallic Ho sample (as shown

in figure 5.20) and thus no superconductivity induced differences were detected in the electronic background or in the temperature dependence of the phonon frequencies and linewidths. This point is interesting. It is surprising that the dc resistivity can fall orders of magnitude at T_c with no effect on the optical properties above 120 cm^{-1}. It may be of interest to extend the measurements to lower frequency.

Figure 5.22 illustrates the procedure used to extract the TO and LO phonon frequencies. The curves shown are for Sm. The solid curves represent the real part of

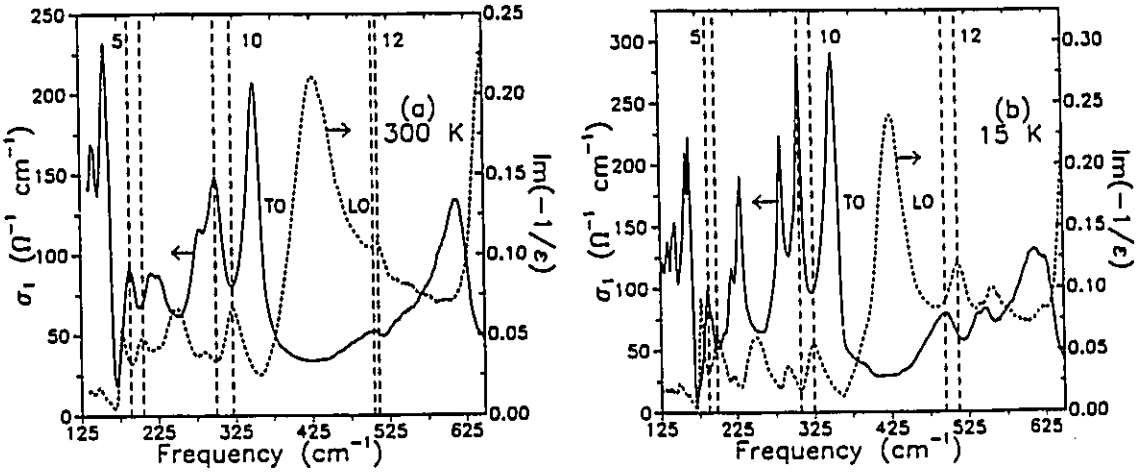

Figure 5.22: Procedure used to extract the LO and TO phonon frequencies. The solid curves represent the real part of the *ab*-plane optical conductivity while the dashed curves are the corresponding dielectric loss function, the peaks of which respectively estimate the TO and LO phonon frequencies. The vertical lines show the LO-TO splitting for three representative modes. The temperature dependence of the LO-TO splitting for the 'ordinary' (*eg.* 5 and 10) and 'coupled' modes (*eg.* 12) is illustrated by comparing the 300 and 15 K spectra [(a) and (b) respectively].

the optical conductivity while the dashed curves are the dielectric loss function. The TO frequencies are given by the peaks in σ_1 while the LO frequencies are determined from peaks in the loss function. The vertical lines are drawn at the TO and LO frequencies and the distance between represents the LO-TO splitting. Note that for

the two representative ordinary modes (5 and 10), the LO-TO splitting decreases as the temperature is lowered from 300 to 15 K while for the coupled mode (12) there is a significant increase.

Figure 5.23 shows for Sm the temperature dependence of selected allowed modes, including 7^{ab}. Note that in all cases the TO frequencies seem to saturate below approximately 100 K. Of interest is the temperature dependence of the LO-TO splitting. From equation 5.8 it is seen that as the LO frequency approaches the TO frequency, that is the LO-TO splitting approaches zero, that the oscillator strength of the mode goes to zero. This is the condition under which there is screening. Note that modes 7^{ab}, 3^{ab} and 5^{ab} show a decrease of the LO-TO splitting as the temperature is lowered. This may be an indication of some temperature dependent screening. Note that the opposite is true for mode 4^{ab}. That is, the LO-TO splitting increases as the temperature is lowered. Of the ordinary modes this is the only one that shows an increase in oscillator strength as the temperature is lowered.

Next the behaviour of the ordinary phonons is compared with that of the coupled modes. From figure 5.22 one finds that in contrast to the ordinary modes which (with the exception of 4^{ab}) show a decrease in LO-TO splitting as the temperature is lowered, the coupled modes show a large increase in splitting between 300 and 15 K. The detailed temperature dependence of the LO-TO splitting is shown in figure 5.24 while the derived dependence of the relative oscillator strength on temperature is shown in figure 5.25 compared to that for several of the symmetry allowed modes. The large increase in the strength of these coupled modes as the temperature is lowered indicates that there is a strong temperature dependence to the coupling mechanism because as discussed in section 5.5, the c-axis modes which are shown in chapter 6 to be responsible, show the usual decrease in S/ϵ_∞ with decreasing temperature.

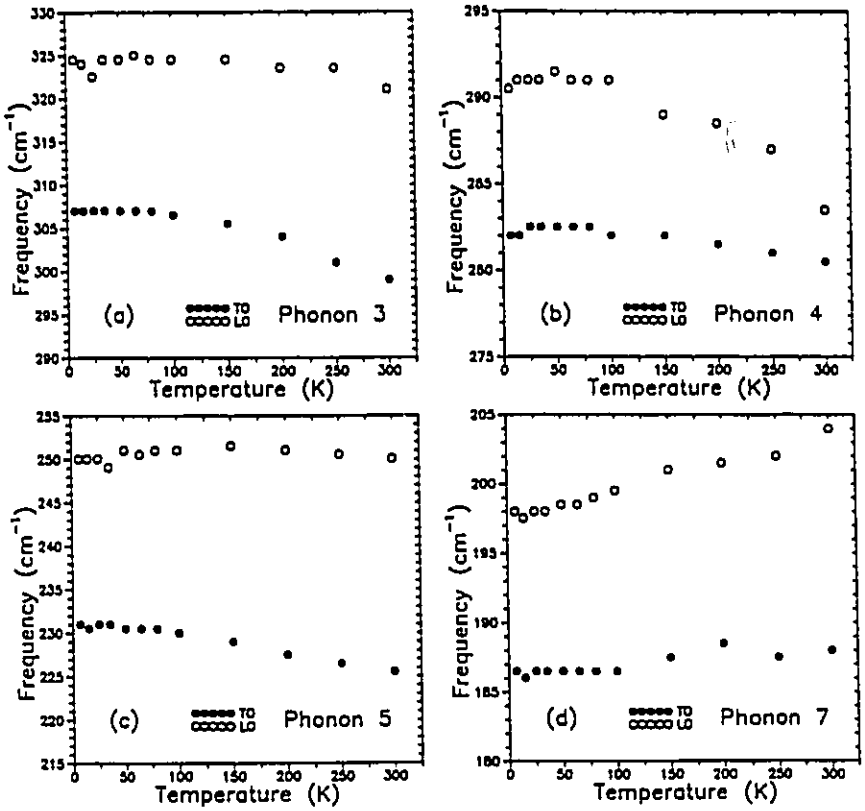

Figure 5.23: Temperature dependence of ω_{TO} and ω_{LO} for selected symmetry-allowed *ab*-plane phonon modes for R ≡ Sm.

5.4.3 Doping Dependence

Perhaps of most interest is the doping dependence of the phonon parameters. In figures 5.26(a) and (b) the dependence of the relative oscillator strength on the level of doping is inferred. For the ordinary modes, (a), the oscillator strength is finite and shows little change between insulating and lightly doped materials, while for the coupled modes, (b), the oscillator strength is essentially zero for the insulators, becoming finite only upon doping. The strong increase of the oscillator strength of the forbidden modes upon doping is understandable because they arise via an interaction with the mid infrared carriers, the density of which also increases with doping (see

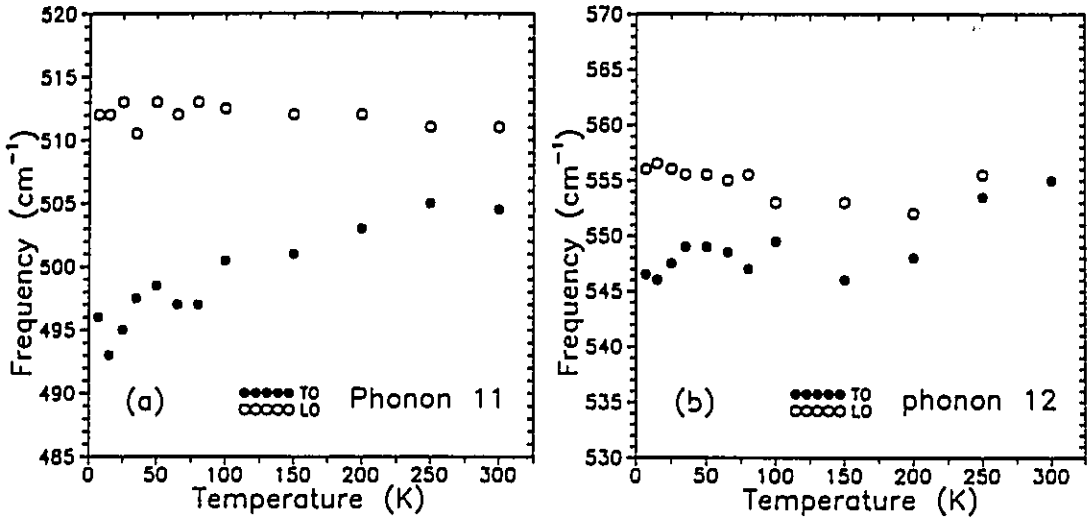

Figure 5.24: Temperature dependence of the LO-TO splitting for the two distinct coupled modes in Sm.

figure 5.9).

Unfortunately, due to the difficulty in extracting the phonon parameters of the more metallic samples as discussed in section 5.3.3 these have not been included. One is also reminded that since the forbidden modes arise via a coupling mechanism (to be discussed in chapter 6) that the method of analysis used to extract S/ϵ_∞ is strictly speaking not applicable. It does, however seem to be a reasonable way to parameterize the data. S/ϵ_∞ is interpreted as a measure of the strength of the coupling in this case.

5.5 Optical properties along the *c*-axis

In this section the *c*-axis optical properties of the $Pb_2Sr_2RCu_3O_8$ series with R $\equiv$ Nd, (an insulator in the *ab*-plane), Sm, Eu, and Gd (lightly doped in the *ab*-plane) and Dy (metallic for E$\|ab$) are examined.

Crystals with a *c*-axis dimension of approximately 0.2 to 0.5 mm were mechanically polished to yield an optical quality *ac*-face. The dimensions of the optical

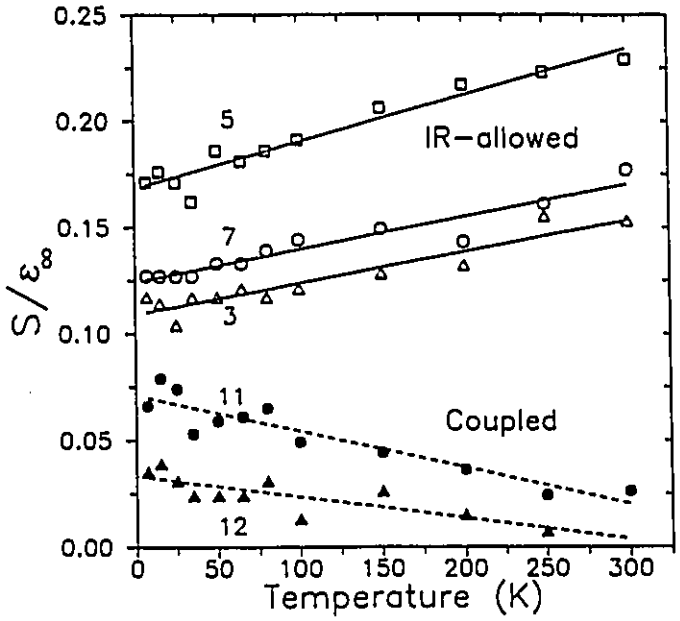

Figure 5.25: Temperature dependence of the relative oscillator strength for selected ordinary modes (open symbols) compared to that of the two distinct coupled modes (solid symbols) for Sm. Mode 4^{ab} (not shown) is the only symmetry allowed mode exhibiting an increase in oscillator strength with decreasing temperature.

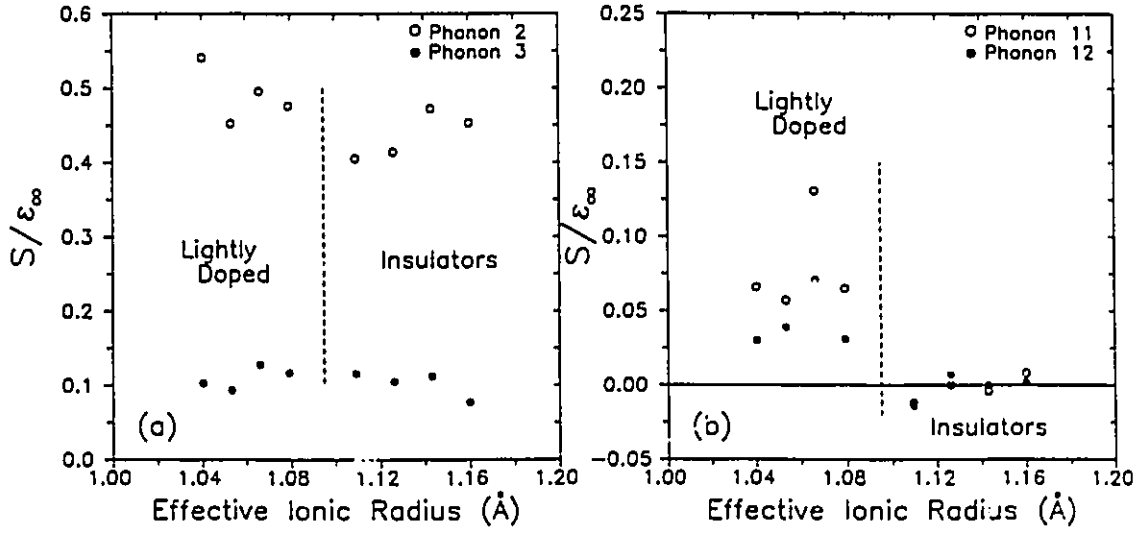

Figure 5.26: Doping dependence of the relative oscillator strength for selected (a) symmetry allowed and (b) forbidden coupled modes.

surface were large enough to allow measurement of individual crystals in contrast to the mosaic of crystals required for the Ca-doped compound discussed in chapter 4. As in the measurement of the mosaic of chapter 4 the *c*-axis was mounted along the direction of preferred polarization of the spectrometer. An appropriate polarizer (determined by whether the far or mid infrared range was being measured) was placed at the intermediate focus of the spectrometer, and the correct polarizer position was determined by measuring the ratio of the chopped signal from the sample to that of the reference as a function of polarizer angle. (For details see the discussion in chapter 4).

Figure 5.27 shows the E$\|c$ reflectivity at 80 and 300 K for the five members of the series investigated, while figure 5.28 gives the corresponding Kramers-Kronig derived optical conductivity. Insulator-like optical properties appear to prevail in all

Table 5.2: Least squares fitted slopes corresponding to the dependence of the *c*-axis phonon frequencies on rare-earth ionic radius at 300 and 80 K in $cm^{-1}/Å$.

Mode	80 K	300 K
1^c	16	-23
2^c	79	122
3^c	125	120
4^c	158	111
5^c	48	25
6^c	4	-32

cases. The phonon parameters extracted via oscillator fitting and the Kramers-Kronig technique are summarized in tables C.14 through C.18 of appendix C. The oscillator strengths show no strong temperature or doping dependences. The dependence of the phonon frequencies on ionic radius of the rare-earth is shown in figures 5.29 (a) and (b) for 300 and 80 K respectively. The slopes of best-fit lines are summarized in table

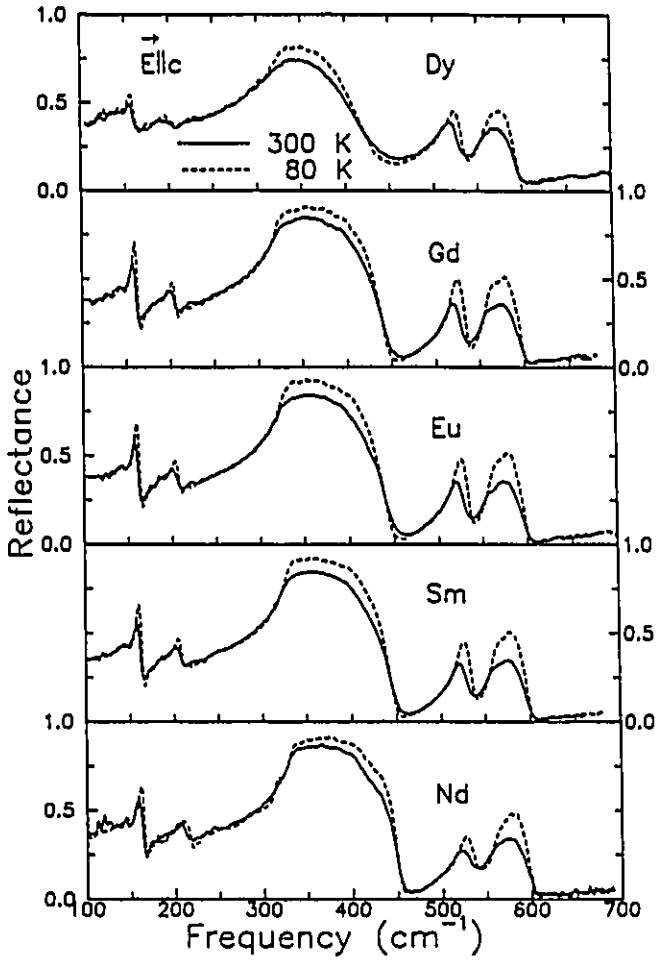

Figure 5.27: Polarized reflectance at 80 and 300 K for various members of the $Pb_2Sr_2RCu_3O_8$ series measured with E$\|c$.

5.2. Phonons 2^c, 3^c and 4^c show a systematic decrease in frequency with decreasing ionic radius. All of the c-axis phonons show the expected hardening with decreasing temperature.

Of greater interest is the dependence on doping of the c-axis properties. Figures 5.30 (a) and (b) summarize respectively the evolution with doping of the reflectance and optical conductivity at 300 K. Eu is used to represent the lightly doped members. The result for the Ca-doped, 'better metal' of chapter 4 is included for further comparison. As expected from the resistivity measurements of figure 5.2

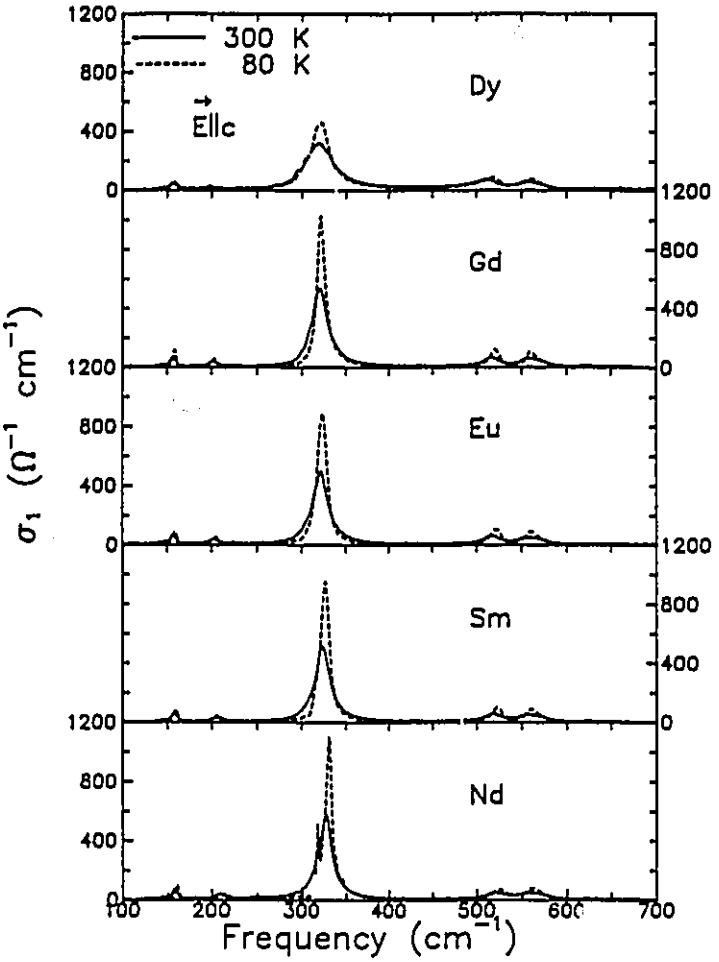

Figure 5.28: Kramers Kronig derived real part of the optical conductivity for members of the $Pb_2Sr_2RCu_3O_8$ series along the *c*-axis at 300 and 80 K.

there is a clear progression in the optical properties along the *c*-axis as well.

A small background conductivity begins to develop with doping, which for example, can be modeled for Dy at 300 K by a Drude component with a plasma frequency of 1370 cm^{-1} and a large scattering rate of 2840 cm^{-1}. There are also some changes in the phonon spectrum, in particular the two phonons near 300 and 500 cm^{-1} show a systematic evolution with doping. As discussed in chapter 4 the 500 cm^{-1} phonon develops a strongly temperature-dependent asymmetric Fano-like lineshape with the increased carrier density of the Ca-doped sample. It is clear that

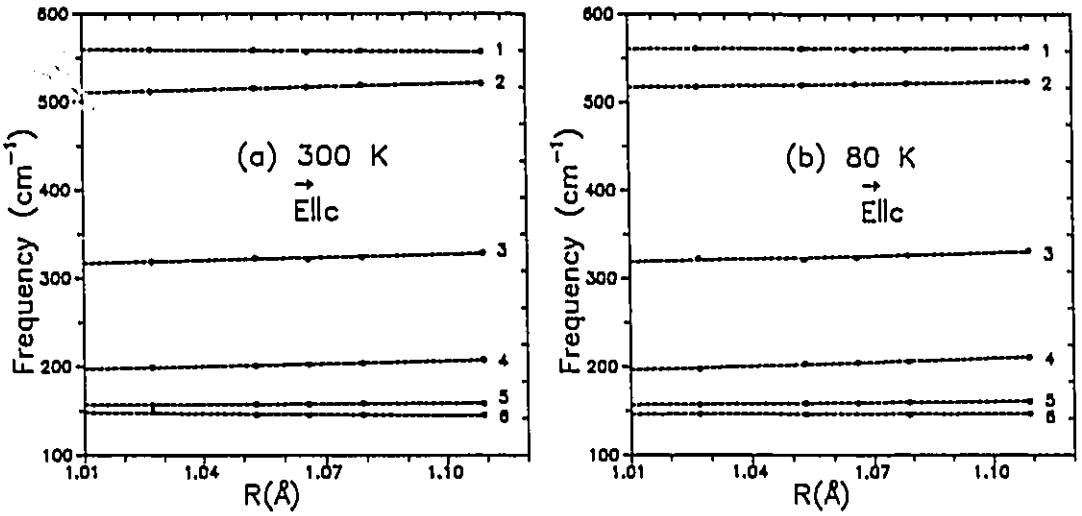

Figure 5.29: Dependence of the c-axis phonon frequencies of the $Pb_2Sr_2RCu_3O_8$ series on the ionic radius of the rare earth at (a) 300 and (b) 80 K.

this phonon is very sensitive to the electronic structure of the CuO_2 planes.

5.6 Phonon Assignments

In this final section discussing the infrared properties of the $Pb_2Sr_2RCu_3O_8$ series an attempt is made to assign the phonon modes to vibrations of specific atoms. Thomsen *et. al.* have carried out a group-theoretical symmetry analysis of the phonon modes of $Pb_2Sr_2(Y/Ca)Cu_3O_8$ based on a space group of Cmmm.[101] Table 5.3 reproduced from reference [101] summarizes the modes of the primitive cell and their expected optical activities. Of course for any given vibration it is not only these atoms that are in motion. There are in principle a total of 26 expected infrared active modes. The orthorhombic distortion is however small and hence the x and y modes (a and b) should be virtually identical with perhaps a small observable splitting in some cases. Thus only 17 modes, 9 polarized in the ab-plane and 8 along the c-axis (z) are expected. Because Thomsen *et. al.* studied a polycrystalline sample they were unable to distinguish c-axis from ab-plane polarized modes. In the present work,

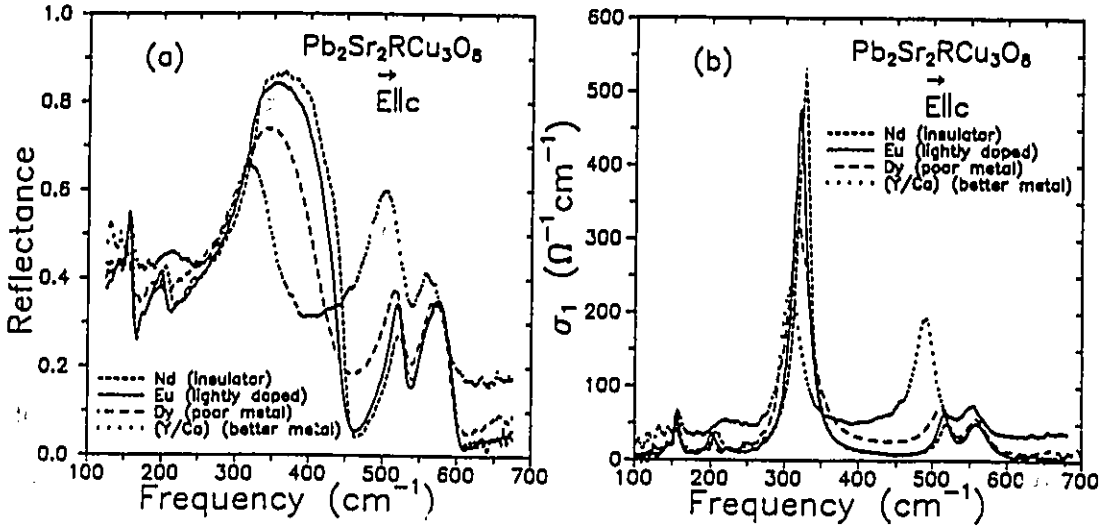

Figure 5.30: Evolution of the E$\|$ c (a) reflectance and (b) conductivity with doping. As indicated by the legend, for E$\|$ ab, Nd is an insulator, Eu is lightly doped, Dy is a poor metal while the Ca-doped Y sample is a better metal.

the phonon frequencies agree well with those of Thomsen *et. al.*, however since polarized measurements of single crystal samples were carried out it is now possible to distinguish the *ab*-plane from the *c*-axis modes and thus make more reliable phonon assignments. In reference [101] modes which are found in the present work to be *c*-axis polarized have been assigned to in-plane motions and *vice versa*.

From the tables in appendix C, 10 ordinary *ab*-plane polarized modes and 7 *c*-axis modes can be identified. Thus there appears to be one additional in-plane mode and one missing *c*-axis mode. Mode 6^{ab} near 210 cm^{-1} is very weak and may be a mode associated with a lower symmetry group since crystallographically deviations from Cmmm have been found.[21] Small structure which may be the missing mode along the *c*-axis is observed near 230 cm^{-1} in some spectra (*eg.* Dy).

Table 5.3: Group-theoretical symmetry analysis of the phonon modes of $Pb_2Sr_2(Y/Ca)Cu_3O_8$ based on Cmmm after Thomsen *et. al.*. 'IR_i' indicates that the mode is infrared active for E polarized along the i axis. 'α_{ij}' indicates Raman activity for the incident and scattered light polarized along the i and j axes respectively. 'S' indicates the silent mode.

Atom	Site Symmetry	Modes	Expected Activity
R, Cu(1)	mmm	B_{1u}, B_{2u}, B_{3u}	IR_z, IR_y, IR_x
Pb, Sr, Cu(2)	mm2	A_g, B_{2g}, B_{3g}	$\alpha_{xx,yy,zz}$, α_{xz}, α_{yz}
O(2), O(1)		B_{1u}, B_{2u}, B_{3u}	IR_z, IR_y, IR_x
O(3)	2	A_g, B_{1g}, $2B_{2g}$, $2B_{3g}$	$\alpha_{xx,yy,zz}$, α_{xy}, α_{xz}, α_{yz}
		A_u, B_{1u}, $2B_{2u}$, $2B_{3u}$	IR_z, S, IR_y, IR_x

5.6.1 *ab*-plane Assignments

The assignment of the *ab*-plane polarized modes will be addressed first. In section 5.4.2 modes 1^{ab} and 2^{ab} have already been assigned to the in-plane bond stretching and bending motions respectively of O(3) and Cu(2) and can thus in terms of table 5.3 be associated with the motion of O(3). Also, mode 7^{ab} has been assigned to in-plane motion of Sr while mode 8^{ab} has been associated with the rare-earth 'R' atom.

Yet unassigned are the modes associated with the motion of the apical oxygen O(1) and with the oxygen in the PbO layers, O(2). Since oxygen is the lightest atom in the compound its vibrations are expected to have the highest frequencies since $\omega \propto m^{-1/2}$ and thus modes 3^{ab} and 4^{ab} are assigned to these two motions. The bending mode associated with the apical oxygen, O(1), is believed to be the 'missing' mode in $YBa_2Cu_3O_{7-\delta}$. That is, in this compound 6 modes are expected but only five are usually observed.[99, 100] In photoinduced absorption experiments however, Ye and McCall *et. al.* have found a shoulder at 320 cm^{-1} which they assign to this

motion.[95] Since Sr is lighter than Pb the mode associated with motion of the O(1) atoms might be expected to be at a higher frequency than that corresponding to the O(2) atoms and hence modes 3^{ab} and 4^{ab} are assigned to O(1) and O(2) respectively.

The lowest frequency mode, 10^{ab}, is assigned to motion of the heaviest atoms; Pb. This leaves only assignment of the motions of the Cu(1) and Cu(2) atoms to modes 9^{ab} and 5^{ab}. The difference in the frequencies of these modes must arise from variation in the surrounding environment. The Cu(1) atoms which sit in the massive PbO-Cu-PbO block will likely correspond to the lower frequency mode, 9^{ab}, leaving 5^{ab} to correspond to Cu(2). These *ab*-plane mode assignments are summarized in table 5.4.

5.6.2 *c*-axis Assignments

Next the *c*-axis polarized modes are considered. Seven modes are clearly observed experimentally, while eight are expected. The lowest frequency mode 7^c at 100 cm^{-1}, observed only for the Ca-doped sample of chapter 4 because the minimum measured frequency was approximately 120 cm^{-1} for the Ca-free samples, is once again as a result of its heavy mass likely due to vibrations of the Pb atoms. In keeping with the assignment of the in-plane modes another low frequency mode is expected due to vertical vibrations of Cu(1). Mode 6^c at 146 cm^{-1} is assigned to this motion. Mode 5^c at 160 cm^{-1} is fairly strong and shows little shift as a result of rare-earth substitution, and hence is probably the result of motion removed from the vicinity of the rare-earth. It is thus assigned to the external mode where Sr vibrates against the internal 'cage' of the perovskite block.

Mode 4^c near 205 cm^{-1} can be confidently assigned to vertical motion of the rare earth. It shifts up in frequency by a large amount when lighter (Y/Ca) is substituted for the lanthanides (figure 5.30) and in addition becomes very broad, splitting into two peaks probably as a result of the substitutional disorder. Within the Ca-free series this mode also softens as the mass of the rare-earth increases.

Table 5.4: *ab*-plane and *c*-axis phonon assignments for $Pb_2Sr_2RCu_3O_8$.

Mode	Approximate Frequency (cm^{-1})	Assignment	Mode	Approximate Frequency (cm^{-1})	Assignment
1^{ab}	600	Cu(2)-O(3) Stretch	1^{c}	560	O(2)-Cu(1)
2^{ab}	350	Cu(2)-O(3) Bending	2^{c}	520	O(1)-Cu(2)
3^{ab}	310	O(1)	3^{c}	320	O(3)-Cu(' ' Bending
4^{ab}	280	O(2)	4^{c}	210	'R'
5^{ab}	230	Cu(2)	5^{c}	160	Sr External
6^{ab}	215		6^{c}	145	Cu(1)
7^{ab}	190	Sr External	7^{c}	100	Pb
8^{ab}	160	'R'			
9^{ab}	140	Cu(1)			
10^{ab}	132	Pb			

The three highest frequency modes are likely due to oxygen bond stretching and bending motions. As in $YBa_2Cu_3O_{7-\delta}$[99] mode 3^c near 320 cm^{-1} is assigned to a vertical Cu(2)-O(3) bond bending motion. This mode softens significantly with decreasing rare earth size (and consequently increasing rare-earth mass) within the Ca-free series. This might be interpreted as being caused by the close proximity of Cu(2) and 'R'. However, from figure 5.30 it is seen that, in contrast to mode 4^c, the frequency of this mode decreases further in the (Y/Ca) sample. The direction of this shift is opposite to what is expected as a result of the mass difference. This suggests that as the level of doping in the CuO_2 planes increases there is a reduction in the force constant associated with this vibration due to some screening of the ionic character of the bonds. The mode near 520 cm^{-1} (mode 2^c) shows an even more dramatic doping-induced softening, shifting down by close to 25 cm^{-1} in going from Dy to (Y/Ca). Since this mode is thus also very sensitive to the level of doping it is assigned to vibrations of O(1), the apical oxygen atom located just above the CuO_2 planes.

This leaves the highest frequency mode near 560 cm^{-1}, phonon 1^c, the frequency of which is essentially independent of rare-earth substitution or level of doping, to be associated with vibrations of O(2) within the O(2)-Cu(1)-O(2) 'stick' environment. In $YBa_2Cu_3O_7$, when Cu(1) is four-coordinated to oxygen ('sticks' and 'chains') this mode occurs near 560 cm^{-1}[87] while in $YBa_2Cu_3O_6$ when Cu(1) is two-coordinated to oxygen ('sticks' only) the mode is observed at 645 cm^{-1}.[99] At intermediate oxygen concentrations both modes are observed.[102] The Cu(1)-O distance is very different for these two cases; $\approx 1.94\AA$ and $\approx 1.81\AA$ for the four- and two-coordinated environments respectively.[103] The larger bond distance can be associated with a smaller force constant and hence a lower frequency vibration. In $Pb_2Sr_2RCu_3O_8$ an intermediate bond length of $\approx 1.88\AA$[21] and the fact that the oxygen atoms associated with the 'sticks' are located in a PbO layer rather than a BaO layer as in $YBa_2Cu_3O_{7-\delta}$ suggests intermediate k, but larger reduced mass

bringing the frequency down to 560 cm^{-1} from 645cm^{-1}. The fact that in all cases no evidence for another mode is observed suggests that the Cu(1) layer in these $Pb_2Sr_2RCu_3O_8$ crystals is truly oxygen-free. The *c*-axis phonon assignments are also summarized in table 5.4. The mode assignments of table 5.4, which in some cases may seem rather arbitrary, have been inferred based on the available information. Further work involving substitutions for other atoms in the structure of $Pb_2Sr_2RCu_3O_8$ will be required in order to make more definite assignments.

Chapter 6

Electron-Phonon Coupling in $Pb_2Sr_2RCu_3O_8$ and Other High-T_c Superconductors

In this chapter, evidence that strong absorption structure observed in the optical conductivity of $Pb_2Sr_2RCu_3O_8$ and other high T_c superconductors is due to coupling of the *ab*-plane mid infrared carriers to longitudinal *c*-axis phonons will be presented.

6.1 Introduction

The non-Drude response of the high temperature superconductors to electromagnetic radiation has been well established in the literature.[62, 80, 104, 105] The optical conductivity has been described by both one and two component approaches. In the one component model the non-Drude behaviour is accounted for by a frequency dependent scattering rate. In the two component picture, which is used exclusively herein, the conductivity is divided into two channels; (1) that of the free-electrons which condense into a delta function in the superconducting state and track the dc-resistivity with a constant plasma frequency and a linearly decreasing scattering rate

in the normal state, and (2) that of the so-called mid infrared carriers which gives rise to a broad absorption extending from low frequencies into the mid infrared region of the spectrum. Both channels are invoked via doping and absent in the insulating parent compound, although as seen in the previous chapter it appears that the mid infrared band grows more rapidly than the Drude component at lower doping levels.

One of the manifestations of this non-Drude response is the 'knee' that develops in the superconducting state reflectance of $YBa_2Cu_3O_{7-\delta}$ near 400 cm^{-1} which leads to a strong 'notch'-like absorption feature in the optical conductivity.[49] This structure has been the focus of much discussion. It has been attributed to the superconducting gap[106] and alternatively to structure in the mid infrared absorption band caused by phonons.[107] The former explanation can be virtually ruled out for several reasons: (1) It has been found that this feature does not shift as the level of doping, and hence T_c, decreases.[108] If it were related to the superconducting energy gap its position should scale with T_c. (2) Although this feature becomes stronger as the temperature is lowered its position does not shift.[49] (3) By subtracting the free carrier component it has been shown that this structure is present in the normal state as well.[49] If it were due to the superconducting energy gap its position should scale with the temperature dependence of the gap parameter and it should disappear above T_c. In spite of these well documented observations there remain those who are unconvinced of its unrelated nature.

It has become clear that $YBa_2Cu_3O_{7-\delta}$ is not the only cuprate superconductor to exhibit such structure. $Bi_2Sr_2CaCu_2O_8$,[64] $Tl_2Ba_2Ca_{n-1}Cu_nO_{2n+4}$,[45, 109] $Pb_2Sr_2(Y/Ca)Cu_3O_8$, $La_{2-x}Sr_xCuO_{4-\delta}$,[110] and $Nd_{2-x}Ce_xCuO_{4-\delta}$[111] all show strong absorption features in the optical conductivity, as does non-superconducting $La_{2-x}Sr_xNiO_{4-\delta}$,[112] a material which is isostructural to $La_{2-x}Sr_xCuO_{4-\delta}$. In each case the structure appears as a minimum in $\sigma_1(\omega)$. There are however significant material to material differences in the number, magnitude, width and position of the minima. For example, the spectrum of $YBa_2Cu_3O_{7-\delta}$ is dominated by this one broad

feature near 420 cm^{-1} (Fig. 6.8b), that of $Tl_2Ba_2CaCu_2O_8$ shows two very deep minima at 350 and 600 cm^{-1} (Fig. 6.9b), while that of $Pb_2Sr_2(Y/Ca)Cu_3O_8$ exhibits two closely spaced sharp minima at 525 and 585 cm^{-1} and a third somewhat broader absorption centered near 430 cm^{-1} (Fig. 6.8a). In addition most systems show an almost gap-like suppression of the mid infrared absorption at low frequencies.

The relative independence of the position of this structure to both temperature and level of doping suggests that it is due to phonons.[107] It was shown by Fano[113] that a sharp level interacting with an electronic continuum gives rise to a minimum in the continuum conductivity (a 'Fano' resonance) if the external field does not interact with the sharp transition. Adapting a model put forth by Rice[114] for organic conductors, Timusk and Tanner[107] modeled the notch-like minimum in the conductivity of $YBa_2Cu_3O_{7-\delta}$ by linearly coupling a phonon to a broad absorption band. The application of this model to the $Pb_2Sr_2RCu_3O_8$ series is presented next.

6.1.1 Coupled Oscillator Model

In reference [107] it was proposed that the 420 cm^{-1} notch in the conductivity of $YBa_2Cu_3O_{7-\delta}$ could be explained by coupling of phonons to the mid infrared electronic continuum. This model, where a phonon is linearly coupled to a broad absorption band, can also account for the evolution of the phonon structure between 400 and 600 cm^{-1} that accompanies the progression from insulating to metallic and superconducting behaviour in the $Pb_2Sr_2RCu_3O_8$ series.

Based on the formalism developed by Rice for organic conductors the generalized dielectric function describing this model is given by:

$$\epsilon = \epsilon_\infty + \left[1 - \frac{\omega_{p_D}^2}{\omega^2 + i\omega\Gamma_D}\right] + \sum_j \frac{\omega_{p_j}^2}{\omega_j^2 - \omega^2 - i\omega\Gamma_j} + \frac{\omega_{p_e}^2}{\omega_e^2 - \sum_k D_k - \omega^2 - i\omega\Gamma_e}\left[1 + \sum_k q_k D_k\right], \quad (6.1)$$

where

$$D_k = \frac{\omega_{p_k}^4}{\omega_k^2 - \omega^2 - i\omega\Gamma_k}. \tag{6.2}$$

Here the first term is the high frequency dielectric constant, and represents the contribution from bound charges beyond the experimental spectral range. The second term is the free electron contribution (with plasma frequency ω_{p_D} and scattering rate Γ_D), the third, a series of j ordinary infrared active phonons (represented by classical Lorentzian oscillators with center frequency ω_j, oscillator strength ω_{p_j} and scattering rate Γ_j), and the fourth the coupling of phonons to an electronic band (ω_e, ω_{p_e}, Γ_e are the position, strength and width respectively, of the electronic oscillator coupled via D to k phonons of center frequency ω_k, strength ω_{p_k}, and scattering rate Γ_k). In the fourth term q_k describes direct coupling of phonon k to the electromagnetic field. The derivation of this expression for the dielectric function is presented in Appendix B.

The simple two-component version utilized by Timusk and Tanner to describe the non-Drude contribution to the optical conductivity of $YBa_2Cu_3O_{7-\delta}$ (one rather broad phonon coupled to a mid infrared absorption band – both represented by Lorentzian oscillators) demonstrated the appearance of a notch-like minimum such as that observed experimentally. In their analysis they omitted the second component of the fourth term of equation 6.1, assuming that the electronic background was high enough to screen the charge of the phonons, q. In an attempt to remove more of the model dependence, Timusk *et. al.*[115] adapted their approach by replacing the arbitrary broad phonon whose parameters arose entirely from a fit to the model, by the suitably scaled neutron phonon density of states difference curve between superconducting and non-superconducting $YBa_2Cu_3O_{7-\delta}$ in order to describe the electron-phonon coupling.

As pointed out in the previous chapter the signature of such electron-phonon coupling is directly observed in the conductivity of the $Pb_2Sr_2RCu_3O_8$ series. As a result of the intrinsically low carrier concentration of even the most highly doped

Table 6.1: Ordinary phonon parameters used to model the evolution in the optical conductivity of the $Pb_2Sr_2RCu_3O_8$ series. All values in cm^{-1}.

j	ω_j	Γ_j	ω_{p_j}
1	620	40	400
2	352	22.5	483
3	307	23.8	328
4	282	16.3	215
5	230	39.8	361
6	212	7	75
7	193	14.6	187
8	169	7.37	288
9	146	10	100

member an overall depression of the conductivity between 400 cm^{-1} and the maximum of the mid infrared absorption is clearly visible, caused by three antiresonant-like minima between 400 and 600 cm^{-1} which arise as a result of coupling to phonons. As seen in chapter 5 the two sharpest modes are directly observable in the reflectance and evolve as the mid infrared band develops providing incontrovertible evidence for this mechanism.

To establish this point more quantitatively equation 6.1 is invoked to model the evolution in the optical conductivity of the $Pb_2Sr_2RCu_3O_8$ series. As found in chapter 5 the insulators can be satisfactorily modeled with only the first and third terms of equation 6.1. The room temperature phonon parameters obtained for Pr in the previous chapter, with the position of the highest frequency phonon shifted to 620 cm^{-1}, are taken to model a representative insulating member of the series. The phonon parameters are summarized in table 6.1, and the resulting model conductivity is shown in figure 6.1. To simulate the doping procedure next a Drude

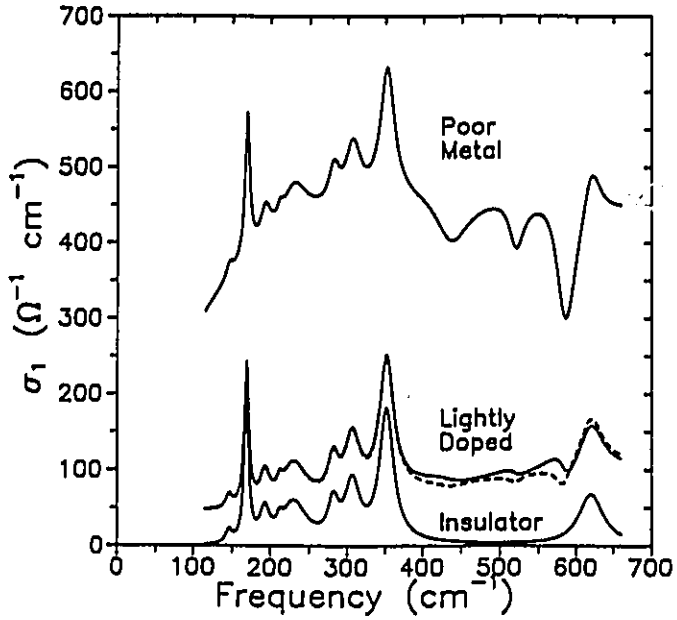

Figure 6.1: Modeling the evolution in the optical conductivity of the $Pb_2Sr_2RCu_3O_8$ series. The dashed curve shows the result for the representative lightly doped member with non-zero q.

component consistent with a typical value for the dc-conductivity is added as well as an overdamped Lorentzian oscillator to describe the mid infrared band whose position width and strength are chosen to agree with the experimental result shown in figure 5.9 of chapter 5. The strength, position, and width of the Lorentzian phonons is left unaltered. This mid infrared electronic continuum is then coupled to three phonons located at 435, 520 and 580 cm^{-1} with the assumption that q is zero. The parameters used for representative lightly doped and poorly metallic members of the series are listed in tables 6.2 and 6.3 while the resulting model conductivity is shown in figure 6.1.

Comparing figure 6.1 with the experimental result shown in figure 5.14 of chapter 5 it is seen that the model captures very well the observed evolution of the optical conductivity with doping. The only discrepancy lies in the position of the peaks in the lightly doped conductivity due to the two highest frequency coupled phonons (or equivalently in the corresponding minima – we refer here to peaks because

Table 6.2: Drude parameters used to model the evolution in the optical conductivity of the $Pb_2Sr_2RCu_3O_8$ series. All values in cm^{-1}.

	Γ_D	ω_{pD}
Insulator	-	0
Lightly Doped	200	775
Poor Metal	200	1225

Table 6.3: Electron-phonon coupling parameters used to model the evolution in the optical conductivity of the $Pb_2Sr_2RCu_3O_8$ series. All values in cm^{-1}.

		ω_e	Γ_e	ω_{pe}
Mid-IR band	Insulator	-	-	0
	Lightly Doped	2000	8500	8500
	Poor Metal	925	5800	12500
	k	ω_k	Γ_k	ω_{pk}
Coupled Phonons	1	435	45	300
	2	520	20	270
	3	585	20	395

that is how these features were interpreted in chapter 5 – at these doping levels it is difficult to choose one over the other). Experimentally the peaks are located near 500 and 550 cm^{-1}, while the model with $q = 0$ places them nearer 520 and 580 cm^{-1}. One possible explanation is that the position of the coupled phonons is different in lightly doped and poorly metallic samples. The phonons which couple to the mid infrared band are believed to be the *c*-axis longitudinal modes (to be discussed in the following section). As can be deduced from the parameters listed in tables C.14-C.18 of Appendix C the position of these modes does not change discontinuously as the level of doping increases. Thus, a more probable explanation is that as a result of the low level of doping the phonons are not screened from the electromagnetic field, and hence have a finite q. The dashed curve in figure 6.1 shows the result of associating a q of -2×10^{-7} cm^2 with each of the coupled phonons. As can be seen the consequence is a shift of the peaks to lower frequency in good agreement with experiment.

6.2 Physical Origin of the Coupled Phonons

It thus appears that the evolution of the phonon structure between 400 and 600 cm^{-1} in the optical conductivity of the $Pb_2Sr_2RCu_3O_8$ series can be well modeled in terms of Fano-type coupling of phonons to the broad mid infrared band. The details of the physical origin of this structure have however remained elusive. That is, given that it is due to phonons, one would like to know more specifically which phonons couple so strongly to the mid infrared electronic continuum. This knowledge may have important implications for the superconducting mechanism in these materials.

Perhaps some insight can be gained by considering the situation in the organic conductors. In the presence of inversion symmetry, phonon modes can be classified as symmetric (Raman active) or antisymmetric (infrared active). In organic conductors it has been found that inversion symmetry can be broken via dimerization and charge transfer processes which leads to infrared activity of otherwise infrared nonactive

symmetric modes. That is, the same modes appear in both the Raman and infrared spectra. A good example is the organic linear chain semiconductor TEA(TCNQ)$_2$. In this compound there are ten totally symmetric, and hence Raman active, intramolecular A_g vibrational modes which, for the isolated molecule, are infrared inactive.[116] The experimental infrared spectrum contains eight sharp absorption peaks below the semiconducting gap near 1600 cm^{-1} and one (possibly two) antiresonant-like minimum in the continuum above the gap.[117] Rice, Pietronero and Brüesch have shown that the infrared spectrum can be understood in terms of a coupling of the conduction electrons to the totally symmetric modes of the TEA(TCNQ)$_2$ molecule.[118] Another example is the (TMTSF)$_2$X family of salts studied by Homes and Eldridge; the spectrum of which is also dominated by electron-coupled A_g modes.[119] In general the positions of the absorption bands in the infrared spectrum fall below the Raman frequency by typically 10% which is expected on theoretical grounds.[114, 120] It is found that the symmetry can be broken not only by charge- but also by spin-density waves. For example, the work of Ng *et. al.*[121] shows the presence of electron-phonon interaction-induced phonon structure at the frequencies of the A_g modes upon formation of a spin-density wave state at low temperatures in the organic compound (TMTSF)$_2$SbF$_6$.

The cuprate superconductors also exhibit inversion symmetry. Evidence for a doping induced violation of the symmetry-dictated mode selection rules has been observed in Raman measurements of $La_{2-x}Sr_xCuO_{4-\delta}$.[122] In chapter 4 a low-lying excitation in the optical conductivity of $Pb_2Sr_2(Y/Ca)Cu_3O_8$ was discovered which may be of magnetic origin and could be related to a possible source of symmetry-breaking in this system.

Since the electron-phonon coupled structure near 420 cm^{-1} in $YBa_2Cu_3O_{7-\delta}$ is rather broad, no serious attempt was made to assign the features to specific phonons. The more distinctive pattern formed by the broad minimum and the two sharp antiresonances at 525 and 585 cm^{-1} in $Pb_2Sr_2RCu_3O_8$ suggested that identifi-

cation of these features with particular phonon modes might be more readily accomplished. Initially, based on published Raman spectra for $Pb_2Sr_2(Y/Ca)Cu_3O_8$,[123] it was thought that these modes might be, as in the organics, totally symmetric A_g modes rendered infrared active via the coupling process. In order to explore this possibility further Raman measurements were carried out on the $Pb_2Sr_2RCu_3O_8$ series which will be discussed next.

6.2.1 Raman Spectra of the $Pb_2Sr_2RCu_3O_8$ Series

The first Raman scattering measurements of $Pb_2Sr_2(Y/Ca)Cu_3O_8$ were carried out on polycrystalline samples by Thomsen *et. al.*.[101] Liu *et. al.* then studied a single crystal sample and were thus able to make proper mode assignments and determine the components of the Raman tensor.[123] Kress *et. al.* later found good agreement between the mode frequencies and assignments determined by Liu *et. al.* and lattice dynamical calculations.[72] Of interest to the present work was the fact that the spectrum contained three totally symmetric A_g modes in the region where the coupled modes appear in the infrared spectrum. The A_g modes occur at 440, 485 and 570 cm^{-1}. The frequencies are not precisely identical to those of the coupled modes although as mentioned above, a small difference occurs in the organics as well and thus may be expected.

In the hope that a study of the doping dependence of the Raman spectra might lead to further insight, Raman scattering spectra were obtained for the $Pb_2Sr_2RCu_3O_8$ series of this work. The Raman measurements were carried out during a visit to Prof. J.C. Irwin's laboratory at Simon Fraser University. A homebuilt triple axis spectrometer with a Mepsicron multichannel detector cooled to approximately -30°C was used. The 514.5 nm line of an argon ion laser was focused onto a small spot on the sample. The output laser power was limited to approximately 50 mW at low temperatures to avoid laser heating of the sample. The actual power incident on the sample is estimated to be more than an order of magnitude less.[124]

The sample was mounted at the tip of a cold-finger cryostat and cooled using a closed cycle helium refrigerator. The temperature was measured with a chromel versus Au 0.07% Fe thermocouple. The spectrum was calibrated with known laser plasma lines by removing a filter to eliminate these during measurements. A nicol prism polarizer was used to examine the different symmetry elements of the Raman tensor.

The spectra were taken with the incident and scattered light propagating along the c-axis. As can be seen from table 5.3 of chapter 5 the totally symmetric A_g modes should be observed in a configuration where both the incident and scattered light is polarized along the x [100] (or equivalently the y [010]) direction, while the B_{1g} mode is observed under a cross-polarized configuration where *eg.* the incident light is polarized along the [100] direction and the scattered light along [010]. The experimental configuration is commonly summarized using the Porto notation of $i(j\ k)l$ where i and l represent the direction of propagation of the incident and scattered light respectively and j and k respectively the polarization of the incident and scattered light. Thus the configuration in which the A_g modes are observed can be written as $z(x\ x)\bar{z}$ or $z(y\ y)\bar{z}$ (where $\bar{z}$ indicates that the direction of propagation is reversed from z by 180°), while that for the B_{1g} mode by $z(x\ y)\bar{z}$ or $z(y\ x)\bar{z}$.

As pointed out by Liu *et. al.* the morphological edges of the sample run in the [110] or [1$\bar{1}$0] directions and thus with the incident light polarized vertically the sample had to be oriented such that the vertical bisected a 90° corner in order to probe the two configurations of interest.

Spectra were measured for all members of the $Pb_2Sr_2RCu_3O_8$ series with the exception of La, although results will be presented herein only for a representative member from each of the three groups. Figure 6.2 shows the polarized $z(y\ y)\bar{z}$ (bottom curve) and $z(y\ x)\bar{z}$ (top) spectra for the lightly doped Gd sample as well as an unanalyzed $z(y\ xy)\bar{z}$ spectrum (middle). The $z(y\ x)\bar{z}$ spectrum is as expected, dominated by the B_{1g} mode at 317 cm^{-1} but consistently in all samples examined, also shows a less intense mode near 80 cm^{-1}. This mode may arise due to structural

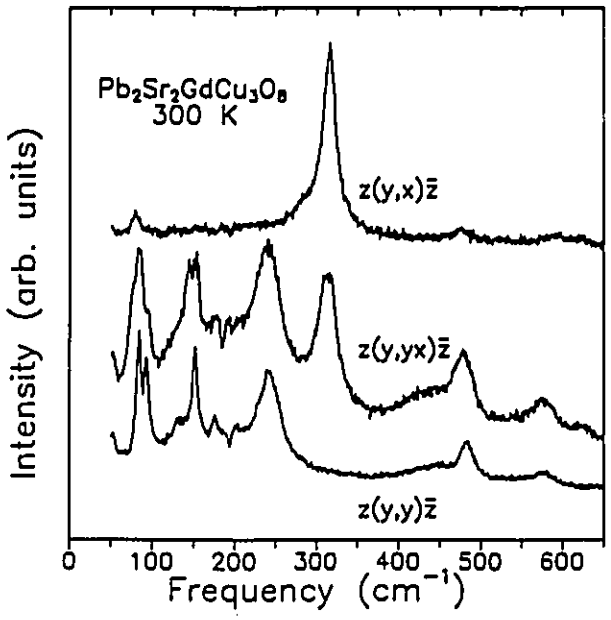

Figure 6.2: Room temperature Raman spectra of $Pb_2Sr_2RCu_3O_8$ with R = Gd for various scattering geometries.

monoclinic distortions[125] which have been observed crystallographically.[21] The $z(y\ y)\bar{z}$ spectrum is dominated by the 6 A_g modes at 580, 485, 445, 240, 150, and 90 cm^{-1}. As well it contains a peak at 180 cm^{-1} which Liu *et. al.*[123] point out is not an A_g eigenmode in the ideal structure but is observed to behave as an A_g mode. They suggest that this mode arises as a result of local symmetry breaking due to atomic displacement of the O(2) atoms within the PbO layers. The strong enhancement of this mode at low temperatures (see figures 6.3, 6.4, 6.5) may be due to ordering of the occupation of one of the four possible sites for the O(2) atoms. (For a discussion of oxygen ordering in the PbO layers of $Pb_2Sr_2RCu_3O_8$ see *eg.* reference [21]). Note that the depolarized spectrum contains the A_g modes as well as the B_{1g} mode. Table 6.4 summarizes the observed mode frequencies, symmetries and assignments (according to reference [123]). The results are in good agreement with those of Liu *et. al.*.

Of greater present interest is the doping dependence of the spectra. Figures 6.3, 6.4, and 6.5 show respectively the temperature dependence of the unpolarized $z(y\ yx)\bar{z}$ spectrum for an insulating (Nd), lightly-doped (Gd) and poorly metallic

Table 6.4: Raman mode frequencies, symmetries and assignments. Note that the assignments are taken from Liu *et. al.*. The mode at 180 cm^{-1} appears to obey A_g symmetry although it is not an expected mode of the ideal structure. The mode at 80 cm^{-1} appears in both symmetries and is likely due to a monoclinic distortion.

Phonon (cm^{-1})	Symmetry	Assignment
80	A_g, B_{1g}	Pb
90	A_g	Pb (primarily)
150	A_g	Sr, Cu(2) in phase
180	A_g	O(2) in-plane bending
240	A_g	Sr, Cu(2) out of phase
317	B_{1g}	O(3) out of phase
445	A_g	O(3) in phase
485	A_g	O(1), O(2) in phase
580	A_g	O(1), O(2) out of phase

(Dy) sample. The apparent decrease in the intensity of the lower frequency modes with decreasing temperature is due to the Bose temperature factor which dictates that the Raman intensity varies with temperature according to:[126]

$$I_{Raman} \propto [1 + \frac{1}{e^{\frac{\omega}{T}} - 1}]. \tag{6.3}$$

For example, in spectra corrected for this factor the doublet near 90 cm^{-1} has an essentially temperature independent intensity. The feature near 340 cm^{-1} which appears

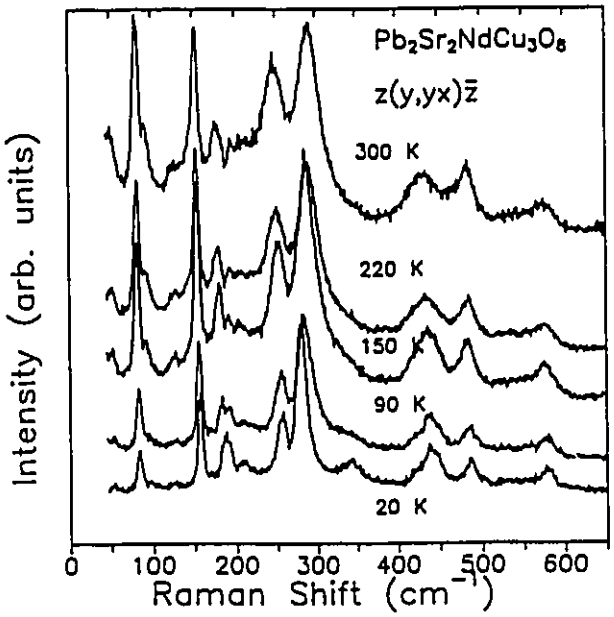

Figure 6.3: Temperature dependence of the $z(y\ yx)\bar{z}$ spectrum of $Pb_2Sr_2RCu_3O_8$ with R=Nd.

at low temperature in the Nd spectrum arises as a result of phonon-crystal field excitation coupling[127] similar to what has been previously observed in $NdBa_2Cu_3O_7$.[128]

Only one mode shows a pronounced doping and temperature dependence. This is the A_g mode near 440 cm^{-1} which has been assigned to the in-phase vibration along the c-axis of the O(3) atoms within the CuO_2 planes. At room temperature this mode progresses from a large dominant mode in the insulating spectrum (Nd), to a weak barely visible mode in the lightly-doped sample (Gd), to an essentially absent mode for the metallic sample (Dy). In the insulating sample the intensity of

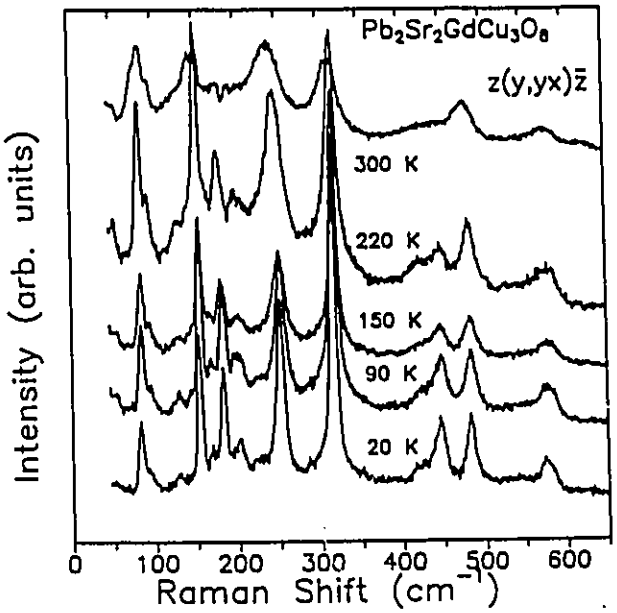

Figure 6.4: Temperature dependence of the $z(y\ yx)\bar{z}$ spectrum of $Pb_2Sr_2RCu_3O_8$ with R=Gd.

this mode shows very little temperature dependence, remaining strong down to 20 K. In contrast, for the lightly-doped samples this mode has a very dramatic temperature dependence, becoming much sharper and more intense as the temperature is lowered. In the metallic samples the temperature dependence is once again small. The mode begins to appear very weakly near 150 K and remains weak down to low temperatures.

The temperature and doping dependence of the intensity of this mode is summarized schematically in figure 6.6. This mode is clearly very sensitive to the electronic structure in the CuO_2 planes. Interestingly the coupled modes in the infrared spectrum show the opposite doping dependence, being absent in insulating samples, appearing weakly at 300 K and growing strongly with decreasing temperature in lightly-doped samples and then appearing very dominantly in the more metallic spectra. One might speculate that the same symmetry-breaking process which is allowing the infrared activity of the coupled modes is governing the behaviour of this Raman mode although at present the relationship (if any) between the Raman spectra and the coupled infrared modes remains unclear and requires further study. We turn next

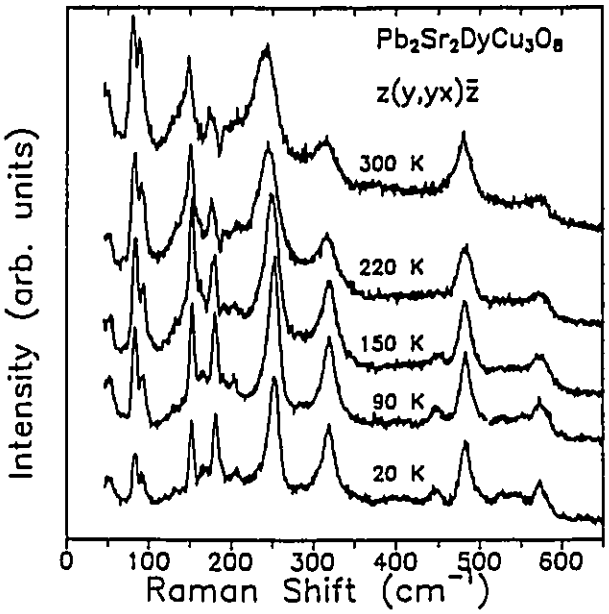

Figure 6.5: Temperature dependence of the $z(y\ yx)\bar{z}$ spectrum of $Pb_2Sr_2RCu_3O_8$ with R=Dy.

to a situation where a more definite correspondence can be inferred.

6.2.2 Coupling to *c*-axis Longitudinal Optical Phonons

In this section a remarkable similarity is elucidated between the *c*-axis dielectric loss function and the *ab*-plane optical conductivity of $Pb_2Sr_2(Y/Ca)Cu_3O_8$ and other cuprate superconductors and is thus presented as universal evidence for a coupling of longitudinal *c*-axis phonons to the mid infrared carriers in high-T_c and isostructural materials.

The *ab*-room temperature reflectivity of $Pb_2Sr_2DyCu_3O_8$ measured on the *ab*-face of a single crystal is reproduced from figure 5.13 of chapter 5 in figure 6.7(a). The geometry of the reflectance measurement is such that the direction of propagation, q, of the electromagnetic radiation is perpendicular to E. That is, when E is polarized within the *ab*-plane q is along the *c*-axis. This experimental configuration, which will be referred to as 'parallel' geometry since q is parallel to *c*, is shown in the

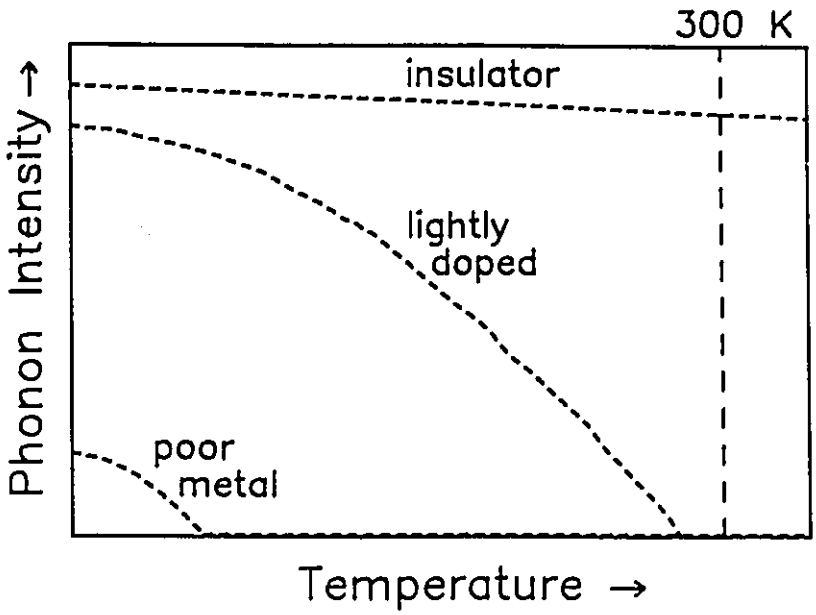

Figure 6.6: Schematic phase diagram denoting the temperature and doping dependence of the totally symmetric 440 cm^{-1} A_g mode. The mode is strong and shows little temperature dependence in insulating samples, appears weakly, or not at all, at 300 K and grows dramatically with decreasing temperature in lightly doped samples, while it is absent at high temperatures in more metallic samples, appearing subsequently very weakly at low temperatures.

inset to figure 6.7(a). The *ab*-properties can also be measured using polarized light on an *ac* (or *bc*) face in which case q propagates along the *b* (or *a* direction). That is, q is perpendicular to *c* and thus this experimental configuration, shown in the inset to figure 6.7(b), is referred to as 'perpendicular' geometry. Because flux grown crystals have small faces normal to the planes parallel geometry has been used almost exclusively for measurement of the low frequency *ab* properties of the high temperature superconductors. In figure 6.7(a) the positions of the doping-induced antiresonances which are of interest here are indicated by the vertical dashed lines. The corresponding Kramers-Kronig derived optical conductivity is shown in the upper curve of figure 6.8(a). As discussed in the previous chapter although $Pb_2Sr_2DyCu_3O_8$ exhibits metallic-like linearly decreasing resistivity and a T_c of 75 K, it has a low dc conductiv-

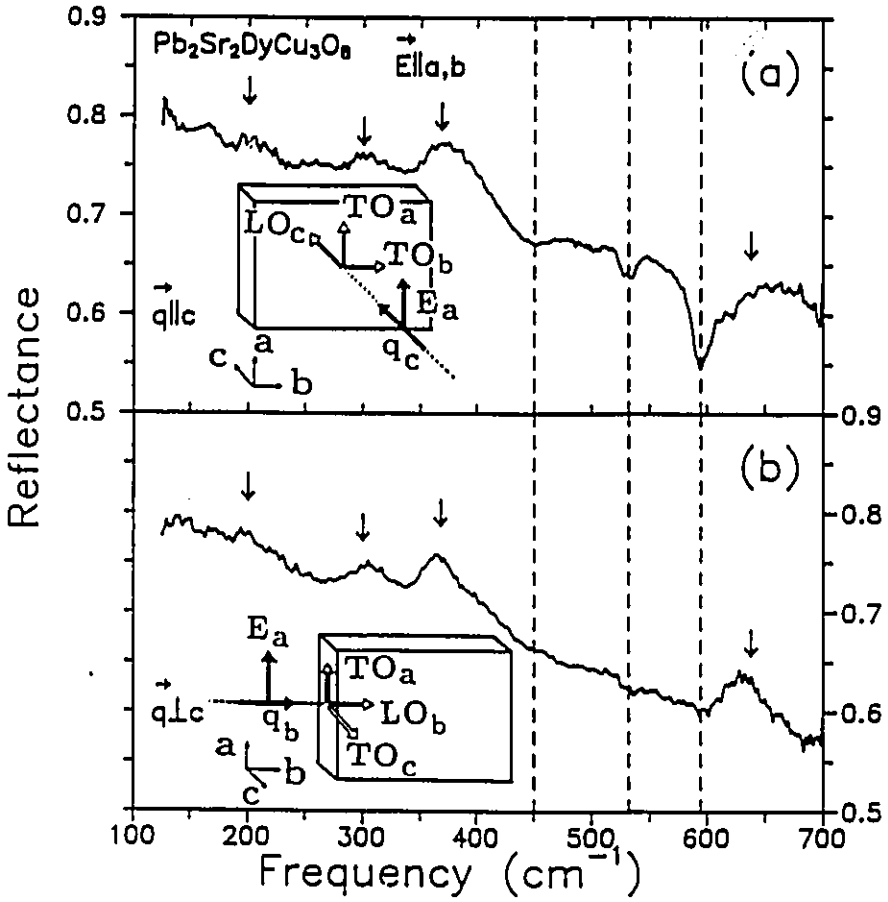

Figure 6.7: E|| *ab* reflectance of $Pb_2Sr_2DyCu_3O_8$ at room temperature for (a) q|| *c* (parallel geometry) and (b) q⊥ *c* (perpendicular geometry). Direct coupling to unscreened TO_a and TO_b modes is indicated by the small arrows in both spectra. Antiresonances due to strong electron-phonon coupling to longitudinal *c*-axis modes in the parallel geometry are indicated by the vertical dashed lines. This coupling is forbidden in perpendicular geometry, as can be seen by comparing the insets to (a) and (b) which show the polarization vectors of phonons allowed by momentum conservation. To first order the Fano resonances are absent in (b).

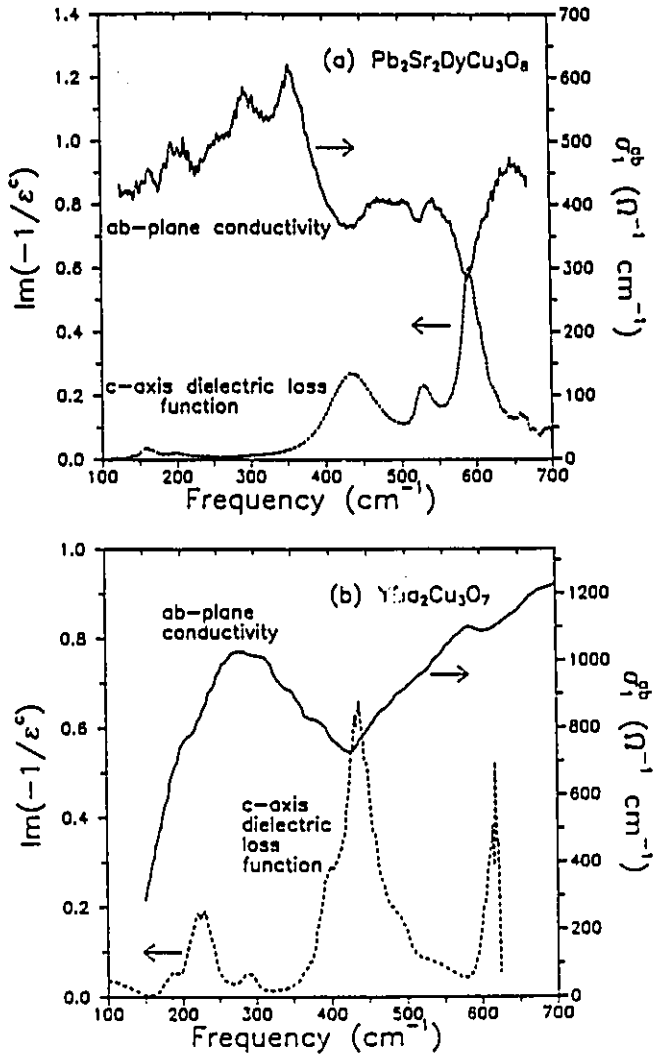

Figure 6.8: Comparison of the *ab*-plane mid infrared component of the optical conductivity of (a) $Pb_2Sr_2DyCu_3O_8$ and (b) $YBa_2Cu_3O_{7-\delta}$ with the dielectric loss function of the c-axis phonons. Note the striking correspondence of the position, width and relative strength of the minima in σ_1^{ab} and the peaks in $\Im(-1/\epsilon^c)$. σ_1^{ab} of $YBa_2Cu_3O_{7-\delta}$ is after Kamáras *et. al.*, while $\Im(-1/\epsilon^c)$ is determined after Homes *et. al.*.

ity and thus, in contrast to other high T_c superconductors such as $YBa_2Cu_3O_{7-\delta}$ and $Bi_2Sr_2CaCu_2O_8$, the non-Drude component dominates the optical properties. Consequently the symmetry-allowed phonons are for the most part unscreened and appear as *peaks* in the optical conductivity (*eg.* at 650, 356, and 298 cm^{-1}). The forbidden coupled modes, which are absent in the undoped insulating parent compound, appear as *minima* at 430, 525 and 585 cm^{-1}. These characteristic properties of the optical conductivity of poorly metallic $Pb_2Sr_2DyCu_3O_8$ are also clearly shown in the model calculation of section 6.1.1.

The lower (dashed) curve of figure 6.8(a) shows the dielectric loss function, $-\Im(1/\epsilon)$, of $Pb_2Sr_2DyCu_3O_8$ with the electric field, E, polarized along the *c*-axis calculated from the Kramers-Kronig derived dielectric function corresponding to the data presented in section 5.5 of chapter 5. A striking similarity between the position, width and relative strength of the peaks of the *c*-axis loss function and the minima in the real part of the *ab*-plane optical conductivity, σ_1^{ab}, is revealed. As discussed previously the peaks in the dielectric loss function essentially yield the positions of longitudinal optical (LO) phonon modes. This result thus suggests that the coupling is to longitudinal *c*-axis modes. The contribution of the phonons to the *c*-axis dielectric loss function of $YBa_2Cu_3O_{7-\delta}$ at 100 K calculated from recent measurements of Homes *et. al.*[87] by subtracting the Drude component is shown in the lower curve of figure 6.8(b). The notch in σ_1^{ab} coincides with a broad peak in $-\Im(1/\epsilon^c)$. Additional weaker features in σ_1^{ab} can be associated with smaller loss function peaks.

In figure 6.9 further evidence that this is behaviour general to the cuprates is derived from similar comparisons between the non-Drude component of the *ab*-plane optical conductivity and the dielectric loss function of the *c*-axis phonons for $Nd_{2-x}Ce_xCuO_{4-\delta}$, $Tl_2Ba_2CaCu_2O_8$, and $Bi_2Sr_2CaCu_2O_8$.[129] In each case minima in σ_1^{ab}, correspond to peaks in $-\Im(1/\epsilon^c)$. Since the number and position of phonons differs from material to material, the observed correlation can hardly be a coincidence, and is thus evidence for a universal coupling of *c*-axis phonons to the *ab*-plane mid

infrared continuum in the cuprate superconductors.

In order to couple to *c*-axis phonons a symmetry-breaking mechanism which yields a dipole moment along the [001]-axis when the electric field is in the *ab*-plane is required. The Cu^{3d}-O^{2p} charge transfer, which is believed to be responsible for the mid infrared absorption, might give rise to a dipole moment along the [001]-direction under a distortion in which the atoms move along the *c*-axis to reduce Coulomb repulsion.

Parallel geometry was used exclusively for all of the measurements of σ_1^{ab} shown in figures 6.8 and 6.9. In parallel geometry the direction of propagation, q, of the electromagnetic radiation is *along the c-axis* and can thus excite phonons propagating in the *c*-direction, thereby providing an explanation for why the coupling is to *longitudinal* *c*-axis phonons.

This hypothesis can be tested experimentally. If the, say, E$\|$ *a* spectrum is measured on an *ac* face then q is along the *b*-axis (*ie.* perpendicular geometry). As shown in the inset to figure 6.7(b) the only Fano coupling possible (assuming an appropriate dipole moment exists) will then be to transverse optical phonons along the *a* and *c*-axes, TO_a and TO_c, and to longitudinal modes along the *b*-axis, LO_b. Direct coupling to unscreened TO_a modes is also allowed. Since there is no incident momentum component in the *c*-direction, Fano-coupling to LO_c phonons is forbidden in this experimental configuration. The reflectance of $Pb_2Sr_2DyCu_3O_8$ measured in perpendicular geometry is shown in the main figure of the lower panel. Remarkably, the spectrum is identical to that of the upper panel (parallel geometry) *with the exception that the Fano-coupling has to first order disappeared* (small remaining structure may be due to polarization leakage or to weak coupling to another allowed symmetry).

Since in the usual parallel geometry (*ie.* measurement of an *ab*-face) there is little evidence for a Fano-type interaction with the allowed *ab*-plane TO phonons, the coupling to these modes must be small. The results of the q$\perp$ *c* measurement of

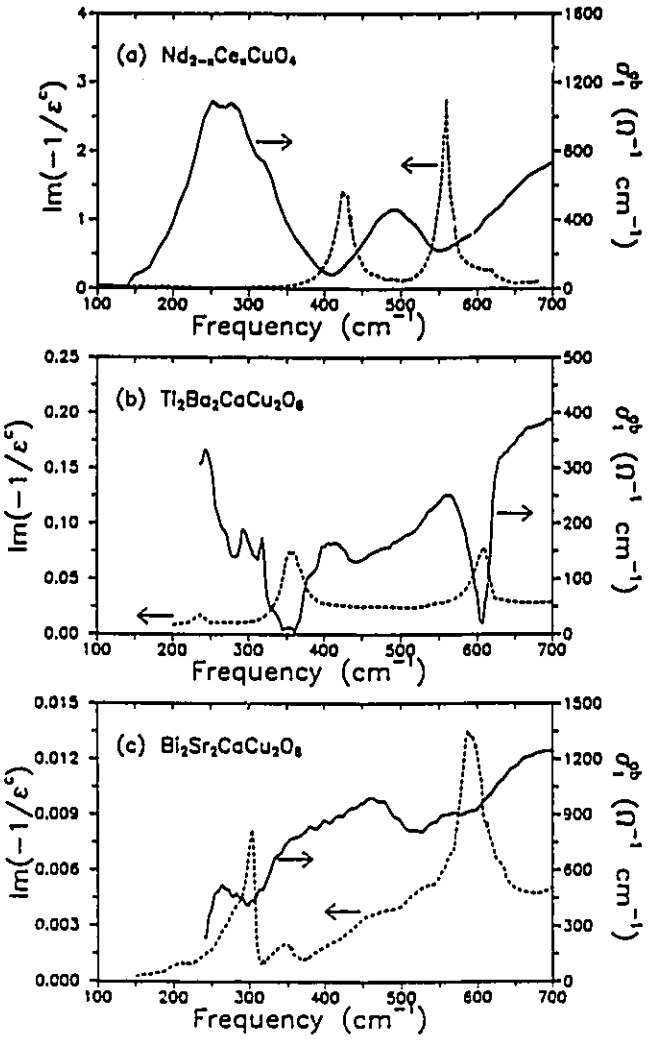

Figure 6.9: Further evidence for a universal coupling of the ab-plane optical conductivity to c-axis phonons is derived from the comparison of σ_1^{ab} with $\Im(-1/\epsilon^c)$ for (a) $Nd_{2-x}Ce_xCuO_{4-\delta}$, (b) $Tl_2Ba_2CaCu_2O_8$, and (c) $Bi_2Sr_2CaCu_2O_8$. The σ_1^{ab} curves shown in (a), (b) and (c) respectively are after Hughes *et. al.*, Foster *et. al.*, and Rvedyk *et. al.* while the $\Im(-1/\epsilon^c)$ curves were obtained via Kramers-Kronig analysis of the reflectance measured by Tajima *et. al.*, Zetterer *et. al.*, and Kamáras *et. al.* respectively.

figure 6.7(b) lead to the conclusion that coupling to TO_c and LO_b is also weak. Since no distinction is made between a and b in pseudotetragonal $Pb_2Sr_2DyCu_3O_8$ (there are no chains as in $YBa_2Cu_3O_{7-\delta}$) it can be concluded that a strong electron-phonon interaction exists only between the ab-plane carriers responsible for the mid infrared absorption and longitudinal c-axis phonons. Coupling between c-axis phonons and a planar electron gas has been treated by Mahan with the conclusion that the electron-phonon coupling is very weak.[130] This suggests that in order to explain the experimental observation further details of the electronic continuum must be taken into account.

The optical conductivity of slightly oxygen-deficient $YBa_2Cu_3O_{7-\delta}$ measured in the usual way on the ab-plane face (parallel geometry) by Orenstein *et. al.*,[62] solid curve, is compared with the only measurement of the ab-optical properties, available at the time of writing, done on a face containing the c-axis ($q \perp c$, by Bauer[86]), dashed curve in figure 6.10. In this system too, the prominent Fano resonance at 420 cm^{-1} vanishes in the perpendicular geometry. Also, recently Železný and Tanner have measured the a, b properties of a $GdBa_2Cu_3O_{7-\delta}$ crystal with a T_c of approximately 50 K on a face containing the c axis (*ie.* in perpendicular geometry).[131] The antiresonance at 420 cm^{-1} is not observed, while in the measurement of Orenstein *et. al.* of the ab-face of an $YBa_2Cu_3O_{7-\delta}$ crystal with a similar T_c it is particularly strong.[62]

The results of figures 6.8, and 6.9 seem to indicate a general coupling to at least all of the higher frequency modes, which are generally attributed to oxygen bond stretching and bending motions, if not to the entire group of c-axis phonons, rather than to certain special branches exhibiting a strong doping induced electron-phonon interaction as was originally proposed.[115] Furthermore, the fact that correlations of the infrared spectra with neutron, and tunnelling data are observed[132] seems to indicate that it is these same phonons that are playing a role in all of these measurements. For example, further evidence that doping brings about changes in

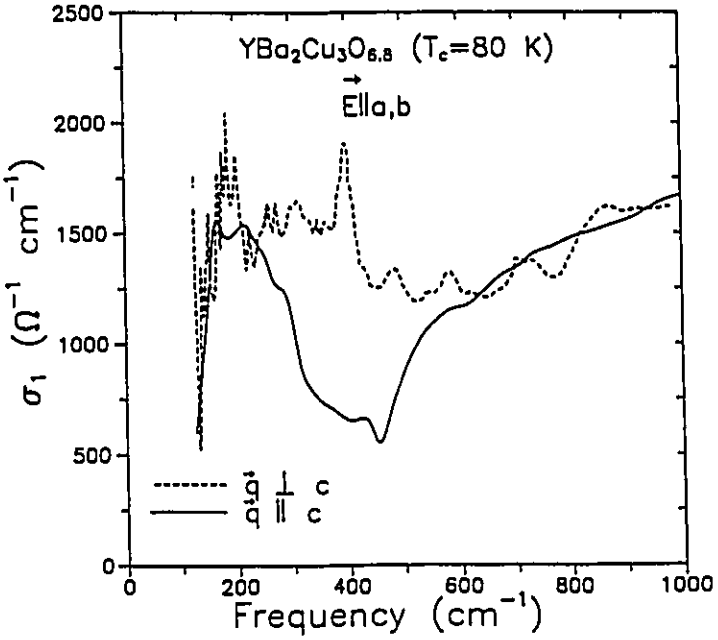

Figure 6.10: Comparison of the optical conductivity of $YBa_2Cu_3O_{6.8}$ (T_c= 80 K) measured in the usual parallel geometry (solid curve, T = 10 K after Orenstein *et. al.*), and in perpendicular geometry (dashed curve, T = 10 K after Bauer). Note that the prominent Fano resonance at 420 cm^{-1} is absent in perpendicular geometry.

the phonon spectrum of $Pb_2Sr_2(Y/Ca)Cu_3O_8$ in this frequency range comes from the neutron-time-of-flight-derived phonon density of states (PDOS) curves of Currat *et. al.*[133], which are reproduced in figure 6.11. Upon doping polycrystalline non-superconducting $Pb_2Sr_2YCu_3O_8$ with Ca they find a considerable increase in the PDOS in the region from 500 to 600 cm^{-1}. This correlation between enhanced PDOS and antiresonant coupling of phonons is also observed in $YBa_2Cu_3O_{7-\delta}$.[115]

A subtle point is whether the coupling is to the *c*-axis LO modes or more generally to the long-range electric field which is described by the dielectric loss function. The fact that no coupling to transverse modes along the *c*-axis is observed in addition to the remarkable similarities displayed not only in the position but in the relative strength and width of the peaks in the loss function with the minima in the optical conductivity suggests the latter. In $Pb_2Sr_2DyCu_3O_8$ and $YBa_2Cu_3O_{7-\delta}$ where the similarity is most striking the comparison is also most reliable due to the

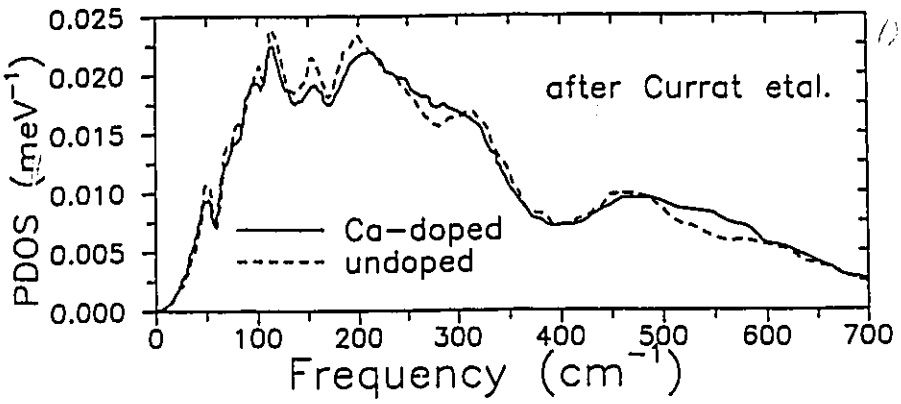

Figure 6.11: Neutron time-of-flight phonon density of states spectra for non-superconducting (x = 0, undoped) and superconducting (x = 0.5, Ca-doped) $Pb_2Sr_2(Y/Ca)Cu_3O_8$ after Currat *et. al.*.

relative independence of the results to subtraction of a dominant, highly frequency-dependent Drude component. In addition, the direct modes of $Pb_2Sr_2DyCu_3O_8$ near 350 and 640 cm^{-1} appear to be broadened in the reflectance corresponding to the Fano-coupled geometry [figure 6.8(a)], which may arise from interaction of the mid infrared background on which they sit with the 'tails' of the loss function.

A question that remains is what, if anything, is the relationship of this doping-induced coupling of the in-plane mid infrared continuum to longitudinal c-axis phonons to the superconductivity exhibited by most of these materials? Perhaps another way of asking this is why have such effects not been observed in other systems which are strongly anisotropic but not susceptible to superconductivity? The proposed mechanism purports to be general to any system where there is an electronic background in one polarization direction, and unscreened phonons along a perpendicular axis. Of relevance may be why the coupling appears to be only to bound rather than Drude-like carriers. The mid infrared band however, is a common feature of metallic oxides[134, 135] while only the high-T_c cuprates and close isostructural relatives seem to have the coupled Fano resonances. The $Pb_2Sr_2RCu_3O_8$ system shows

incontrovertibly that the coupling process is activated as soon as the mid infrared band begins to develop, and is thus present in lightly doped and non-superconducting samples (*eg.* $Pb_2Sr_2SmCu_3O_8$ and $Pb_2Sr_2TbCu_3O_8$) . Also, $La_{2-x}Sr_xNiO_{4-\delta}$ is presumably non-superconducting but is isostructural to $La_{2-x}Sr_xCuO_{4-\delta}$ which has a T_c of 40 K. Both materials have Fano resonances in addition to direct TO coupling.[110, 112] A diamagnetic moment was originally detected in a sample of $La_{2-x}Sr_xNiO_{4-\delta}$ with $x \approx 0.2$ and taken as evidence for a superconducting state,[136] however this result has not been reproduced in attempts by other workers.[137] This may nevertheless indicate a susceptibility of this system as well, to superconductivity. That is, the symmetry breaking mechanism which allows the Fano coupling to the longitudinal *c*-axis modes may contribute to, but not be the sole dictating factor governing the superconducting pairing. The nature of the symmetry-breaking remains at present unknown although evidence for a low-lying mode which shows a very pronounced temperature dependence below T_c is observed in the optical conductivity of $Pb_2Sr_2(Y/Ca)Cu_3O_8$ as discussed in chapter 4, and may in some way, be connected. It should be pointed out that this mode appears at T_c while the Fano resonances are present in the normal state as well. The unusual behaviour of the optical conductivity below T_c may however, be a consequence of the same process which allows the Fano coupling.

Chapter 7

Conclusion

7.1 Remarks

The underlying theme behind this work has been the investigation of the extent of the anisotropy between *ab*-plane and *c*-axis properties of $Pb_2Sr_2RCu_3O_8$. Various electrical, magnetic and optical properties were examined. The anisotropy has been found to be moderate, similar to that of $YBa_2Cu_3O_{7-\delta}$, and thus significantly less than that of the highly anisotropic Bi- and Tl-based compounds. It may thus be possible to draw some conclusions regarding the role of the interlayer structure in determining the extent of the anisotropy.

Upon comparison of $YBa_2Cu_3O_{7-\delta}$ and $Bi_2Sr_2CaCu_2O_8$ which are both double-plane cuprates, as is $Pb_2Sr_2RCu_3O_8$, three significant structural differences which are probable contributing factors are apparent. (1) The length of the interlayer structure along the *c*-axis; $\approx 8\AA$ in $YBa_2Cu_3O_{7-\delta}$ and $12\AA$ in $Bi_2Sr_2CaCu_2O_8$. The more quasi-two dimensional behaviour of $Bi_2Sr_2CaCu_2O_8$ may arise from the larger spacing between conducting CuO_2 planes. (2) The conducting CuO chain layer in $YBa_2Cu_3O_{7-\delta}$. This may provide additional electronic coupling between successive CuO_2 plane bilayers which is absent in $Bi_2Sr_2CaCu_2O_8$. (3) The $a/2$ shift every other formula unit in $Bi_2Sr_2CaCu_2O_8$. This causes the apical Cu(2)-O(1) bonds which are

presumably important for c-axis transport, to 'zig-zag' back and forth every other formula unit, thus interrupting the coherent sequence that exists in $YBa_2Cu_3O_{7-\delta}$. (See figure 1.4).

The fact that the interlayer spacing in $Pb_2Sr_2(Y/Ca)Cu_3O_8$ is, as it is in $Bi_2Sr_2CaCu_2O_8$, $\approx 12\mathring{A}$ while it is significantly less anisotropic suggests that this alone is not the governing factor. In $YBa_2Cu_3O_{7-\delta}$ the anisotropy increases significantly upon removal of oxygen, and consequently carriers, from the CuO chain layer.[91, 92] This indicates that the ab-plane carrier density is indeed important. In $Pb_2Sr_2(Y/Ca)Cu_3O_8$ the same trend is observed. That is, increased anisotropy in samples with a lower level of doping. Curiously however the absolute carrier density in $Pb_2Sr_2(Y/Ca)Cu_3O_8$ is significantly less than in both $YBa_2Cu_3O_{7-\delta}$ and $Bi_2Sr_2CaCu_2O_8$ suggesting that this is also not the only factor responsible for the difference. With respect to presence or absence of an $a/2$ structural shift, at present what can be concluded is that this cannot be ruled out as a contributing factor. Both of the moderately anisotropic materials $Pb_2Sr_2(Y/Ca)Cu_3O_8$ and $YBa_2Cu_3O_{7-\delta}$ have no such shift while the highly anisotropic Bi- and Tl-compounds do. It would be of interest to examine the single TlO-layer, double CuO_2-plane compound $TlBa_2CaCu_2O_7$[138] which has no such shift to determine whether the anisotropy is significantly less than in its double TlO-layer relative.

A related issue is the intrinsic nature of the c-axis conductivity. It has been suggested that insulating behaviour along the c-axis is a characteristic of a true high T_c superconductor comprised of conducting CuO_2 plane layers separated by a non-conducting interlayer structure,[139] and that the quasi-metallic behaviour in $YBa_2Cu_3O_{7-\delta}$ is an anomaly caused by the additional conducting CuO chain layer. The results of this work would seem to argue against this interpretation. Although there is no additional interlayer conduction channel in $Pb_2Sr_2(Y/Ca)Cu_3O_8$ the c-axis dc-resistivity exhibits a positive temperature coefficient consistent with a quasi-metallic state and the optical conductivity shows the presence of a non-zero electronic

background.

The reduced *ab*-plane carrier density, inferred from a high normal state resistivity, large magnetic penetration depth and low optical plasma frequency, is surprising given the relatively high value of T_c, 80 K. For example Uemura *et. al.* have placed the known high T_c cuprate superconductors on a curve which shows that T_c increases with increased carrier density.[140] This data is shown in figure 7.1 with a point corresponding to the present work superimposed. It is far removed from the 'universal' curve.

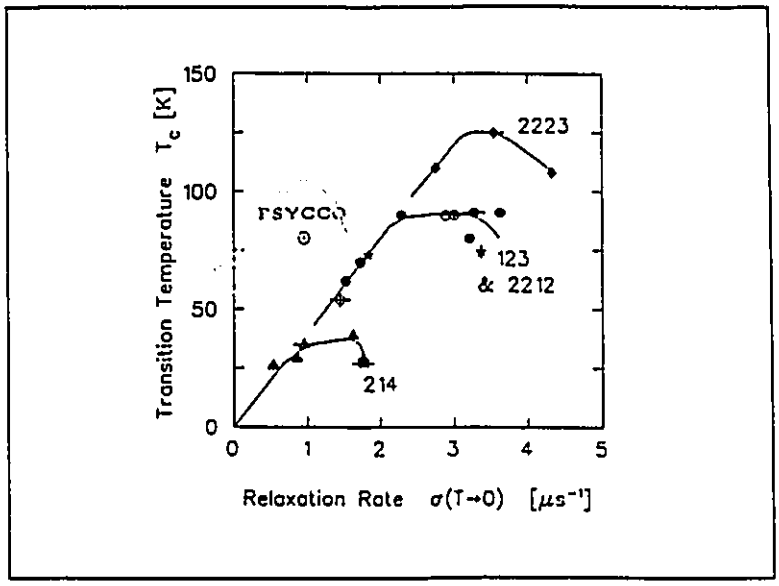

Figure 7.1: Dependence of T_c on carrier density from Uemura *et. al.*. The μSR relaxation rate is proportional to the carrier density. A data point for $Pb_2Sr_2(Y/Ca)Cu_3O_8$ from the present work has been superimposed. Note that it is significantly removed from the 'universal' curve.

The reduced carrier density has enabled observation of some unusual properties in $Pb_2Sr_2(Y/Ca)Cu_3O_8$, such as the curious development of a large peak in the optical conductivity below T_c which may be an indication of non *s*-wave pairing or the development of novel magnetic structure.

An evolution of Fano-type coupling with doping has been observed. Aided

in part by the low carrier concentration which enabled these features to be observed clearly in the normal state where they are overwhelmed by the large Drude response in $YBa_2Cu_3O_{7-\delta}$ and $Bi_2Sr_2CaCu_2O_8$, as well as the more complicated structure which dictates the presence of a greater number of higher frequency phonon modes thereby rendering a sharper, more distinct pattern, it was possible to infer that the *ab*-plane mid infrared electronic continuum is coupling to *c*-axis longitudinal modes. This hypothesis was confirmed by experiment via measurement of the *ab*-continuum on a face containing the *c*-axis showing an absence of such coupling which, for this experimental geometry, is forbidden by momentum conservation. The ostensible absence of this coupled-phonon structure in the normal state of $YBa_2Cu_3O_{7-\delta}$ and $Bi_2Sr_2CaCu_2O_8$ and its sudden appearance below T_c upon condensation of the Drude carriers has resulted in its being mistakenly attributed to the superconducting energy gap.[106] Even its revelation upon subtraction of the dominating Drude component in the normal state,[49] and the demonstration that its position is independent of T_c[108, 62] in $YBa_2Cu_3O_{7-\delta}$ has not convinced all of the unrelated nature. It is hoped that this new development will aid in finally resolving the issue.

7.2 Future Work

The $Pb_2Sr_2RCu_3O_8$ system is open to considerable future work. In general it has been overlooked by the high T_c community and many potentially interesting experiments are just now in progress or have yet to be done. For example the preliminary results of a recent μSR experiment indicate an unusual non-*s* wave $(T/T_c)^2$ dependence to the relaxation rate (proportional to λ^{-2}) at low temperature.[42] Hughes *et. al.* have shown that there is a remarkable similarity between the Fano-coupled phonon structure in the optical conductivity of $Nd_{2-x}Ce_xCuO_{4-y}$ with features in the tunnelling conductance.[111] Since this structure is prominent and distinct in $Pb_2Sr_2(Y/Ca)Cu_3O_8$ it would be of significant interest to do this measurement. The

unusual behaviour of the superconducting state optical conductivity and the implication of the observed Fano-coupling that a symmetry-breaking process exists, as well as other indications such as the foot in the resistivity and the peak in the low-field magnetization just below T_c suggests an examination of magnetic ordering via neutron scattering and nuclear magnetic resonance techniques.

Extensions of the work presented herein can also be made. It is of interest to examine the effect of oxygenation of the Cu(1) layer on the physical properties, in particular on the extent of the anisotropy, and to make comparisons with $YBa_2Cu_3O_{7-\delta}$.

Thomas *et. al.* have shown a relationship between the mid infrared conductivity of very lightly doped semiconducting cuprate materials and various excitations such as the two-magnon Raman scattering spectrum and the antiferromagnetic exchange energy.[141] The Ca-free $Pb_2Sr_2RCu_3O_8$ series has several very lightly doped members where one can look for a similar correspondence. Additional knowledge regarding the development of the electronic structure with doping could arise from photoinduced absorption measurements on the highly insulating and transparent La and Ce members of the Ca-free series. Particularly it would be of interest to determine whether the Fano-coupling can be photoinduced in insulating samples. This could differentiate between an impurity-doped mechanism for the necessary symmetry-breaking process and simply the absence of a background conductivity to which the phonons can couple in insulating samples, suggesting an intrinsic nature. Also of interest would be to examine the temperature dependence of the coupled-phonon structure above room temperature for a possible correlation with *eg.* the antiferromagnetic ordering temperature which is near 400 K in insulating samples.[142] Further comparison of both the normal and superconducting state conductivity in the absence of such coupling with that in the presence thereof should be carried out, for example, by making polarized measurements along the *a* and *b* directions of the *ac*, *bc* and *ab* faces of an untwinned single crystal of $YBa_2Cu_3O_{7-\delta}$.

Further investigation of the doping and temperature dependence of the Ra-

man spectrum of the Ca-free $Pb_2Sr_2(Y/Ca)Cu_3O_8$ series is warranted. In particular the phonon near 440 cm^{-1} shows a very pronounced dependence on both temperature and doping which qualitatively can be represented by a phase diagram reminiscent of the corresponding one for magnetic ordering in the cuprates. Also of interest will be to examine the effect of superconductivity on the electronic Raman background given the unusual behaviour of the optical conductivity.

Two important questions regarding the Fano-coupling which remain unanswered are the source of the symmetry breaking process and the relationship to superconductivity. Experiments which may shed light on the former have been discussed above. The latter may be even more difficult to determine since the coupling is clearly associated with the mid infrared electronic continuum and not the carriers which form the superconducting condensate. Nevertheless, thus far this phenomenon has only been observed in systems which are very closely structurally related to the cuprate superconductors. The presence of such coupling in non-superconducting $La_{2-x}Sr_xNiO_4$ and $Pb_2Sr_2RCu_3O_8$ with R $\equiv$ Sm, Tb rules out a direct consequence. However, it is quite possible that the mechanism by way of which superconducting pairing is realized, given that other critical constraints are also satisfied, gives rise as well to the longitudinal c-axis coupling. This observation should thus not be ignored in the continuing search for the superconducting mechanism of the high T_c superconductors.

Appendix A

Demagnetization and the Volume Fraction of Superconducting Material

A.1 Volume Fraction of Superconducting Material

Two factors which can affect the interpretation of magnetization data of a superconductor are the extent to which the sample is single phase and the extent to which the field within the sample is increased above that of the external applied field. This section deals with the former while the latter will be addressed in that which follows.

Consider a low field magnetization measurement of a sample that is composed of a fraction 'x' of superconducting material, and '1-x' of a non-magnetic impurity. (If the foreign component is magnetic the situation becomes more complicated – this will not be dealt with here). The measured magnetization, $M_{measured}$, will then be given by:

$$M_{measured} = xM_{SC} + (1-x)M_{impurity}, \tag{A.1}$$

where M_{SC}, and $M_{impurity}$ are the contributions to the total magnetization from the superconducting and impurity components respectively. As discussed in Chapter 2, the low field magnetization of a superconductor is given by:

$$M_{SC} = -\frac{1}{4\pi}H, \tag{A.2}$$

where H is the applied field, while that of a non-magnetic impurity is by definition zero. That is,

$$M_{impurity} = 0. \tag{A.3}$$

Thus, the measured magnetization is given by:

$$M_{measured} = -\frac{x}{4\pi}H. \tag{A.4}$$

The volume fraction of superconducting material, x, is then:

$$x = -4\pi\frac{M_{measured}}{H}. \tag{A.5}$$

But $\frac{M_{measured}}{H}$ is simply the slope of the low-field magnetization curve at constant temperature. Thus, the working equation is:

$$x = -4\pi(\text{SLOPE}), \tag{A.6}$$

where 'SLOPE' is the initial slope of the field dependent magnetization curve.

A.2 Demagnetization

In this section it is shown how the field within a sample can be enhanced over that of the external applied field. This has important implications for the determination of the lower critical field and the volume fraction of superconducting material.

A.2.1 Details

Consider a solenoid of n turns of wire, with a current 'i' running through each. The resultant flux distribution is as demonstrated in figure A.1. The magnetic field is given by $H = B$. Now place a superconducting sphere in the center of the solenoid. Since, at low fields, the flux must be excluded from the interior of the superconducting sample, the external flux (and hence the external field) must redistribute as illustrated in figure A.2. Electromagnetic theory states that the circulation of the magnetic field, H around a closed path, l is given by:

$$\oint H \cdot dl = I, \tag{A.7}$$

where I is the total current threading the chosen path. Thus for the path 'ABCDEFA' of figure A.1:

$$\oint_{ABCDEFA} H \cdot dl = \int_{AB} H_a \cdot dl + \int_{BCDEFA} H_{ef} \cdot dl = ni, \tag{A.8}$$

where H_a is the field between A and B in the absence of the superconducting sample, and H_{ef} that outside A and B in the absence of the sample. Similarly for figure A.2:

$$\oint_{ABCDEFA} H \cdot dl = \int_{AB} H_i \cdot dl + \int_{BCDEFA} H_e \cdot dl = ni, \tag{A.9}$$

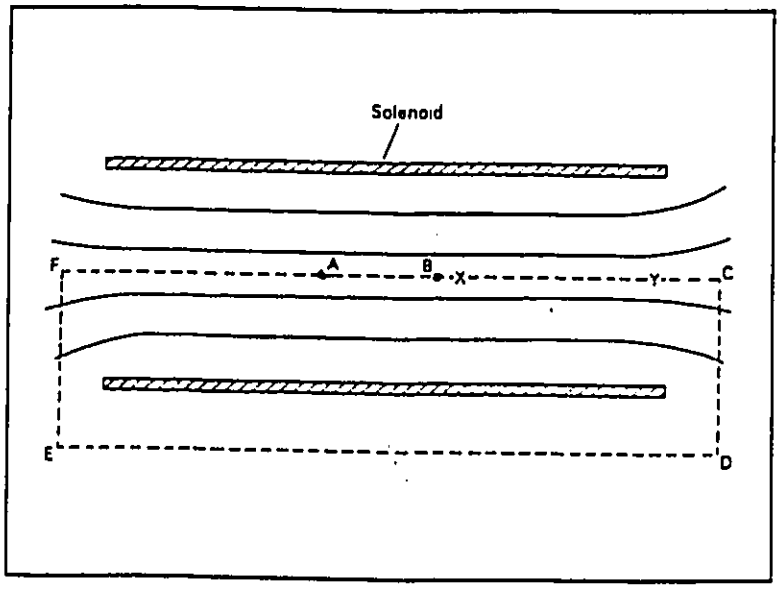

Figure A.1: Resultant flux distribution for a solenoid of n turns with current i running through each. (Adapted after [25]).

where H_i and H_e are respectively the fields within and outside of the sample. Equating A.8 and A.9 yields:

$$\int_{AB} H_a \cdot dl + \int_{BCDEFA} H_{e\prime} \cdot dl = \int_{AB} H_i \cdot dl + \int_{BCDEFA} H_e \cdot dl. \qquad \text{(A.10)}$$

Now consider the two points labelled 'X' and 'Y' in figures A.1 and A.2. Clearly at X:

$$H_e < H_{e\prime}, \qquad \text{(A.11)}$$

while at Y:

$$H_e \approx H_{e\prime}, \qquad \text{(A.12)}$$

so that in general

$$H_e \leq H_{e\prime}. \qquad \text{(A.13)}$$

From equation A.10 then

$$H_i \geq H_a, \qquad \text{(A.14)}$$

which can be written as

$$H_i = H_a - H_d, \qquad \text{(A.15)}$$

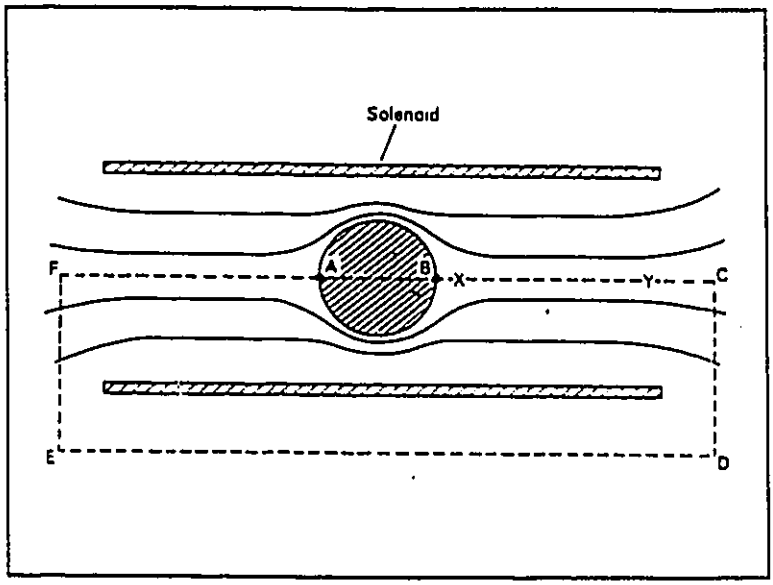

Figure A.2: Resultant flux distribution when a superconducting sample is placed in the center of the solenoid of figure A.1. (After [25]).

where $H_d \leq 0$ is the demagnetizing field. Thus, in summary, the internal field experienced by the superconducting sample, H_i exceeds the applied external field H_a by an amount $-H_d$ (where H_d is negative). In general H_d is non-uniform, but for certain geometries such as ellipsoidal or cylindrical, one can write:

$$H_i = H_a - 4\pi n M \tag{A.16}$$

where 'n' is a constant known as the demagnetization factor. As an example, table A.1 lists the demagnetization constant for fields applied both radially and perpendicular to a cylindrical sample of radius 'R' and thickness 't' shown diagramatically in figure A.3. Clearly from the discussion above the radial field, H_ρ, is least perturbed for a thin ($t \rightarrow 0$) sheet-like ($R \rightarrow \infty$) sample (*ie.* from table A.1, n_ρ=0 for $\frac{t}{2R} = 0$). Similarly the axial field, H_z, will be least affected by a long thin sample (*ie.* $t \rightarrow \infty, R \rightarrow 0$) so that $n_z \rightarrow 0$ for $\frac{t}{2R} \rightarrow \infty$ in table A.1. Thus it can be understood why, experimentally, the demagnetization factor for the $H \parallel c$ geometry of the plate-like cuprate superconductors (with the c-direction being the short dimension) is larger than for the $H \perp c$ geometry.

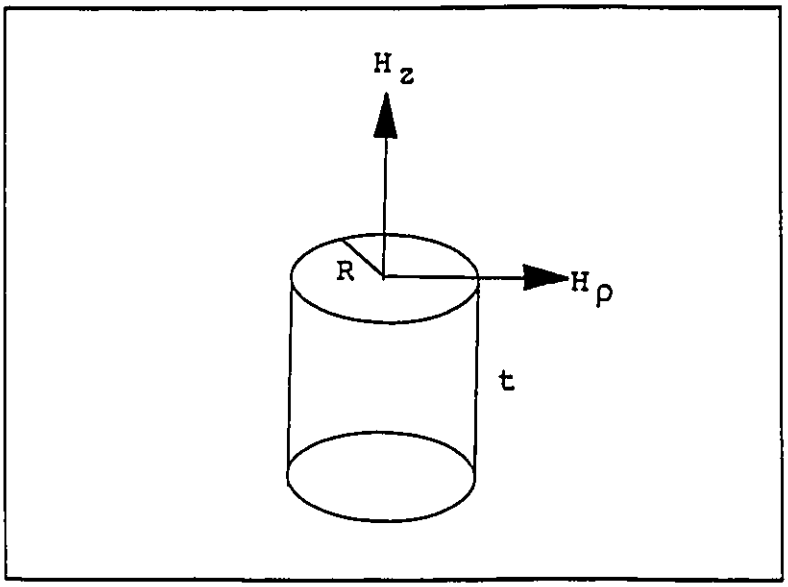

Figure A.3: Sample geometry corresponding to table A.1.

Table A.1: Demagnetization factors for a cylindrical sample of radius R and thickness t for the field applied both radially, n_ρ, and axially, n_z. (Values taken from [31]).

$\frac{t}{2R}$	n_z	n_ρ	$\frac{t}{2R}$	n_z	n_ρ
0	1	0	2.5	0.149	0.425
0.2	0.680	0.159	3.0	0.127	0.436
0.4	0.528	0.235	4.0	0.0978	0.451
0.6	0.430	0.284	5.0	0.0793	0.460
0.8	0.361	0.319	6.0	0.0666	0.467
1.0	0.311	0.344	8.0	0.0503	0.475
1.5	0.230	0.384	10.0	0.0403	0.480
2.0	0.181	0.409	∞	0	1

A.2.2 Volume Fraction Revisited

The demagnetizing field will also affect the calculation of the volume fraction of superconducting material. For a superconductor $M = -\frac{1}{4\pi}H_i$ so that equation A.16 can be rearranged to read:

$$H_a = H_i - 4\pi n\frac{1}{4\pi}H_i, \tag{A.17}$$

so that

$$H_i = \frac{1}{1-n}H_a. \tag{A.18}$$

But, the volume fraction of superconducting material, x, is given by $-4\pi\frac{M}{H}$ where $H = H_i$ *ie.* the field experienced by the sample. Thus,

$$x = -4\pi(1-n)\frac{M}{H_a}, \tag{A.19}$$

where H_a is the applied field. The working result is thus

$$x = -4\pi(1-n)(\text{SLOPE}), \tag{A.20}$$

where, as before, 'SLOPE' is the slope of the low field M versus H curve.

A.2.3 The Intermediate State

Another consequence of the presence of the demagnetizing field is the development of macroscopic normal regions within the superconducting sample known as the intermediate state.

Consider what happens when $H_i = H_c$ where H_c is the critical field. *ie.* a field, $H_a\prime$, is applied such that from equation A.18:

$$H_c = \frac{1}{1-n}H_a\prime. \tag{A.21}$$

Rearranging this

$$H_a\prime = (1-n)H_c. \tag{A.22}$$

Now, since $n > 0$, $H_a\prime < H_c = H_i$. Does the sample become normal because the internal field is equal to the critical field? This cannot be so because if the sample

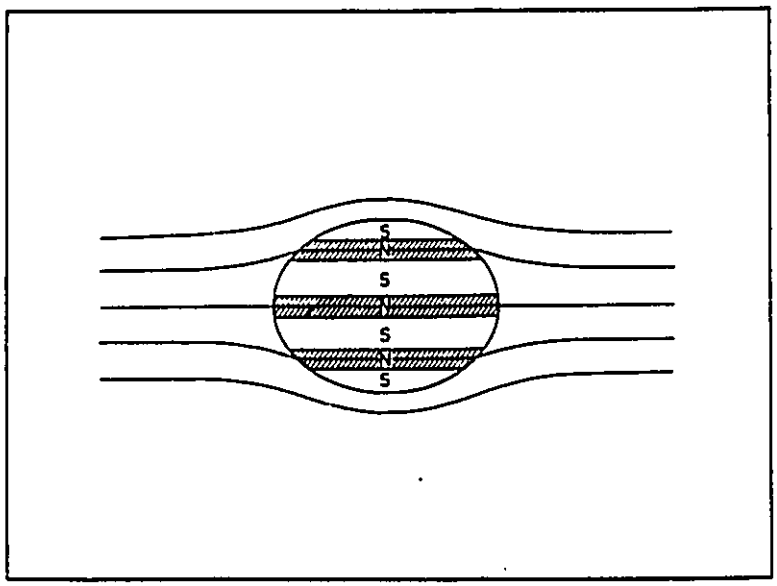

Figure A.4: Schematic representation of the intermediate state. (After [25]).

reverts to the normal state $M = 0$ and consequently $n = 0$ so that now $H_i = H_a{}' < H_c$. *ie.* the sample is normal in a field smaller than H_c! What actually happens is that macroscopic normal regions appear in the sample through which the flux can penetrate as illustrated in figure A.4. Thus in effect, we are reducing the volume fraction of superconducting material is reduced such that from $H_a{}' \leq H \leq H_c$ the fraction decreases steadily from 1 to zero so that as expected it is only at $H = H_c$ that the entire sample becomes normal. The situation depicted in figure A.4 is referred to as the intermediate state.

Appendix B

Optical Analysis

B.1 Introduction

In this appendix, which has been adapted from reference [52], an elementary discussion of the optical properties of a solid is presented with an emphasis on measurement and subsequent analysis via reflectance spectroscopy. The approach is that of Wooten.[143] The discussion of the Lorentz-Drude oscillator model has been extended from that of reference [52] to include the coupled electron-phonon model.

B.2 Interaction of Electromagnetic Radiation with Matter

An elementary discussion of the optical properties of solids can be found in most introductory texts on solid state physics.[50, 144] A brief account of the more salient features is presented here.

As is customary in electromagnetic theory, Maxwell's equations in macroscopic form are given (in Gaussian units) by:

$$\nabla \cdot \mathbf{E} = 4\pi\rho^{total}\,, \tag{B.1}$$

$$\nabla \times \mathbf{E} = -\frac{1}{c}\frac{\partial \mathbf{B}}{\partial t}, \tag{B.2}$$

$$\nabla \cdot \mathbf{B} = 0, \tag{B.3}$$

$$\nabla \times \mathbf{B} = \frac{1}{c}\frac{\partial \mathbf{E}}{\partial t} + \frac{4\pi}{c}\mathbf{J}^{total}, \tag{B.4}$$

where E and B are the electric and magnetic fields respectively, ρ^{total} and $\mathbf{J}^{total}$ are respectively the total charge and current densities and c is the speed of light in a vacuum.

ρ^{total} is comprised of a contribution due to polarization of the electronic charge distribution of each atom with respect to the nucleus in the presence of an electric field given by $-\nabla \cdot \mathbf{P}$, where P is the dipole moment per unit volume (polarization), and a contribution due to the presence of an external charge density, ρ^{ext}.

Thus,

$$\rho^{total} = -\nabla \cdot \mathrm{P} + \rho^{ext}. \tag{B.5}$$

Contributions to J^{total} arise in four ways: (1) polarization of the lattice due to a time varying electric field which contributes a factor of $\frac{\partial \mathrm{P}}{\partial t}$ to the current density, (2) magnetization effects resulting from electron spin whose corresponding current density distribution is $c(\nabla \times \mathrm{M})$ where M is the magnetic dipole moment per unit volume, (3) motion of conduction electrons where the contribution is denoted by J^{cond} and (4) external sources whose contribution is J^{ext}. Thus,

$$\mathrm{J}^{total} = \frac{\partial \mathrm{P}}{\partial t} + c(\nabla \times \mathrm{M}) + \mathrm{J}^{cond} + \mathrm{J}^{ext}. \tag{B.6}$$

Equations B.1 and B.4 can be written, using B.5 and B.6 as:

$$\nabla \cdot \mathrm{E} = -4\pi \nabla \cdot \mathrm{P} + 4\pi \rho^{ext}, \tag{B.7}$$

$$\nabla \times \mathrm{B} = \frac{1}{c}\frac{\partial \mathrm{E}}{\partial t} + \frac{4\pi}{c}\left(\frac{\partial \mathrm{P}}{\partial t} + c(\nabla \times \mathrm{M}) + \mathrm{J}^{cond} + \mathrm{J}^{ext}\right). \tag{B.8}$$

Defining the displacement as:

$$\mathrm{D} = \mathrm{E} + 4\pi \mathrm{P} = \epsilon_1 \mathrm{E}, \tag{B.9}$$

and the magnetic field strength as:

$$\mathrm{H} = \mathrm{B} - 4\pi \mathrm{M} = \frac{1}{\mu}\mathrm{B}, \tag{B.10}$$

where the assumption that the polarization and the magnetization can be linearly related to the electric and magnetic fields via the constants ϵ_1 and $1/\mu$ respectively has been made, Maxwell's equations can then be written as:

$$\nabla \cdot (\epsilon_1 \mathrm{E}) = 4\pi \rho^{ext}, \tag{B.11}$$

$$\nabla \times \mathrm{E} = -\frac{\mu}{c}\frac{\partial \mathrm{H}}{\partial t}, \tag{B.12}$$

$$\nabla \cdot (\mu \mathrm{H}) = 0, \tag{B.13}$$

$$\nabla \times \mathrm{H} = \frac{1}{c}\frac{\partial}{\partial t}(\epsilon_1 \mathrm{E}) + \frac{4\pi}{c}\mathrm{J}^{cond} + \frac{4\pi}{c}\mathrm{J}^{ext}. \tag{B.14}$$

In equations B.11–B.14 above, μ is the magnetic permeability and is equal to unity for nonmagnetic materials, and ϵ_1, the dielectric function, is a real quantity which connects the field D with the field E existing at all other locations and earlier times.

In the absence of external sources and using $\mathrm{J}^{cond} = \sigma_1 \mathrm{E}$, Maxwell's equations for a non-magnetic, isotropic material become:

$$\nabla \cdot \mathrm{E} = 0 \,, \tag{B.15}$$

$$\nabla \times \mathrm{E} = -\frac{1}{c}\frac{\partial \mathrm{H}}{\partial t}, \tag{B.16}$$

$$\nabla \cdot \mathrm{H} = 0 \,, \tag{B.17}$$

$$\nabla \times \mathrm{H} = \frac{\epsilon_1}{c}\frac{\partial \mathrm{E}}{\partial t} + \frac{4\pi\sigma_1}{c}\mathrm{E} \,, \tag{B.18}$$

where σ_1 is an 'optical' conductivity because it arises from electronic transitions accompanying photon absorption.

Using Maxwell's equations as given above and the vector identity:

$$\nabla \times (\nabla \times \mathrm{E}) = \nabla(\nabla \cdot \mathrm{E}) - \nabla^2 \mathrm{E} \,, \tag{B.19}$$

the wave equation for a plane wave propagating in an energy-absorbing medium is obtained:

$$\nabla^2 \mathrm{E} = \frac{\epsilon_1 \mu}{c^2}\frac{\partial^2 \mathrm{E}}{\partial t^2} + \frac{4\pi\sigma_1}{c^2}\frac{\partial \mathrm{E}}{\partial t}. \tag{B.20}$$

A vector field, F, can be divided into longitudinal and transverse components according to:

$$\mathrm{F} = \mathrm{F}^T + \mathrm{F}^L \,. \tag{B.21}$$

Furthermore, it can be shown that in general:

$$\nabla \times \mathrm{F} = \nabla \times \mathrm{F}^T \,, \tag{B.22}$$

$$\nabla \cdot \mathrm{F} = \nabla \cdot \mathrm{F}^L \,. \tag{B.23}$$

Thus, since $\nabla \cdot \mathbf{E} = 0$, the solution to equation B.20 is necessarily transverse (*ie.* E is perpendicular to the direction of propagation of the electromagnetic wave in the medium, q). Substitution into equation B.20 of a plane wave solution:

$$\mathbf{E} = \mathbf{E}_o e^{i(\mathbf{q}\cdot\mathbf{r}-\omega t)} , \tag{B.24}$$

where $\mathbf{E}_o$ is perpendicular to q, as required above, and which is valid at energies in the far-infrared where the spatial variation of E is large compared to lattice dimensions, gives:

$$q^2 = \frac{\omega^2}{c^2}\left(\epsilon_1 + i\frac{4\pi\sigma_1}{\omega}\right) . \tag{B.25}$$

Using equation B.25 and recalling that the velocity of the electromagnetic wave in a medium is given by $v = \omega/q$, and the usual definition of the index of refraction, $N = c/v$, the complex index of refraction is given by:

$$N = n + ik = \sqrt{\epsilon_1 + i\frac{4\pi\sigma_1}{\omega}} . \tag{B.26}$$

Defining the complex dielectric function and conductivity to be respectively:

$$\epsilon = \epsilon_1 + i\epsilon_2 = N^2 , \tag{B.27}$$

$$\sigma = \sigma_1 + i\sigma_2 , \tag{B.28}$$

yields:

$$\epsilon_1 = (n^2 - k^2) = 1 - \frac{4\pi\sigma_2}{\omega} , \tag{B.29}$$

$$\epsilon_2 = 2nk = \frac{4\pi\sigma_1}{\omega} . \tag{B.30}$$

Note that here n represents the real part of the complex refractive index, not the demagnetization factor as in appendix A.

N, ϵ and σ are the optical properties of primary interest. From these relations it is clear that knowledge of any one gives the others. The remainder of this appendix is concerned with the determination of these quantities and includes a discussion of a theoretical model for ϵ based on the classical theories of Lorentz and Drude which

is extended to include a coupled electron-phonon interaction, the relationship of n and k to the experimentally observable quantity; the reflectance, and the numerical procedures involved in extracting the optical constants from reflectance data including Kramers-Kronig analysis, oscillator model fits and sum rules.

B.3 Oscillator Model for ϵ

In the Lorentz model, the equation of motion for a bound oscillator (assumed for the sake of this discussion to be an electron) of charge e and mass m driven by a time varying electric field $\mathbf{E} = E_o e^{-i\omega t}$ is given by:

$$e\mathbf{E} - m\omega_o{}^2\mathrm{x} - m\Gamma\dot{\mathrm{x}} = m\ddot{\mathrm{x}} \ , \tag{B.31}$$

where the first term is the driving force, the second term is a Hooke's law restoring force which binds the electron to the atom at a resonance frequency ω_o, and the last term is a damping term which arises as a result of various scattering mechanisms. Here Γ is the scattering rate, which is related to the lifetime, τ by $\Gamma = 1/\tau$. x is the coordinate frame for the electron.

Equation B.31 can be extended to include linear coupling to a phonon in coordinate frame y by adding a term, gy, where g is the coupling constant:

$$g\mathrm{y} + e\mathbf{E} - m\omega_o{}^2\mathrm{x} - m\Gamma\dot{\mathrm{x}} = m\ddot{\mathrm{x}} \ , \tag{B.32}$$

A solution of the form $\mathrm{x} = x_o e^{-i\omega t}$ and $\mathrm{y} = y_o e^{-i\omega t}$ yields:

$$x_o = \frac{\frac{g}{m}y_o + \frac{e}{m}E_o}{\omega_o{}^2 - \omega^2 - i\omega\Gamma} \ . \tag{B.33}$$

Writing:

$$D_o = \frac{1}{\omega_o{}^2 - \omega^2 - i\omega\Gamma} \ , \tag{B.34}$$

one obtains,

$$x_o = D_o[\frac{g}{m}y_o + \frac{e}{m}E_o] \tag{B.35}$$

Now consider the phonon of resonance frequency, ω', mass, m', effective charge, q', and scattering rate Γ'. The equation of motion is then:

$$g\mathrm{x} + q'\mathrm{E} - m'\omega'^2\mathrm{y} - m'\Gamma'\dot{\mathrm{y}} = m'\ddot{\mathrm{y}} \ , \tag{B.36}$$

Note that the phonon is coupled to the electron associated with the x coordinate frame of equation B.32 via the same coupling constant g. Again applying the plane wave solution yields:

$$y_o = \frac{\frac{g}{m'}x_o + \frac{q'}{m'}E_o}{\omega'^2 - \omega^2 - i\omega\Gamma'} \ . \tag{B.37}$$

With

$$D' = \frac{1}{\omega'^2 - \omega^2 - i\omega\Gamma'} \ , \tag{B.38}$$

one finds,

$$y_o = D'[\frac{g}{m'}x_o + \frac{q'}{m'}E_o]. \tag{B.39}$$

Substituting equation B.39 into B.35 yields:

$$x_o = D_o[\frac{g}{m}D'(\frac{g}{m'}x_o + \frac{q'}{m'}E_o) + \frac{e}{m}E_o]. \tag{B.40}$$

Rearranging:

$$x_o[\frac{1}{D_o} - \frac{g}{m}D'\frac{g}{m'}] = E_o[\frac{e}{m} + \frac{g}{m}D'\frac{q'}{m'}]. \tag{B.41}$$

Recalling that for the electron the magnitude of the polarization is given by $P_o = N_o e x_o$ and that from equation B.9 $\epsilon = 1 + 4\pi\frac{P_o}{E_o}$, the dielectric function can be written using B.41 as:

$$\epsilon = 1 + 4\pi N_o e\frac{[\frac{e}{m} + \frac{gq'}{mm'}D']}{[\frac{1}{D_o} - \frac{g^2}{mm'}D']}, \tag{B.42}$$

where N_o is the density of bound electrons. Thus, with equation B.34:

$$\epsilon = 1 + \frac{4\pi N_o e^2}{m}\frac{[1 + \frac{gq'}{m'e}D']}{[\omega_o{}^2 - \omega^2 - i\omega\Gamma - \frac{g^2}{mm'}D']}. \tag{B.43}$$

Writing:

$$\omega_p{}^2 = \frac{4\pi N_o e^2}{m} \ , \tag{B.44}$$

where ω_p is referred to as the plasma frequency;

$$\epsilon = 1 + \frac{\omega_p^2}{\omega_o^2 - D - \omega^2 - i\omega\Gamma}[1 + qD], \tag{B.45}$$

where:

$$D = \frac{g^2}{mm'}D' = \frac{\omega_{p'}^2}{\omega'^2 - \omega^2 - i\omega\Gamma'}, \tag{B.46}$$

$$\omega_{p'}^2 = \frac{g^2}{mm'}, \tag{B.47}$$

and,

$$q = \frac{mq'}{ge}. \tag{B.48}$$

Note that since an energy loss mechanism has been explicitly included, the dielectric function is now a complex quantity.

It can be shown that for a series of k phonons coupled to the same electronic oscillator at ω_o, the dielectric function is given by:

$$\epsilon = 1 + \frac{\omega_p^2}{\omega_o^2 - \sum_k D_k - \omega^2 - i\omega\Gamma}[1 + \sum_k q_k D_k], \tag{B.49}$$

where:

$$D_k = \frac{\omega_{p'_k}^2}{\omega_k'^2 - \omega^2 - i\omega\Gamma_k'}, \tag{B.50}$$

$$\omega_{p'_k}^2 = \frac{g_k^2}{mm_k'}, \tag{B.51}$$

and,

$$q_k = \frac{mq_k'}{g_k e}. \tag{B.52}$$

From equation B.45 the dielectric function for a collection of j uncoupled oscillators, bound with resonance frequencies ω_j, is given upon setting $D = 0$ by:

$$\epsilon = 1 + \sum_j \frac{\omega_{p_j}}{\omega_j^2 - \omega^2 - i\Gamma_j\omega}, \tag{B.53}$$

where ω_{p_j} is the plasma frequency associated with the electron bound with resonance frequency ω_j and scattering rate Γ_j. In equation B.53 $\sum_j \omega_{p_j} = \frac{4\pi N_{tot}e^2}{m}$, where N_{tot} is the total number of bound electrons.

The quantum mechanical analog can be shown to be:

$$\epsilon = 1 + \frac{4\pi N_{tot} e^2}{m} \sum_j \frac{f_j}{\omega_j{}^2 - \omega^2 - i\Gamma_j \omega} \tag{B.54}$$

where ω_j is the transition frequency of an electron between two atomic states separated in energy by $\hbar\omega_j$, and f_j, the oscillator strength, is a measure of the relative probability of a quantum mechanical transition, and satisfies:

$$\sum_j f_j = 1 \ . \tag{B.55}$$

This is known as the f-sum rule.

In a free-electron metal the conduction electrons are neither bound nor coupled, and hence in equation B.45 $D = 0$ and there is no restoring force (ie. $\omega_o = 0$). Thus, the contribution to the dielectric function from the free electrons with plasma frequency, ω_{P_D}, and scattering rate, Γ_D, is:

$$- \frac{\omega_{pD}^2}{\omega^2 + i\omega\Gamma_D} \ . \tag{B.56}$$

Combining B.56, B.53 and B.49 yields:

$$\begin{aligned} \epsilon \ = \ & 1 - \frac{\omega_{pD}^2}{\omega^2 + i\omega\Gamma_D} + \sum_j \frac{\omega_{p_j}^2}{\omega_j{}^2 - \omega^2 - i\Gamma_j\omega} + \\ & \frac{\omega_{p_e}^2}{\omega_e^2 - \sum_k D_k - \omega^2 - i\omega\Gamma_e}[1 + \sum_k q_k D_k]; \end{aligned} \tag{B.57}$$

the dielectric function for a system of free electrons, j bound oscillators of frequencies ω_j and k phonons of frequencies ω_k coupled to an electronic oscillator positioned at ω_e. Note that the subscript e has been added to denote the oscillator to which the phonons couple. D_k is given, by equation B.50.

B.4 Relationship between Reflectance and Refractive Index

As can be deduced from the previous section ϵ_1, ϵ_2, and hence σ_1 and σ_2 contain valuable information pertaining to the physical properties of the solid, such as, the

extent of the free carrier response and the excitations that are present. They are, however, difficult to measure directly. The real and imaginary parts of the refractive index, n and k respectively, (and hence, ϵ_1, ϵ_2, and σ_1, σ_2) are fortunately related to the experimentally accessible quantity the reflectance, R, by the generalized Fresnel reflection coefficients, which for an angle of incidence, ϕ, measured from the surface normal are given by:[145]

$$R_s = \frac{(a - \cos\phi)^2 + b^2}{(a + \cos\phi)^2 + b^2} , \tag{B.58}$$

$$R_p = R_s \frac{(a - \sin\phi\tan\phi)^2 + b^2}{(a + \sin\phi\tan\phi)^2 + b^2} , \tag{B.59}$$

where R_s is the component of specular reflection perpendicular to the plane of incidence and R_p is the parallel component. The measured reflectance is given by:

$$R = \frac{1}{2}[R_p(1 + p) + R_s(1 - p)] , \tag{B.60}$$

where p is the polarization of the incident radiation given by:

$$p = \frac{I_p - I_s}{I_p + I_s} . \tag{B.61}$$

I_s and I_p represent respectively the components of the incident radiant flux density perpendicular and parallel to the plane of incidence. For unpolarized light $I_s = I_p$ and $p = 0$ so that $R = \frac{1}{2}(R_s + R_p)$. The parameters a and b are related to the optical constants n and k by:

$$a^2 = \frac{1}{2}\left\{[(n^2 - k^2 - \sin^2\phi)^2 + 4n^2k^2]^{\frac{1}{2}} + (n^2 - k^2 - \sin^2\phi)\right\} , \tag{B.62}$$

$$b^2 = \frac{1}{2}\left\{[(n^2 - k^2 - \sin^2\phi)^2 + 4n^2k^2]^{\frac{1}{2}} - (n^2 - k^2 - \sin^2\phi)\right\} . \tag{B.63}$$

At normal incidence, ($\phi = 0$), $R_s = R_p = R$ and equations B.58 through B.63 reduce to:

$$R = \frac{(n - 1)^2 + k^2}{(n + 1)^2 + k^2} . \tag{B.64}$$

The Fresnel coefficients are derived by consideration of the boundary conditions of E and H at a vacuum-crystal interface.[146] The derivation for the reflectance at

normal incidence using this approach is fairly straightforward and can be found in the literature.[143]

Usually a reflectance measurement is made at near-normal incidence (*ie.* $\phi \sim 15°$). Examination of the Fresnel coefficients for near normal incidence leads to the conclusion that the reflectance is not significantly changed from that at normal incidence.[147] It is therefore usual to use the normal incidence expression for the reflectance, equation B.64, in a near-normal incidence experiment.

B.5 Analysis of Reflectance via Modeling of the Dielectric Function

Equations B.58 through B.64 cannot be solved explicitly for n and k. There are several methods by way of which n and k can be deduced. Several techniques exist which can be used if n and k are required at only a single wavelength.[145] These methods typically involve measurement of both R_s and R_p at one angle of incidence, or one component at two angles of incidence. The work of this thesis is concerned with the optical properties over a range of frequencies so that measurements of this sort are impractical. Establishing the frequency dependence of the optical properties from a measurement of the frequency dependence of the reflectance is usually accomplished in one of two ways, which serve as the topics of discussion in this and the following section.

Equations B.29 and B.30 can be solved for n and k to yield:

$$n = \frac{1}{\sqrt{2}}\sqrt{\sqrt{\epsilon_1{}^2 + \epsilon_2{}^2} + \epsilon_1}\ , \tag{B.65}$$

$$k = \frac{1}{\sqrt{2}}\sqrt{\sqrt{\epsilon_1{}^2 + \epsilon_2{}^2} - \epsilon_1}\ . \tag{B.66}$$

Substituting B.65 and B.66 into B.64 yields:

$$R = \frac{\sqrt{\epsilon_1{}^2 + \epsilon_2{}^2} + 1 - \sqrt{2(\sqrt{\epsilon_1{}^2 + \epsilon_2{}^2} + \epsilon_1}}{\sqrt{\epsilon_1{}^2 + \epsilon_2{}^2} + 1 + \sqrt{2(\sqrt{\epsilon_1{}^2 + \epsilon_2{}^2} + \epsilon_1}}\ . \tag{B.67}$$

By assuming a model with variable parameters such as that given in equation B.57, for the dielectric function, the experimentally measured reflectance data can be fit to equation B.67 above. The fitting parameters are ω_{p_D} and Γ_D, the plasma frequency and scattering rate of the free electrons, ω_{p_j}, ω_j and Γ_j, the strength, frequency and scattering rate of finite-frequency-centered oscillators (*eg.* IR-allowed phonons), and ω_e, Γ_e and ω_{p_e} the center frequency, scattering rate and plasma frequency of an electronic oscillator to which k phonons with position ω_k, scattering rate Γ_k and coupling strength, ω_{p_k} are coupled. Often the term of unity in equation B.57 is replaced by ϵ_∞, the high frequency dielectric constant, which may be enhanced from unity to represent effects due to excitations at energies above the range investigated, and thus becomes another parameter of the fit. Determination of these fitting parameters can provide useful information about the physical system under investigation.

B.6 Analysis using Kramers Kronig Dispersion Relations

An alternate method of analyzing the reflectance data is to make use of the Kramers-Kronig dispersion relations. In general a dispersion relation is an integral formula which relates a dispersive process to an absorption process. Dispersion relations follow from the principle of causality, the assertion that there can be no response before the arrival of a stimulus. The stimulus that is of concern in the study of the optical properties of a solid is an electromagnetic wave. Causality applies to this system in that energy cannot be reflected or absorbed before the arrival of the electromagnetic radiation at the crystal interface.

A response function describes the response of the system at time t to a stimulus at an earlier time t_o:

$$X(t) = \int_{-\infty}^{+\infty} G(t,t')f(t')dt' \ , \tag{B.68}$$

where $X(t)$ is the response of the system at time t to stimulus $f(t')$ acting for all times $t' \geq t_o$, and $G(t,t')$ is the response function, which by causality, is necessarily zero for $t < t_o$. Fourier transformation leads to the relation:

$$X(\omega) = G(\omega)f(\omega) \ , \tag{B.69}$$

so that the stimulus, $f(\omega)$, is simply multiplied by a number, $G(\omega)$, to give the response, $X(\omega)$.

It can be shown that the real and the imaginary parts of the response function, $G(\omega)$, are related according to:

$$\Re G(\omega) = \frac{2}{\pi} P \int_0^\infty \frac{\omega' \Im G(\omega')}{\omega'^2 - \omega^2} d\omega' \ , \tag{B.70}$$

$$\Im G(\omega) = -\frac{2\omega}{\pi} P \int_0^\infty \frac{\Re G(\omega')}{\omega'^2 - \omega^2} d\omega' \ , \tag{B.71}$$

where P refers to the principal value. These equations are known as the Kramers-Kronig dispersion relations. Dispersion relations of this form exist for many physical quantities including the real and imaginary parts of the refractive index, the dielectric function and the optical conductivity. These dispersion relations are powerful aids in the analysis of optical properties. For example, they provide the basis for the derivation of a very useful version of the f-sum rule:

$$\int_0^\infty \sigma_1(\omega) d\omega = \frac{{\omega_p}^2}{8} \ . \tag{B.72}$$

Unfortunately, for direct application to experiments, these equations have only limited usefulness.

Experimentally, R, the ratio of the reflected to incident intensities is measured. It is related to r, the complex ratio of outgoing to incoming electromagnetic fields by:

$$R(\omega) = r(\omega) r^*(\omega) \ , \tag{B.73}$$

where

$$r(\omega) = \frac{n - 1 + ik}{n + 1 + ik} \ . \tag{B.74}$$

Writing the complex reflectance amplitude as:

$$r(\omega) = \sqrt{R(\omega)}e^{i\theta(\omega)} , \tag{B.75}$$

equations B.74 and B.75 can be solved to yield n and k in terms of $R(\omega)$ and $\theta(\omega)$. Thus, if $R(\omega)$ and $\theta(\omega)$ are known then n and k, and hence, ϵ_1, ϵ_2, and σ_1, σ_2 can be calculated. R is measured experimentally and θ is related to R through the Kramers-Kronig relation:

$$\theta(\omega) = -\frac{\omega}{\pi}\int_0^\infty \frac{\ln R(\omega') - \ln R(\omega)}{\omega'^2 - \omega^2}d\omega' , \tag{B.76}$$

where the principal value has been eliminated by subtracting an integral that is identically equal to zero.

Experimentally the reflectance is measured only over a finite range of frequencies, $\omega_1 \leq \omega \leq \omega_2$, and thus extrapolations of the function $R(\omega)$ are required for the limits of the integration.

In the high frequency limit extrapolations that are commonly used include a power law: $R(\omega) = R(\omega_2)[\omega_2/\omega]^p$, an exponential: $R(\omega) = R(\omega_2)e^{B(\omega_2-\omega)}$ or simply a constant: $R(\omega) = C$. The parameters p, B and C are chosen to provide physically reasonable results. Evaluation of equation B.72 should yield a value consistent with the total number of electrons expected to contribute to the optical conductivity:

$$\omega_p^2 = \frac{4\pi N_{tot}e^2}{m}. \tag{B.77}$$

For example, in aluminum, which has three valence electrons, one must choose an extrapolation such that upon integrating the frequency-dependent conductivity up to a reasonably large cutoff beyond which it is negligible, one finds a value for N_{tot} of $3e$/atom.

The long wavelength extrapolation is usually provided by either an oscillator fit to the reflectance data as described in the previous section or by the Hagen-Rubens relation which is valid for $\omega/\Gamma \ll 1$ and is given by:[148]

$$R(\omega) = 1 - \frac{2}{n} = 1 - 2\sqrt{\frac{2\omega\Gamma}{\omega_p{}^2}} . \tag{B.78}$$

Since both the oscillator fit and the Kramers-Kronig methods of evaluating reflectance data involve a degree of uncertainty, *ie.* the extrapolations to low and high frequency in the case of Kramers-Kronig analysis and the model chosen for the dielectric function in the oscillator fit method, the results should be carefully considered and tested for their dependence on these approximations.

A more thorough, detailed treatment of the numerical procedures for analyzing reflectance data including discussions of oscillator least squares fitting, possible extrapolations for the Kramers-Kronig analysis, their validity, and the uncertainty introduced through their use can be found in the literature.[143, 148, 148]

Appendix C

Experimentally Derived Phonon Parameters

Table C.1: E$\|$ a, b phonon parameters for $Pb_2Sr_2RCu_3O_8$ with R $\equiv$ La at 300 and 80 K derived from oscillator fitting (brackets) and the Kramers-Kronig technique. Values for ϵ_∞ of 13.2 and 11.5 were obtained at 300 and 80 K respectively.

Mode	T (K)	ω_{TO} ($\pm$1 cm^{-1})		ω_{LO} ($\pm$1 cm^{-1})		Γ ($\pm$1 cm^{-1})		S	
1^{ab}	300	575.5	(576)	616	(602)	25	(30)	0.7 $\pm$ 0.1	(1.2)
	80	589	(587)	625	(616)	15	(27)	0.7 $\pm$ 0.1	(1.2)
2^{ab}	300	348	(348)	420	(388)	11.5	(7.3)	2.7 $\pm$ 0.3	(3.2)
	80	350.5	(351)	422.5	(388)	6	(5.3)	2.6 $\pm$ 0.5	(2.6)
3^{ab}	300	311	(309)	320	(356)	31 $\pm$ 2	(60)	1.4 $\pm$ 0.7	(4.3)
	80	316	(315)	328	(347)	25.5	(32)	1.9 $\pm$ 0.4	(2.5)
4^{ab}	300	286	(286)	296	(290)	31 $\pm$ 2	(10)	2.3 $\pm$ 0.7	(0.3)
	80	289.5	(289)	301.5	(303)	14	(9)	2.0 $\pm$ 0.3	(1.1)
5^{ab}	300	229.5	(232)	252	(263)	31.5	(29)	3.8 $\pm$ 1.1	(3.8)
	80	237	(237)	257	(276)	14	(21)	2.7 $\pm$ 0.4	(4.1)
7^{ab}	300	193.5	(195)	205	(207)	26.5	(14)	3.2 $\pm$ 1.0	(1.7)
	80	188	(188)	197.5	(192)	5.5	(5)	0.5 $\pm$ 0.3	(0.5)
8^{ab}	300	165.5	(165)	181	(224)	12.5	(10)	10.4 $\pm$ 1.5	(11.2)
	80	166	(166)	183	(231)	6	(10)	4.4 $\pm$ 1.1	(10.8)

Table C.2: E$\|$ a,b phonon parameters for $Pb_2Sr_2RCu_3O_8$ with R $\equiv$ Ce at 300 and 80 K derived from oscillator fitting (brackets) and the Kramers-Kronig technique. Values for ϵ_∞ of 6.38 and 6.58 were obtained at 300 and 80 K respectively.

Mode	T	ω_{TO}		ω_{LO}		Γ		S	
	(K)	($\pm$1	cm^{-1})	($\pm$1	cm^{-1})	($\pm$1	cm^{-1})		
1^{ab}	300	580.5	(582)	604.5	(597)	20	(21.1)	0.3 ± 0.1	(0.3)
	80	591	(591)	616.5	(607)	8	(10.3)	0.3 ± 0.1	(0.4)
2^{ab}	300	351.5	(352)	428.5	(403)	20.5	(22.7)	0.7 ± 0.1	(2.0)
	80	354	(352)	429.5	(397)	7	(12.4)	1.4 ± 0.2	(1.8)
3^{ab}	300	305.5	(307)	324.5	(341)	18.5	(16)	1.8 ± 0.2	(1.5)
	80	311.5	(312)	328	(348)	7	(8.7)	1.5 ± 0.2	(1.6)
4^{ab}	300	290.5	(290)	293	(299)		(18)		(0.4)
	80	291.5	(292)	294.5	(301)	11 ± 2	(8)	0.6 ± 0.1	(0.4)
5^{ab}	300	238.5	(241)	242	(251)	25	(20)	0.7 ± 0.2	(0.5)
	80	248	(248)	254.5	(262)	21.5	(17)	0.9 ± 0.1	(0.7)
7^{ab}	300	184.5	(186)	196.5	(202)	8.5	(11.3)	1.1 ± 0.2	(1.1)
	80	180.5	(181)	194	(195)		(5.5)	0.9 ± 0.3	(1.1)
8^{ab}	300	149.5	(149)	164	(186)	9	(9)	2.8 ± 0.5	(3.5)
		138.5				3		0.3 ± 0.1	
	80	147.5	(149)	165.5	(196)	2 ± 0.5	(7.8)	2.0 ± 0.5	(4.8)
		144				2		1.1 ± 0.6	
10^{ab}	300	135							
	80	134	(132)		(134)	3	(3)	0.5 ± 0.2	(0.2)

Table C.3: E$\|$ a, b phonon parameters for $Pb_2Sr_2RCu_3O_8$ with R $\equiv$ Pr at 300 and 80 K derived from oscillator fitting (brackets) and the Kramers-Kronig technique. Values for ϵ_∞ of 6.98 and 7.18 were obtained at 300 and 80 K respectively.

Mode	T (K)	ω_{TO} ($\pm$1 cm^{-1})		ω_{LO} ($\pm$1 cm^{-1})		Γ ($\pm$1 cm^{-1})		S	
1^{ab}	300	606	(599)	631	(627)	56.5	(65)	0.5 $\pm$ 0.1	(0.7)
	80	614.5	(613)	639.5	(637)	44	(48)	0.5 $\pm$ 0.1	(0.6)
2^{ab}	300	354	(352)	420.5	(397)	19.5	(22.5)	1.7 $\pm$ 0.2	(1.9)
	80	354.5	(354)	421.5	(397)	15.5	(16.9)	1.8 $\pm$ 0.2	(1.9)
3^{ab}	300	306	(307)	320.5	(346)	30 $\pm$ 2	(23.8)	1.3 $\pm$ 0.5	(1.1)
	80	311	(313)	327	(335)	11	(14.2)	0.9 $\pm$ 0.2	(1.0)
4^{ab}	300	282	(282)	288.5	(293)	19 $\pm$ 2	(16.3)	0.8 $\pm$ 0.4	(0.6)
	80	284.5	(287)	296.5	(302)	14	(11.5)	0.9 $\pm$ 0.3	(0.8)
5^{ab}	300	228.5	(230)	248.5	(267)	33.5	(39.8)	1.5 $\pm$ 0.8	(2.5)
	80	234	(237)	255.5	(268)	14	(18.9)	1.4 $\pm$ 0.4	(2.0)
6^{ab}	300	207.5	(212)		(214)	10	(7)	0.4 $\pm$ 0.3	(0.1)
	80	211.5	(212)	213	(214)	8.5	(7)	0.1 $\pm$ 0.2	(0.1)
7^{ab}	300	190.5	(193)	199	(206)	9 $\pm$ 2	(14.6)	0.5 $\pm$ 0.4	(0.9)
	80	189.5	(191)	197	(201)	9	(12.4)	0.4 $\pm$ 0.3	(0.8)
8^{ab}	300	168	(169)	178.5	(201)	10	(7.37)	3.2 $\pm$ 0.8	(2.9)
	80	170.5	(172)	181	(202)	3.5	(3.55)	1.5 $\pm$ 0.6	(2.7)
9^{ab}	300		(146)		(151)		(10)		(0.5)
	80		(146)		(151)		(10)		(0.5)

Table C.4: E$\|$ a, b phonon parameters for $Pb_2Sr_2RCu_3O_8$ with R $\equiv$ Nd at 300 and 80 K derived from oscillator fitting (brackets) and the Kramers-Kronig technique. Values for ϵ_∞ of 7.08 and 7.19 were obtained at 300 and 80 K respectively.

Mode	T (K)	ω_{TO} ($\pm$1 cm^{-1})		ω_{LO} ($\pm$1 cm^{-1})		Γ ($\pm$1 cm^{-1})		S	
1^{ab}	300	614.5	(613)	643	(638)	31.5	(53.3)	0.4 $\pm$ 0.1	(0.6)
	80	627	(625)	650.5	(646)	18.5	(34.6)	0.3 $\pm$ 0.1	(0.5)
2^{ab}	300	355.5	(354)	422	(396)	17	(21.4)	1.7 $\pm$ 0.2	(1.8)
	80	356.5	(354)	422.5	(394)	12.5	(14.9)	1.8 $\pm$ 0.2	(1.7)
3^{ab}	300	306	(306)	322	(334)	27 $\pm$ 2	(25.4)	1.5 $\pm$ 0.4	(1.4)
	80	310	(312)	327.5	(337)	11.5	(15.4)	1.1 $\pm$ 0.2	(1.2)
4^{ab}	300	280.5	(280)	284.5	(289)	17 $\pm$?	(15.3)	0.5 $\pm$ 0.4	(0.5)
	80	284	(285)	292.5	(298)	9.5	(8.9)	0.8 $\pm$ 0.2	(0.7)
5^{ab}	300	231	(231)	249	(268)	32 $\pm$ 2	(34.3)	2.3 $\pm$ 0.5	(2.4)
	80	234.5	(237)	254	(269)	5	(17.4)	1.0 $\pm$ 0.3	(2.1)
6^{ab}	300	212	(210)		(213)	7	(7.1)	0.2 $\pm$ 0.4	(0.2)
	80	212	(212)		(214)	6.5	(7)	0.3 $\pm$ 0.5	(0.1)
7^{ab}	300	193.5	(194)	198	(208)	5.5	(14.6)	0.4 $\pm$ 0.2	(1.0)
	80	192	(192)	198.5	(202)	13	(10.7)	0.9 $\pm$ 0.3	(0.8)
8^{ab}	300	171	(171)	179.5	(198)	9.5	(7.4)	2.7 $\pm$ 0.5	(2.4)
		164.5							
	80	170	(171)	181	(201)	2 $\pm$ 0.5	(2.8)	1.9 $\pm$ 0.5	(2.7)
		164.5				4.5		1.2 $\pm$ 0.4	
9^{ab}	300								
	80	145.5	(146)		(151)	7	(10)	0.1 $\pm$ 0.1	(0.5)

Table C.5: Detailed temperature dependence of the 'ordinary' E$\|a,b$ phonon parameters for $Pb_2Sr_2RCu_3O_8$ with R $\equiv$ Sm derived from the Kramers-Kronig technique.

Mode		7 K	15 K	25 K	35 K	50 K	65 K	80 K	100 K	150 K	200 K	250 K	300 K
1[a,b]	ω_{TO}		621	622	620.5	621.5	622	620.5	621.5	618.5	615	615	611.5
2[a,b]	ω_{TO}	350	350.5	350.5	350.5	351	351	351	351.5	351.5	351	351	350.5
	ω_{LO}	426	424.5	425.5	426.5	426.5	426.5	426.5	427	428	429	428	427
	S/ϵ_∞	0.481	0.467	0.474	0.481	0.476	0.476	0.476	0.476	0.483	0.494	0.487	0.484
3[a,b]	ω_{TO}	307	307	307	307	307	307	307	306.5	305.5	304	301	299
	ω_{LO}	324.5	324	322.5	324.5	324.5	325	324.5	324.5	324.5	323.5	323.5	321
	S/ϵ_∞	0.117	0.114	0.104	0.117	0.117	0.121	0.117	0.121	0.128	0.132	0.155	0.153
4[a,b]	ω_{TO}	282	282	282.5	282.5	282.5	282.5	282.5	282	282	281.5	281	280.5
	ω_{LO}	290.5	291	291	291	291.5	291	291	291	289	288.5	287	283.5
	S/ϵ_∞	0.061	0.065	0.061	0.061	0.065	0.061	0.061	0.065	0.050	0.050	0.043	0.022
5[a,b]	ω_{TO}	231	230.5	231	231	230.5	230.5	230.5	230	229	227.5	226.5	225.5
	ω_{LO}	250	250	250	249	251	250.5	251	251	251.5	251	250.5	250
	S/ϵ_∞	0.171	0.176	0.171	0.162	0.186	0.181	0.186	0.191	0.206	0.217	0.223	0.229
6a[a,b]	ω_{TO}	218.5	218.5	218.5	218.5	218.5	218	218.5	218	218	217	217	215.5
	ω_{LO}	221	221.5	221.5	222	222	221.5	221.5	222	221.5	222	224	222.5
	S/ϵ_∞	0.023	0.028	0.028	0.032	0.032	0.032	0.028	0.037	0.032	0.047	0.066	0.066
6b[a,b]	ω_{TO}	208	208	207.5	207.5	208	208	207.5	207.5	206.5			
	ω_{LO}	209	209	208	208.5	209	209.5	209.5	209	210			
	S/ϵ_∞	0.010	0.010	0.005	0.010	0.010	0.014	0.019	0.015	0.034			
7[a,b]	ω_{TO}	186.5	186	186.5	186.5	186.5	186.5	186.5	186.5	187.5	188.5	187.5	188
	ω_{LO}	198	197.5	198	198	198.5	198.5	199	199.5	201	201.5	202	204
	S/ϵ_∞	0.127	0.127	0.127	0.127	0.133	0.133	0.139	0.144	0.149	0.143	0.161	0.177
8[a,b]	ω_{TO}	164	164	164	164	164	164	164	163.5	162	161.5		
	ω_{LO}	177.5	177.5	177.5	177.5	177.5	178	178	178	178	178		
	S/ϵ_∞	0.171	0.171	0.171	0.171	0.171	0.178	0.178	0.185	0.207	0.215		
8b[a,b]	ω_{TO}	159.5	159.5	159.5	159.5	159.5	159.5	158.5	158	157.5	157	158	157
	ω_{LO}	162	162	161.5	162	162	161.5	161.5	161.5	160	160	178	177.5
	S/ϵ_∞	0.032	0.032	0.025	0.032	0.032	0.025	0.038	0.045	0.032	0.039	0.269	0.278
9[a,b]	ω_{TO}	144.5	144.5	144.5	145.5	144	144.5	143	144.5	143.5	144	142	140
	ω_{LO}	149.5	149.5	150	149.5	149	150	150	149.5	149	148	148	148.5
	S/ϵ_∞	0.070	0.070	0.078	0.056	0.071	0.078	0.100	0.070	0.078	0.056	0.086	0.125
10[a,b]	ω_{TO}	136	135	136.5	136	136	136	135.5	135.5	135.5	134.5	132.5	
	ω_{LO}	138.5	138.5	139	139	138.5	139	138.5	139	138	137.5	137.5	
	S/ϵ_∞	0.037	0.053	0.052	0.045	0.037	0.045	0.045	0.052	0.037	0.045	0.077	

Table C.6: Detailed temperature dependence of the 'ordinary' E$\|a,b$ phonon parameters for $Pb_2Sr_2RCu_3O_8$ with R $\equiv$ Eu derived from the Kramers-Kronig technique.

Mode		7 K	15 K	25 K	35 K	50 K	65 K	80 K	100 K	150 K	200 K	250 K	300 K
1[a,b]	ω_{TO}	632.5	633	632.5	631	632.5	630.5	630	628.5	626	627	622	617
2[a,b]	ω_{TO}	355.5	355.5	356	356	356	356.5	356.5	356	356.5	357	356.5	355.5
	ω_{LO}	434	436	433	434.5	433.5	433.5	436	436	437.5	440	438	440
	S/ϵ_∞	0.490	0.500	0.479	0.490	0.483	0.479	0.496	0.500	0.506	0.519	0.509	0.532
3[a,b]	ω_{TO}	306.5	307	306.5	307.5	306.5	306.5	306.5	307	305	304	300	297.5
	ω_{LO}	320	322	323.5	322.5	324	323.5	325.5	324.5	324	324	322	323
	S/ϵ_∞	0.090	0.100	0.114	0.100	0.117	0.114	0.128	0.117	0.128	0.136	0.152	0.179
4[a,b]	ω_{TO}	282.5	282.5	282.5	283	283	282	282.5	283	283	280.5	278	280
	ω_{LO}	290	291	290.5	290	289	290	291.5	290	287.5	285	286.5	283.5
	S/ϵ_∞	0.054	0.061	0.057	0.050	0.043	0.058	0.065	0.050	0.032	0.032	0.062	0.025
5[a,b]	ω_{TO}	231.5	232	232.5	231	232	232	232	231.5	231.5			
	ω_{LO}	240	243	244	244	246	244	246.5	246	248	249.5	245	247.5
	S/ϵ_∞	0.075	0.097	0.101	0.116	0.124	0.106	0.129	0.129	0.148			
6a[a,b]	ω_{TO}	218.5	219	218.5	219	218.5	219	218.5	219	216.5	220.5	213	211.5
	ω_{LO}	222	225.5	223	222.5	222	224	225	223.5	224.5			
	S/ϵ_∞	0.032	0.060	0.042	0.032	0.032	0.046	0.060	0.042	0.075	0.280	0.323	0.369
7[a,b]	ω_{TO}	192.5	193.5	192.5	192	192	193	192.5	192.5	195.5	193.5	193	193.5
	ω_{LO}	198	199	199	198	200	200.5	201.5	203.5	202	203.5	204	203
	S/ϵ_∞	0.058	0.058	0.069	0.063	0.085	0.079	0.096	0.118	0.068	0.106	0.117	0.101
8a[a,b]	ω_{TO}	168.5	169	169	169.5	168.5	168.5	169.5	169	169.5	170	167.5	167.5
	ω_{LO}	176.5	177	176	177.5	176	180	179.5	179	178.5	179.5	179	178.5
	S/ϵ_∞	0.097	0.097	0.085	0.097	0.091	0.141	0.121	0.122	0.109	0.115	0.142	0.136

Table C.7: Detailed temperature dependence of the 'coupled' E$\|a,b$ phonon parameters for $Pb_2Sr_2RCu_3O_8$ with R $\equiv$ Sm derived from the Kramers-Kronig technique.

Mode		7 K	15 K	25 K	35 K	50 K	65 K	80 K	100 K	150 K	200 K	250 K	300 K
11^{ab}	ω_{TO}	496	493	495	497.5	498.5	497	497	500.5	501	503	505	504.5
	ω_{LO}	512	512	513	510.5	513	512	513	512.5	512	512	511	511
	S/ϵ_∞	0.066	0.079	0.074	0.053	0.059	0.061	0.065	0.049	0.044	0.036	0.024	0.026
12^{ab}	ω_{TO}	546.5	546	547.5	549	549	548.5	547	549.5	546	548	553.5	555
	ω_{LO}	556	556.5	556	555.5	555.5	555	555.5	553	553	552	555.5	
	S/ϵ_∞	0.035	0.039	0.031	0.024	0.024	0.024	0.031	0.013	0.026	0.015	0.007	

Table C.8: Detailed temperature dependence of the 'coupled' E$\|a,b$ phonon parameters for $Pb_2Sr_2RCu_3O_8$ with R $\equiv$ Eu derived from the Kramers-Kronig technique.

Mode		7 K	15 K	25 K	35 K	50 K	65 K	80 K	100 K	150 K	200 K	250 K	300 K
11^{ab}	ω_{TO}	486	486.5	485	486	487	489	487.5	489.5	490.5	491	494	488.5
	ω_{LO}	518	519	518.5	519	519	518.5	518.5	516.5	517	516	515.5	512
	S/ϵ_∞	0.136	0.138	0.138	0.140	0.136	0.124	0.131	0.113	0.111	0.104	0.089	0.099
12^{ab}	ω_{TO}	542.5	542	543.5	544	543.5	540	542	540	543.5	543.5	542.5	546
	ω_{LO}	564	564	566	564	562	562.5	561	561	560	561	559	557
	S/ϵ_∞	0.081	0.083	0.085	0.075	0.069	0.085	0.071	0.079	0.062	0.065	0.062	0.041

Table C.9: E$\|a,b$ phonon parameters for $Pb_2Sr_2RCu_3O_8$ with R $\equiv$ Gd at 300 and 80 K derived from the Kramers-Kronig technique.

Mode	T (K)	ω_{TO} (± 1 cm^{-1})	ω_{LO} (± 1 cm^{-1})	S/ϵ_∞
1^{ab}	300	630.5	662.5	0.104
	80	641	669	0.089
2^{ab}	300	356	434	0.486
	80	356	429	0.452
3^{ab}	300	302	321	0.130
	80	307.5	321.5	0.093
4^{ab}	300	280.5	285	0.032
	80	282.5	287.5	0.036
5^{ab}	300	215	245	0.299
	80	228	245.5	0.159
6^{ab}	300			
	80		224	
7^{ab}	300	196	204.5	0.089
	80	192	200.5	0.091
8^{ab}	300	165.5	175	0.118
	80	165	175.5	0.131
11^{ab}	300		506.5	
	80	497.5	511.5	0.057
12^{ab}	300		546	
	80	545	555.5	0.039

Table C.10: E$\|a,b$ phonon parameters for $Pb_2Sr_2RCu_3O_8$ with R $\equiv$ Tb at 300 and 80 K derived from the Kramers-Kronig technique.

Mode	T (K)	ω_{TO} ($\pm$1 cm^{-1})	ω_{LO} ($\pm$1 cm^{-1})	S/ϵ_∞
1^{ab}	300	615.5	647.5	0.107
	80	626.5	656.5	0.098
2^{ab}	300	349.5	436	0.556
	80	348	432	0.541
3^{ab}	300	303	322	0.275
	80	309	324.5	0.103
4^{ab}	300	285.5	289.5	0.028
	80	284	292.5	0.061
5^{ab}	300	236.5	246.5	0.086
	80	235	248	0.114
6^{ab}	300	218		
	80	221	224.5	0.032
7^{ab}	300	192.5	205.5	0.140
	80	189	198	0.098
8^{cb}	300	163	174.5	0.208
		154.5		
	80	161.5	173.5	0.183
		157.5		
11^{ab}	300	492.5	494	0.006
	80	495	511	0.066
12^{ab}	300	544	536	0
	80	544	552	0.030

Table C.11: E$\|a,b$ phonon parameters for $Pb_2Sr_2RCu_3O_8$ with R $\equiv$ Dy at 300 and 80 K derived from the Kramers-Kronig technique.

Mode	T (K)	ω_{TO} (± 1 cm^{-1})	ω_{LO} (± 1 cm^{-1})	S/ϵ_∞
1^{ab}	300	651		
	80	653		
2^{ab}	300	357	442	0.533
	80	357.5	432	0.460
3^{ab}	300	296.5	337	0.292
	80	310	345	0.239
4^{ab}	300	260	276	0.127
	80	259.5	293	0.275
5^{ab}	300	215		
	80	225.5		
7^{ab}	300	197.5		
	80	189.5		
8^{ab}	300	169.5		
	80			
9^{ab}	300			
	80	143		
11^{ab}	300	528		
	80	530		
12^{ab}	300	591		
	80	589.5		

Table C.12: E$\|a,b$ phonon parameters for $Pb_2Sr_2RCu_3O_8$ with R $\equiv$ Y at 300 and 80 K derived from the Kramers-Kronig technique.

Mode	T (K)	ω_{TO} ($\pm$1 cm^{-1})	ω_{LO} ($\pm$1 cm^{-1})	S/ϵ_∞
2^{ab}	300	365	454	0.547
	80	367	460	0.571
$3a^{ab}$	300	332	349	0.105
	80	331	353	0.137
$3b^{ab}$	300	303	320	0.115
	80	301	320	0.130
4^{ab}	300		288	
	80	289	293	0.028
11^{ab}	300	525		
	80	529		
12^{ab}	300	592		
	80	586		

Table C.13: E$\|a,b$ phonon parameters for $Pb_2Sr_2RCu_3O_8$ with R $\equiv$ Ho at 300 and 80 K derived from the Kramers-Kronig technique.

Mode	T (K)	ω_{TO} (± 1 cm^{-1})	ω_{LO} (± 1 cm^{-1})	S/ϵ_∞
1^{ab}	300	634		
	80	645.5		
2^{ab}	300	356	454	0.626
	80	353.5	449.5	0.617
3^{ab}	300	296	340	0.319
	80	305	345.5	0.283
4^{ab}	300	275	283	0.059
	80	267	296	0.229
$4b^{ab}$	300	244	258.5	0.122
	80			
5^{ab}	300	229		
	80			
7^{ab}	300	200		
	80			
8^{ab}	300	164	184.5	0.266
	80			
11^{ab}	300	524.5		
	80	527		
12^{ab}	300	589		
	80	580		

Table C.14: E$\|c$ phonon parameters for $Pb_2Sr_2RCu_3O_8$ with R $\equiv$ Nd at 300 and 80 K derived from oscillator fitting (brackets) and the Kramers-Kronig technique. Values for ϵ_∞ of 5.73 and 5.89 were obtained at 300 and 80 K respectively.

Mode	T (K)	ω_{TO} ($\pm$1 cm^{-1})		ω_{LO} ($\pm$1 cm^{-1})		Γ ($\pm$1 cm^{-1})		S	
1^c	300	557	(562)	600	(577)	35	(31)	0.3 $\pm$ 0.1	(0.3)
	80	563	(564)	601	(577)	20	(19)	0.3 $\pm$ 0.1	(0.3)
2^c	300	521	(520)	533	(530)	28 $\pm$ 2	(22.5)	0.3 $\pm$ 0.1	(0.2)
	80	524	(524)	538	(535)	16	(16.5)	0.2 $\pm$ 0.1	(0.3)
3^c	300	329	(327)	451	(477)	17	(21.5)	5.7 $\pm$ 0.4	(6.5)
	80	332	(330)	451	(476)	7	(13.5)	4.7 $\pm$ 0.7	(6.3)
4^c	300	208	(209)	213	(221)	11	(15.5)	0.5 $\pm$ 0.2	(0.7)
	80	211	(212)	218	(224)	11	(11.5)	0.6 $\pm$ 0.2	(0.7)
5^c	300	158	(158)	164	(173)	6	(5.5)	1.1 $\pm$ 0.3	(1.1)
	80	161	(161)	166	(175)	3.5	(3.5)	1.0 $\pm$ 0.4	(1.1)
6^c	300	145	(145)	146	(148)	4	(4)	0.2 $\pm$ 0.2	(0.3)
	80	147	(147)	148	(150)	4	(4)	0.2 $\pm$ 0.1	(0.2)

Table C.15: E$\|$ c phonon parameters for $Pb_2Sr_2RCu_3O_8$ with R $\equiv$ Sm at 300 and 80 K derived from oscillator fitting (brackets) and the Kramers-Kronig technique. Values for ϵ_∞ of 5.34 and 5.64 were obtained at 300 and 80 K respectively.

Mode	T	ω_{TO}		ω_{LO}		Γ		S	
	(K)	($\pm$1	cm^{-1})	($\pm$1	cm^{-1})	($\pm$1	cm^{-1})		
1^c	300	558	(561)	597	(575)	30.5	(29)	0.3 $\pm$ 0.1	(0.3)
	80	560.5	(562)	598	(576)	16	(17)	0.3 $\pm$ 0.1	(0.3)
2^c	300	519	(517)	531	(528)	17.5	(18.5)	0.2 $\pm$ 0.1	(0.2)
	80	522	(522)	536.5	(534)	12.5	(11.5)	0.3 $\pm$ 0.1	(0.3)
3^c	300	324	(322)	448	(472)	17	(24.5)	5.3 $\pm$ 0.4	(6.1)
	80	326.5	(325)	446	(469)	9.5	(13.5)	5.7 $\pm$ 0.7	(6.1)
4^c	300	204	(205)	208	(217)	10	(13.5)	0.5 $\pm$ 0.1	(0.6)
	80	206	(206)	209.5	(217)	6	(8.5)	0.5 $\pm$ 0.1	(0.6)
5^c	300	158	(158)	162.5	(171)	5.5	(4.5)	1.1 $\pm$ 0.3	(0.9)
	80	159.5	(159)	164.5	(172)	3	(2.5)	1.1 $\pm$ 0.4	(1.0)
6^c	300	145	(146)	145.5	(151)	10 $\pm$ 2	(12.5)	0.4 $\pm$ 0.1	(0.4)
	80	145.5	(146)	146.5	(150)	5 $\pm$ 2	(6.5)	0.3 $\pm$ 0.1	(0.3)

Table C.16: E$\|c$ phonon parameters for $Pb_2Sr_2RCu_3O_8$ with R $\equiv$ Eu at 300 and 80 K derived from oscillator fitting (brackets) and the Kramers-Kronig technique. Values for ϵ_∞ of 5.40 and 5.86 were obtained at 300 and 80 K respectively.

Mode	T	ω_{TO}		ω_{LO}		Γ		S	
	(K)	($\pm$1	cm^{-1})	($\pm$1	cm^{-1})	($\pm$1	cm^{-1})		
1^c	300	556	(561)	597	(575)	29.5	(28)	0.3 $\pm$ 0.1	(0.3)
	80	560	(562)	597.5	(576)	16	(16.5)	0.3 $\pm$ 0.1	(0.3)
2^c	300	516.5	(516)	531	(527)	17	(17.5)	0.2 $\pm$ 0.1	(0.2)
	80	521	(521)	535.5	(534)	12.5	(10.5)	0.3 $\pm$ 0.1	(0.3)
3^c	300	321.5	(320)	446.5	(471)	18	(25.5)	5.9 $\pm$ 0.4	(6.3)
	80	324	(322)	443.5	(466)	10	(14)	5.8 $\pm$ 0.7	(6.4)
4^c	300	202.5	(203)	206	(215)	10	(13)	0.5 $\pm$ 0.2	(0.6)
	80	205	(205)	208	(215)	6	(7)	0.5 $\pm$ 0.2	(0.6)
5^c	300	157	(157)	162.5	(171)	4.5	(4.5)	1.0 $\pm$ 0.3	(1.0)
	80	159	(159)	164	(172)	2.5	(2)	1.0 $\pm$ 0.3	(1.0)
6^c	300	144.5	(145)		(148)	4	(4)	0.3 $\pm$ 0.2	(0.2)
	80		(146)		(148)		(4)		(0.2)

Table C.17: E$\|c$ phonon parameters for $Pb_2Sr_2RCu_3O_8$ with R $\equiv$ Gd at 300 and 80 K derived from oscillator fitting (brackets) and the Kramers-Kronig technique. Values for ϵ_∞ of 5.92 and 5.78 were obtained at 300 and 80 K respectively.

Mode	T (K)	ω_{TO} ($\pm$1 cm^{-1})		ω_{LO} ($\pm$1 cm^{-1})		Γ ($\pm$1 cm^{-1})		S	
1[c]	300	558.5	(561)	598	(576)	26.5	(28)	0.3 $\pm$ 0.1	(0.3)
	80	561	(561)	596.5	(574)	14	(17)	0.3 $\pm$ 0.1	(0.3)
2[c]	300	515.5	(516)	529.5	(526)	17	(15.5)	0.3 $\pm$ 0.1	(0.2)
	80	520	(520)	535.5	(532)	11	(10)	0.3 $\pm$ 0.1	(0.3)
3[c]	300	323	(319)	446.5	(469)	20.5	(25.5)	6.3 $\pm$ 0.5	(6.9)
	80	321.5	(321)	443	(467)	9	(16)	5.8 $\pm$ 0.7	(6.4)
4[c]	300	201	(201)	204.5	(211)	9	(10.5)	0.5 $\pm$ 0.2	(0.6)
	80	203.5	(203)	207	(213)	5.5	(6)	0.5 $\pm$ 0.2	(0.6)
5[c]	300	157	(157)	162	(169)	4	(4)	0.9 $\pm$ 0.3	(1.0)
	80	158.5	(159)	163.5	(172)	2.5	(2)	1.1 $\pm$ 0.5	(1.0)
6[c]	300	145	(146)	146	(152)	6	(11.5)	0.3 $\pm$ 0.3	(0.5)
	80	146	(146)	146.5	(149)	5	(5)	0.3 $\pm$ 0.1	(0.2)

Table C.18: E$\|c$ phonon parameters for $Pb_2Sr_2RCu_3O_8$ with R $\equiv$ Dy at 300 and 80 K derived from oscillator fitting (brackets) and the Kramers-Kronig technique. Values for ϵ_∞ of 6.25 and 7.6 were obtained at 300 and 80 K respectively. In addition, a small Drude background with $\omega_p = 1370$ and $\Gamma = 2840$ cm^{-1} at 300 K and $\omega_p = 1370$ and $\Gamma = 3570$ cm^{-1} at 80 K was included in the fit.

Mode	T	ω_{TO}		ω_{LO}		Γ		S	
	(K)	($\pm$1	cm^{-1})	($\pm$1	cm^{-1})	($\pm$1	cm^{-1})		
1[c]	300	559	(562)	593.5	(572)	32	(22)	0.3 $\pm$ 0.1	(0.2)
	80	561.5	(565)	595	(577)	24	(17)	0.3 $\pm$ 0.1	(0.3)
2[c]	300	511	(510)	530	(526)	25.5	(28.5)	0.3 $\pm$ 0.2	(0.4)
	80	517.5	(517)	534.5	(532)	22.5	(18)	0.3 $\pm$ 0.1	(0.4)
3[c]	300	318.5	(318)	438	(458)	37	(28.5)	6.8 $\pm$ 0.5	(6.7)
	80	322.5	(321)	432	(453)	26	(26.5)	6.8 $\pm$ 0.5	(7.1)
4[c]	300	199	(196)	204	(200)	17.5	(15)	0.3 $\pm$ 0.3	(0.3)
	80	197.5	(198)	200	(204)	14.5	(15)	0.5 $\pm$ 0.3	(0.5)
5[c]	300	156	(156)	160	(164)	5	(6)	0.6 $\pm$ 0.3	(0.6)
	80	157	(157)	161.5	(167)	7	(6)	1.0 $\pm$ 0.3	(1.0)
6[c]	300	148	(148)	148.5	(151)		(7)		(0.3)
	80	146.5	(148)	147.5	(151)	5	(7)	0.2 $\pm$ 0.2	(0.3)

Bibliography

[1] L.R. Testardi, J.H. Wernich, and W.A. Royer, Sol. St. Comm. **15**, 1, (1974).

[2] J.G. Bednorz and K.A. Müller, Z. Phys. B **64**, 189, (1986).

[3] J.M. Tarascon, P. Barboux, L.H. Greene, B.G. Bagley, G.W. Hull, Y. LePage, and W.R. McKinnon, Physica C **153- 155**, 566, (1988).

[4] P.W. Anderson, Science **235**, 1196, (1987).

[5] C.T. Chen, F. Sette, Y. Ma, M.S. Hybertsen, E.B. Stechel, W.M.C. Foulkes, M. Schluter, S.-W. Cheong, A.S. Cooper, L.W. Rupp, Jr., B. Batlogg, Y.L. Soo, Z.H. Ming, A. Krol, and Y.H. Kao, Phys. Rev. Lett. **66**, 104, (1991).

[6] A. Fujimori, E. Takayama-Muromachi, Y. Uchida, and B. Okai, Phys. Rev. B **35**, 8814, (1987).

[7] N.P. Ong, Z.Z. Wang, J. Clayhold, J.M. Tarascon, L.H. Greene, and W.R. McKinnon, Phys. Rev. B **35**, 8807, (1987).

[8] T. Takahashi, H. Matsuyama, H. Katayama-Yoshida, Y. Okabe, S. Hosoya, K. Seki, H. Fujimoto, M. Sato, and H. Inokuchi, Nature **334**, 691, (1988).

[9] S. Uchida, T. Ido, H. Takagi, T. Arima, Y. Tokura, and S. Tajima, Phys. Rev. B **43**, 7942, (1991).

[10] H. Eskes, M.B.J. Meinders, and G.A. Sawatzky, Phys. Rev. Lett. **67**, 1035, (1991).

[11] J. Orenstein, G.A. Thomas, D.H. Rapkine, C.B. Bethea, B.F. Levine, R.J. Cava, E.A. Reitman, and D.W. Johnson, Jr., Phys. Rev. B 36, 729, (1987).

[12] S.L. Herr, K. Kamarás, C.D. Porter, M.G. Doss, D.B. Tanner, D.A. Bonn, J.E. Greedan, C.V. Stager, and T. Timusk, Phys. Rev. B 36, 733, (1987).

[13] S.L. Cooper, G.A. Thomas, A.J. Millis, P.E. Sulewski, J. Orenstein, D.H. Rapkine, S-W. Cheong, and P.L. Trevor, Phys. Rev. B 42, 10785, (1990).

[14] K. Kitazawa and S. Tajima in *Some Aspects of Superconductivity*, edited by L.C. Gupta (Nova Scientific Publ., USA, 1990).

[15] G. Calestanti and C. Rizzoli, Nature 328, 606, (1987).

[16] G. Burns, G.V. Chandrashekhar, F.H. Dacol, M.W. Shafer, and P. Strobel, Sol. St. Comm. 67, 603, (1988).

[17] S. Martin, A.T. Fiory, R.M. Fleming, L.F. Schneemeyer, and J.V. Waszczak, Phys. Rev. Lett. 60, 2194 (1988).

[18] D.R. Harshman and A.P. Mills, Jr., Phys. Rev. B 45, 10684, (1992).

[19] R.J. Cava, B. Batlogg, J.J. Krajewski, L.W. Rupp, L.F. Schneemeyer, T. Siegrist, R.B. vanDover, P. Marsh, W.F. Peck, Jr., P.K. Gallagher, S.H. Glarum, J.H. Marshall, R.C. Farrow, J.V. Waszczak, R. Hull, and P. Trevor, Nature 336, 211, (1988).

[20] J.S. Xue, M. Reedyk, J.E. Greedan, and T. Timusk, (accepted for publication in J. of Sol. St. Chem.).

[21] J.S. Xue, J.E. Greedan, and M. Maric, (accepted for publication in J. of Sol. St. Chem.).

[22] J.S. Xue, Ph.D. Thesis, McMaster University, 1992.

[23] J.S. Xue, M. Reedyk, A. Dabkowski, H. Dabkowska, J.E. Greedan, and C.H. Chen, J. Crys. Growth **113**, 371, (1991).

[24] M. Reedyk, T. Timusk, J.S. Xue, and J.E. Greedan, Phys. Rev. B **45**, 7406, (1992).

[25] A.C. Rose-Innes, and E.H. Rhoderick, *Introduction to Superconductivity* (Pergamon Press, Toronto, 1978).

[26] M. Tinkham, *Introduction to Superconductivity* (Robert E. Krieger Publishing Company, Malabar, Florida, 1980).

[27] C. P. Bean, Rev. Mod. Phys. **36**, 31, (1964).

[28] J.S. Xue, private communication.

[29] M.B. Salamon in *Physical Properties of High Temperature Superconductors* I, edited by Donald M. Ginsberg (World Scientific, Singapore, 1989).

[30] M. Naito, A. Matsuda, K. Kitazawa, S. Kambe, I. Tanaka, and H. Kojima, Phys. Rev. B **41**, 4823, (1990).

[31] G. W. Crabtree, Phys. Rev. B **16**, 1117, (1977).

[32] U. Welp, W. K. Kwok, G. W. Crabtree, K. G. Vandervoort, and J. Z. Liu, Phys. Rev. Lett. **62**, 1908, (1989).

[33] K.G. Vandervoort, U. Welp, J.E. Kessler, H. Claus, G.W. Crabtree, W.K. Kwok, A. Umezawa, B.W. Veal, J.W. Downey, and A.P. Paulikas, Phys. Rev. B **43**, 13042, (1991).

[34] W.K. Kwok, U. Welp, G.W. Crabtree, K.G. Vandervoort, R. Hulscher, Y. Zheng, B. Dabrowski, and D.G. Hinks, Phys. Rev. B **40**, 9400, (1989).

[35] D.C. Johnston and J.H. Cho, Phys. Rev. B **42**, 8710, (1990).

[36] W.E. Lawrence and S. Doniach, *Proc. 12th Intern. Conf. on Low Temp. Physics - Kyoto, Japan, 1970*, edited by E. Kanda (Keigaku, Tokyo, 1971).

[37] W.C. Lee, R.A. Klemm, and D.C. Johnston, Phys. Rev. Lett. 63, 1012, (1989), and W.C. Lee, J.H. Cho, and D.C. Johnston, Phys. Rev. B 43, 457, (1991).

[38] K. Kanoda, T. Kawagoe, M. Hasumi, T. Takahashi, S. Kagoshima, and T. Mizoguchi, J. Phys. Soc. Jpn. 57, 1554, (1988).

[39] Z. Hao, J.R. Clem, M.W. McElfresh, L. Civale, A.P. Malozemoff, and F. Holtzberg, Phys. Rev. B 43, 2844, (1991).

[40] J.B. Bieri and K. Maki, Phys. Rev. B 42, 4854, (1990), B. Zhao, K. Shiraki, Y. Horie, S. Mase, Y. Zhang, Y. Zhao, L. Chen, P. Xu, and L. Li, Physica C 167, 42, (1990), Y. Matsuda, T. Hirai, S. Komiyama, T. Tarashima, Y. Bando, K. Iijima, K. Yamamoto, and K. Hirata, Phys. Rev. B 40, 5176, (1989), M. Hikita and M. Suzuki, Phys. Rev. B 39, 4756, (1989), and B. Oh, A.D. Kent, M. Naito, M.R. Beasley, T.H. Geballe, R.H. Hammond, A. Kapitulnik, and J.M. Graybeal, Phys. Rev. B 37, 7861, (1988).

[41] E.J. Nicol, private communication.

[42] J.H. Brewer, private communication.

[43] L. Krusin-Elbaum, R. L. Greene, F. Holtzberg, A. P. Malozemoff, and Y. Yeshurun, Phys. Rev. Lett. 62, 217, (1989); B. Pümpin, H. Keller, W. Kündig, W. Odermatt, I. M. Savić, J. W. Schneider, H. Simmler, P. Zimmermann, E. Kaldis, S. Rusiecki, Y. Maeno, and C. Rossel, Phys. Rev. B 42, 8019, (1990).

[44] E. W. Scheidt, C. Hucho, K. Lüders, and V. Müller, Sol. St. Comm. 71, 505, (1989).

[45] C. M. Foster, K. F. Voss, T. W. Hagler, D. Mihailović, A. J. Heeger, M. M. Eddy, W. L. Olson, and E. J. Smith, Sol. St. Comm. 76, 651, (1990).

[46] S. Mitra, J. H. Cho, W. C. Lee, D. C. Johnston, and V. G. Kogan, Phys. Rev. B 40, 2674, (1989).

[47] L. Krusin-Elbaum, A. P. Malozemoff, Y. Yeshurun, D. C. Cronemeyer, and F. Holtzberg, Phys. Rev. B 39, 2936, (1989).

[48] A. Schilling, F. Hulliger and H. R. Ott, Physica C 168, 272, (1990).

[49] K. Kamarás, S. L. Herr, C. D. Porter, N. Tache, D. B. Tanner, S. Etemad, T. Venkatesan, E. Chase, A. Inam, X. D. Wu, M. S. Hegde, and B. Dutta, Phys. Rev. Lett. 64, 84, (1990).

[50] N. W. Ashcroft and N. D. Mermin, *Solid State Physics* (Holt, Rinehart and Winston, Philadelphia, 1976).

[51] L.J. van der Pauw, Phillips Res. Rep. 13, 1, (1958).

[52] M. Reedyk, M.Sc. Thesis, McMaster University, 1988.

[53] J. Hornstra and L.J. van der Pauw, J. Electron. Control 7, 169, (1959).

[54] Y. Iye, T. Sakakibara, N. Miura, H. Takeya, and H. Takei, Physica C 153-155, 26, (1988).

[55] T.A. Friedmann, M.W. Rabin, J. Giapintzakis, J.P. Rice, and D.M. Ginsberg, Phys. Rev. B 42, 6217, (1990).

[56] T.T.M. Palstra, B. Batlogg, R.B. van Dover, L.F. Schneemeyer, and J.V. Waszczak, Phys. Rev. B 41, 6621, (1990).

[57] K.C. Woo, K.E. Gray, T.T. Kampwirth, J.H. Kang, S.J. Stein, R. East, and D.M. McKay, Phys. Rev. Lett. 63, 1877, (1989).

[58] B. Oh *et. al.*, Phys. Rev. B 37, 7861, (1988).

[59] Y. Yeshurun, and A.P. Malozemoff, Phys. Rev. Lett. 60, 2202, (1988).

[60] R.C. Budhani, D.O. Welch, M. Suenaga, and R.L. Sabatini, Phys. Rev. Lett. 64, 1666, (1990).

[61] K.F. Renk, B. Gorshunov, J. Schutzmann, A. Pruckl, B. Brunner, J. Betz, S. Orbach, N. Klein, G. Muller, and H. Piel, Europhys. Lett. 15, 661, (1991).

[62] J. Orenstein, G.A. Thomas, A.J. Millis, S.L. Cooper, D.H. Rapkine, T. Timusk, L.F. Schneemeyer, and J.V. Waszczak, Phys. Rev. B 42, 6342, (1990).

[63] L.D. Rotter, Z. Schlesinger, R.T. Collins, F. Holtzberg, C. Field, U. Welp, G.W. Crabtree, J.Z. Liu, Y. Fang, K.G. Vandervoort, and S. Flesher, Phys. Rev. Lett. 67, 2741, (1991).

[64] M. Reedyk, D.A. Bonn, J.D. Garrett, J.E. Greedan, C.V. Stager, and T. Timusk, Phys. Rev. B. 38, 11981, (1988).

[65] D. Miller and P.L. Richards, (submitted to Phys. Rev. B).

[66] T. Pham, M.W. Lee, H.D. Drew, U. Welp, and Y. Fang, Phys. Rev. B 44, 5377, (1991).

[67] C.C. Homes, M. Reedyk, D.A. Crandles, T. Timusk, (submitted to J. Appl. Optics).

[68] J. Kircher, M. Cardona, M. Garriga, B. Nick, M. Dürrler, A. Zibold, and H.P. Geserich, Physica C 174, 377, (1991).

[69] W.A. Challenger, P.L. Richards, S.C. Zilio, and H.L. Garvin, Infrared Physics, 20, 215, (1980).

[70] H. Romberg, N. Nücker, J. Fink, Th. Wolf, X.X. Xi, B. Koch, H.P. Geserich, M. Dürrler, W. Assmus, and B. Gegenheimer, Z. Phys. B 78, 367, (1990).

[71] S.L. Cooper, A.L. Kotz, M.A. Karlow, M.V. Klein, W.C. Lee, J. Giapintzakis, and D.M. Ginsberg, Phys. Rev. B 45, 2549, (1992).

[72] W. Kress, J. Prade, U. Schröder, A.D. Kulkarni, and F.W. de Wette, Physica C 162-164, 1345, (1989).

[73] E.T. Heyen, R. Liu, M. Garriga, B. Gegenheimer, C. Thomsen, and M. Cardona, Phys. Rev. B 41, 830, (1990).

[74] L.F. Mattheiss, and D.R. Hamann, Phys. Rev. B 39, 4780, (1989).

[75] D.B. Romero, C.D. Porter, D.B. Tanner, L. Forro, D. Mandrus, L. Mihaly, G.L. Carr, and G.P. Williams, Phys. Rev. Lett. 68, 1590, (1992).

[76] P. Monthoux, A.V. Balatsky, and D. Pines, Phys. Rev. Lett. 67, 3448 (1991).

[77] T.E. Mason, G. Aeppli, and H.A. Mook, Phys. Rev. Lett. 68, 1414 (1992).

[78] A.S. Barker, Jr., B.I. Halperin, and T.M. Rice, Phys. Rev. Lett. 20, 384, (1968).

[79] D.A. Bonn, J.D. Garrett, and T. Timusk, Phys. Rev. Lett. 61, 1305 (1988).

[80] G.A. Thomas in *High Temperature Superconductivity*, Proceedings of the Thirty-Ninth Scottish Universities Summer School in Physics, St. Andrews, 1991, D.P. Tunstall, W. Barford and P. Osborne, Eds., Adam Hilger (1992).

[81] P.J. Hirschfeld, P. Wölfe, J.A. Sauls, D. Einzel, W.O. Putikka, Phys. Rev. B 40, 6695 (1989).

[82] R.A. Klemm, K. Scharnberg, D. Walker, and C.T. Rieck, Z. Phys. B 72, 139, (1988).

[83] J.P. Carbotte, private communication.

[84] B. Koch, M. Dürrler, Th. Wolf, G. Roth, G. Zachmann, Sol. St. Comm. 71, 495, (1989).

[85] R.T. Collins, Z. Schlesinger, F. Holtzberg, and C. Field, Phys. Rev. Lett. 63, 422, (1989).

[86] M. Bauer, Ph.D. Thesis, Tübingen, 1990.

[87] C.C. Homes, N. Cao, T. Timusk, R. Liang, and W.N. Hardy, (submitted to Phys. Rev. Lett.).

[88] K. Tamasaku, Y. Nakamura, and S. Uchida, (submitted to Phys. Rev. Lett.).

[89] M.P.A. Fisher, G. Grinstein, and S.M. Girvin, Phys. Rev. Lett. 64, 587, (1990).

[90] D. Mandrus, L. Forro, C. Kendziora, and L. Mihaly, Phys. Rev. B 44, 2418, (1991).

[91] G.T. Seidler, T.F. Rosenbaum, and B.W. Veal, Phys. Rev. B 45, 10162, (1992).

[92] D.A. Brawner, Z.Z. Wang, and N.P. Ong, Phys. Rev. B 40, 9329, (1989).

[93] Y.H. Kim, A.J. Heeger, L. Acedo, G. Stucky, and F. Wudl, Phys. Rev. B 36, 7252, (1987).

[94] Y.H. Kim, C.M. Foster, A.J. Heeger, S. Cox, and G. Stucky, Phys. Rev. B 38, 6478, (1988).

[95] H.J. Ye, R.P. McCall, W.E. Farneth, E.M. McCarron III, and A.J. Epstein, Phys. Rev. B 43, 10574, (1991).

[96] T. Arima, K. Kikuchi, M. Kasuya, S. Koshihara, Y. Tokura, T. Ido, and S. Uchida, Phys. Rev. B 44, 917, (1991).

[97] This is the Lyddane-Sachs-Teller relation. A discussion can be found in most introductory solid state physics texts. (See for example reference [50]).

[98] S. Tajima, T. Ido, S. Ishibashi, T. Itoh, H. Eisaki, Y. Mizuo, T. Arima, H. Takagi, and S. Uchida, Phys. Rev. B 43, 10496, (1991).

[99] M. Bauer, I.B. Ferreira, L. Genzel, M. Cardona, P. Murugaraj, and J. Maier, Sol. St. Comm. 72, 551, (1989).

[100] M.K. Crawford, W.E. Farneth, E.M. McCarron III, and R.K. Bordia, Phys. Rev. B 38, 11382, 1988.

[101] C. Thomsen, M. Cardona, R. Liu, Hj. Mattausch, W. König, F. Garciá-Alvarado, B. Suárez, E. Morán, and M. Alario-Franco, Sol. St. Comm. 69, 857, (1989).

[102] C.C. Homes, private communication.

[103] G. Burns, F.H. Dacol, C. Field, and F. Holtzberg, Physica C 181, 37, (1991).

[104] T. Timusk and D.B. Tanner, Optical Properties of High-Temperature Superconductors, in *Physical Properties of High-Temperature Superconductors*, Donald M. Ginsberg, editor, (World Scientific, Singapore, 1989).

[105] D.B. Tanner and T. Timusk, Optical Properties of High-Temperature Superconductors, in *Physical Properties of High-Temperature Superconductors III*, Donald M. Ginsberg, editor, (World Scientific, Singapore, 1992).

[106] Z. Schlesinger, R.T. Collins, F. Holtzberg, C. Feild, S.H. Blanton, U. Welp, G.W. Crabtree, Y. Fang, and J.Z. Liu, Phys. Rev. Lett. 65, 801, (1990).

[107] T. Timusk and D.B. Tanner, Physica C 169, 425, (1990).

[108] S.L. Cooper, G.A. Thomas, A.J. Millis, S.L. Cooper, D. Rapkine, T. Timusk, L.F. Schneemeyer, and J.V. Waszszak, Phys. Rev. B 40, 11358, (1989).

[109] V.M. Burlakov, S.V. Shulga, J. Keller, and K.F. Renk, Physica C 190, 304, (1992).

[110] M. Shimada, M. Shimizu, J. Tanaka, I. Tanaka, and H. Kojima, Physica C 193, 277, (1992).

[111] R.A. Hughes, Y. Lu, T. Timusk, and J.S. Preston, (accepted for publication, Phys. Rev. B).

[112] D.A. Crandles, private communication.

[113] U. Fano, Phys. Rev. 124, 1866, (1961).

[114] M.J. Rice, Phys. Rev. Lett. 37, 36, (1976).

[115] T. Timusk, C.D. Porter, and D.B. Tanner, Phys. Rev. Lett. 66, 663, (1991).

[116] A. Girlando, and C. Pecile, Spectrochim. Acta 29A, 1859, (1973).

[117] A. Brau, P. Brüesch, J.P. Farges, W. Hinz, and D. Kuse, Phys. Status Solidi (b) 62, 615, (1974).

[118] M.J. Rice, L. Pietronero and P. Brüesch, Sol. St. Comm. 21, 757, (1977).

[119] C.C. Homes and J.E. Eldridge, Phys. Rev. B 42, 9522, (1990).

[120] B. Horovitz, Sol. St. Comm. 41, 729, (1982).

[121] H.K. Ng, T. Timusk, and K. Bechgaard, Phys. Rev. B 30, 5842, (1984).

[122] S. Sugai, Physica C 185-189, 76 (1991).

[123] Ran Liu, M. Cardona, B. Gegenheimer, E.T. Heyen, and C. Thomsen, Phys. Rev. B 40, 2654, (1989).

[124] E. Altendorf, private communication.

[125] J.C. Irwin, private communication.

[126] E. Burstein, Interaction of Phonons with Photons: Infrared, Raman, and Brillouin Spectra, in *Phonons and Phonon Interactions*, Thor A. Bak, ed., (W.A. Benjamin, Inc., New York, 1964).

[127] M. Cardona, private communication.

[128] E.T. Heyen, R. Wegerer, and M. Cardona, Phys. Rev. Lett. 67, 144, (1991); Physica C 185-189, 1043, (1991); E.T. Heyen, R. Wegerer, E. Schönherr, and M. Cardona, Phys. Rev. B 44, 10195, (1991).

[129] The curve for the non-Drude component of σ_1^{ab} of $Nd_{2-x}Ce_xCuO_{4-\delta}$ has been reproduced from Ref. [111]. The *c*-axis dielectric loss function of $Nd_{2-x}Ce_xCuO_{4-\delta}$ was obtained by performing a Kramers-Kronig (KK) analysis of the reflectance measured by S. Tajima *et. al.*, (Ref. [98]), with high frequency extensions taken from the work of E.V. Abel' *et. al.*, Sol. St. Comm. 79, 931, (1991) and S. Uchida *et. al.*, (Ref. [9]). σ_1^{ab} of $Tl_2Ba_2CaCu_2O_8$ is the 10 K result from the work of Ref. [45], while $\Im(-1/\epsilon^c)$ was obtained via KK analysis of the reflectance of T. Zetterer *et. al.* J. Opt. Soc. Am. B 6, 420, (1989), for polycrystalline $Tl_2Ba_2CaCu_2O_8$ and subtracting a Drude component of $\omega_p = 2776$ cm^{-1}, $\Gamma = 162$ cm^{-1}, (obtained by fitting the optical conductivity to a Drude-Lorentz model), from the derived dielectric function. This process should yield the optical properties of the *c*-axis phonons since the reflectance of polycrystalline samples is known to be dominated by the A_u modes. Similarily, while the *ab*-plane conductivity for $Bi_2Sr_2CaCu_2O_8$ is the non-Drude component of the 100 K result of Ref. [64], the loss function is derived from KK analysis of the 100 K reflectance for a polycrystalline sample, [K. Kamáras *et. al.*, Phys. Rev. B 43, 11381, (1991)], and subtracting a Drude component of $\omega_p = 6200$ cm^{-1}, $\Gamma = 85$ cm^{-1}, again obtained from a fit to the optical conductivity.

[130] G.D. Mahan, Phys. Rev. B 43, 2934, (1991).

[131] Private communication from D. Tanner to T. Timusk.

[132] Comparisons to neutron data are made in Refs. [24], [111] and [115]. A discussion of the relationship to tunnelling measurements can be found in Ref. [111].

[133] R. Currat, A.J. Dianoux, P. Monceau, and J.J. Capponi, Phys. Rev. B 40, 11362, (1989).

[134] Y. Watanabe, D.C. Tsui, J.T. Birmingham, N.P. Ong, and J.M. Tarascon Phys. Rev. B 43, 3026, (1991).

[135] D.A. Crandles, T. Timusk, and J.E. Greedan Phys. Rev B 44, 13250, (1991).

[136] Z. Kakol, J. Spalek, and J.M. Honig, J. of Sol. St. Chem. 79, 288, (1989).

[137] R.J. Cava, B. Batlogg, T.T. Palstra, J.J. Krajewski, W.F. Peck, Jr., A.P. Ramirez, and L.W. Rupp, Jr., Phys. Rev. B 43, 1229, (1991).

[138] B. Morosin, D.S. Ginley, P.F. Hlava, M.J. Carr, R.J. Baughman, J.E. Schirber, E.L. Venturini, and J.F. Kwak, Physica C 156, 413, (1988).

[139] P.W. Anderson, Physica C 185-189, 11, (1991).

[140] Y.J. Uemura, G.M. Luke, B.J. Sternlieb, J.H. Brewer, J.F. Carolan, W.N. Hardy, R. Kadono, J.R. Kempton, R.F. Kiefl, S.R. Kreitzman, P. Mulhern, T.M. Riseman, D. Ll. Williams, B.X. Yang, S. Uchida, H. Takagi, J. Gopalakrishnan, A.W. Sleight, M.A. Subramanian, C.L. Chien, M.Z. Cieplak, Gang Xiao, V.Y. Lee, B.W. Statt, C.E. Stronach, W.J. Kossler, and X.H. Yu, Phys. Rev. Lett. 62, 2317, (1989).

[141] G.A. Thomas, D.H. Rapkine, S.L. Cooper, S.-W. Cheong, A.S. Cooper, L.F. Schneemeyer, and J.V. Waszczak, Phys. Rev. B 45, 2474, (1992).

[142] P. Mendels, X. Labouze, G. Collin, and H. Alloul, Physica C 185-189, 1191, (1991).

[143] F. Wooten, *Optical Properties of Solids* (Academic Press, New York, 1972).

[144] C. Kittel, *Introduction to Solid State Physics, 5th ed.* (John Wiley and Sons, New York, 1976).

[145] W. R. Hunter, in *Handbook of Optical Constants of Solids*, E. D. Palik, ed., (Academic Press, Orlando, 1985).

[146] R. F. Potter, in *Optical Properties of Solids*, S. Nudelman and S. S. Mitra, eds., (Plenum Press, New York, 1969).

[147] E. Hecht and A. Zajac, *Optics* (Addison-Wesley Publishing Company, Reading Ma., 1979), pp. 75-76.

[148] F. Stern, Solid State Physics 15, 300, 1963.

[148] M. Cardona, in *Optical Properties of Solids*, S. Nudelman and S. S. Mitra, eds., (Plenum Press, New York, 1969).